ABSTRACT

Title of dissertation: MODELING AND DESIGN OF MICROWAVE-MILLIMETERWAVE FILTERS AND MULTIPLEXERS

Yunchi Zhang, Doctor of Philosophy, 2006

Dissertation directed by: Professor Kawthar A. Zaki
Department of Electrical and Computer Engineering

Modern communication systems require extraordinarily stringent specifications on microwave and millimeter-wave components. In mobile and integrated communication systems, miniature, ultra-wideband and high performance filters and multiplexers are required for microwave integrated circuits (MICs) and monolithic microwave integrated circuits (MMICs). In satellite communications and wireless base stations, small volume, high quality, high power handling capability and low cost filters and multiplexers are required. In order to meet these requirements, three aspects are mainly pursued: design innovations, precise CAD procedures, and improved manufacturing technologies. This dissertation is, therefore, devoted to creating novel filter and multiplexer structures, developing full-wave modeling and design procedures of filters and multiplexers, and integrating waveguide structures for MICs and MMICs in Low Temperature Co-fired Ceramic (LTCC) technology.

In order to realize miniature and broadband filters, novel multiple-layer cou-

pled stripline resonator structures are proposed for filter designs. The essential of the resonators is investigated, and the design procedure of the filters is demonstrated by examples. Rigorous full-wave mode matching program is developed to model the filters and optimize the performance. The filters are manufactured in LTCC technology to achieve high-integration. In order to obtain better quality than planar structures, new ridge waveguide coupled stripline resonator filters and multiplexers are introduced for LTCC applications. Planar and waveguide structures are combined in such filter and multiplexer designs to improve the loss performance. A rigorous CAD procedure using mode matching technique is developed for the modeling and design. To design wideband multiplexers for LTCC applications, ridge waveguide divider junctions are presented to achieve wideband matching performance. Such junctions and ridge waveguide evanescent-mode filters are cascaded together to realize the multiplexer designs. The design methodology, effects of spurious modes and LTCC manufacturing procedure are discussed. Additional important issues of microwave filter and multiplexer designs addressed in this dissertation are: (1) Systematic approximation, synthesis and design procedures of multiple-band coupled resonator filters. Various filter topologies are created by analytical methods, and utilized in waveguide and dielectric resonator filter designs. (2) Dual-mode filter designs in circular and rectangular waveguides. (3) Systematic tuning procedure of quasi-elliptic filters. (4) Improvement of filter spurious performance by stepped impedance resonators (SIRs). (5) Multipaction effects in waveguide structures for space applications.

MODELING AND DESIGN OF MICROWAVE-MILLIMETERWAVE FILTERS AND MULTIPLEXERS

by

Yunchi Zhang

Dissertation submitted to the Faculty of the Graduate School of the
University of Maryland, College Park in partial fulfillment
of the requirements for the degree of
Doctor of Philosophy
2006

Advisory Committee:

Professor Kawthar A. Zaki, Chair/Advisor
Professor Christopher Davis
Professor Isaak D. Mayergoyz
Professor Neil Goldsman
Professor Amr Baz

DEDICATION

To my parents and Ningning.

ACKNOWLEDGMENTS

I would like to express my deep and sincere gratitude to my advisor Prof. Kawthar A. Zaki for her invaluable guidance and enthusiastic support during the course of this work. Her wide knowledge and logical way of thinking have been of great value for me. Her understanding, encouraging and trusting have provided a good basis for the present thesis. My sincere thanks are due to Dr. Jorge A. Ruiz-Cruz, Universidad Autónoma de Madrid, Spain, for his unselfishly sharing programs, friendly help, and valuable comments. I owe him lots of gratitude for assisting me to understand the numerical methods. He could not even realize how much I have learned from him. I am greatly indebted to Dr. Ali E. Atia, president of Orbital Communications International, for his innovative ideas and precious suggestions. The conversations with him have inspired me to think of many interesting areas of research. I am very grateful to four other faculty members of the University of Maryland at College Park, Dr. Christopher Davis, Dr. Isaak D. Mayergoyz, Dr. Neil Goldsman, and Dr. Amr Baz, for serving in my Advisory Committee. I would also like to thank Andrew J. Piloto, Kyocera American, for allowing me to have the opportunity to participate in his projects. Finally and most importantly, I wish to acknowledge that this dissertation could not have been accomplished without the love, encouragement, understanding, patience, and devotion of my beautiful wife, Ningning Xu.

Contents

List of Tables

List of Figures

Chapter 1

Introduction

1.1 Microwave-Millimeterwave Components

Microwave and millimeter-wave frequency bands have been widely employed for many commercial and military applications such as radar systems, communication systems, heating systems, and medical imaging systems. Radar systems are used for detecting, locating and sensing remote targets. Examples of some radar systems are air-traffic control systems, missile tracking radars, automobile collision-avoidance systems, weather prediction systems, and motion detectors. Communication systems have been developed rapidly in recent years in order to support a wide variety of applications. Examples of communication systems include direct broadcast satellite (DBS) television, personal communications systems (PCSs), wireless local area networks (WLANs), global positioning systems (GPSs), cellular phone and video systems, and local multipoint distribution systems (LMDS).

Microwave and millimeter-wave components are required in all the aforementioned systems. Typical components are [1–3]: filters, multiplexers, couplers, transformers, polarizers, orthomode transducers (OMTs), power dividers, circulators, switches, low noise amplifiers (LNAs), frequency synthesizers, power amplifiers, and oscillators. In order to illustrate the basic functions of these components, a satellite payload system [4, 5] as shown in Fig. 1.1 is briefly described as a demonstration. The payload system performs the critical function in a satellite to amplify the weakened *uplink* signal prior to its retransmission on the *downlink* leg. A receiving and transmitting antenna operating with two polarizations, namely vertical (V) and horizontal (H), in two frequency bands is positioned at the front end of the system. The upper frequency band is for receiving the *uplink* signal, while the lower one is for transmitting the *downlink* signal. Dual polarizations are used to accommodate more carriers. The two polarizations are separated by the OMT, which routes the two polarizations to two different physical ports. Waveguide diplexers in each port of the OMT are employed to separate the received and transmitting signals. The received signal is then amplified and frequency-converted by the wideband receivers. The receiver usually consists of LNA, mixer, and preamplifier. The redundant receivers controlled by switches are added for fail-safe purposes. The input multiplexer (IMUX) in the system separates the broadband input signal into the frequency channels (carriers), and each channel is then amplified by the power amplifiers. The power amplifier may be a traveling-wave tube amplifier (TWTA) or solid-state active amplifier. The amplified signals in each of the channels are combined by the output mul-

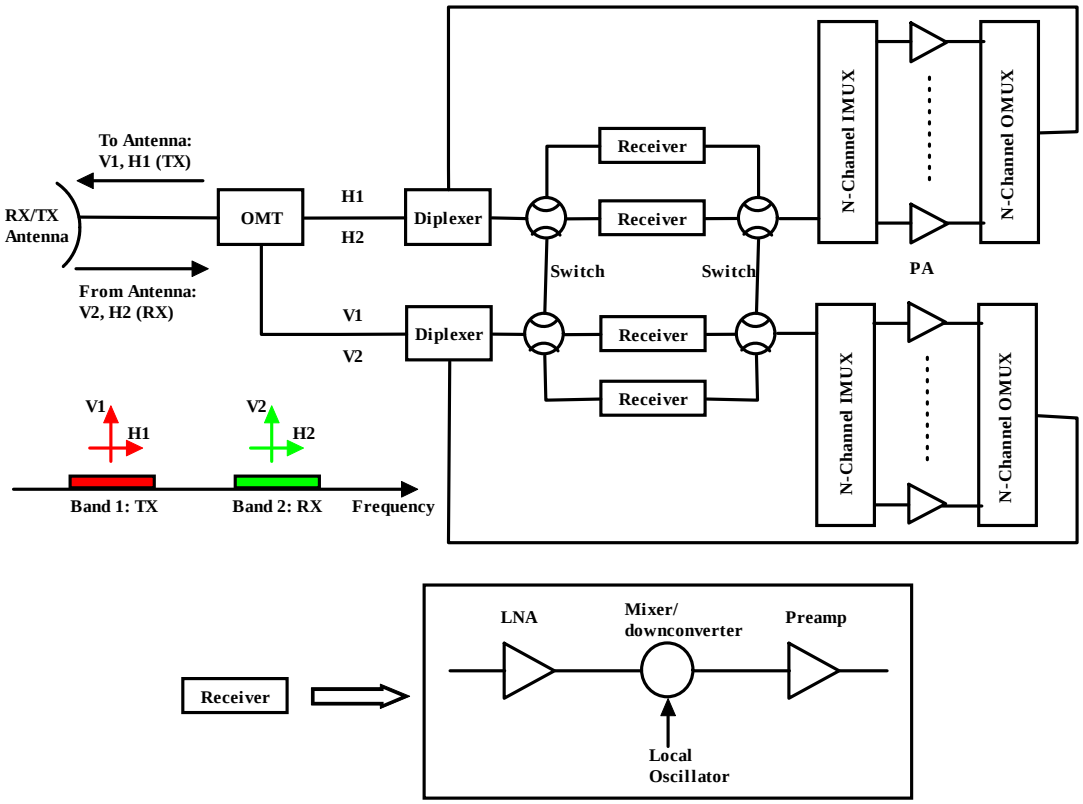

Figure 1.1: An example of a satellite payload system.

tiplexers (OMUX) at the final stage for retransmitting. This presented payload system demonstrates some examples of the microwave passive and active components, which are also often used in other microwave/RF systems. The passive components in the system are OMT, diplexers and multiplexers, while the active components are LNAs, mixers, power amplifiers, switches, and oscillators.

This dissertation is devoted to the modeling and design of the microwave passive components in various transmission media and technologies, namely waveguide, planar, dielectric resonator (DR), and low temperature co-fired ceramics (LTCC). Microwave passive components with very strict specifications have been required by modern microwave systems. The specifications are mainly related to band-

width, spurious, quality factor, linearity, volume and mass, power handling capability, cost, and development time. For example, high integration of microwave integrated circuits (MICs) and monolithic microwave integrated circuits (MMICs) requires miniature and broadband filters and multiplexers. Wireless base station requires filters and multiplexers with small volume, low loss, high power handling capability and high rejection levels. Satellite communication systems need multiplexers with many channels and very small guard bands. The objective of this dissertation is to provide some new ideas for the design of microwave passive components with very strict specifications.

1.2 CAD of Microwave Components

1.2.1 Overview

Computer aided design (CAD) of microwave components has advanced steadily over the past few decades with the improvement of computers. Many versatile CAD tools have been developed, and are being used to design all kinds of microwave components. The main purpose of CAD is to obtain the physical dimensions of a component with the prescribed specifications, and reduce or even avoid the experimental debugging and tuning period after the manufacture of the component. The final objective is, actually, to shorten the development time and reduce the total cost. However, not all the components used nowadays, especially the ones with very demanding specifications, can be designed optimally and effi-

ciently by the available CAD tools. The development of efficient CAD tools is, therefore, still a very active research area.

The traditional CAD methods are based on the equivalent circuit theory, which were first used by the members of the radiation laboratory of the Massachusetts Institute of Technology (MIT) for the design of microwave components [6–8]. The circuit-theory-based CAD introduces single (fundamental) mode equivalent circuits to represent complex waveguide discontinuities in terms of simple lumped circuit elements (inductors, capacitors, transformers, and resistors, etc.). The complex electromagnetic field problems can then be solved with simple calculations based on network theory, and the computational effort required to obtain the final results is minimal. Many equivalent circuit models for waveguide discontinuities and junctions can be found in [7]. These models, together with the network synthesis theory [9], have been applied for the design of many devices.

Although single mode equivalent networks have proved to be very valuable engineering tools, they also have serious drawbacks [3, 10, 11]. The most important one is that equivalent circuit models only take the fundamental mode of the waveguide into account to represent the distributed discontinuities in terms of lumped elements. However, the discontinuities in close proximity usually excite many higher order modes that are not considered in the equivalent circuit models. Thus, the single mode equivalent networks are no longer valid for these cases. In reality, designed prototypes using the equivalent circuit theory usually need more experimental debugging and tuning.

Field-theory-based CAD or full-wave analysis of microwave components is

an alternative to the previous circuit-theory-based approach. Basically, the field-theory-based CAD tools are created based on the direct or approximate solution of Maxwell's equations [12–15]. The development of computers has allowed the realization of many numerical field-solvers that seemed infeasible many years ago because of the lack of computational power. The field-theory-based approach is superior to the circuit-theory-based one because i) it predicts very accurate frequency response; ii) it takes higher order mode effects into account; iii) it can potentially include all the electromagnetic effects: radiation, excitation, and loss, etc.; iv) it can be used to calculate and observe the field distribution in components; v) it is valid for any frequency or wavelength range; vi) it can be developed to analyze a discontinuity with an arbitrary shape. The most significant limitation on field-solver tools is the long solution time to analyze a complex component given available computer resources: Central Processing Unit (CPU) speed, memory amount, and disk storage. Many researchers are now working on developing efficient algorithms to speed up the performance of field-solver tools.

When lengthy simulation prevents one from analyzing complete components with a field-solver, *hybrid* approaches can be employed to improve the efficiency. One approach is to identify the key elements (discontinuities and junctions, etc.) of the problem that need the field-solver, and to approximate the rest with the equivalent circuit theory. An example is shown in Fig. 1.2 to demonstrate this approach. The physical layout in Fig. 1.2(a) is a coupled-line bandpass filter in microstrip technology. This filter structure has been subdivided using the library of elements (transmission lines, mitered bends, and coupled-lines, etc.) in the

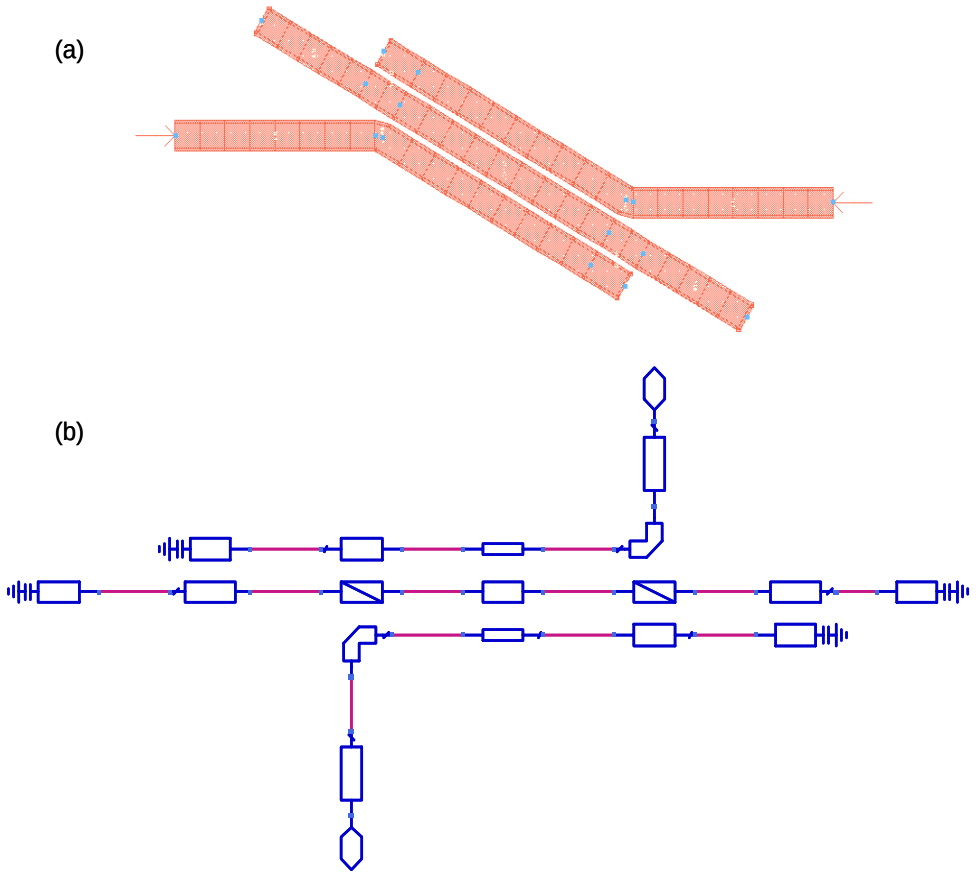

Figure 1.2: (a) Physical layout of a coupled microstrip line filter. (b) The layout of (a) has been subdivided using the standard library elements for analysis.

simulators for analysis. For the transmission lines, the physical dimensions are related to impedance and electrical length through a set of closed form equations (i.e. equivalent circuit model). For a discontinuity like the miter bend, a field-solver can be used for the analysis to take the parasitic effects into account. Shown in Fig. 1.3 is another example using the hybrid approach to design a combline filter. The filter structure in Fig. 1.3(a) has been subdivided into many pieces as in Fig. 1.3(b). Each piece is parameterized and analyzed by a field solver with higher-order modes included. All the pieces are then cascaded together in a circuit

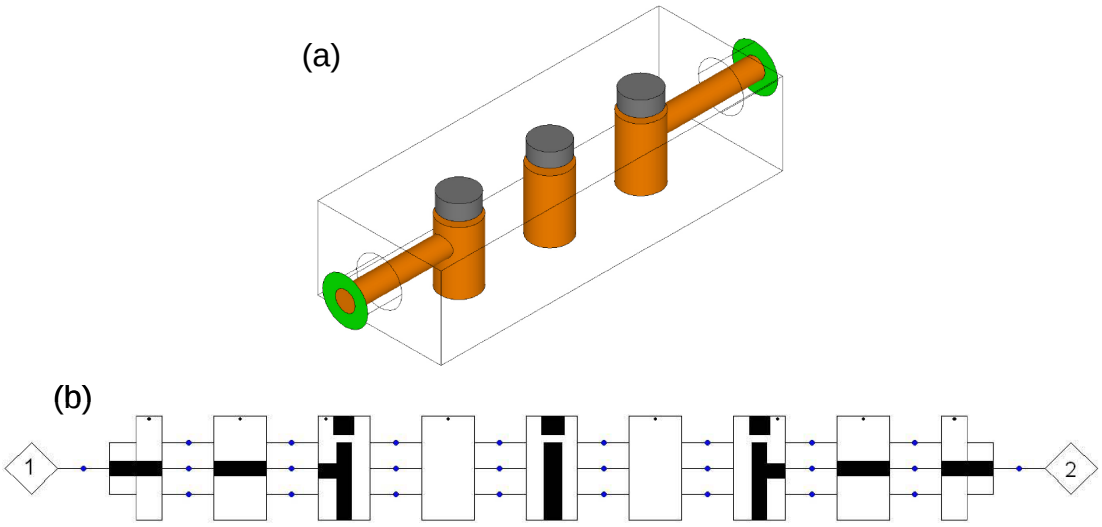

Figure 1.3: (a) 3D structure of a combline filter. (b) Subdivided circuits of (a) for analysis. (reprinted from the archived seminar in Ansoft.com.)

simulator to obtain the frequency response. The tuning procedure is performed in the circuit simulator to acquire the optimal design and improve the design efficiency. The development time can be significantly reduced and the accuracy is still maintained. Another possible hybrid approach is to model a component using a hybrid of two or more different numerical methods. The basic idea is to segment the component into different parts which are treated separately by different numerical techniques [16]. Each part can be characterized by a multiple-mode matrix, such as the Generalized Scattering Matrix (GSM) and the Generalized Admittance Matrix (GAM). The response of the whole component can be obtained by cascading all the part matrices together. For example, the finite element method (FEM) can be combined with the mode matching method (MMM) to analyze and design many waveguide components [17–19]. Some commercial CAD tools using this hybrid approach are also available [20, 21].

1.2.2 General Numerical Methods

The purpose of all numerical methods in electromagnetics is to find approximate solutions of Maxwell's equations (or equations derived from them) that satisfy the given boundary and initial conditions. Various numerical techniques are available, and distinguished themselves from others mainly in three aspects [11]: i) The approximated electromagnetic quantity (electric field, magnetic field, potential, current distribution, and charge distributions, etc.). ii) The expansion functions used to approximate the unknown solutions. iii)The strategy (algorithms) employed to determine the coefficients of the expansion functions. The most representative numerical methods [14] are:

- Finite Difference Method [22]. This method can be categorized more as Finite Difference in Time Domain (FDTD) [23, 24] and Finite Difference in Frequency Domain (FDFD) [25]. The finite difference method is well known to be the least analytical.

- Finite Element Method (FEM) [26, 27]. FEM has variational features in the algorithm that makes it different from the finite difference method. The recently proposed Boundary Element Method (BEM) [28] is the combination of the boundary integral equation and a discretization technique similar to the FEM as applied to the boundary.

- Transmission Line Matrix method (TLM) [29, 30]. The field problem is converted to a three dimensional equivalent network problem in this method.

- The Method of Moments (MoM) [15]. In the narrower sense, MoM is the method of choice for solving problems stated in the form of an electric field integral equation or a magnetic field integral equation.

- Mode Matching Method (MMM) [3, 10]. MMM is actually a field-matching method that is usually used to obtain the GSMs or GAMs of waveguide discontinuities (steps and junctions, etc.). The range of problems that can be handled by MMM is constrained by the geometries and materials. Other recently proposed advanced methods expanded from MMM are Boundary Integral-Resonant Mode Expansion method (BIRME) [31, 32] and Boundary Contour Mode Matching method (BCMM) [33–35]. These methods can be employed to deal with the discontinuities with non-canonical shapes. MMM is well known to be a very efficient method.

- Spectral Domain Method (SDM) [36]. SDM is a Fourier-transformed version of the integral equation method applied to planar structures. SDM is numerically rather efficient, but its range of applicability is generally restricted to well-shaped structures.

A wide variety of commercial software tools based on the aforementioned numerical techniques are available. Some of the well known software tools are listed in Table 1.1. In reality, which numerical method (or commercial software) to use usually depends on the geometry, accuracy, and efficiency. For example, if a component only involves canonical waveguide structures, MMM is usually employed due to its high efficiency and good accuracy. To analyze a multiple-layer

Table 1.1: Available commercial CAD software tools

Software Name	Vendor	Solver Method
HFSS	Ansoft	FEM
CST Microwave Studio	CST	Several solvers in FD and TD
Sonnet Suites	SONNET	MoM with uniform cells
IE3D	Zeland Software, Inc.	MoM with non-uniform cells
Momentum	Agilent Technologies	MoM
Empire	IMST	FDTD
WASP-NET	MIG Innovation Group	hybrid MMM/FEM/MoM/FD
μWave Wizard	MiCIAN	MMM; hybrid MMM/FEM

quasi-planar structure, MoM is normally a good choice. As mentioned before, the hybrid approaches should also be considered for complicated structures.

1.2.3 Mode Matching Method

MMM is one of the most frequently used methods for formulating boundary-value problems. It can be considered as one of the most successful and efficient approaches for solving various problems, such as filters, couplers, multiplexers, impedance transformers, power dividers, horns and other passive devices in waveguides, striplines, and microstrip lines [37–43]. MMM is usually employed to solve two kinds of problems. One is the scattering problem. Generally speaking,

when the geometry of the structure can be identified as a junction (or discontinuities) of two or more regions, MMM can then be used to solve the GSM, GAM, or GIM (Generalized Impedance Matrix) characterization of the structure. If a microwave component consists of a few junctions that are characterized by GSMs solved in MMM, the scattering parameters of the component can easily be obtained by cascading the GSMs together [14]. The other kind of problem that can be handle by MMM is the eigenvalue problem. MMM can be formulated to obtain the resonant frequency of a cavity, the cutoff frequencies of a waveguide, or the propagation constant of a transmission line. The analysis in MMM of ceramic cavities, generalized ridge waveguides, striplines, microstrip lines, and some non-canonical waveguides as in Fig. 1.4 can be found in [35, 41, 44–46]. The microwave components presented in this dissertation are mostly designed in MMM. Therefore, a brief introduction of MMM is given in this section.

To analyze a component or structure in MMM, three steps are usually followed. The first step is to find the normal eigenmodes in each individual region (waveguide, coaxial line, stripline, and microstrip line, etc.) so that the general electromagnetic field in each region can be expressed as a series of the normal eigenmodes (with unknown coefficients at this step). The normal eigenmodes belong to one out of three groups: Transverse Electric (TE), Transverse Magnetic (TM) or Transverse Electromagnetic (TEM) modes. The exact analytical solutions can be obtained for some canonical structures, such as rectangular waveguides, circular waveguides, and coaxial waveguides [3, 7, 47, 48], while for non-canonical structures as shown in Fig. 1.4, numerical methods are usually

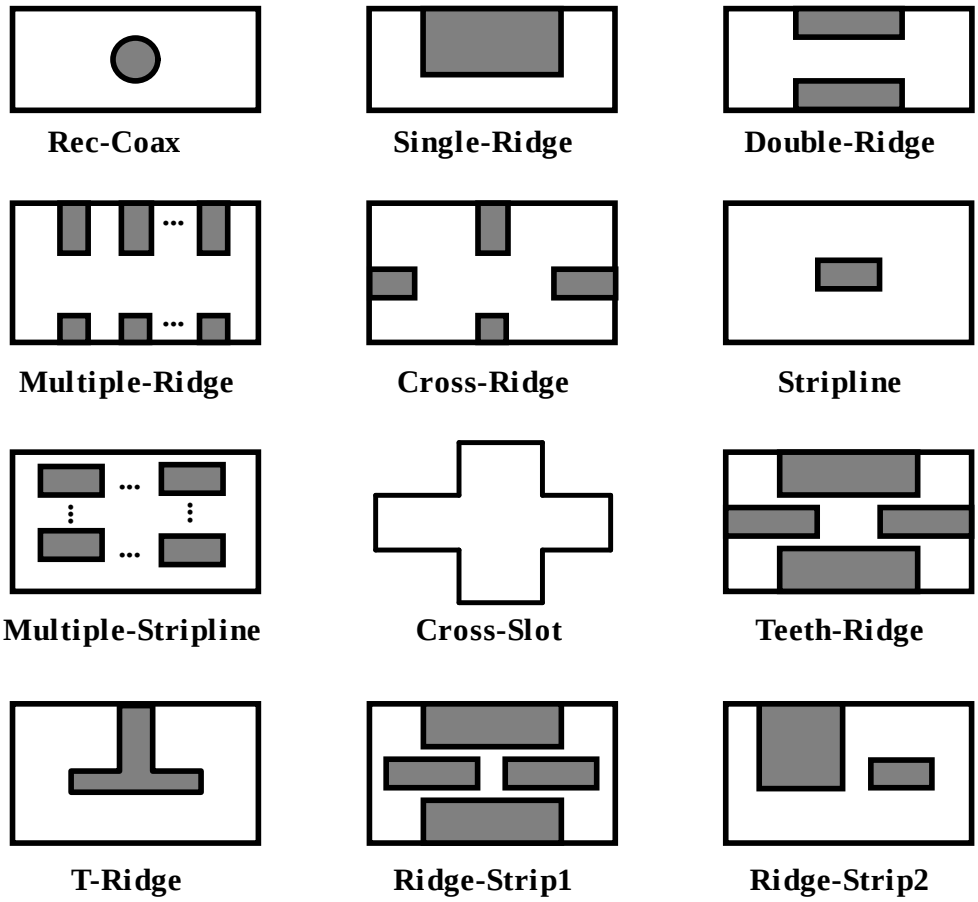

Figure 1.4: Examples of non-canonical waveguide geometries that can be analyzed by mode matching method.

required to find the eigenmodes. Two numerical techniques that are actually two-dimensional MMM have been mostly used: Generalized Transverse Resonance (GTR) [14, 35, 41, 45, 46, 49–51] and Boundary Contour Mode-Matching (BCMM) [33–35, 52, 53]. In this dissertation, the GTR technique has been used in some of the designs, therefore, a detailed discussion about GTR is given in Appendix A (p. 255). Basically, the cutoff frequencies and field distributions of the normal eigenmodes are obtained in this first step. For the non-canonical structures, the fields of each eigenmode are usually expanded in a series of plane

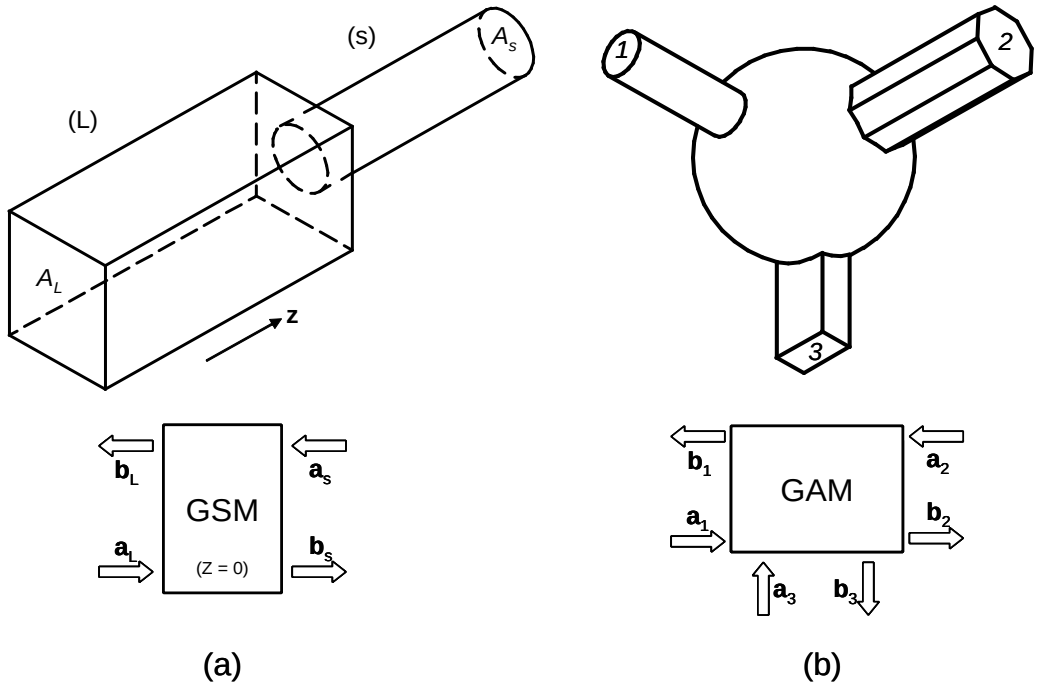

Figure 1.5: (a) A generic step discontinuity structure that can be characterized by GSM. (b) A generic multiple-port junction structure that can be characterized by GAM.

waves or circular waves with the solved coefficients.

The second step is to characterize the junctions in one component by GSMs, GAMs or GIMs based on the field-matching procedure. Basically, the fields in each individual region are described as the weighted sum of the normal eigenmodes solved in the first step. The so-obtained field expansions are then matched in the plane of the junction or discontinuity to derive the GSM or GAM. The orthogonality property of the eigenmodes should be applied in this step. Two kinds of junctions are usually treated by MMM. One is the step discontinuity as shown in Fig. 1.5(a) that is characterized by GSM. The general formulations to calculate the GSM are given in Table 1.2. The other kind of junction is the

generic multiple-port junction discontinuity as shown in Fig. 1.5(b) that is usually characterized by GAM. The basic procedure to calculate the GAM for such a junction is to compute the magnetic field (corresponding to current) on the ports when an electric field (corresponding to voltage) is excited in one of the connection apertures. The ports except the excited port should be short-circuited during this computation, which is consistent with the definition of the admittance matrix. Once the fields are known on each port, the elements of the GAM can easily be obtained. The general GAM formulations can be found in [10, 35, 44], and are not listed here. In general, the finite number of normal eigenmodes is used to approximate the fields since it is not possible to extract an exact solution with an infinite number of eigenmodes. The accuracy of the approximated results should be verified carefully because of the relative convergence problem found in the evaluation of the mode-matching equations [54].

The third step of MMM is to obtain the scattering parameters of a component by cascading the GSMs or GAMs of the junctions in the component together. For instance, shown in Fig. 1.6(a) is an H-plane inductive window filter consisting of only step discontinuities. The way to analyze it is just to characterize each step as a GSM, and then perform the cascading. Fig. 1.6(b) is an H-plane manifold triplexer. Two H-plane T-junctions are employed to fulfill the manifold junction and connect the three channel filters. To analyze this component, the GAMs for the T-junctions and the GSMs for the channel filters are calculated first, and then cascaded together to obtain the GSM of the whole triplexer. One necessary procedure before cascading is to transform the GAMs or GIMs of multiple-port

Table 1.2: Formulations to calculate the GSM of a generic step discontinuity.

Property	**Formulations [10, 35, 36]**
Transverse Fields of Region L	$\overrightarrow{\mathbf{E}}_t^{(L)}\Big\|_{z=0} = \sum_{n=1}^{N_L}\left(a_n^{(L)} + b_n^{(L)}\right)\overrightarrow{\mathbf{e}}_n^{(L)}$ $\overrightarrow{\mathbf{H}}_t^{(L)}\Big\|_{z=0} = \sum_{n=1}^{N_L}\left(a_n^{(L)} - b_n^{(L)}\right)\overrightarrow{\mathbf{h}}_n^{(L)}$ *Normalization:* $Q_n^{(L)} = \iint_{A_L}\overrightarrow{\mathbf{e}}_n^{(L)} \times \overrightarrow{\mathbf{h}}_n^{(L)} \cdot \widehat{z}dS$
Transverse Fields of Region s	$\overrightarrow{\mathbf{E}}_t^{(s)}\Big\|_{z=0} = \sum_{m=1}^{N_s}\left(a_m^{(s)} + b_m^{(s)}\right)\overrightarrow{\mathbf{e}}_m^{(s)}$ $\overrightarrow{\mathbf{H}}_t^{(s)}\Big\|_{z=0} = \sum_{m=1}^{N_s}\left(a_m^{(s)} - b_m^{(s)}\right)\overrightarrow{\mathbf{h}}_m^{(s)}$ *Normalization:* $Q_m^{(s)} = \iint_{A_s}\overrightarrow{\mathbf{e}}_m^{(s)} \times \overrightarrow{\mathbf{h}}_m^{(s)} \cdot \widehat{z}dS$
E-Field Matching Condition	$\widehat{z} \times \overrightarrow{\mathbf{E}}^{(L)} = \begin{cases} 0, & in\ A_L - A_s,\ z = 0 \\ \widehat{z} \times \overrightarrow{\mathbf{E}}^{(s)} & in\ A_s,\ z = 0 \end{cases}$
H-Field Matching Condition	$\widehat{z} \times \overrightarrow{\mathbf{H}}^{(L)} = \widehat{z} \times \overrightarrow{\mathbf{H}}^{(s)},\ \ in\ A_s,\ z = 0$
Derived Linear System	$\begin{cases} \mathbf{Q}_L\left(\mathbf{a}_L + \mathbf{b}_L\right) = \mathbf{X}^T\left(\mathbf{a}_s + \mathbf{b}_s\right) \\ \mathbf{X}\left(\mathbf{a}_L - \mathbf{b}_L\right) = -\mathbf{Q}_s\left(\mathbf{a}_s - \mathbf{b}_s\right) \end{cases}$ *where* $\mathbf{Q}_g = diag\left[Q_n^{(g)}\right]_{n=1,\ldots,N_g},\ g = L,\ s$ $\mathbf{a}_g = \left[\cdots a_n^{(g)} \cdots\right]_{n=1,\ldots,N_g}^T$ $\mathbf{b}_g = \left[\cdots b_n^{(g)} \cdots\right]_{n=1,\ldots,N_g}^T$ $[\mathbf{X}]_{mn} = \iint_{A_s}\overrightarrow{\mathbf{e}}_m^{(s)} \times \overrightarrow{\mathbf{h}}_n^{(L)} \cdot \widehat{z}dS$
GSM Formulation	$\mathbf{S} = \begin{bmatrix} \mathbf{Q}_L^{-1}\mathbf{X}^T\mathbf{F}\mathbf{X} - \mathbf{I} & \mathbf{Q}_L^{-1}\mathbf{X}^T\mathbf{F}\mathbf{Q}_s \\ \mathbf{F}\mathbf{X} & \mathbf{F}\mathbf{Q}_s - \mathbf{I} \end{bmatrix}$ $\mathbf{F} = 2\left(\mathbf{Q}_s + \mathbf{X}\mathbf{Q}_L^{-1}\mathbf{X}^T\right)^{-1},\ \mathbf{I}$ *is identity matrix.*

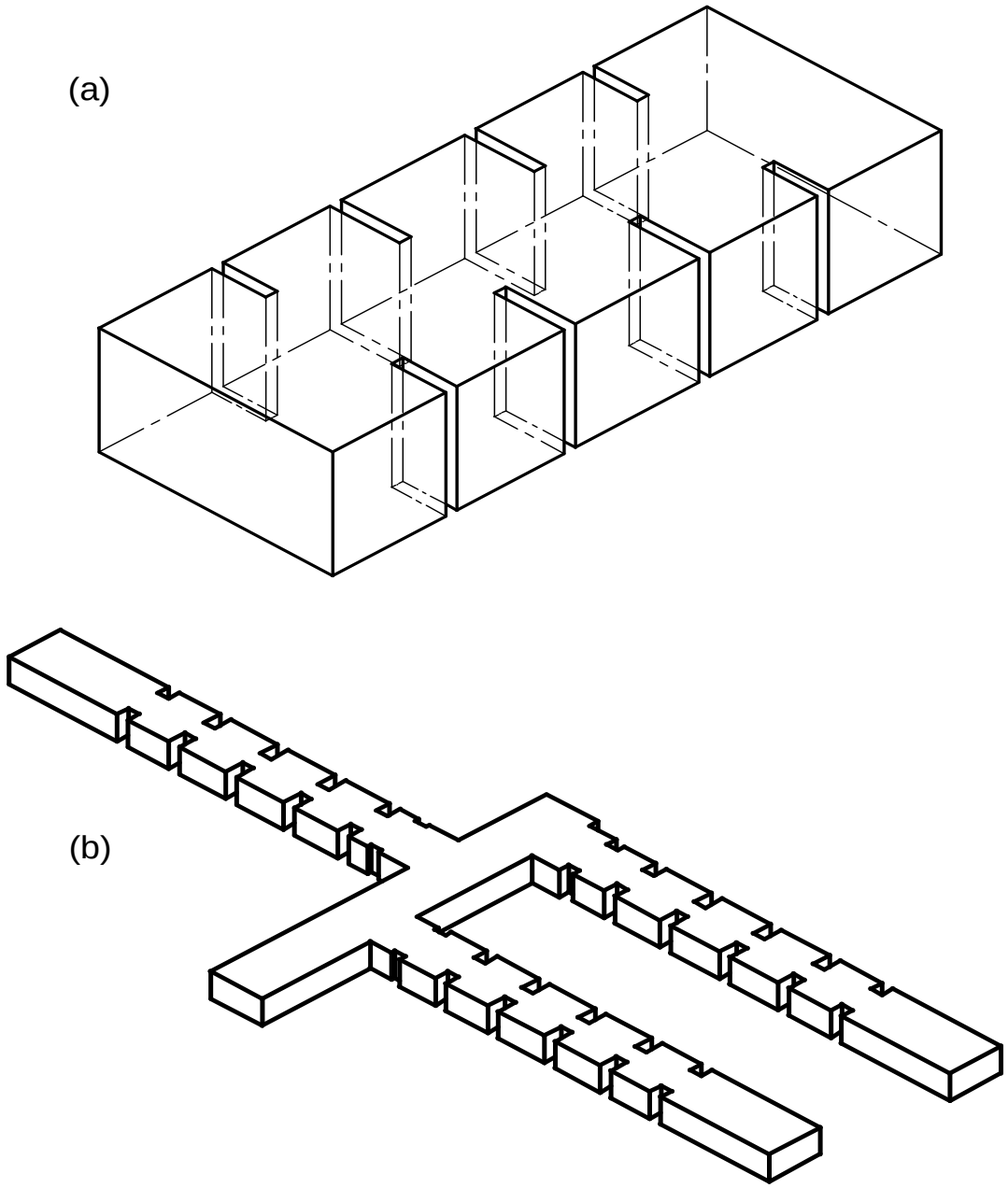

Figure 1.6: (a) An example of components consisting of only step discontinuities. (b) An example of components using multiple-port junctions.

junctions to equivalent GSMs. The relationship between the GSM, GAM and GIM is given as the following equations [10, 35].

$$\begin{aligned} \widetilde{\mathbf{Y}} &= \widetilde{\mathbf{Z}}^{-1} = (\mathbf{I}-\mathbf{S})(\mathbf{I}+\mathbf{S})^{-1} \\ \widetilde{\mathbf{Z}} &= \widetilde{\mathbf{Y}}^{-1} = (\mathbf{I}+\mathbf{S})(\mathbf{I}-\mathbf{S})^{-1} \\ \mathbf{S} &= \left(\mathbf{I}+\widetilde{\mathbf{Z}}\right)^{-1}\left(\mathbf{I}-\widetilde{\mathbf{Z}}\right) = \left(\mathbf{I}-\widetilde{\mathbf{Y}}\right)\left(\mathbf{I}+\widetilde{\mathbf{Y}}\right)^{-1} \end{aligned} \tag{1.1}$$

where $\mathbf{I}$ is the identity matrix. $\widetilde{\mathbf{Y}}$ and $\widetilde{\mathbf{Z}}$ are normalized or scaled versions of the general GAM and GIM. The normalization or scale factors depend on the relationship between the modal amplitudes and the voltages and currents [35]. It must be pointed out that the phase delay of the connecting transmission structures between the junctions must be taken into account for the cascading of GSMs. Usually the number of modes used for the connections is much less than the number of modes for the characterization of junctions since most of the modes are evanescent in the connecting structures. To be complete, the resulting GSM $\mathbf{S}^C$ of cascading two GSMs $\mathbf{S}^L$ and $\mathbf{S}^R$ is given by [3, 35]

$$\mathbf{S}^C = \begin{bmatrix} \mathbf{S}_{11}^L + \mathbf{S}_{12}^L \mathbf{W} \mathbf{S}_{11}^R \mathbf{S}_{21}^L & \mathbf{S}_{12}^L \mathbf{W} \mathbf{S}_{12}^R \\ \mathbf{S}_{21}^R \left(\mathbf{I} + \mathbf{S}_{22}^L \mathbf{W} \mathbf{S}_{11}^R\right) \mathbf{S}_{21}^L & \mathbf{S}_{22}^R + \mathbf{S}_{21}^R \mathbf{S}_{22}^L \mathbf{W} \mathbf{S}_{12}^R \end{bmatrix} \tag{1.2}$$

where

$$\mathbf{W} = \left[\mathbf{I} - \mathbf{S}_{11}^R \mathbf{S}_{22}^L\right]^{-1}, \ \mathbf{I} \text{ is identity matrix.}$$

1.3 Practical Realization Technologies

In practice, which technology to use for the realization of microwave passive components, especially filters and multiplexers, is related to many factors: frequency

range, quality factor Q, physical size, power handling capability, temperature drifting, and cost, etc. A comprehensive consideration of these factors is usually needed before choosing a realization technology for the desired components. Some technologies are listed and discussed next.

1. Lumped-element filters and multiplexers. The microwave frequency is up to about 18 GHz. The unloaded Q averages about 200 (Q is dependent on frequency), and over 800 may be achieved at lower frequencies [55]. The dimensions are much smaller than distributed components, which is a major advantage. The power handling capability is very low unless superconducting technology is applied. The production cost is quite low. Lumped-element realizations of microwave components are not often used nowadays because the wavelength is so short compared with the dimensions of circuit elements.

2. Vacuum- or Air-filled Metallic-form components. Microwave components implemented by vacuum- or air-filled rectangular waveguides, ridge waveguides, circular waveguides, and coaxial TEM lines belong to this category. The Q factors can be realized from 5 to 20000 [9, 56, 57]. Waveguide filters and multiplexers are often employed for space and satellite applications to achieve high power handling capability and high Q factor (silver-plated material can be used for higher Q). The metallic-form components are usually bulky, and aluminum is mostly used to have a light weight. The temperature stability of metallic-form components usually needs to be improved for the space and satellite applications due to the severe environment condition. The temperature drifting effect can be compensated or reduced by three ways: considerate design methodology, employing special

materials (e.g., Invar), and smart mechanical structures. Coaxial TEM filters and multiplexers are well-known for the low cost and the relatively high Q factor (1 - 5000) [56, 58], and many standard components for wireless base stations are available commercially.

3. Planar structures. Microwave components realized by microstrip lines, striplines, coplanar lines (waveguides), and suspended striplines belong to this category. The main purpose of planar structures is to achieve the miniaturization of the components. Planar structures are mostly employed for MICs and MMICs. The power handling capability and Q factors are usually very low. Planar structures are the most flexible methods to implement filters, and a variety of structures have been and are being created by researchers.

4. Dielectric resonator filters and multiplexers. Dielectric resonator filters and multiplexers are mostly employed to achieve very high Q and very good temperature stability [57, 58]. The common designs use a cylindrical puck of ceramic suspended on a supporter within a metallic housing. The fundamental mode, hybrid modes, or multiple degenerate modes of the dielectric resonators can be applied for the filter designs. More than 50000 unloaded Q factor and less than 1 ppm/°C temperature coefficient can be achieved by some ceramic materials.

5. Low Temperature Co-fired Ceramic (LTCC) technology. LTCC technology is commonly used for multiple-layer structures and packaging. Standard LTCC technology is applied from a few hundred MHz to about 40 GHz. The advantages of LTCC are cost efficiency for high volumes, high packaging density, reliability, and relatively higher Q than planar structures. Many waveguide

components have been manufactured by LTCC technology [59–64] to achieve a relatively good Q factor. The unloaded Q factor is from 1 to 250 (depending on the employed vendors). The basic way to realize waveguides in LTCC technology is to use metallization and via fences to approximate the conductors and metallic housing.

6. High temperature superconducting (HTS) components. In principle, superconductivity enables resonators with near-infinite unloaded Q to be constructed in a very small size. Examples can be found in [65, 66]. The disadvantages of the HTS components are the bulky cooling system and the high power consumption.

7. Surface acoustic wave (SAW) components. SAW devices operate by manipulating acoustic waves propagating near the surface of piezoelectric crystals. The frequency can be up to 3 GHz [57]. The main advantage of SAW components is their very small size in applications such as cellular handsets. The Q factor, power handling capability and temperature stability are usually poor. Examples can be found in [67, 68].

8. Micromachined electromechanical systems (MEMS). MEMS-based products combine both mechanical and electronic devices on a monolithic microchip to obtain superior performance over solid-state components, especially for wireless applications. The advantages of microwave-MEMS components are miniature size, relatively low loss, and tunable property. MEMS technology is suitable for handset filters, transceiver duplexers, tunable resonators, switches, and tunable filters, etc. Micromechanical resonators with 7450 Q factor at 100 MHz have been

demonstrated in [69]. Examples of tunable filters can be found in [70]. Tuning bandwidths of up to 30% with 300 Q are possible using MEMS technology [56].

1.4 Dissertation Objectives

This dissertation is devoted to creating novel filter and multiplexer structures that will satisfy very stringent specifications, developing the precise modeling and design procedures for microwave components, and integrating 3D component structures for microwave integrated circuits.

With this general objective, the dissertation mainly concentrates on five different topics: i) Approximating, synthesizing and realizing generalized multiple-band quasi-elliptic filters. ii) Creating novel resonator structures to implement miniature, ultra-wideband, and high performance filters. iii) Developing waveguide structures to implement wideband filters and multiplexers, and integrating them in LTCC technology to achieve higher Q than planar structures. iv) Developing techniques to improve the spurious performance of the filters. v) Creating EM/Circuit combinational techniques for the filter and multiplexer designs.

Many CAD tools have been used in this dissertation to perform the designs, which include ad hoc mode-matching programs and some commercial software tools in other numerical methods [71–73]. No matter which CAD tool has been used, systematic modeling and design procedures have always been followed. A systematic debugging and tuning procedure has also been created for quasi-elliptic filter designs.

LTCC technology has been employed to produce highly integrated microwave circuits in this dissertation. Many multiple-layer and waveguide structures have been designed and implemented for LTCC applications.

1.5 Dissertation Organization

The dissertation is organized in five chapters, including this introduction chapter. In chapter 2, the generalized approximation and synthesis methods of multiple-band quasi-elliptic filters are presented. An optimum equal-ripple performance for a multiple-band quasi-elliptic filter with any number of passbands and stopbands can be obtained by the approximation procedure, which also allows the use of real or complex transmission zeros in the filter functions. For the synthesis method, a powerful building-block cascading technique is developed to synthesize various realizable network topologies.

Chapter 3 mainly concentrates on microwave filter designs. It begins with a discussion of the generalized filter design methodology that can be applied to any filter structure regardless of the geometry and implementation technology. In order to achieve miniaturization and wideband performance, novel double-layer coupled stripline resonator filter structures are developed. The modeling and design of such filters are performed in MMM and verified by HFSS. LTCC technology is employed to manufacture the filters to achieve high integration. The measured results demonstrate good agreement with the simulations. The idea of a double-layer resonator structures is then expanded to multiple-layer coupled resonator

structures. Two filter designs using triple-layer coupled stripline resonators and double-layer coupled hairpin resonators are performed to validate the concept. In order to obtain a good quality factor with compact size, ridge waveguide coupled stripline resonator filter structures, which can be in-line or folded, are created for LTCC applications. Analysis and optimization in MMM are used to design such filters. A stepped impedance resonator (SIR) structure is also applied in the filters to improve the spurious performance. The dual-mode technology is applied for the realization of quasi-elliptic filters. A dual-mode circular waveguide filter is designed and tuned to demonstrate the feasibility to realize an asymmetric filter in dual-mode technology, while a dual-mode rectangular waveguide filter is modeled and designed in MMM to show the realizability of having a dual-mode quasi-elliptic filter without any tuning screws. Finally, a systematic tuning procedure for quasi-elliptic filters is presented. A dielectric resonator filter is tuned step by step to illustrate the procedure.

Chapter 4 studies the modeling and design of microwave multiplexers. Generalized design methodologies are discussed at the beginning. Several multiplexer designs are then performed for different perspectives. In order to obtain wideband multiplexer designs in LTCC technology, ridge waveguide divider junctions are investigated and employed to realize multiplexers with the use of ridge waveguide evanescent-mode filters. Such structures can be highly integrated in LTCC technology and are appropriate for ultra-wideband multiplexer designs. The analysis and optimization of such multiplexers are completely performed in MMM. Ku band waveguide multiplexers for space applications are then presented. The mul-

tipaction discharge effect on the power handling capability is discussed, and the estimation method of multipaction threshold is explained. To avoid the tuning of such multiplexers after manufacturing, round corners generated by the finite radius of the drill tool are included in the design step. A discretized step model is employed in the analysis of MMM to represent the round corners. In order to obtain miniaturized multiplexers with good quality factors, the stripline bifurcation and T-junctions are used with the ridge waveguide coupled stripline resonator filters for multiplexer realizations. A diplexer design using stripline bifurcation junction is performed in MMM to demonstrate its feasibility. Finally, a wideband waveguide diplexer is realized by a waveguide E-plane bifurcation junction, ridge waveguide evanescent-mode filter, and iris coupled rectangular waveguide filter for high power application. The modeling and design of this diplexer are performed in MMM and verified by HFSS.

In chapter 5, conclusions of this dissertation are summarized, and future research work of interest is also addressed.

1.6 Dissertation Contributions

The main contributions of this dissertation are given as followings.

1. The generalized approximation procedure and the building-block synthesis method are developed for multiple-band quasi-elliptic function filters. An optimum equal-ripple performance in all passbands and stopbands is guaranteed.

2. Double-layer coupled stripline resonator filter structures are created for achieving the miniature and wideband performance. The modeling and design procedure of such filters in MMM is developed.

3. Multiple-layer coupled resonator structures are proposed for miniature and broadband filter designs. The validity of the concept has been proved by two filter design examples.

4. Ridge waveguide coupled stripline resonator filters and multiplexers are invented to have a compact structure as well as a good quality factor. The complete analysis and optimization procedure in MMM is developed.

5. Dual-mode filter technology is applied for the realization of asymmetric filters. The feasibility is illustrated by a dual-mode circular waveguide filter prototype.

6. A dual-mode rectangular filter structure is created for implementing quasi-elliptic filters without any tuning screws. The analysis and optimization are carried out in MMM.

7. A systematic tuning procedure is proposed for quasi-elliptic filters. The procedure is generalized, and can be applied to any realization technology.

8. Ridge waveguide divider-type multiplexers are created to achieve high integration and ultra-wideband performance for LTCC applications. The modeling and design are performed in MMM.

Chapter 2

Multiple-Band Quasi-Elliptic Function Filters

2.1 Introduction

In recent years, with the development of concurrent multiple-band amplifiers [74] and multiple-band antennas [75], multiple-band filters have been finding applications in both space and terrestrial microwave telecommunication systems. The system architecture is dramatically simplified by using these multiple-band components because non-contiguous channels can be transmitted to the same geographical region through only one beam [76]. Incorporating multiple passbands within the single filter structure offers advantages over the equivalent multiplexing solution, in terms of mass, volume, manufacturing, tuning and cost.

Three approaches are usually employed to implement multiple-band filters. The first approach is to use a multiplexing method. Single-band bandpass filters

are designed for each passband in a multiple-band filter. Their input/output ports are then connected together through junctions. This approach usually leads to a complex design procedure since junctions and filters have to be optimized to have a good multiplexing performance and comply with the mechanical constraints. The second approach is to use the multiple harmonic resonating modes of the resonators [77, 78]. Each harmonic mode is employed to fulfill one passband. This approach has the difficulty of tuning the harmonic modes to the desired center frequencies of each passband. Therefore, it is often applied for dual-band filter designs. The third approach is to design a single circuit realizing multiple-band characteristics. This approach requires the approximation and synthesis of an advanced filtering function, but makes the hardware implementation easier since the classical filter architecture can be used.

This chapter discusses the approximation and synthesis methods for the third approach. Some recent work on this subject has demonstrated the techniques to synthesize dual-band filters [79–81]. However, a generalized solution for multiple-band filters with real, imaginary or complex transmission zeros has not been provided yet. In this chapter, an efficient method based on iteration is presented for generating symmetric or asymmetric multiple-band transfer functions with real, imaginary or complex transmission zeros.

A filter design procedure commonly consists of three steps.

1. Solution to the approximation problem. A rational transfer function needs to be found for multiple-band characteristics.

2. Solution to the synthesis problem. An equivalent lumped-element net-

work is synthesized to realize the transfer function.

3. Solution to the hardware implementation. Physical dimensions of a distributed filter structure are obtained by full-wave numerical methods or tuning methods based on the equivalent network.

Step 1 and 2 are presented in detail in this chapter, while step 3 is only briefly discussed and more information can be found in later chapters.

2.2 The Approximation Problem

2.2.1 Problem Statement

The approximation problem for multiple-band filters is mainly concerned with obtaining realizable rational transfer functions of minimum degree with respect to desired specifications, such as insertion loss, return loss, phase linearity, and group delay, to produce the required amplitude response in all passbands and stopbands, and the phase response in the passbands [82].

For any two-port lossless filter network composed of N coupled resonators, the transfer and reflection functions may be expressed as the ratio of Nth degree complex polynomials [83]

$$S_{11}(s) = \frac{F(s)}{E(s)} \text{ and } S_{21}(s) = \frac{P(s)}{\varepsilon E(s)} \tag{2.1}$$

where s is the complex frequency $s = \sigma + j\omega$, ε is a constant scale factor to adjust the equiripple levels. All the polynomials are monic. The polynomials $F(s)$, $P(s)$, and $E(s)$ must satisfy the following conditions to have a realizable lossless two

port network [57, 84]:

1. $E(s)$ is a strict Hurwitz polynomial, i.e. all its roots must lie in the left half s-plane.

2. The polynomial $P(s)$ is of degree $M \leq N-1$ and satisfies the condition $P = (-1)^{N+1}P^*$, i.e. its roots must be symmetric with respect to the imaginary axes.

3. $F(s)$ is of degree N.

4. The conservation of energy for a lossless network generates the equation:

$$E(s)E^*(s) = F(s)F^*(s) + \frac{1}{\varepsilon^2}P(s)P^*(s) \tag{2.2}$$

Using (2.2), the transfer and reflection functions can be expressed as

$$|S_{11}(j\omega)|^2 = \frac{\varepsilon^2 C^2(\omega)}{1+\varepsilon^2 C^2(\omega)} \quad |S_{21}(j\omega)|^2 = \frac{1}{1+\varepsilon^2 C^2(\omega)} \tag{2.3}$$

where $C(\omega)$ is known as the characteristic function which will be defined later. The approximation problem is therefore simplified to find the characteristic function $C(\omega)$, and thus the polynomials $F(s)$, $P(s)$ and $E(s)$.

2.2.2 Determination of Characteristic Function $C(\omega)$

The determination of the characteristic function is based on the low-pass prototype multiple-band filters as shown in Fig. 2.1. A set of passbands and stopbands are specified by the normalized real frequency points. Each band is defined by two frequency points except that the two outside stopbands are each specified by one point. The aim is to obtain an equiripple performance in each passband and

stopband, which will yield an *optimum* filtering function mathematically. In Fig. 2.1, ω_0 is the right band-edge equiripple frequency point of the first stopband (the left one is at negative infinity). ω_1 and ω_2 are the two band-edge equiripple frequency points for the first passband. ω_3 and ω_4 are the band-edge equiripple frequency points for the second stopband. Similar specifications are given for other filter bands. It should be noted that the left (right) band-edge point of the most left (right) passband is usually taken as -1 $(+1)$ (ω_1 and ω_{10} in Fig. 2.1) for the normalization. Given the specified passbands and stopbands, the requirements are usually given on the minimum return loss (or maximum insertion loss) of the passbands. The attenuation of the stopbands is normally controlled by the number of transmission zeros. Other requirements, like phase and group delay, can also be considered by using real or complex transmission zeros. According to the author's knowledge, there are no known analytical solutions to the approximation problem of multiple-band filters. A numerical method based on iteration is used to obtain the optimum solution, which will be discussed next.

Roots of polynomials $F(s)$ and $P(s)$ are the poles and transmission zeros of the multiple-band filtering function. The characteristic function $C(\omega)$ is defined as:

$$C(\omega) \triangleq \frac{A(\omega)}{B(\omega)} = \frac{\prod_{i=1}^{N}(\omega - p_i)}{\prod_{j=1}^{M}(\omega - z_j)} \tag{2.4}$$

where p_i, $i = 1, 2, ..., N$, are poles of the passbands and must be real. z_j, $j = 1, 2, ..., M$, are transmission zeros of stopbands and can be real, imaginary or

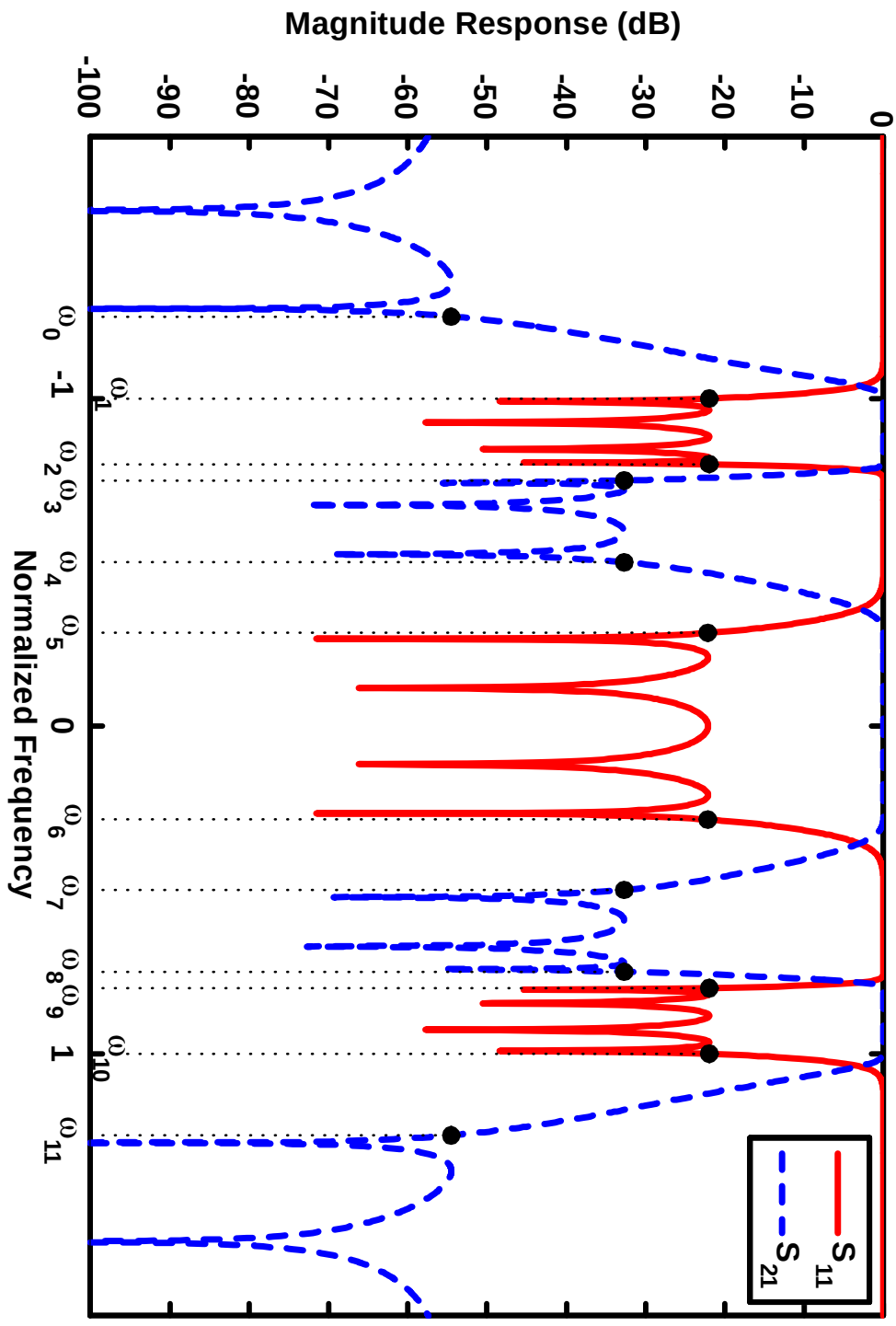

Figure 2.1: Low-pass prototype multiple-band filter

complex. It must be noticed that p_i and z_j are now defined in the ω-domain. $M \leq N-1$ must be satisfied in order to have at least one transmission zero at infinity. By separating the real values of z_j from the imaginary and complex values, $C(\omega)$ can be rewritten as:

$$C(\omega) = \frac{\prod_{i=1}^{N}(\omega - p_i)}{\prod_{j=1}^{L}(\omega - r_j)\prod_{k=1}^{T}(\omega - c_k)} \tag{2.5}$$

where r_j, $j = 1, 2, ..., L$, are real values of z (imaginary transmission zeros in s-domain). c_k, $k = 1, 2, ..., T$, are imaginary or complex values of z (real or complex transmission zeros in s-domain). c_k must be given in conjugated pair. The total number of transmission zeros $M = L + T$. Usually, real or complex transmission zeros are used to improve the phase linearity or the flatness of group delay. Their values will be prescribed and fixed during the approximation procedure. Therefore, the approximation problem can be re-phrased as:

Given the frequency range (band-edge equiripple points) of each passband and stopband in a multiple-band filter, the number of poles in each passband, the number of imaginary zeros in each stopband, the prescribed real or complex zeros, and the minimum return loss in each passband, the goal is to find the values of poles (p_i in (2.5)) and imaginary zeros (r_j in (2.5)) for an optimum multiple-band filtering function, namely equiripple performance in each frequency band.

The procedure for finding the equiripple response starts with the initial guessing of a set of poles and zeros in every frequency band. The critical frequencies, at which $C(\omega)$ has its extremes, are then determined by solving for the roots

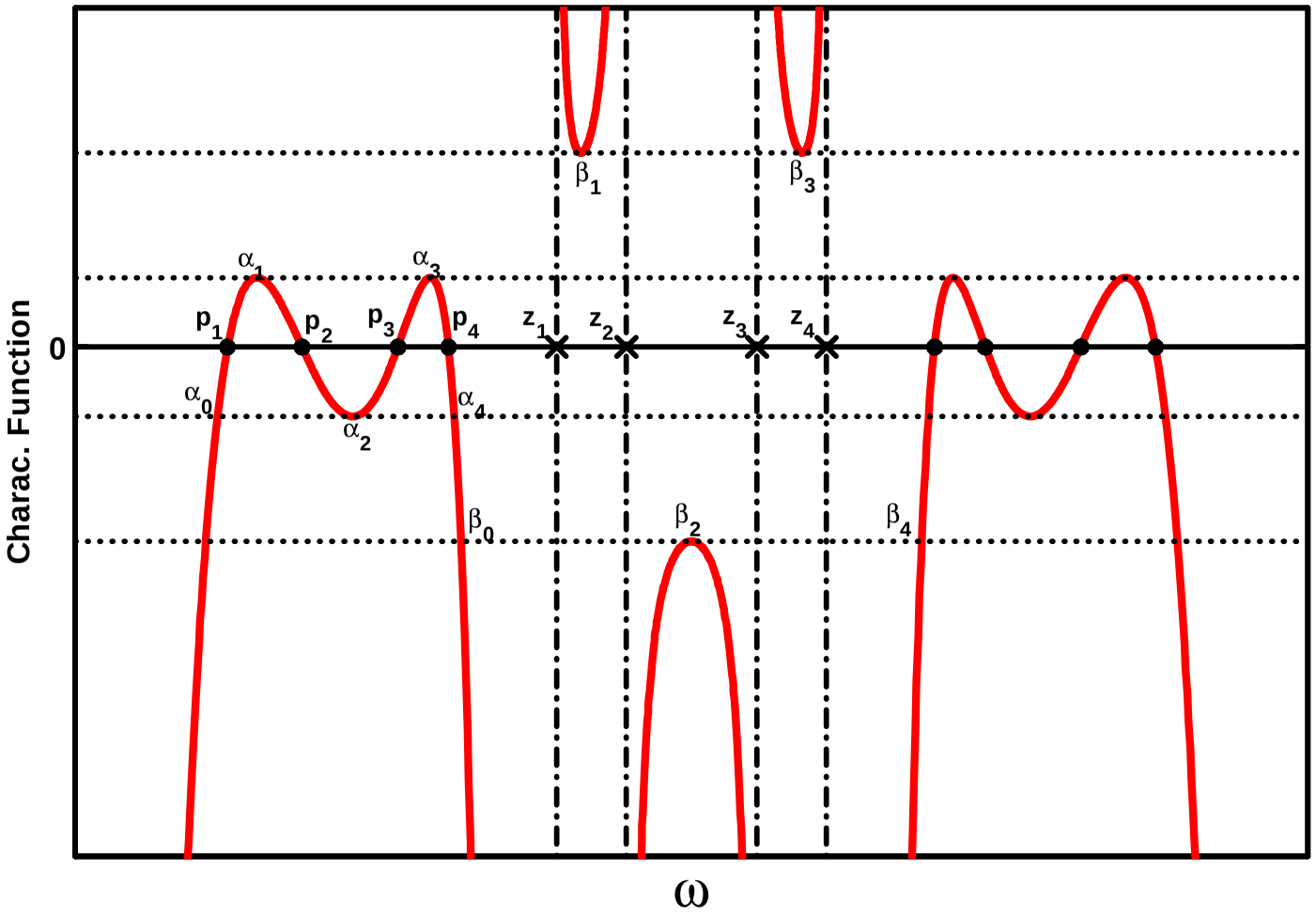

Figure 2.2: A typical curve of the characteristic function with the critical frequency points

of the derivative of $C(\omega)$:

$$\frac{dC(\omega)}{d\omega} = B(\omega)A^{'}(\omega) - A(\omega)B^{'}(\omega) = 0 \tag{2.6}$$

A typical curve of $C(\omega)$ is shown in Fig. 2.2. Only three frequency bands, two passbands and one stopband are displayed in the figure. Additional frequency bands in a multiple-band filter show the similar behavior. Let the roots of (2.6) in one passband be $\alpha_1, \alpha_2..., \alpha_{K-1}$, where K is the number of poles in this passband. Let α_0 and α_K represent the two band-edge equiripple points that are given at the beginning. Therefore,

$$\alpha_0 < \alpha_1 < \alpha_2... < \alpha_i... < \alpha_{K-1} < \alpha_K$$

Each pole of p's in the passband should lie between two successive α's as shown in Fig. 2.2, i.e. $\alpha_{i-1} < p_i < \alpha_i$. With the first guess of p's, the absolute values of $C(\omega)$ at α's usually are not equal (unless we are very lucky). Thus, new values of p's need to be found for an updated characteristic function, which will be closer to an equiripple performance, according to the solved values of α's. Let $C_0(\omega)$ be the initial characteristic function and

$$C_1(\omega) = (\omega - p_l^{'})\frac{\prod_{i=1, i\neq l}^{N}(\omega - p_i)}{\prod_{j=1}^{M}(\omega - z_j)} \tag{2.7}$$

be the updated characteristic function with a new value $p_l^{'}$ for the replacement of the old value p_l in $C_0(\omega)$. $p_l^{'}$ is used to force $C_1(\omega)$ to have equal absolute values at α_{l-1} and α_l, that is

$$C_1(\alpha_{l-1}) = -C_1(\alpha_l) \tag{2.8}$$

It must be pointed out that the index l for p_l is a global index in all the poles of the multiple-band filter. It can be easily transformed into the local index in the poles of a single passband. This transforming procedure has been ignored for the sake of concision. From (2.7) and (2.8),

$$(\alpha_{l-1}-p_l^{'})\frac{\prod_{i=1,i\neq l}^{N}(\alpha_{l-1}-p_i)}{\prod_{j=1}^{M}(\alpha_{l-1}-z_j)}=-(\alpha_l-p_l^{'})\frac{\prod_{i=1,i\neq l}^{N}(\alpha_l-p_i)}{\prod_{j=1}^{M}(\alpha_l-z_j)} \tag{2.9}$$

and

$$\frac{(\alpha_{l-1}-p_l^{'})}{(\alpha_{l-1}-p_l)}C_0(\alpha_{l-1})=-\frac{(\alpha_l-p_l^{'})}{(\alpha_l-p_l)}C_0(\alpha_l) \tag{2.10}$$

After more manipulations, $p_l^{'}$ is solved as

$$p_l^{'}=\frac{p_l\left[\alpha_{l-1}C_0(\alpha_{l-1})+\alpha_lC_0(\alpha_l)\right]-\alpha_{l-1}\alpha_l\left[C_0(\alpha_{l-1})+C_0(\alpha_l)\right]}{p_l\left[C_0(\alpha_{l-1})+C_0(\alpha_l)\right]-\left[\alpha_lC_0(\alpha_{l-1})+\alpha_{l-1}C_0(\alpha_l)\right]} \tag{2.11}$$

For one stopband as in Fig. 2.2, let the roots of (2.6) in this stopband be $\beta_1,\beta_2...,\beta_{I-1}$, where I is the number of zeros in this stopband. Let β_0 and β_I represent the two band-edge equiripple points that are given at the beginning. Each zero of z's in the stopband should lie between two successive β's as shown in Fig. 2.2, i.e. $\beta_{j-1}<z_j<\beta_j$. Similar to the case of the passband, the objective is to find new values of z's for an updated characteristic function to be closer to an equiripple performance. The updated characteristic function $C_1(\omega)$ will be expressed as

$$C_1(\omega)=\frac{1}{(\omega-z_l^{'})}\frac{\prod_{i=1}^{N}(\omega-p_i)}{\prod_{j=1,j\neq l}^{M}(\omega-z_j)} \tag{2.12}$$

where $z_l^{'}$ is the new zero value for the replacement of the old value z_l, such that

$$C_1(\beta_{l-1}) = -C_1(\beta_l) \tag{2.13}$$

Thus,

$$\frac{1}{(\beta_{l-1} - z_l^{'})} \frac{\prod_{i=1}^{N}(\beta_{l-1} - p_i)}{\prod_{j=1, j\neq l}^{M}(\beta_{l-1} - z_j)} = -\frac{1}{(\beta_l - z_l^{'})} \frac{\prod_{i=1}^{N}(\beta_l - p_i)}{\prod_{j=1, j\neq l}^{M}(\beta_l - z_j)} \tag{2.14}$$

which yields

$$z_l^{'} = \frac{z_l \left[\beta_{l-1} C_0(\beta_l) + \beta_l C_0(\beta_{l-1})\right] - \beta_{l-1}\beta_l \left[C_0(\beta_{l-1}) + C_0(\beta_l)\right]}{z_l \left[C_0(\beta_{l-1}) + C_0(\beta_l)\right] - \left[\beta_{l-1} C_0(\beta_{l-1}) + \beta_l C_0(\beta_l)\right]} \tag{2.15}$$

One iteration to obtain an updated characteristic function is complete once all the updated poles and zeros are found for each passband and stopband in a multiple-band filter. The roots of (2.6) using the updated characteristic function are calculated again to check the values of $C(\omega)$. The iteration continues until an equiripple performance with acceptable tolerance in every frequency band is simultaneously achieved. The convergence of the iteration procedure is guaranteed using the above updating method, and usually less than 20 iterations are required.

2.2.3 Determination of $E(s)$, $F(s)$, and $P(s)$

After the poles and zeros are obtained by the iteration procedure, the polynomials $F(s)$ and $P(s)$ are given as:

$$F(s) = \prod_{i=1}^{N}(s - jp_i), \quad P(s) = \prod_{k=1}^{M}(s - jz_k) \tag{2.16}$$

Equation (2.2) is then used to obtain the polynomial $E(s)$. After some derivations, the following expression is obtained.

$$E_{left}(s)E_{right}(s) = F^2(s) + (-1)^{N-M}\frac{P^2(s)}{\varepsilon^2} \tag{2.17}$$

where $E_{left}(s)$ is a polynomial with all its roots in the left half s-plane, which is actually the wanted polynomial. $E_{right}(s)$ has all its roots in the right half s-plane. The value of ε can be determined by the specified minimum return loss in the passbands. Therefore, the roots of the right-hand-side expression of (2.17) are found first. $E(s)$ is then constructed by using the roots in the left half s-plane.

The unitary conditions on the scattering parameters are [2, 47]

$$\begin{aligned} S_{11}S_{11}^* + S_{21}S_{21}^* &= 1 \\ S_{22}S_{22}^* + S_{12}S_{12}^* &= 1 \\ S_{11}S_{12}^* + S_{21}S_{22}^* &= 0 \end{aligned} \tag{2.18}$$

According to (2.18), it may be shown that [47] the phases ϕ, θ_1, and θ_2 of $S_{21}(s)$, $S_{11}(s)$, and $S_{22}(s)$, respectively, are related by:

$$\phi - \frac{\theta_1 + \theta_2}{2} = \frac{\pi}{2}(2k \pm 1), \ k \text{ is any integer} \tag{2.19}$$

Thus, to ensure the orthogonality between $F(s)$ and $P(s)$, $P(s)$ given in (2.16) should be updated as [85]:

$$P(s) = \begin{cases} P(s), & \text{if } (N-M) \text{ is odd} \\ j \cdot P(s), & \text{if } (N-M) \text{ is even} \end{cases} \tag{2.20}$$

After $E(s)$, $F(s)$, and $P(s)$ are known, the transfer and reflection functions of a multiple-band filter can be obtained straightforwardly.

Table 2.1: Three multiple-band filter examples in the sense of approximation. The zeros at infinity are not counted in the item #Zero.

e.g.	Passband	#Pole	Stopband	#Zero	Prescribed Zero
1.	-1.0 to -0.3	4	$-\infty$ to -1.3	0	$2+3j$
			-0.18 to 0.25	3	
	0.5 to 1.0	4			$-2+3j$
			1.3 to $+\infty$	1	
2.	-1.0 to -0.78	4	$-\infty$ to -1.25	1	none
			-0.75 to 0.5	4	
	-0.35 to 0.285	4			
			0.57 to 0.75	3	
	0.8 to 1.0	4			
			1.25 to $+\infty$	2	
3.	-1.0 to -0.78	3	$-\infty$ to -1.25	1	none
			-0.72 to -0.65	3	
	-0.6 to -0.35	3			
			-0.1 to 0.12	2	
	0.3 to 0.57	3			
			0.65 to 0.75	3	
	0.8 to 1.0	3			
			1.25 to $+\infty$	1	

2.2.4 Examples of Approximation Problem

The above-presented iteration procedure to solve the approximation problem of multiple-band filters works for all kinds of situations with any number of frequency bands: symmetric, asymmetric, and prescribed real or complex zeros. Three examples are given to illustrate the validity of the procedure. The detailed information for them is shown in Table 2.1. All examples are using normalized

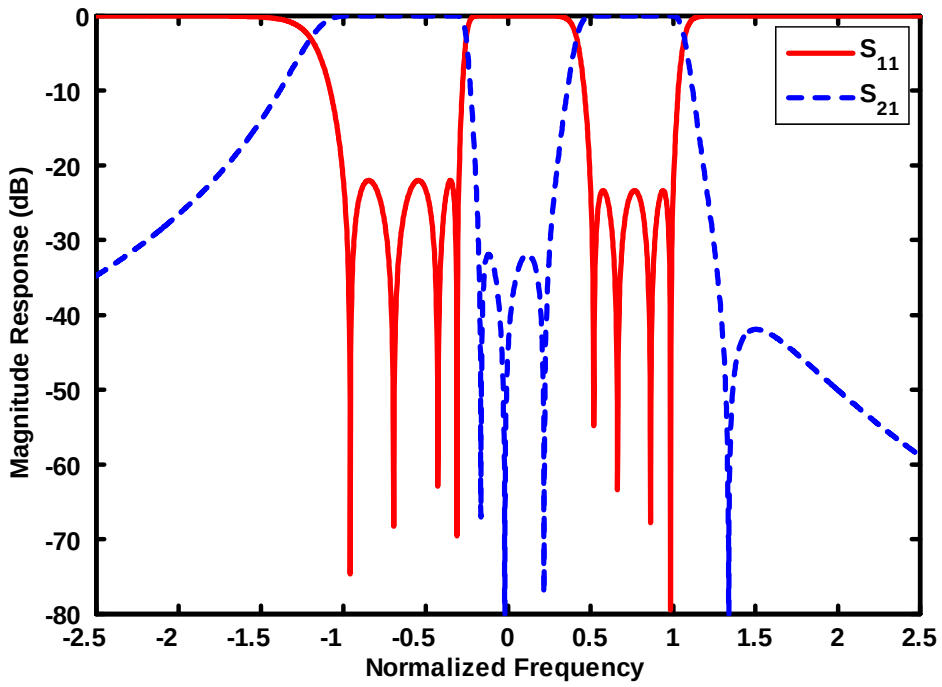

Figure 2.3: The approximation example 1 with prescribed complex zeros.

frequency. The minimum return loss of the passbands for all examples is 22 dB.

The number of passbands is 2, 3, and 4 for example 1, 2 and 3, respectively. The approximated magnitude responses of the three examples are shown in Fig. 2.3, Fig. 2.4, and Fig. 2.5, respectively. The iteration procedure converges in less than 1 second. The number of iterations needed for convergence is 16, 22, and 15 for example 1, 2 and 3, respectively. The equiripple levels in different passbands are not necessarily identical. However, it is possible to achieve identical equiripple levels by manipulating the number of poles and the bandwidth of each passband. The attenuation in stopbands is controlled by the number of zeros in each stopband, the bandwidth, and the number of poles of the nearby passbands. For a practical problem, a process of *run-and-try* is usually required.

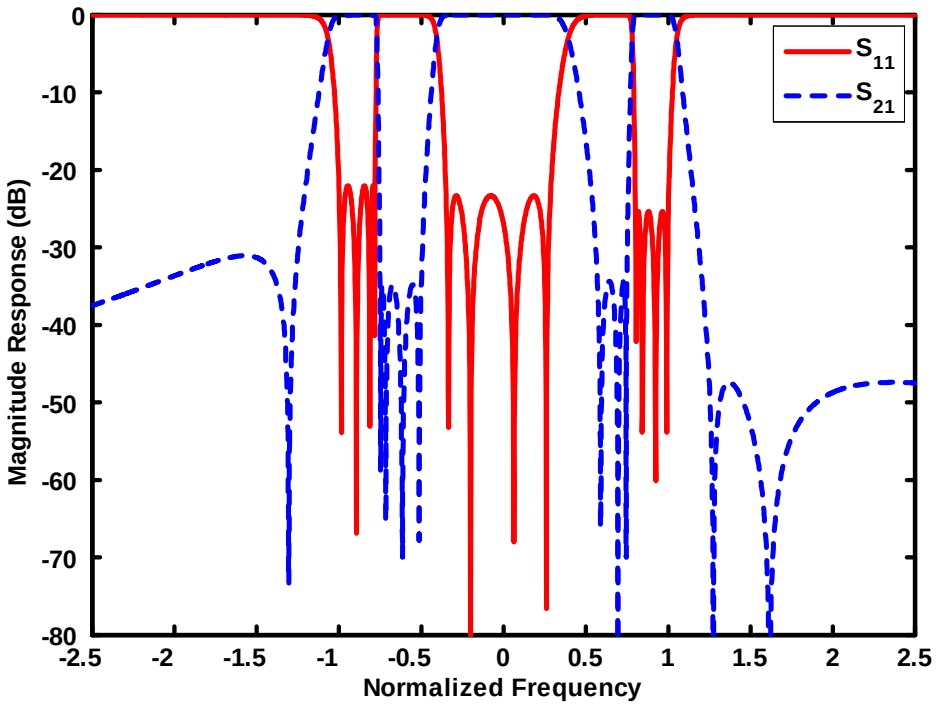

Figure 2.4: Magnitude response of the approximation example 2.

The values of poles and zeros in s-domain and ε for example 1 are

$$Poles: \begin{cases} -j0.9587 & -j0.6955 & -j0.4276 & -j0.3121 \\ j0.5189 & j0.6628 & j0.8629 & j0.9846 \end{cases}$$

$$Zeros: \quad -j0.1661 \quad -j0.0193 \quad j0.2186 \quad j1.3385 \quad 2+j3 \quad -2+j3$$

$$\varepsilon: \quad 80.2473$$

The poles, zeros, and ε for example 2 are

$$Poles: \begin{cases} -j0.9855 & -j0.8931 & -j0.8121 & -j0.7829 & -j0.3356 & -j0.2017 \\ j0.0638 & j0.2599 & j0.8042 & j0.8424 & j0.9228 & j0.9905 \end{cases}$$

$$Zeros: \begin{cases} -j1.3028 & -j0.7469 & -j0.7144 & -j0.6141 & -j0.5130 \\ j0.5907 & j0.6950 & j0.7451 & j1.2757 & j1.6125 \end{cases}$$

$$\varepsilon: \quad 16.0215$$

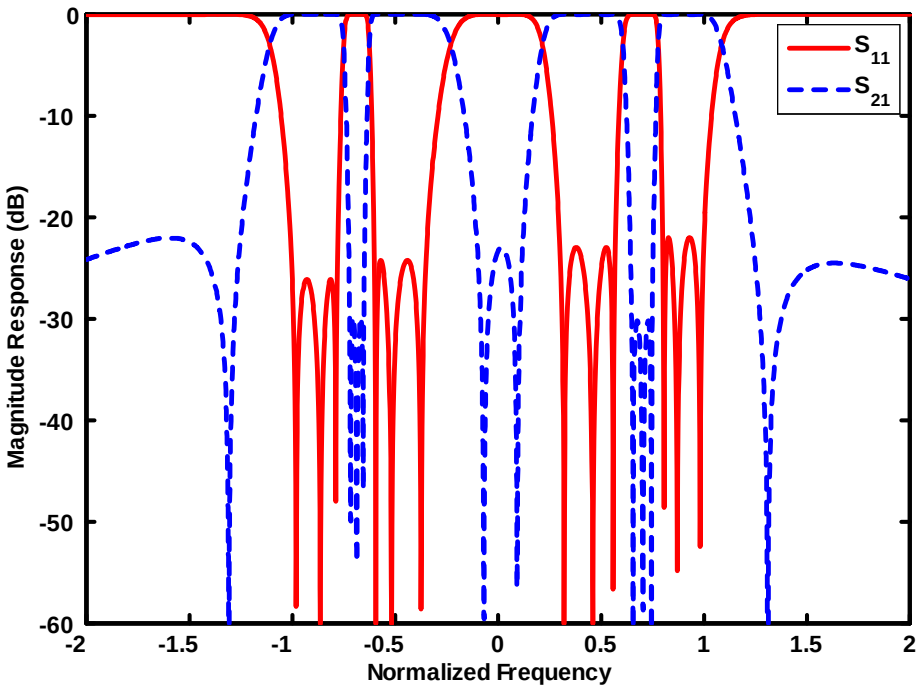

Figure 2.5: Magnitude response of the approximation example 3.

The poles, zeros, and ε for example 3 are

$$Poles: \begin{cases} -j0.9811 & -j0.8638 & -j0.7875 & -j0.5933 & -j0.5172 & -j0.3744 \\ j0.3203 & j0.4595 & j0.5597 & j0.8063 & j0.8708 & j0.9810 \end{cases}$$

$$Zeros: \begin{cases} -j1.3062 & -j0.7156 & -j0.6841 & -j0.6540 & -j0.0673 \\ j0.0940 & j0.6568 & j0.7043 & j0.7451 & j1.3110 \end{cases}$$

ε: 4.0433

2.3 The Synthesis Problem

2.3.1 Problem Statement

Once the polynomials of the transfer and reflection functions of a multiple-band filter are solved in the approximation problem, a lumped-element lossless network

needs to be synthesized to realize the desired filtering function. Many synthesis methods have been presented in published books and literature for single-band filtering functions. They are also applicable to multiple-band filters since the filtering functions are constructed in the exactly same way mathematically (polynomials are created based on the poles and zeros). Actually, two aspects can be considered. One is that a single-band filter is a special case of a multiple-band filter. The other one is that a multiple-band filter is in fact a single-band filter with some transmission zeros inside the passband. The second aspect explains why the synthesis methods for single-band filters will also work for multiple-band filters.

The synthesis problem is to find the element values, namely coupling matrix, of a lumped-element lossless network to realize the approximated filtering function. The network topology should be simple enough to be realized by a classical hardware implementation, for example, waveguide and planar structures. The available synthesis methods can be separated into two categories. One is based on the extraction procedure, which is usually a synthesis cycle to extract certain elements one by one. For instance, the Darlington's procedure [57, 84]. The other category is based on the matrix and eigenvalue theory, which usually takes one single step to yield all the elements of a generalized network. Once a generalized network is obtained, more operations are usually performed on it to generate one realizable network topology. This generalized network is therefore referred as a starting network. The methods belonging to the second category are mostly used nowadays, which will be discussed next.

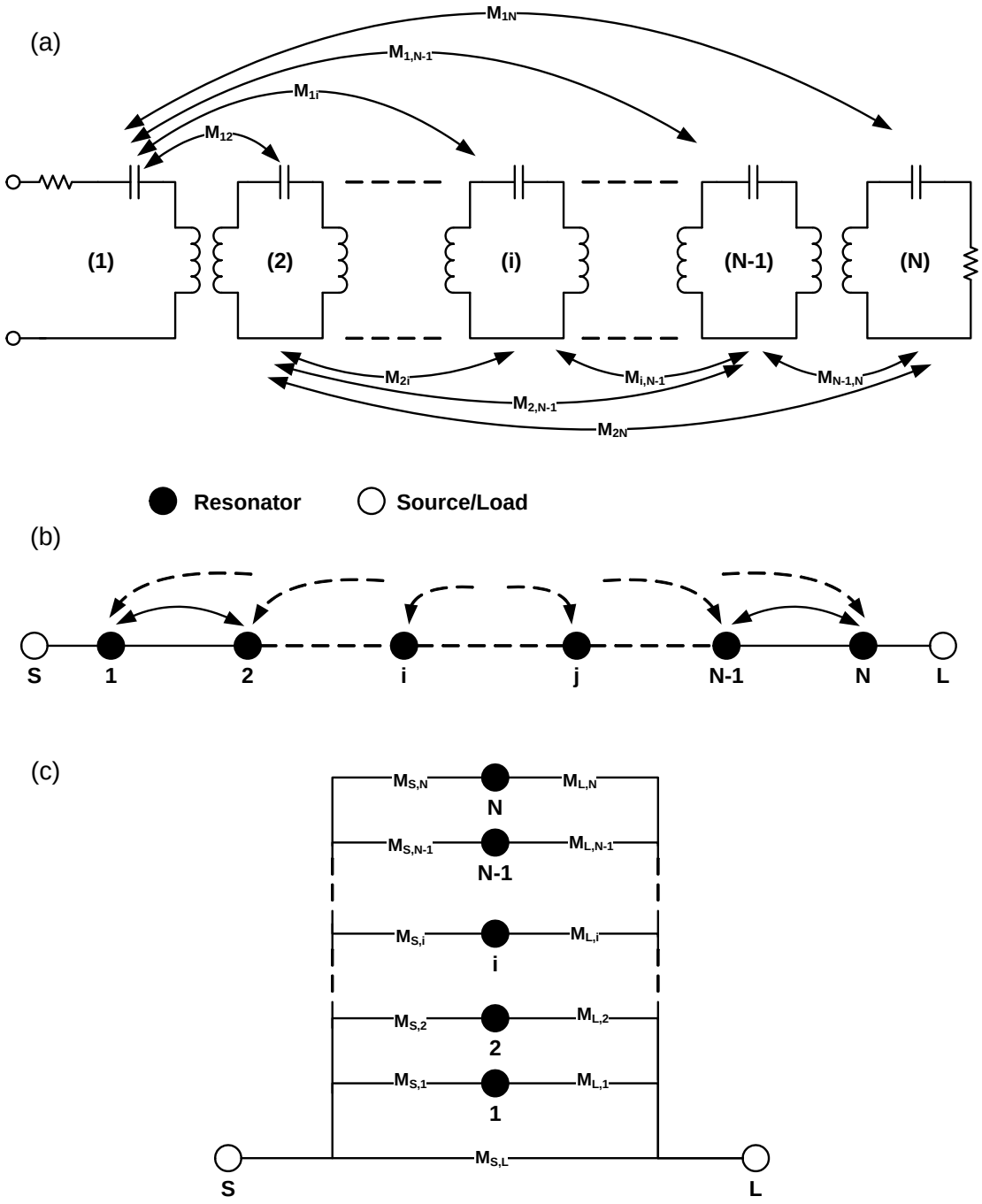

Figure 2.6: The synthesized starting networks for a multiple-band filter. (a) Coupled Resonator Network. (b) Compact notation of coupled resonator network. (c) Transversal array network in compact notation.

2.3.2 Overview of Coupling Matrix Synthesis

One starting network first presented by Atia et al [86] is the multiple coupled resonator network as shown in Fig. 2.6(a) and (b). This network can have a maximum of $N-2$ finite transmission zeros (assuming the filter order is N) since the source and load are each coupled to only one resonator. The other starting network presented by Cameron [85] is the canonical transversal array network as shown in Fig. 2.6(c). It has the advantage of being able to synthesize the fully canonical filtering functions (N poles with N transmission zeros) since multiple source and load couplings are accommodated. The synthesis procedures of these two networks have been clearly presented in [86] and [85]. The steps to obtain the coupling matrix of each equivalent network are briefly given in Table 2.2.

The coupling matrix topologies of the above two starting networks are too complicated to be realized by hardware structures (one element is coupled to many other elements). A similarity transformation (or rotation) procedure is usually used to annihilate unwanted couplings and reduce the coupling matrix to a desired realizable topology. The use of similarity transforms ensures that the eigenvalues and eigenvectors of the coupling matrix are preserved, such that under analysis, the transformed matrix will yield exactly the same transfer and reflection characteristics as the original matrix [83, 85, 86]. Let M_0 and M_1 be the original and transformed matrix, respectively, then the equation for a similarity transform is given as:

$$M_1 = R \cdot M_0 \cdot R^t \tag{2.21}$$

Table 2.2: Brief synthesis procedures of coupled resonator network and transversal array network.

Coupled Resonator Network Synthesis [86]
1. Generating admittance matrix Y from $E(s)$, $F(s)$, and $P(s)$
2. Computing eigenvalues λ_i and residues R from Y
3. Determining diagonal matrix $\Lambda = diag(\lambda_1, ..., \lambda_i, ...\lambda_n)$
4. Getting transformer ratios and creating an orthogonal matrix T from R
5. Constructing coupling matrix $M = T\Lambda T^t$
Transversal Array Network Synthesis [85]
1. Generating admittance matrix Y from $E(s)$, $F(s)$, and $P(s)$
2. Computing eigenvalues λ_i, and residues R from Y
3. Constructing coupling matrix M from λ_i's and R
4. Calculating source/load coupling if $N = M$.

where R is a rotation matrix and R^t is the transpose of R. R has the same dimensions as M_0 (assuming $N \times N$) and is defined as an identity matrix with a pivot $[i, j]$ $(i \neq j)$, i.e. elements $R_{i,i} = R_{j,j} = \cos\theta_r$, $R_{i,j} = -R_{j,i} = -\sin\theta_r$, $(i, j \neq 1, N)$. θ_r is the angle of the rotation. The similarity transform using pivot $[i, j]$ has two properties [83]: i) only elements in rows and columns i and j may be affected. ii) If two elements facing each other across the rows i, j or columns i, j are both zero before the transform, they will still be zero after the transform. To reduce an unwanted element to zero, the rotation angle θ_r can be selected as in

Table 2.3: Formulas to select the rotation angle of a similarity transform.

Element to be Reduced	**Pivot**	**Angle θ_r**
$[i,k]$ or $[k,i]$ $(k \neq i,j)$	$[i,j]$	$\tan^{-1}(M_{ik}/M_{jk})$ or $\tan^{-1}(M_{ki}/M_{kj})$
$[j,k]$ or $[k,j]$ $(k \neq i,j)$	$[i,j]$	$\tan^{-1}(-M_{jk}/M_{ik})$ or $\tan^{-1}(-M_{kj}/M_{ki})$
$[i,j]$	$[i,j]$	$\frac{1}{2}\tan^{-1}(\frac{2M_{ij}}{M_{jj}-M_{ii}}) + \frac{k\pi}{2}$ or $\pm\frac{\pi}{4}$ if $M_{ii} = M_{jj}$

Table 2.3. Usually several sequential transforms are required to obtain a desired topology.

Many network topologies have been published in the literature based on analytical or numerical procedures. Some well-known topologies are shown in Fig. 2.7. Shown in Fig. 2.7(a) and (b) are the canonical folded networks in even and odd orders for symmetric and asymmetric filtering functions, respectively. The folded network is a fundamental topology because many other topologies are generated from it. Its synthesis procedure can be generalized to any order and completely analytical [83, 85, 86]. Fig. 2.7(c) shows the topologies consisting of extended-box sections. They are applicable for both symmetric and asymmetric cases. However, the number of transmission zeros is constrained by the minimum path rule [57]. The synthesis procedures may be analytical or numerical [87–90]. Cul-De-Sac topologies are shown in Fig. 2.7(d). This kind of topology has only one loop section and one negative coupling in the network. The maximum number of transmission zeros that can be generated is $N-1$. A Cul-De-Sac network can be synthesized analytically to any order [83, 85]. Shown in Fig. 2.7(e-g) are the

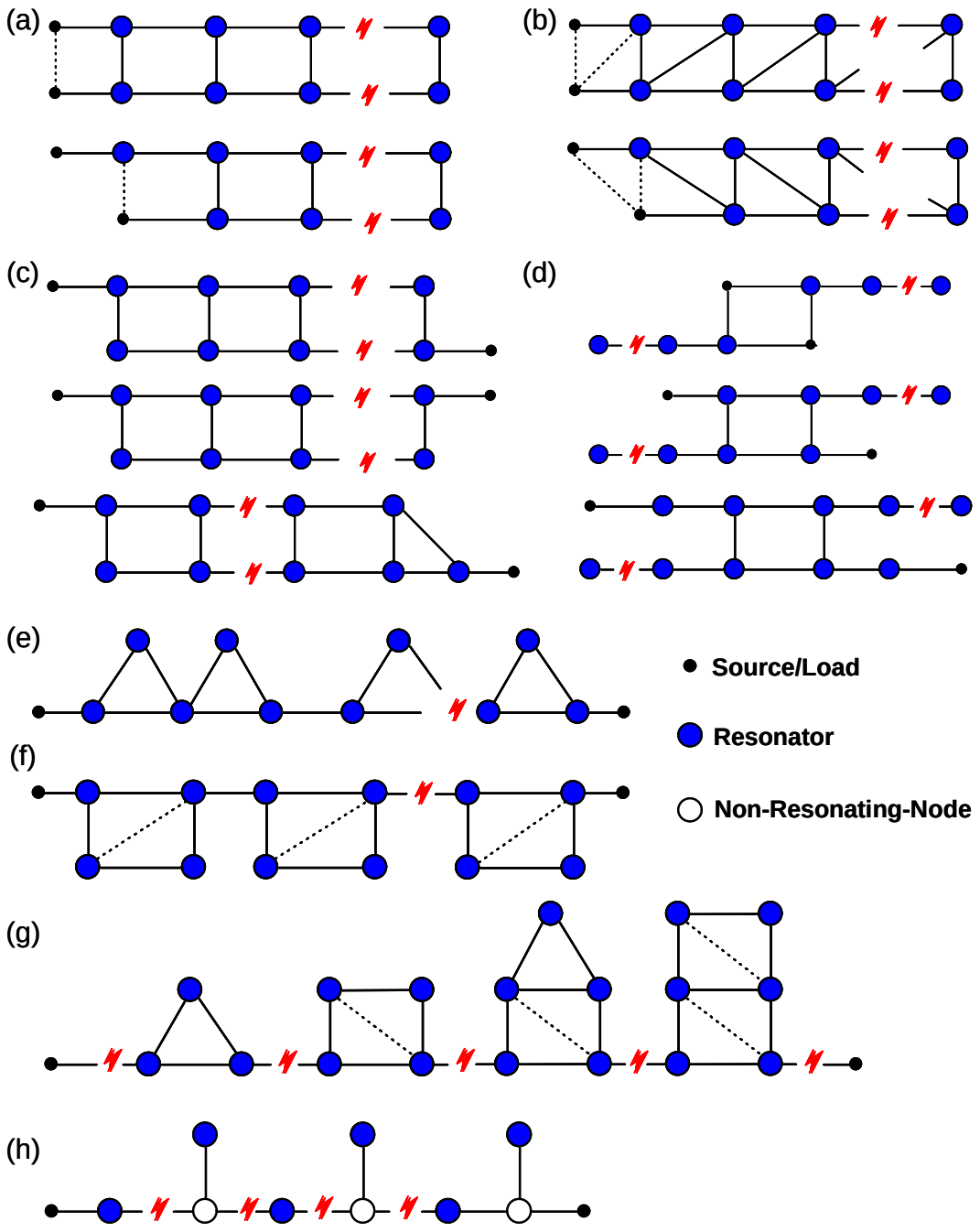

Figure 2.7: Well-known filter topologies. (a) Canonical folded network for symmetric cases (even and odd orders). (b) Canonical folded network for asymmetric cases (even and odd orders). (c) Extented-box sections (three cases). (d) Cul-De-Sac (three cases). (e) Cascaded Triplets. (f) Cascaded Quartets. (g) Cascaded N-tuplets. (h) In-line topology.

topologies of cascaded triplets, cascaded quartets, and cascaded N-tuplets. Their synthesis is based on the extraction of zeros and can be completely analytical [91, 92]. One advantage of such networks is that the zero-generating locations can be controlled through the synthesis procedure. An in-line topology using Non-Resonating-Nodes (NRNs) is shown in Fig. 2.7(h). The elements are extracted one by one according to the admittance matrix [93]. Many other discussions on linear phase filters and dual-band filters are given in [79–81, 94, 95].

2.3.3 Cascaded Building-blocks

One important topology is the cascaded N-tuplet (CN) topology as in Fig. 2.7(g), which consists of pure or mixed blocks of cascaded triplets (CT), cascaded quartets, and cascaded quintets, etc. Actually, the synthesis of CN topology is based on the building block technique: *a network is separated into two or more blocks first, and then any transformation procedures can be applied on each block to obtain a desired topology without affecting other blocks.* Basically, two steps are required: i) Gathering N elements for a N-tuplet block. ii) Reducing the gathered N-tuplet block to be a canonical folded topology or other topologies based on the well-know rotation procedures. The reduction procedure at the second step will only transform the N-tuplet block without affecting other elements outside this block.

A pure CT network topology is appropriate for the building block technique because it can be easily separated into blocks by simple rotations. Fig. 2.8 shows one example to obtain a cascaded quintet block from the CT topology. Other N-

(a)

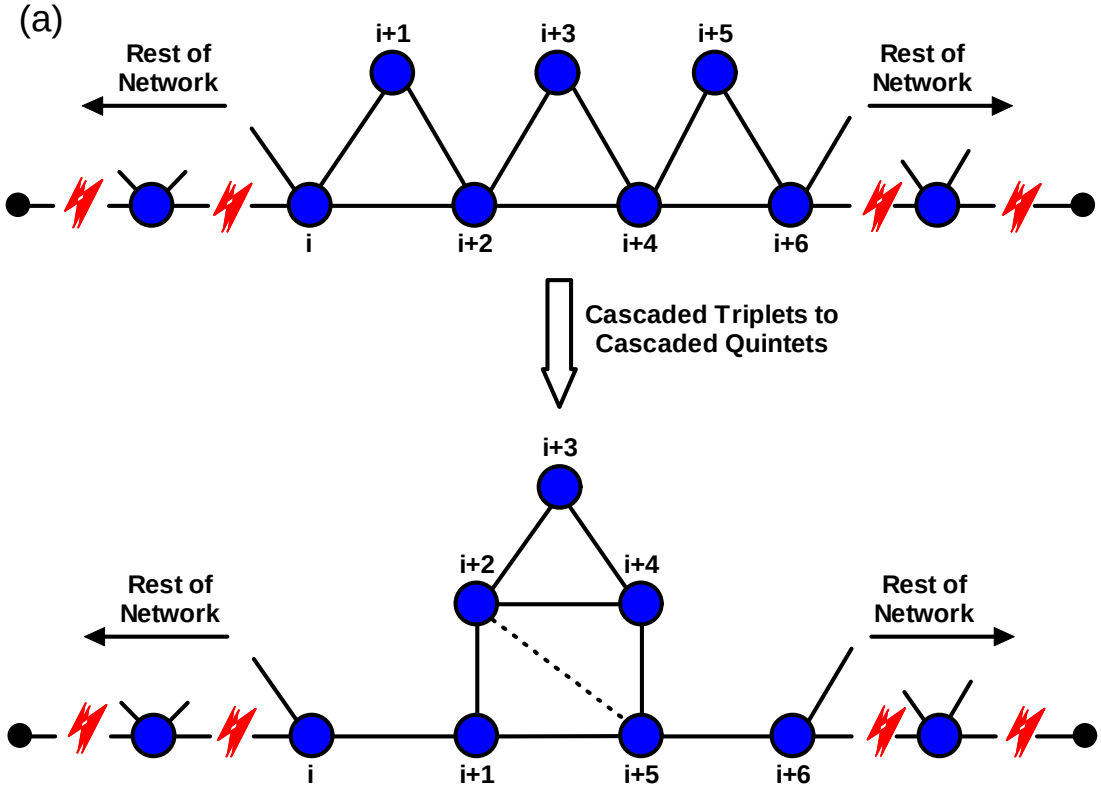

(b)

# of Rotation	Pivot	Element to be Annihilated	Rotation Angle
Gathering 5 elements for Quintet block			
1.	[i+1, i+2]	$M_{i,i+2}$	$\tan^{-1}(-M_{i,i+2}/M_{i,i+1})$
2.	[i+4, i+5]	$M_{i+4,i+6}$	$\tan^{-1}(M_{i+4,i+6}/M_{i+5,i+6})$
Reducing the gathered 5-element block to folded topology			
3.	[i+3, i+4]	$M_{i+1,i+4}$	$\tan^{-1}(-M_{i+1,i+4}/M_{i+1,i+3})$
4.	[i+2, i+3]	$M_{i+1,i+3}$	$\tan^{-1}(-M_{i+1,i+3}/M_{i+1,i+2})$
5.	[i+3, i+4]	$M_{i+3,i+5}$	$\tan^{-1}(M_{i+3,i+5}/M_{i+4,i+5})$

Figure 2.8: One transformation example using the building block technique. (a) Diagram from cascaded triplets to cascaded quintets. (b) The sequential rotations.

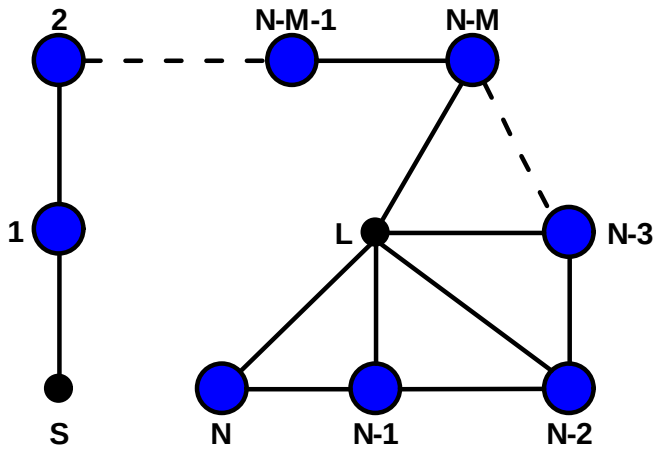

Figure 2.9: Wheel network topology for an Nth order filtering function with M transmission zeros. It can be transformed to CT topology analytically.

tuplet blocks can be generated in a similar way. In fact, a generalized computer program can be easily written for generating all possible N-tuplet blocks from a pure CT network. It must be pointed out that one N-tuplet block is usually responsible for $N-2$ transmission zeros.

The pure CT topology can be obtained by an analytical procedure, which makes the generation of CN topology totally analytical. The CT topology can be generated from the wheel topology as in Fig. 2.9 by extracting the zeros one by one, which means extracting the triplet blocks one by one because one triplet block corresponds to one zero. The detailed procedure has been presented in [92].

2.3.4 Synthesis Example

A synthesis example is performed to show the validity of the above discussion. Shown in Fig. 2.10(a) is a dual-passband asymmetric filtering function having six

poles and three transmission zeros. Its dual passbands are: $[-1$ to $-0.3]$ and $[0.42$ to $1]$. Its stopbands are: $[-0.11$ to $0.1]$ and $[1.4$ to $+\infty]$. Four possible network topologies as shown in Fig. 2.10(b) have been synthesized to realize the filtering function, namely folded topology, Cul-De-Sac topology, Cascaded triplets topology, and Cascaded Quartet-Triplet topology. The synthesized coupling matrix for each topology is given as the followings.

1. Non-zero elements in the coupling matrix of the folded network are: $M_{S1} = 0.8999$; $M_{11} = 0.0843$; $M_{12} = 0.8793$; $M_{22} = 0.0365$; $M_{23} = 0.3674$; $M_{25} = 0.3777$; $M_{26} = 0.3313$; $M_{33} = -0.0654$; $M_{34} = 0.3423$; $M_{35} = -0.0810$; $M_{44} = -0.1853$; $M_{45} = 0.3907$; $M_{55} = -0.2708$; $M_{56} = 0.8145$; $M_{66} = 0.0843$; $M_{6L} = 0.8999$.

2. Non-zero elements in the coupling matrix of the Cul-De-Sac topology are: $M_{S1} = 0.8999$; $M_{11} = 0.0843$; $M_{12} = 0.7296$; $M_{15} = -0.4909$; $M_{22} = 0.2905$; $M_{23} = 0.3391$; $M_{26} = 0.7296$; $M_{33} = 0.2222$; $M_{44} = -0.4729$; $M_{45} = 0.4234$; $M_{55} = -0.5249$; $M_{56} = 0.4909$; $M_{66} = 0.0843$; $M_{6L} = 0.8999$.

3. Non-zero elements in the coupling matrix of the CT network are: $M_{S1} = 0.8999$; $M_{11} = 0.0843$; $M_{12} = 0.4460$; $M_{13} = 0.7578$; $M_{22} = -0.0336$; $M_{23} = -0.2039$; $M_{33} = 0.3007$; $M_{34} = -0.2729$; $M_{35} = 0.6052$; $M_{44} = -0.2098$; $M_{45} = 0.3210$; $M_{55} = 0.4604$; $M_{56} = 0.4547$; $M_{5L} = 0.5716$; $M_{66} = -0.9183$; $M_{6L} = 0.6950$.

4. Non-zero elements in the coupling matrix of the CQ-CT topology are: $M_{S1} = 0.8999$; $M_{11} = 0.0843$; $M_{12} = 0.5701$; $M_{14} = 0.6695$; $M_{22} = -0.0639$; $M_{23} = 0.0574$; $M_{24} = 0.0861$; $M_{33} = 0.1585$; $M_{34} = 0.3972$; $M_{44} = -0.0374$;

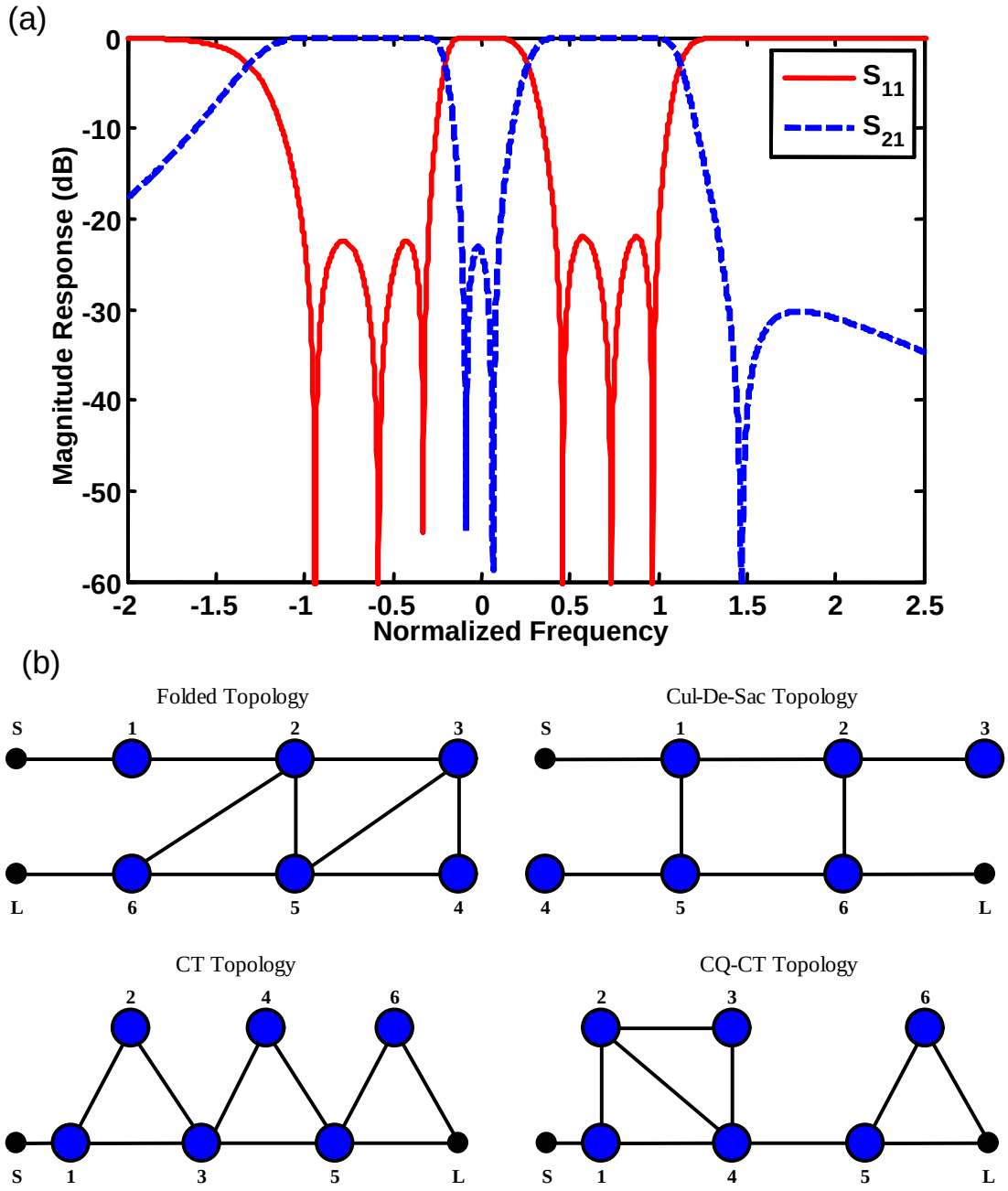

Figure 2.10: A multiple-band filter synthesis example. (a) Magnitude response of the multiple-band filtering function (6 poles and 3 zeros) in normalized frequency. (b) Possible network topologies: folded network; Cul-De-Sac network; Cascaded Triplets network; Cascaded Quartet and Triplet network.

$M_{45} = 0.6850$; $M_{55} = 0.4604$; $M_{56} = 0.4547$; $M_{5L} = 0.5716$; $M_{66} = -0.9183$; $M_{6L} = 0.6950$.

The last triplet building block (including load) in the CT network has exactly the same coupling values as the last triplet in the CQ-CT network because these two building blocks are synthesized to correspond to the same transmission zero ($j1.4711$). This effect also proves the validity of the building block technique. Cul-De-Sac topology has the least number of cross couplings, which makes the hardware implementation easier than others. However, the filter response will be more sensitive than others to the hardware dimensions due to the less number of couplings. Usually, the greater the number of cross couplings in one topology, the more difficult the hardware implementation and the better the sensitivity. In practice, in order to decide which topology to use for the hardware implementation, a sensitivity test on different topologies should be performed first. A trade-off is then made between the sensitivity and the hardware complexity. Other factors including the maximum achievable coupling value, the size constraints, and the assembly requirements, etc. should also be considered.

2.4 Hardware Implementation

2.4.1 Filter Transformation

The approximation and synthesis problems discussed above are based on the normalized frequencies. In practical applications, frequency transformation is, there-

fore, necessary to apply the synthesized normalized coupling matrix for hardware implementation. If f_1 and f_2 denote the most left and most right passband edges of a practical multiple-band filter, then the filter response can be obtained by using the following frequency substitution:

$$\omega \leftarrow \frac{f_0}{f_2 - f_1}\left(\frac{f}{f_0} - \frac{f_0}{f}\right) = \frac{f_0}{bw}\left(\frac{f}{f_0} - \frac{f_0}{f}\right) \tag{2.22}$$

where ω is the normalized frequency as in Fig. 2.1. f_0 is the center frequency of the multiple-band filter that is defined as $f_0 = \sqrt{f_1 f_2}$. bw is the whole bandwidth of the multiple-band filter that is defined as $bw = f_2 - f_1$. Therefore, the frequency transformation maps the practical multiple-band filter to the normalized one as follows:

$$\omega = \frac{f_0}{bw}\left(\frac{f}{f_0} - \frac{f_0}{f}\right) = \begin{cases} -1, & \text{when } f = f_1 \\ 0, & \text{when } f = f_0 \\ +1, & \text{when } f = f_2 \end{cases} \tag{2.23}$$

It must be noted that the center frequency f_0 and bandwidth bw of a multiple-band filter are defined for the whole filter response (i.e. from the most left passband edge f_1 to the most right passband edge f_2.), rather than each passband in the multiple-band filter. Actually, if the multiple-band filter is considered to be a special case of a single-band filter with transmission zeros inside the passband, the definitions of f_0 and bw above will be exactly same as the single-band filter.

2.4.2 Filter Realization

Given the center frequency f_0, bandwidth bw and other specifications, a multiple-band filter after frequency transformation can be approximated and synthesized

through the afore-presented procedures, and a normalized coupling matrix for a desired topology can be obtained. The normalized coupling matrix must be transformed to the actual coupling values for filter realization as follows:

$$\begin{cases} M_{ij} \cdot bw, & \text{in frequency unit} \\ M_{ij} \cdot \frac{bw}{f_0}, & \text{in normal unit} \end{cases} \tag{2.24}$$

During the filter realization, the center frequency f_0 and the actual coupling values of the multiple-band filter are mapped to the physical structures and dimensions by appropriate CAD tools. Tuning and optimization are usually required to obtain the desired filter performance. Actually, the realization methodology of multiple-band filters is completely identical with single-band filters. The detailed information about filter realization can be found in Chapter 3.

Chapter 3

Microwave Filter Designs

3.1 Design Methodology

3.1.1 Introduction

Microwave filters are among the most commonly used passive components in any microwave system. They are usually distributed networks that may consist of periodic structures in order to exhibit passband and stopband characteristics in various frequency bands. A design method must be able to determine the physical dimensions of a filter structure having the desired frequency characteristics. Research on microwave filters has spanned more than sixty years, and the number of contributions devoted to the design methods of microwave filters is enormous. Reviews on the topic of filter designs in a historical perspective can be found in [9, 55, 56].

In the following subsection, a generalized design method for a wide variety of

microwave and millimeter-wave filters will be presented. The method depends on a combination of a simple synthesis and an accurate analysis based on advanced numerical methods. Basically, the filter designs proceed from the synthesis of the lumped-element low-pass prototypes. The physical dimensions/parameters of filter structures are then related to the corresponding parameters of the prototypes by numerical analysis. Optimization and tuning procedures are usually involved in microwave filter designs. For most of the filter designs, field-theory-based analysis is an integrated part of the design process. Such analysis methods allow filter responses to be predicted very accurately, so that experimental adjustments of the manufactured components can be reduced or eliminated. For some filter structures that can not be efficiently optimized by numerical methods due to the structure complexity or the lengthy simulation speed, experimental tuning is a necessary step in the design procedure. The tuning process can be guided by computer programs that enable parameter extractions.

The analysis of filter structures in this dissertation is mostly addressed by the mode matching method (MMM). MMM has the advantage of high efficiency, which makes it the most preferable for the full-wave analysis and optimization procedure. However, MMM is a structure-related method, which means that knowledge of different structures needs to be studied individually in order to create specific MMM codes to perform the rigorous full-wave analysis on them. Other numerical methods, such as FEM and MoM, provided by the commercial software tools [71–73] are also employed in this dissertation to analyze some structures that can not be tackled by MMM and verify the final designs performed in MMM. In

addition, the post-processing features, like field calculations and plots, in these commercial software tools are also used to gain an insight into the component operation.

3.1.2 Generalized Design Approach

A generalized design procedure shown in Fig. 3.1 as a flow chart has been followed in this dissertation to perform the filter designs. The detailed functions of each step will be discussed in the following sections.

1. The design procedure begins with the desired filter performance. The performance is usually determined by the requirement of a microwave system and expressed in terms of electrical, mechanical, and environmental parameters. Commonly used electrical parameters are: center frequency, bandwidth, insertion loss, gain flatness, return loss, stopband attenuation, group delay or phase linearity, and power handling capability, etc. Mechanical requirements are usually characterized by constraints of the maximum volume, weight, and filter interfaces. Environmental requirements include resistance for vibration and shock and the temperature limits (i.e., the electrical performance must be maintained in the specified environments). Even though the objective of a design is to satisfy all the given specifications, sometimes a compromise has to be made between the electrical, mechanical and environmental requirements to obtain a feasible physical structure. Therefore, final specifications of a filter design are usually decided with the consideration of the system requirements, the physical realizability, the design

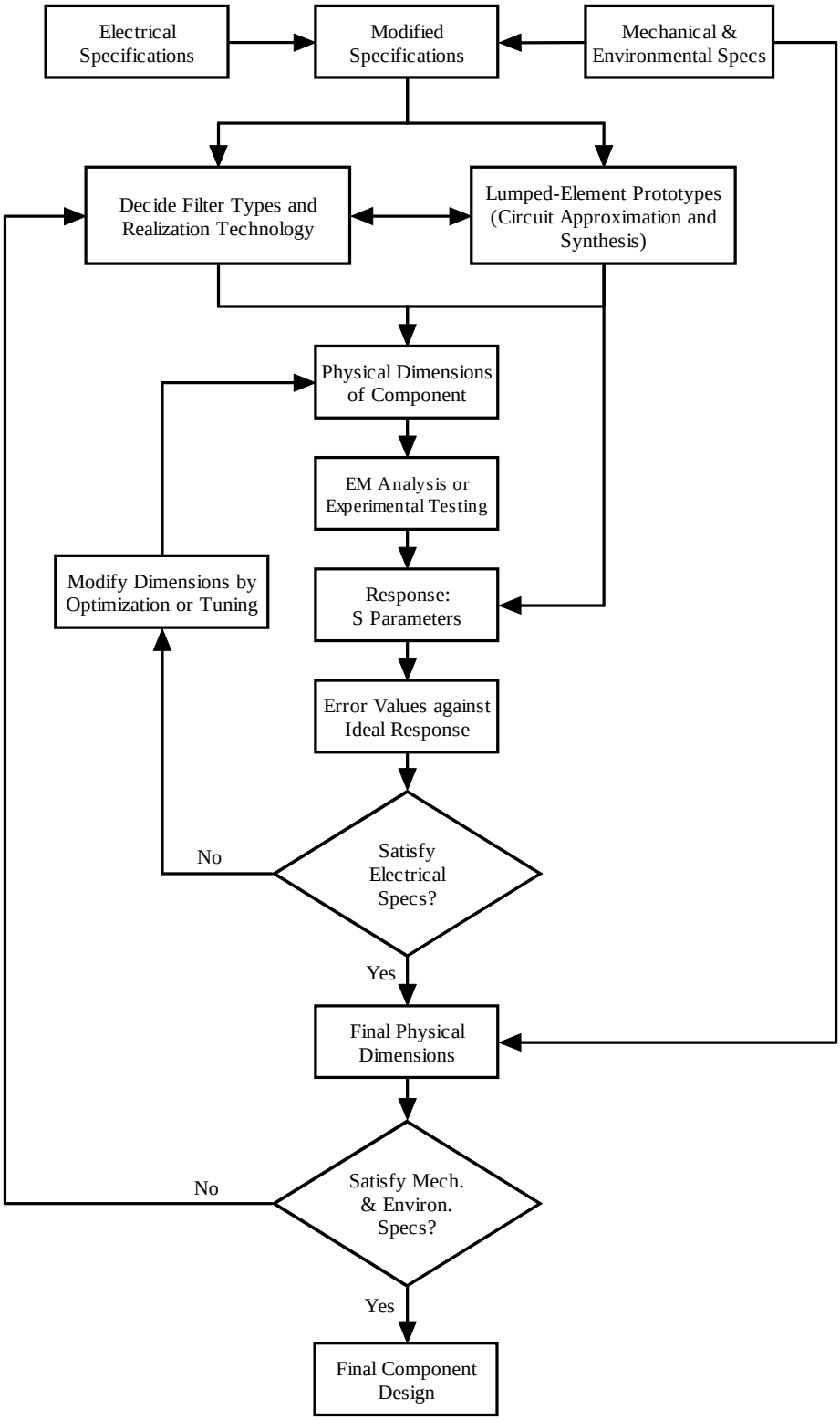

Figure 3.1: The flow chart of generalized filter design procedure.

Table 3.1: Qualitative comparison between different realization technologies [35].

Realization Technology	Size	Loss	Bandwidth	Spurious	Power Handling
Rectangular Waveguide	medium/large	low	small	medium	very high
Ridge Waveguide	small	medium	medium/large	very good	high
Circular Waveguide	medium/large	low	small	medium	very high
Coaxial TEM Lines	small	medium	small/medium	good	medium
Planar Structure	very small	high	medium/large	good	very low
Dielectric Loaded	small/medium	very low	very small	very poor	low

feasibility, and the cost.

2. With the desired specifications of a filter design, an appropriate filter type and a suitable realization technology should be selected before the actual design procedure. The possible filter types are Butterworth, Chebyshev, Bessel, Quasi-elliptic, and Elliptic, etc. Chebyshev and Quasi-elliptic filters are the most often used filter types. For Quasi-elliptic filters, a proper topology needs to be se-

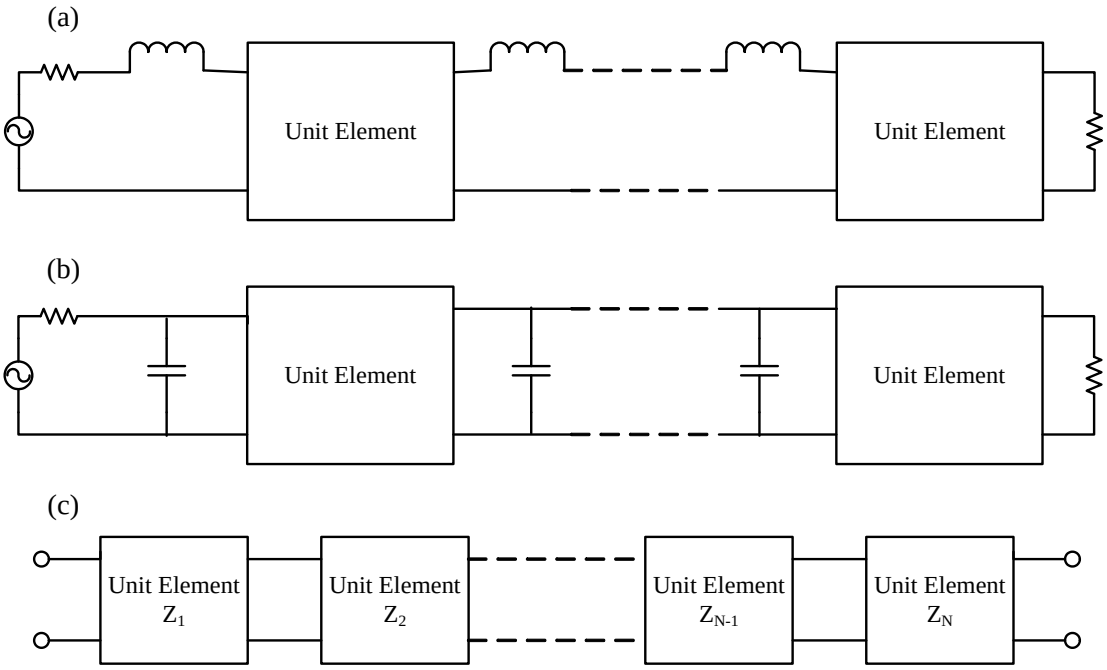

Figure 3.2: Low-pass filter prototypes. (a) Unit elements with series inductors. (b) Unit elements with parallel capacitors. (c) Cascade of unit elements.

lected based on the knowledge of the complexity and the sensitivity (as described in Chapter 2, p. 54). Since different realization technologies have different effects on the electrical, mechanical and environmental performance, the choice of a technology is usually based on available data or previous experiences for typical performance of various technologies. In Table 3.1, such data are summarized for several technologies [35].

3. After the filter type and topology have been selected, an ideal circuit prototype is synthesized for the purpose of realization. In conventional form, the synthesis of an electrical filter is accomplished by determination of lumped elements of a network which will produce the required frequency response. However, for microwave filters, the lumped-element networks usually need to be transformed

to an appropriate format that would lead to the physical dimensions of the device. The commonly used networks for low-pass and bandpass filters are discussed next. The prototypes for highpass and bandstop filters can also be obtained by using the well-known transformations from low-pass prototypes.

- One ideal prototype for low-pass filter is using the unit elements with series inductors or parallel capacitors as shown in Fig. 3.2(a) and (b), where a unit element is a lossless transmission line of unit length, for example quarter wavelength. Kuroda's identities are usually used for the transformation of this prototype network [2]. Detailed information about the transformation procedure can be found in [96]. Another ideal prototype for low-pass filter is the stepped impedance unit element network as in Fig. 3.2(c). This prototype consists entirely of a cascade of unit elements with different characteristic impedances. The detailed synthesis theory on this prototype has been given in [82, 97, 98]. Other ideal prototypes for low-pass filter can be found in [57].

- One ideal prototype for bandpass filter is the multiple coupled resonator network discussed in chapter 2. The values of mutual couplings (impedance inverters or admittance inverters) and self couplings need to be found for a selected network topology by using the synthesis methods given in chapter 2. Some other prototypes for extracted-pole filters and linear phase filters can be found in [99–101].

4. The initial dimensions of the physical filter structure are found according

to the synthesized circuit prototypes and the selected realization technology. The response of the initial filter structure should be close to the ideal response of the equivalent circuit. The initial dimensions are commonly generated by mapping the physical dimensions with the elements of the synthesized equivalent circuit. The possible mapping methods are given as below.

- Commensurate network transformations are usually used for low-pass filter realizations. Unit elements are implemented as transmission lines with the required electrical length and characteristic impedance. Inductors and capacitors are transformed into short-circuited or open-circuited stubs using Richard's transformation [2, 57]. This method is commonly applied to TEM transmission line low-pass filters, however, it can also be used on pseudo-low-pass filter designs with waveguide structures, such applications can be found in [102–104].

- Classical formulas approximating electromagnetic modes are used to relate the waveguide dimensions (especially junctions) to the circuit elements, which can be found in [7]. Other circuit models taking into account some higher order modes for the discontinuities are presented in [105–107], which is more accurate than the formulas in [7].

- Full-wave numerical techniques are employed to analyze the cavity, discontinuity, and part region in a filter structure, so that the equivalent circuit parameters can be generated to model these structures. All the aforementioned numerical methods can be used for the analysis, however, the efficiency, the

capability, and the accuracy should be considered to select an appropriate method. Basically, numerical methods are used to determine the resonant frequency of the cavity, the inter-coupling values between two cavities, and the external coupling of input/output interface [45, 108–111]. Usually, a curve or table relating the determined values to the physical dimensions can be obtained. The initial physical dimensions are then determined by interpolation method based on the synthesized circuit prototype. The response of the initial filter structure is mostly very close to the desired one due to the precise analysis of the full-wave numerical methods.

5. Optimization or tuning of the complete component is performed to improve the filter performance once the initial dimensions of the filter structure have been obtained. if a filter structure can be rigorously and efficiently analyzed by full-wave numerical techniques, a full-wave optimization procedure is usually applied to find the optimum dimensions that will generate the desired response. Some common optimization algorithms are: Quasi-Newton, Simplex, Random walk, Simulated Annealing and Gradient Technique. The detailed information regarding the features of each algorithm can be found in [35, 112–114]. Optimization routines usually need to minimize an error function. A typical error function is expressed as

$$\begin{aligned} err(\overline{x}) \;=\; & \sum_{i=1}^{N_p} w_p \left\{ dB\left[S_{11}(\overline{x}, f_{p,i})\right] + r \right\}^2 + \sum_{i=1}^{N_s^I} w_s^I \left\{ dB\left[S_{21}(\overline{x}, f_{s,i}^I)\right] + a^I \right\}^2 \\ & + \sum_{i=1}^{N_s^{II}} w_s^{II} \left\{ dB\left[S_{21}(\overline{x}, f_{s,i}^{II})\right] + a^{II} \right\}^2 \end{aligned} \tag{3.1}$$

where N_p, N_s^I, and N_s^{II} are the number of frequency points in the passband, stopband I (lower), and stopband II (higher), respectively. f's represent the sampled frequency points in passband and stopband. $\overline{x}$ is the geometrical parameters of the filter to be optimized. w's are the weight factors for controlling the contributions of each error element. Operator $dB(\cdot)$ is to transform S-parameters in unit of dB. r, a^I, and a^{II} are the desired return loss, attenuation in stopband I, and attenuation in stopband II, respectively. In practical design, the optimization should go gradually to achieve the ultimate goal, which means that some intermediate less-aggressive goals should be fulfilled by the optimizer first.

Tuning procedure is also often required to improve the performance of some filter structures that can not be analyzed and optimized by the numerical methods efficiently. Tuning procedure can be categorized as: numerical tuning and experimental tuning. CAD software tools are still used in the numerical tuning procedure, however, several methods, like electromagnetic-circuit combination method [11], space-mapping method [115–118] and parameter extraction method [119] are employed to improve the tuning efficiency. Laboratory instruments, like network analyzer, are used in the experimental tuning. The efficiency of this tuning procedure is commonly related to accumulated experience. Computer-aided tuning methods are also available for experimental tuning [120–122], and still very interesting research topics.

6. Experimental testing needs to be performed to check the electrical and environmental specifications after the final dimensions have been obtained for a filter structure. If electrical performance, like insertion loss, or environmental

performance, like temperature drifting, do not satisfy the requirements, some modifications must be made to improve them. In some worst cases, the whole design process has to be started over again.

Most of the filters can be designed by following the procedure in Fig. 3.1. Some of the steps might be simplified or avoided depending on the specifications and the complexity of the filter. However, what has not been mentioned is that a designer should always gain an insight into the filter structures and be able to control all the design aspects. A good understanding of the filter structure and operation can make the filter design much easier.

3.1.3 Determination of Couplings

Coupled resonator circuit prototypes are most commonly used in the design of microwave coupled resonator bandpass filters in the sense that they can be applied to any type of resonator despite its physical structure. They have been applied to the design of waveguide filters [123, 124], dielectric resonator filters [125], ceramic combline filters [126], microstrip filters [127–130], superconducting filters [131], and micromachined filters [132]. The design method is based on the coupling coefficients of the inter-coupled resonators and the external couplings of the input and output resonators (i.e. the coupling matrix discussed in chapter 2). Therefore, a relationship between the coupling coefficients and the physical structures needs to be established. The formulations for extracting the couplings are given next for different cases.

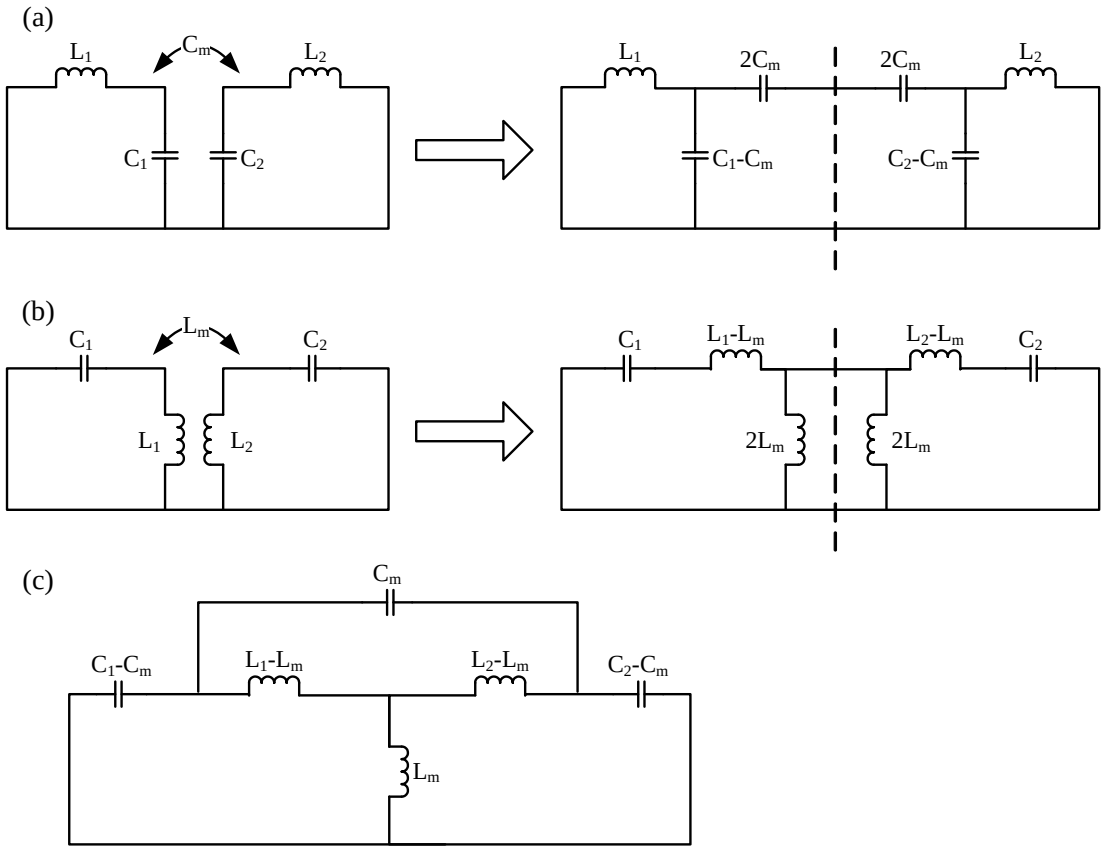

Figure 3.3: Inter-coupling between coupled resonators. (a) Coupled resonator circuit with electric coupling. (b) Coupled resonator circuit with magnetic coupling. (c) Coupled resonator circuit with mixed electric and magnetic coupling.

A. Inter-coupling between coupled resonators

Shown in Fig. 3.3 is the equivalent lumped-element circuit model for the inter-coupling between two coupled resonators. Three different coupling cases are displayed: electric, magnetic, and mixed couplings. $L_1(L_2)$ and $C_1(C_2)$ are self-inductance and self-capacitance for resonator 1(2), so that $1/\sqrt{LC}$ equals the angular resonant frequency of uncoupled resonators. C_m and L_m represent the mutual capacitance and mutual inductance, respectively. When the two res-

onators are having the identical resonant frequency, they are called synchronously tuned. Otherwise, they are called asynchronously tuned. A general formulation for extracting coupling coefficient is given as [127]:

$$k = \pm \left(\frac{f_{01}}{f_{02}} + \frac{f_{02}}{f_{01}} \right) \sqrt{\left(\frac{f_{p2}^2 - f_{p1}^2}{f_{p2}^2 + f_{p1}^2} \right)^2 - \left(\frac{f_{02}^2 - f_{01}^2}{f_{02}^2 + f_{01}^2} \right)^2} \tag{3.2}$$

where $f_{0i} = 1/(2\pi\sqrt{L_i C_i})$ for $i = 1, 2$. f_{p1} and f_{p2} are the two natural resonant frequencies of the whole coupling circuit/structure. k is the coupling coefficient with the following general definition:

$$k = \left(\frac{C_m^2}{C_1 C_2} + \frac{L_m^2}{L_1 L_2} - \frac{2 L_m C_m}{\sqrt{L_1 C_1 L_2 C_2}} \right)^{1/2} \tag{3.3}$$

For synchronously tuned coupled resonators, $f_{01} = f_{02}$, the formulation for extracting the coupling coefficient is simplified as:

$$k = \pm \frac{f_{p2}^2 - f_{p1}^2}{f_{p2}^2 + f_{p1}^2} \tag{3.4}$$

Therefore, in order to solve the coupling coefficient between two coupled physical structures/cavities, a full-wave numerical method can be employed to find the natural resonant frequencies of two resonant peaks, observable from the resonant frequency response or obtainable from the eigenmode solvers. The formulations given above are then used to calculate the coupling coefficient. The sign of the coupling coefficient is related to the phase response. If one particular coupling is referred as positive coupling, then the negative coupling would imply that its phase response is opposite to that of the positive coupling.

One special case is the symmetrically coupled resonators. One natural resonant frequency is equivalent to the resonant frequency f_e with an electric wall

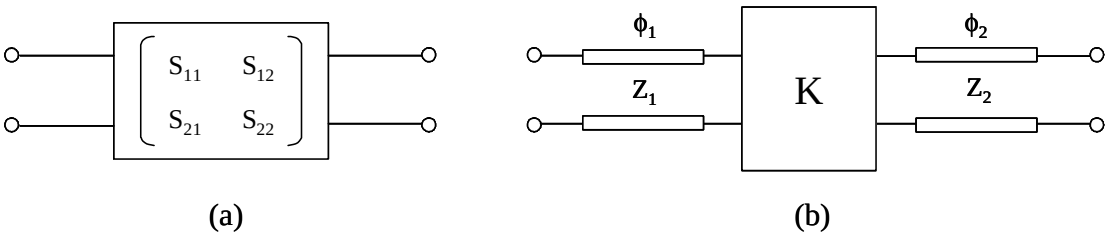

Figure 3.4: (a) Two-port scattering matrix of a lossless, reciprocal microwave coupling structure. (b) A circuit representation of the coupling structure by k-inverter and transmission lines.

inserted at the symmetry plane, and the other one is equivalent to the resonant frequency f_m with a magnetic wall inserted at the symmetry plane. Therefore, only half of the coupling structure needs to be solved in the simulator with the electric wall and the magnetic wall, respectively. The coupling coefficient will be given as:

$$k = \frac{f_e^2 - f_m^2}{f_e^2 + f_m^2} \tag{3.5}$$

The sign of the coupling is also determined by this expression. When k has a negative (positive) sign, the coupling is mainly electric (magnetic).

For some physical coupling structures, the coupling coefficient can be extracted from the relationship between the two-port scattering parameters and the equivalent circuit model using a k-inverter. Basically, the two-port scattering parameters (as in Fig. 3.4(a)) can be represented by a k-inverter with two offset transmission lines (as in Fig. 3.4(b)). This method is particularly useful for waveguide evanescent-mode filter designs. If the two-port scattering matrix of a lossless, reciprocal microwave coupling structure (with respect to the reference

planes of the discontinuities) can be solved by full-wave numerical methods, the k value and phase offsets of the transmission lines can be solved as [45, 133]:

$$\begin{aligned} \text{For } k &< 1\text{: } k = \sqrt{\frac{1-|S_{11}|}{1+|S_{11}|}},\ \phi_i = -\frac{1}{2}\theta_i + \frac{1}{2}\pi \\ \text{For } k &> 1\text{: } k = \sqrt{\frac{1+|S_{11}|}{1-|S_{11}|}},\ \phi_i = -\frac{1}{2}\theta_i,\ i = 1, 2 \end{aligned} \tag{3.6}$$

where $S_{11} = |S_{11}|\, e^{j\theta_1}$, and $S_{22} = |S_{22}|\, e^{j\theta_2}$. In practical designs, the phase offsets ϕ_1 and ϕ_2 of the two transmission lines should be used to adjust the lengths of the two coupled resonators to compensate the loading effect.

B. External input and output couplings

Shown in Fig. 3.5(a) is an equivalent circuit of the external coupled resonator structure, where R is the external coupling resistance connected to the lossless LC resonator. In order to extract the coupling resistance R, the phase and phase variation responses of S_{11} are firstly solved. The coupling resistance R is then calculated as [134, 135]:

$$R = -\frac{4}{f_l \left.\frac{d\phi}{df}\right|_{\min}} \tag{3.7}$$

where ϕ is the phase angle of the input reflection coefficient. f_l is the loaded frequency of the resonator corresponding to the frequency point of the minimum phase variation. Typical phase and phase variation responses are shown in Fig. 3.5(b). The external Q can be obtained as

$$Q_e = \frac{f_l}{R} \tag{3.8}$$

In practice, the phase and phase variation response of S_{11} of a physical input/output coupling structure can be solved by full-wave numerical methods.

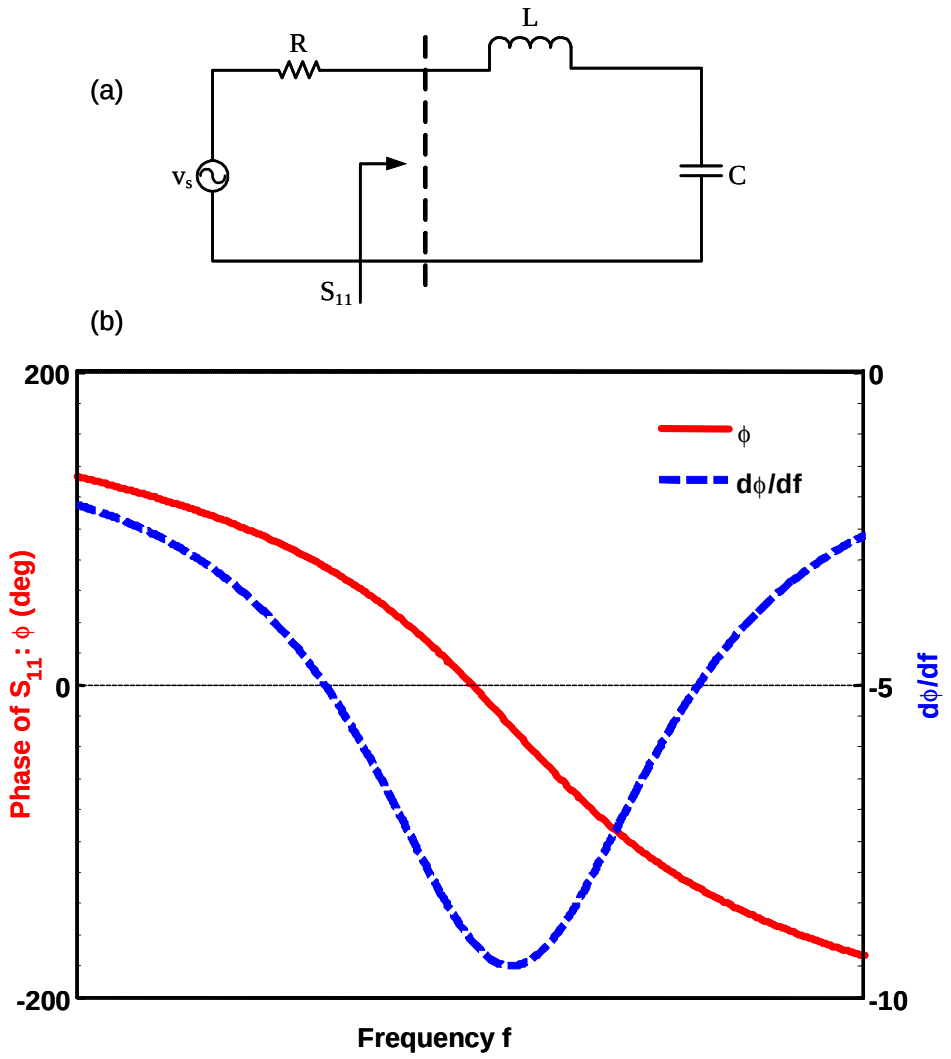

Figure 3.5: (a) An equivalent circuit of the input/output resonator with an external coupling resistance. (b) Typical phase response and phase variation response of the reflection coefficient S_{11}.

It should be commented that the reference plane of S_{11} in the EM simulation may be different from the shown circuit in Fig. 3.5(a), which will lead to an extra phase shift with respect to the shown curve in Fig. 3.5(b). However, the phase variation response is not dependent on the reference plane, which guarantees the accuracy of the formulas.

3.2 Miniature Double-layer Coupled Stripline Resonator Filters in LTCC Technology

3.2.1 Introduction

Miniature broadband filters compatible with printed circuit board (PCB) and monolithic microwave integrated circuit (MMIC) fabrication technologies are required in many communication systems. The filter size is usually constrained by the size of the employed resonator structures, and the filter bandwidth is limited by the achievable maximum couplings between these resonators. Many available compact resonator structures can be found in the literatures. Some of them, such as stripline resonator with one grounded end [1], hairpin resonator [136], etc., have the size constraint of quarter wavelength. Others, such as folded quarter-wavelength resonator [137], ring resonator [138], spiral resonator [139], etc., have smaller size than quarter wavelength, but are usually not applicable for broadband filter designs due to the difficulty in realizing strong couplings.

In this section a novel double-layer coupled stripline resonator structure is proposed to design broadband filters with compact size less than $\lambda/8 \times \lambda/8 \times h$ (filter height h is usually very small and approximately equal to the substrate height of the stripline). The size of the proposed resonator structure can be less than $\lambda/12$, and the coupling between two resonators can be realized strong enough for filter designs up to 60% bandwidth by proper mechanisms. Physical realization of the resonator structure can be easily performed in LTCC technology

which is a suitable manufacturing choice for a high-integration level of multiple-layer structures.

Two types of filter configurations can be implemented using the proposed resonator structures: combline and interdigital. In this section, two examples of interdigital filters and one example of combline filter are designed to validate the concept. Experimental results of the two interdigital filters are also presented. The two interdigital filters have the identical specifications, but employ different resonator dimensions to investigate the LTCC manufacturing effects on filter performance.

3.2.2 Filter Configuration

A. Proposed Resonator Structure

The proposed double-layer coupled stripline resonator structure is shown in Fig. 3.6. The idea is to introduce a strong capacitive loading effect inside the resonator to reduce its physical length [140]. The resonator structure consists of two strongly coupled strips as shown in Fig. 3.6(b). The opposite ends of these two strips are shorted to ground as in Fig. 3.6(c), so the coupling between these two strips will behave like a capacitance that will lower the resonant frequency. Due to this capacitive coupling effect, the total physical length lr of the resonator will be much shorter than a quarter wavelength at the desired resonant frequency. The physical length lr of the resonator is determined by three factors: the width ws of the two strips, the coupled (overlapped) length lc, and the vertical distance

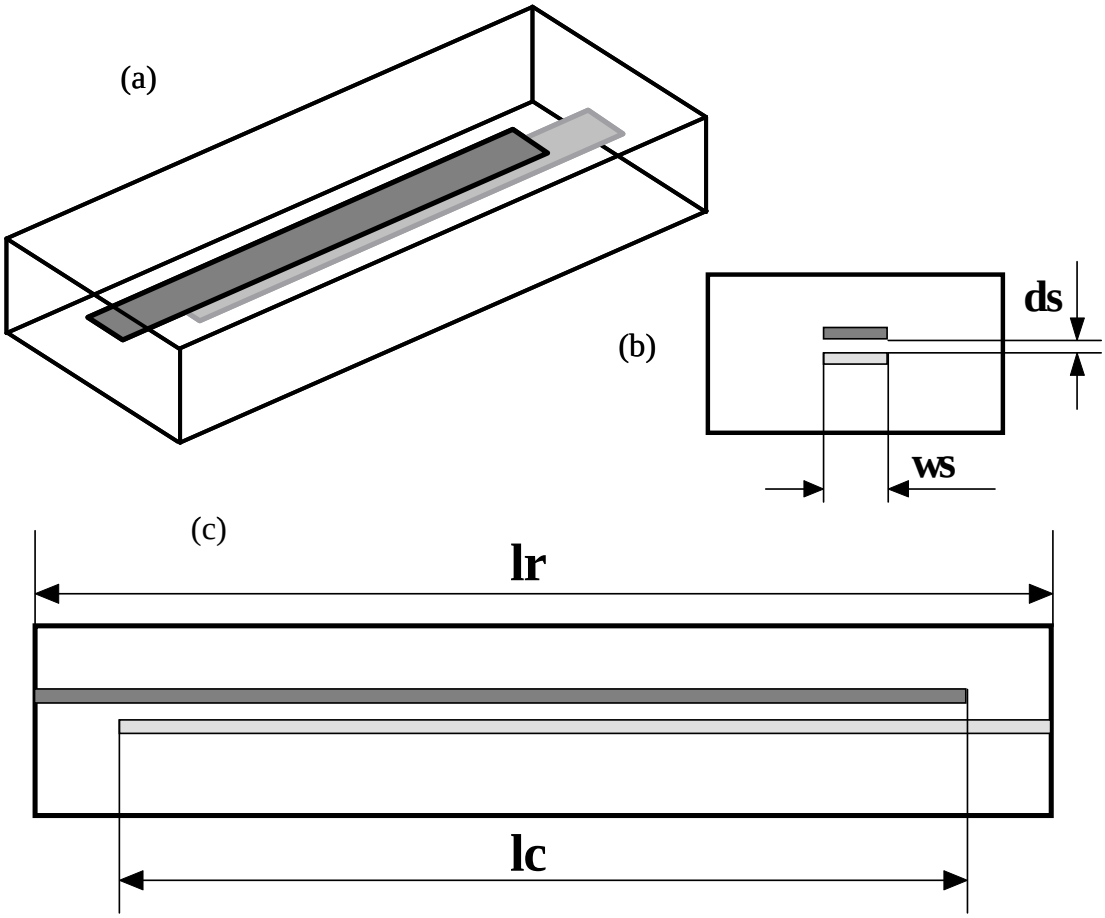

Figure 3.6: Double-layer coupled stripline resonator structure. (a) 3D view. (b) Cross section. (c) Side view. The structure is filled with a homogeneous dielectric material.

ds between them because these three factors will affect the capacitive coupling between the two strips. Actually, a resonator with physical length less than $\lambda/12$ at the desired resonant frequency can be realized by such a configuration with properly selected dimensions of these three factors.

It must be noted that the vertical distance *ds* between the two strips and the whole height of the resonator must be integer-multiple of the thickness of one ceramic layer in LTCC technology.

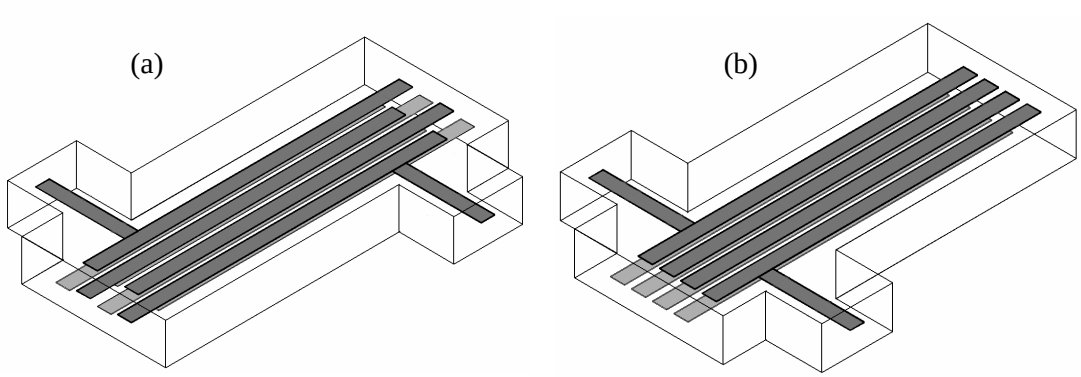

Figure 3.7: Filter configurations using double-layer coupled stripline resonators. (a) Interdigital filter configuration. (b) Combline filter configuration.

B. Possible Filter Configurations

Shown in Fig. 3.7 are two possible filter configurations using the proposed double-layer coupled stripline resonators: interdigital as in Fig. 3.7(a) and combline as in Fig. 3.7(b). These two filter structures are more compact compared with conventional one layer microstrip/stripline interdigital and combline filters. The input/output external couplings are realized by the tapped-in $50ohm$ striplines. The inter-coupling between resonators is achieved by the fringing fields between two resonator lines. Usually, the coupling between two interdigital resonators is stronger than the coupling between two combline resonators having the same spacing. Shown in Fig. 3.8 are the coupling curves for both cases with identical resonator dimensions (Dimensions are given in design example I). The smaller is the separation between the two resonators, the more noticeable is the coupling difference between the two configurations. Therefore, the interdigital configuration is more appropriate for broadband filter designs, while the combline configuration is a proper choice for some relatively narrower bandwidth filter de-

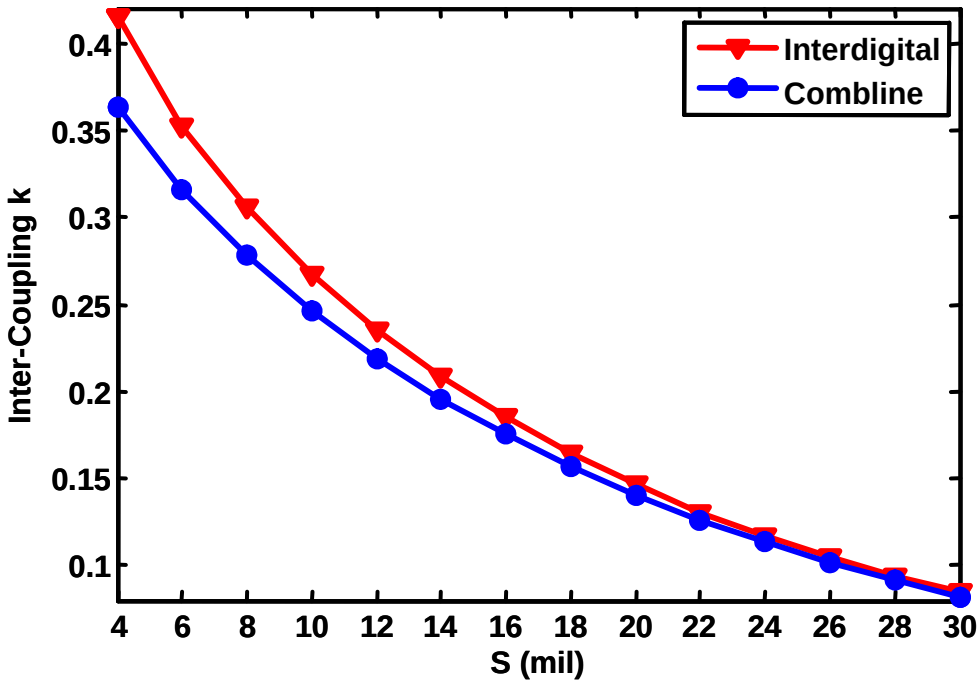

Figure 3.8: Inter-coupling curves of interdigital and combline configurations. Identical resonators are used. S is the separation between two resonators.

signs since it has more compact size than the interdigital one. To decide which configuration to use for a given filter specification, the maximum achievable coupling value with the minimum realizable space (the size of space is constrained by the physical implementation technology) between two combline resonators should be firstly checked. If this value is larger than all the required couplings of the desired filter, the combline configuration should be employed. Otherwise, an interdigital configuration should be the choice.

3.2.3 Filter Design and Modeling

The general design procedure discussed in the previous section is used to design the filters with either of the proposed configurations in Fig. 3.7. Basically, three

main steps are implemented: i) Initial filter dimensions are determined according to the given filter specifications. ii) Optimization using MMM is performed to find the optimum filter dimensions. iii) Ansoft HFSS is employed to check the optimum design from the second step and fine-tune the filter dimensions if needed. The detailed information of each step is illustrated below.

A. Initial Design

Given the specifications of a desired filter, the filter design starts with synthesizing a circuit model prototype. Physical realization is then performed according to such ideal model. The initial design procedure for the presented filters is given as follows.

1. An ideal circuit model is generated according to the filter requirements [1].

2. The dimensions of the double-layer coupled stripline resonator are determined in terms of the center frequency of the filter.

3. Determine the tapped-in stripline position to achieve the external coupling R [111].

4. Determine the separations between resonators to provide the required inter-couplings [127].

5. Assemble the tapped-lines and resonators together according to the calculated dimensions. Initial filter responses can be obtained by full-wave electromagnetic simulation in MMM or HFSS.

One of the advantages of combline and interdigital filters is that the resonant

frequency of the resonators will not be changed much by the loading effects of the couplings. Therefore, the initial filter response is usually a good starting point (typically return loss is below 10 dB) for further optimization.

B. Optimization by MMM

The initial design procedure given above does not take into account the higher order modes and the non-adjacent couplings between resonators, which have more effects on broadband filter designs than narrow-band ones. To achieve the desired filter performance, optimization by MMM can be employed. To demonstrate the optimization procedure by MMM, an interdigital filter configuration is used (The combline case is similar).

Shown in Fig. 3.9(a) is an interdigital filter with two stripline ports along z-axis. To model this filter configuration, the MMM should be applied along the z-direction. The cross sections involved are a stripline (I), an asymmetric stripline (II), side view of double-layer coupled stripline resonator (III), a rectangular waveguide (IV), and so on (as in Fig. 3.9(b)). Eigenmodes and eigenfields of these cross sections can be solved by the GTR technique (see Appendix A, p. 255). The typical electric field distributions of the fundamental mode of section (I) and (III) are shown in Appendix B (Fig. B.1(a) and (b), p. 269). The discontinuities between the cross sections are modeled by GSMs that can be obtained by MMM program based on the formulations in Appendix C (p. 271). Finally, the overall response can be computed by cascading all the GSMs together using (1.2). In principle this MMM approach is rigorous, but the convergence and simulation speed must be considered. The rectangular waveguides separating the discontinu-

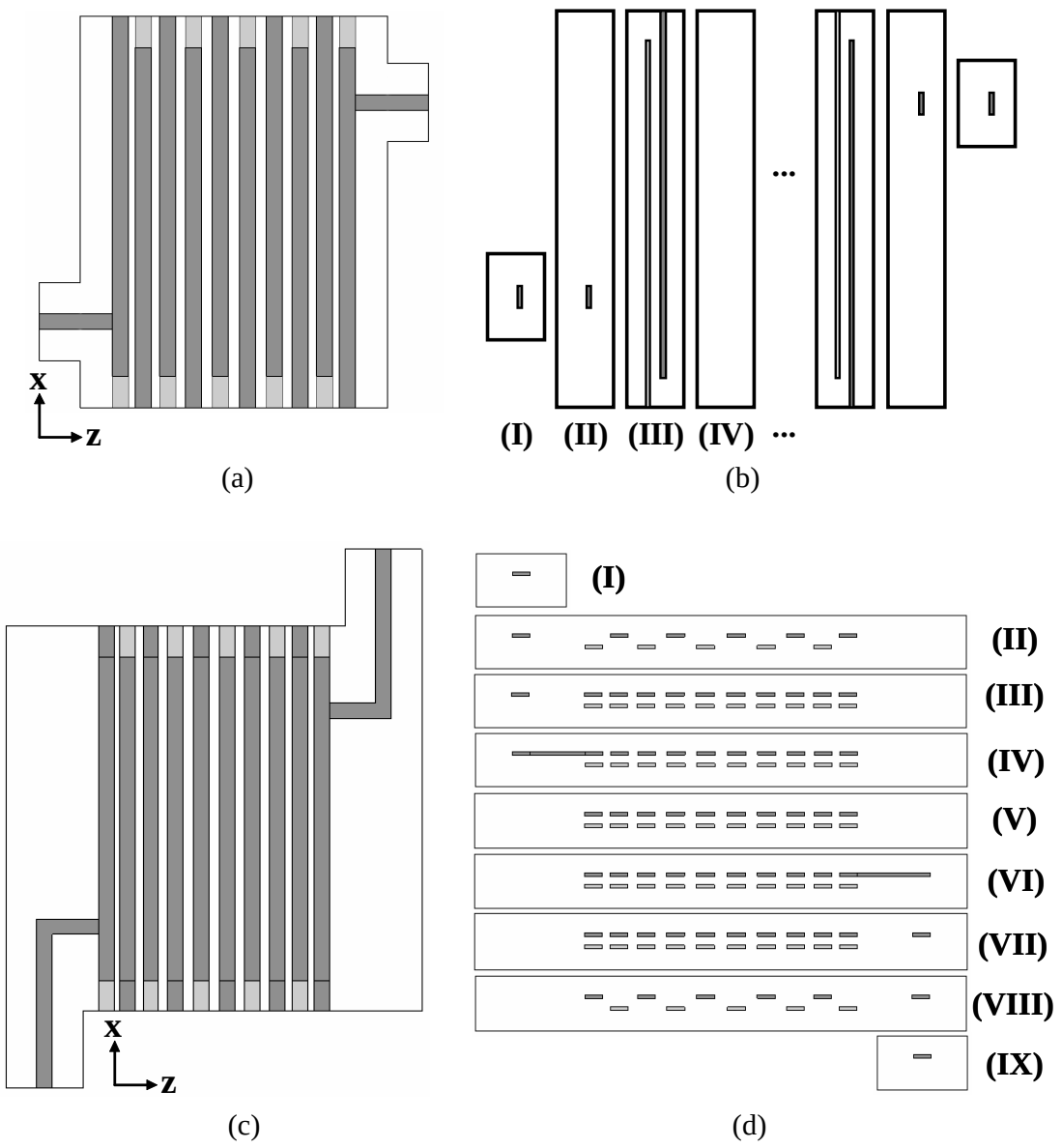

Figure 3.9: A 10th order interdigital filter using double-layer coupled stripline resonators. (a) Physical structrure with ports along z-axis. (b) Involved cross sections of structure in (a) along z-axis. (c) Physical structrure with ports bent along x-axis. (d) Involved cross sections of structure in (c) along x-axis.

ities are very short, and the fundamental resonating modes of the interdigital filter are mainly operating with TEM^x fields, while the fields in cross sections of III, IV, etc. are presented as a summation of TE^z and TM^z modes in the MMM analysis. As a consequence, a very large number of modes are needed for convergence, which would result in large computation time and numerical errors. Therefore, this approach is not appropriate for optimization.

Shown in Fig. 3.9(c) is the same filter as in Fig. 3.9(a) with 90° bends added at the input and output ports along x-direction. MMM simulation can, therefore, be applied along x-direction for this transformed topology. The benefit of doing MMM simulation along x-direction is that the fundamental modes of the cross-sections along x-axis will be TEM^x modes, which correspond to the main operating resonant modes of the filter. This means that MMM simulation with only TEM^x modes can generate acceptable results close to the converged ones (actually, the effects of non-adjacent couplings are included in these TEM^x modes). MMM simulation with only TEM^x modes is also fast and appropriate for optimization. The same situation can also be found in [35] for conventional interdigital filters.

For the filter structure In Fig. 3.9(c), there are several cross sections involved along x-direction, and some of them have $N \geq 1$ internal conductors. For these cross sections, N orthogonal TEM^x modes exist and must be included in the MMM simulation. Shown in Fig. 3.9(d) are the nine cross sections of the filter topology in Fig. 3.9(c) along positive x-direction in sequence. The number of TEM^x modes for each section is: one TEM^x mode in section (I) and (IX), eleven

TEM^x modes in section (II) and (VIII), twenty TEM^x modes in section (IV), (V) and (VI), and twenty-one TEM^x modes in section (III) and (VII). The GTR technique is well suited to calculate the eigenmodes and eigenfields of these cross sections (A computer program has been created for generalized waveguide cross-sections based on the GTR formulations in Appendix A, p. 255). Shown in Fig. B.1(e) (p. 269) are the typical electric field distribution of two TEM^x modes of cross-section (V) (Totally 20 orthogonal TEM^x modes exist inside section (V).), from which the interactions between non-adjacent strips can be noticed. Actually, these interactions are corresponding to the non-adjacent couplings between the resonators.

After the eigenfields of all the TEM^x modes have been solved for each cross section, the discontinuities between these cross sections can be characterized by GSMs (a computer program can be created based on the formulations in Appendix C, p. 271) and the overall response can be obtained by means of GSM cascading using (1.2). In order to have more accurate response, higher order TE and TM modes should be included in the simulation.

For the odd-order filter shown in Fig. 3.10, the structure is symmetric about the middle plane. In order to analyze this structure, MMM simulation is performed twice on the one-port half structure separated by the middle plane: once is placing a perfect electric wall (PEW, corresponding to short circuit) at the symmetry plane, and the other once is placing a perfect magnetic wall (PMW, corresponding to open circuit) at the symmetry plane. Two results of reflection coefficients S_{11e} and S_{11m} are obtained from the MMM simulation corresponding

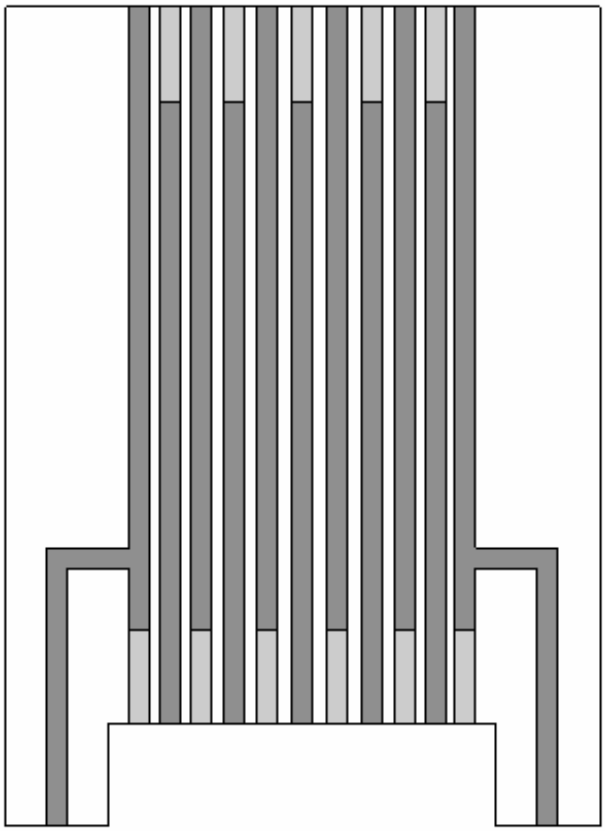

Figure 3.10: An odd-order (11th) interdigital filter using double-layer coupled stripline resonators.

to PEW and PMW, respectively. The whole filter responses are then calculated by [141]

$$S_{11} = S_{22} = \frac{S_{11m} + S_{11e}}{2} \text{ and } S_{12} = S_{21} = \frac{S_{11m} - S_{11e}}{2} \tag{3.9}$$

The tapped-line position, widths of resonators and separations between resonators can be optimized to improve the filter performance, which means that the modes of the cross sections need to be recalculated for each cycle of optimization. The optimization speed is still acceptable since only TEM modes are being used. This MMM approach is also applicable for combline filters. The error function to

be minimized for the optimization is constructed depending on the locations of the poles (f_{pi}) and equiripple points (f_{ei}).

$$err = \sum_{i=1}^{N_p} w_{pi} \left|S_{11}(f_{pi})\right|^2 + \sum_{i=1}^{N_e} w_{ei} \left(\left|S_{11}(f_{ei})\right| - \varepsilon\right)^2 \tag{3.10}$$

where N_p and N_e are the number of poles and equiripple points, respectively. w_p and w_e are the optimization weights. ε represents the equiripple return loss.

C. Fine-Tuning in HFSS (if needed)

The simulated filter response by MMM with only TEM modes might be different from the converged one. Many higher order TE and TM modes must be included in MMM simulation to obtain the converged response, which makes the final tuning too difficult since the modes of cross sections have to be recalculated each time. Hence, Ansoft HFSS is then applied to verify the design and fine-tune the filter if needed. The parameter extraction method [119] can be employed to guide the fine-tuning in HFSS to speed up the procedure. Basically, only the tapped-line position and the width of the first resonator are needed to be tuned in this step.

HFSS is not used in the previous optimization step because of the slow simulation speed. For the design examples given next, it takes MMM about five hours and 1000 iterations to generate the desired performance after the eigenmodes and eigenfields have been calculated (TEM modes are used). While it takes HFSS more than six hours to obtain the converged response for one single filter structure. For an optimization procedure of 1000 iterations, it will take HFSS about 6000 hours to acquire the optimum performance, which is not acceptable in practice.

A desktop PC using 3.0-GHz Pentium 4 processor and 4-GB memory is employed to perform the simulations.

3.2.4 Design Examples

Three design examples are performed to show the feasibility. Two interdigital filters with the same specifications but different resonator dimensions are manufactured to investigate the effects of the LTCC manufacturing procedure. One combline filter is designed only for demonstration.

A. Design Example I

A design of a ten-pole Chebyshev filter with a center frequency of 1.125 GHz and 500-MHz bandwidth is performed. The relative bandwidth is about 45%. The desired stopband rejection level below 0.75 GHz and above 1.5 GHz must be larger than 50 dB. The external couplings and the normalized inter-couplings are

$$\begin{aligned} R_{in} = R_{out} = 0.98562 \quad & m_{1,2} = m_{9,10} = 0.81907 \\ m_{2,3} = m_{8,9} = 0.58576 \quad & m_{3,4} = m_{7,8} = 0.54538 \\ m_{4,5} = m_{6,7} = 0.53288 \quad & m_{5,6} = 0.52976 \end{aligned} \tag{3.11}$$

The interdigital filter configuration to be employed is shown in Fig. 3.9(c). This filter will be embedded inside a PCB system using LTCC technology, and the stack-up options with other components set many constraints on the vertical dimensions. Shown in Fig. 3.11 is the end view of the filter along x-direction. The height of the whole filter box is $h = 59.28mil$, the vertical position of the lower strip is $h1 = 25.94mil$, and the vertical position of the upper strip is $h2 = 29.69mil$. Only one ceramic layer (thickness is about $3.74mil$) exists between the

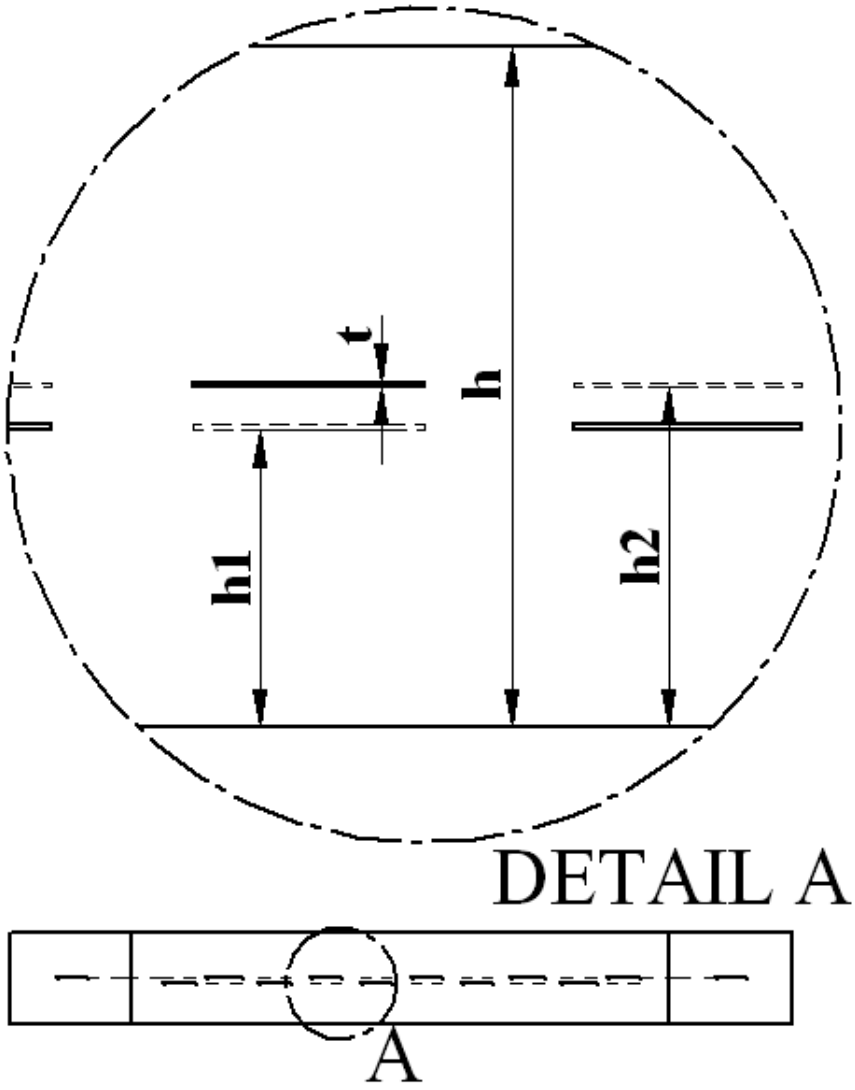

Figure 3.11: The end view along x-direction of the filter configuration in Fig. 3.9(c).

two strips. The metallization thickness of the strip is $t = 0.4mil$ and the relative permittivity of the ceramic is $\varepsilon_r = 5.9$, which are determined by the selected LTCC technology.

Fig. 3.12(a) is the configuration to determine the resonator dimensions to have the fundamental resonating mode at the center frequency 1.125 GHz. Two ports are weakly coupled to the resonator and the peak frequency point of the

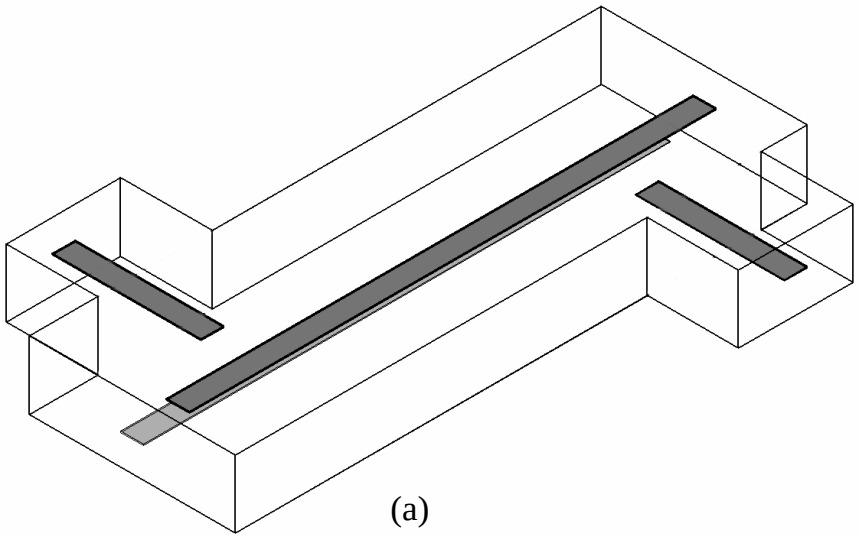

(a)

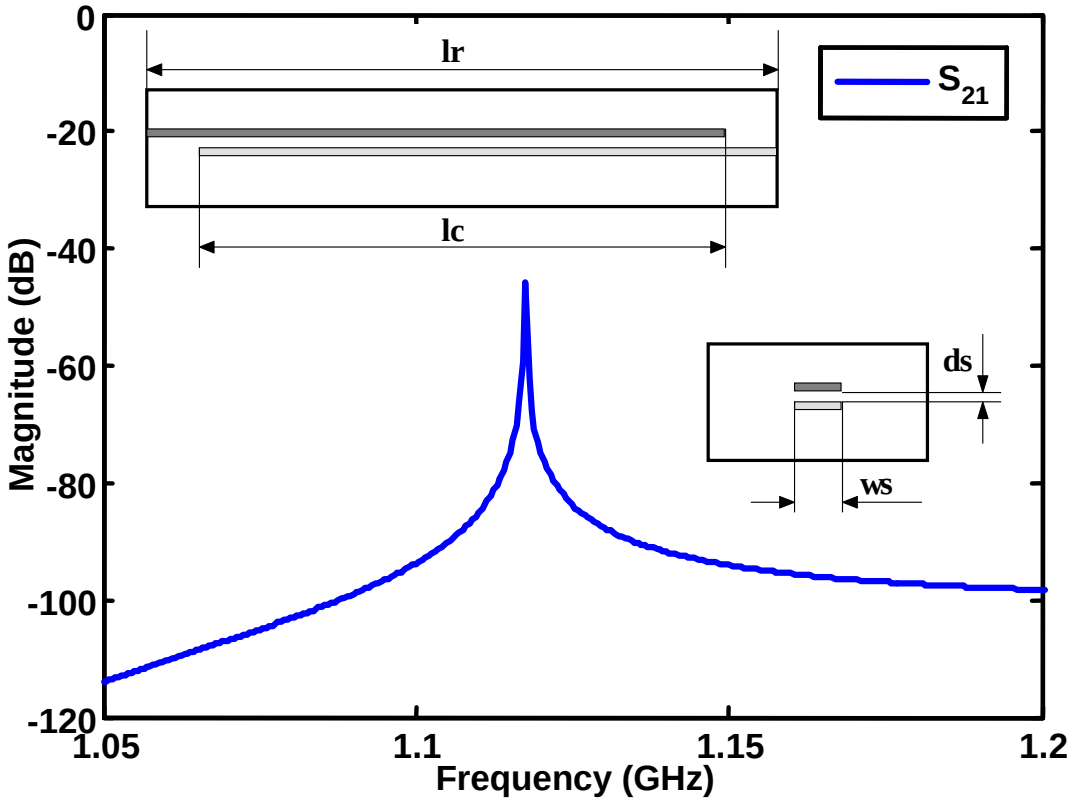

(b)

Figure 3.12: (a) Configuration to decide the dimensions of the resonator. (b) Typical frequency response of S_{21} for configuration (a).

simulated S_{21} response as in Fig. 3.12(b) is the resonant frequency. The length lr of the resonator is selected as $lr = 500mil$. The coupled length lc and width ws of the two strips (two strips in one resonator have the same dimensions) are being swept until the required resonant frequency 1.125 GHz is achieved. The found values are $lc = 420mil$ and $ws = 20mil$.

The configuration for computing the external coupling is shown in Fig. 3.13(a). The coupling extraction method is discussed in the previous section. Basically, the reflection coefficient S_{11} is obtained by MMM with respect to the different tapped-in positions (*htapin* in Fig. 3.13(b)), and equation (3.7) is used to calculate the coupling values. The external coupling curve is presented in Fig. 3.13(b), which shows the external coupling is linearly proportional to the tapped-in position. The value of *htapin* to have $R = 0.98562$ is about $432mil$.

Fig. 3.14(a) shows the configuration to calculate the inter-coupling value, in which the two ports are very weakly coupled to the coupled resonator structure. The typical simulated magnitude and phase responses of such configuration are displayed in Fig. 3.14(b), where two peak frequency points correspond to the natural frequencies. The inter-coupling value k can be calculated by (3.4) with respect to the different separations between the resonators. The computed inter-coupling curve is shown in Fig. 3.15 and the separations are calculated by interpolation to have the desired inter-coupling values. The found separations for the five desired adjacent couplings in (3.11) are: $S1 = 7.1mil$, $S2 = 11.9mil$, $S3 = 13.0mil$, $S4 = 13.4mil$, and $S5 = 13.5mil$, respectively (variable definitions are given in Fig. 3.17). The relationship between k and the normalized

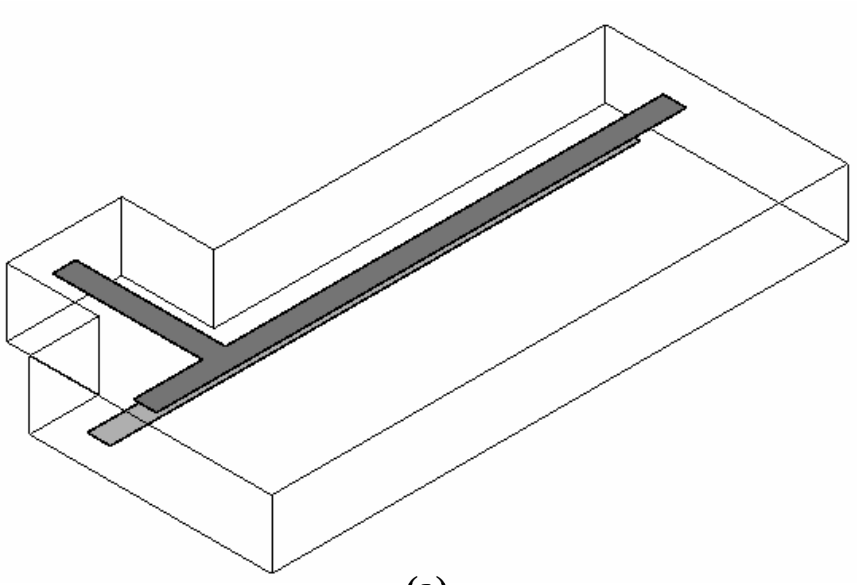

(a)

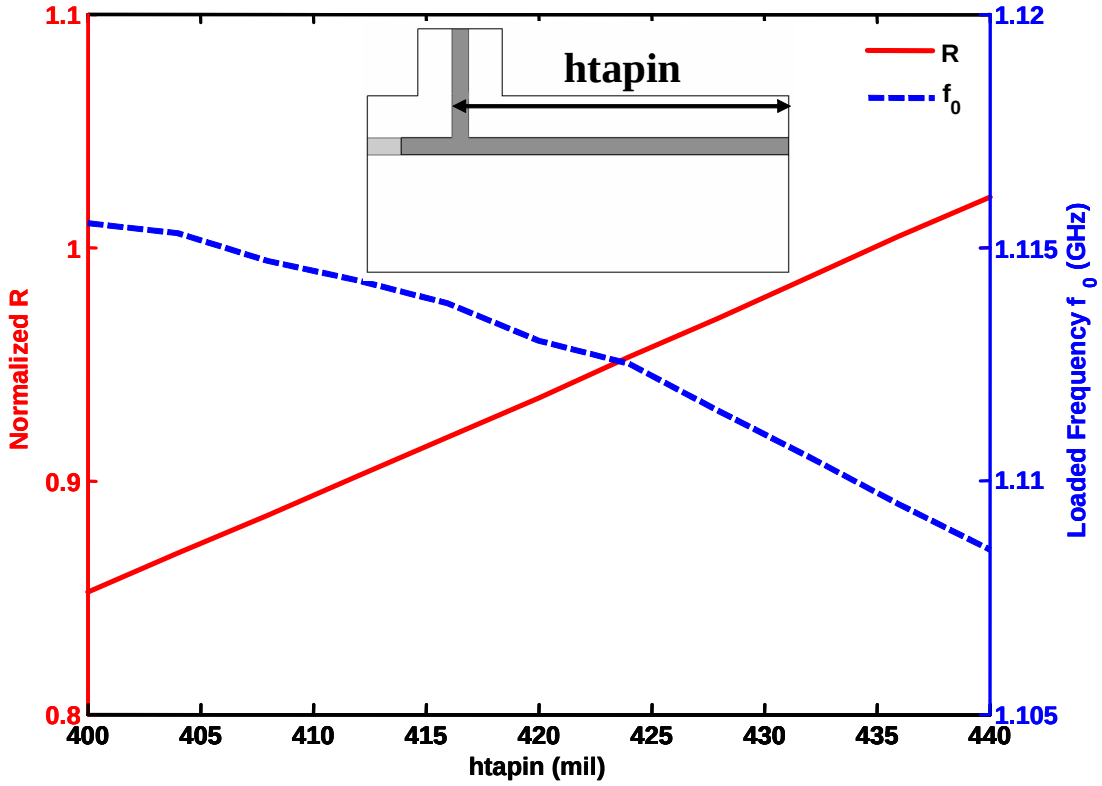

(b)

Figure 3.13: (a) The configuration to calculate the external coupling R. (b) External coupling curve: normalized R and loaded frequency f_0 vs tapped-in position *htapin*

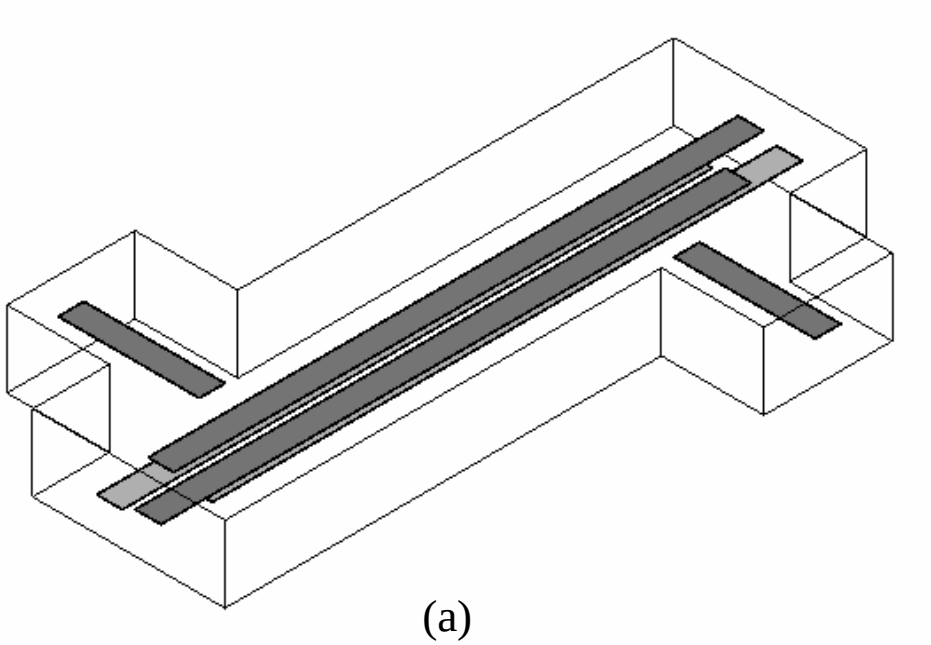

(a)

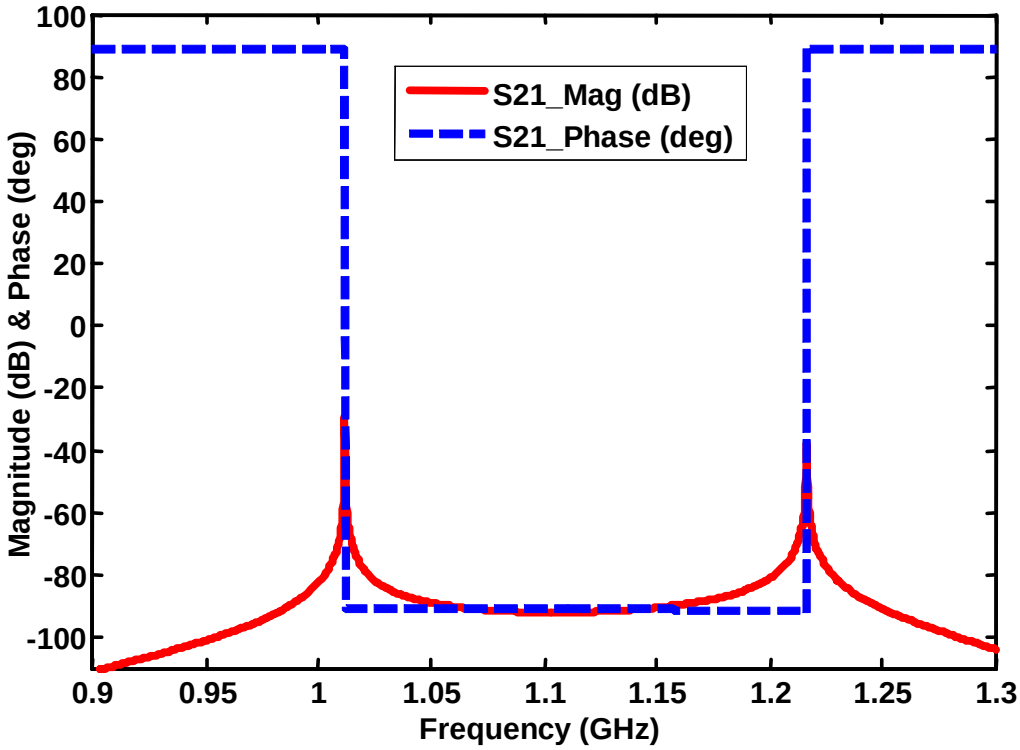

(b)

Figure 3.14: (a) The configuration to calculate the inter-coupling between two resonators. (b) The typical simulated magnitude and phase responses of configuration (a).

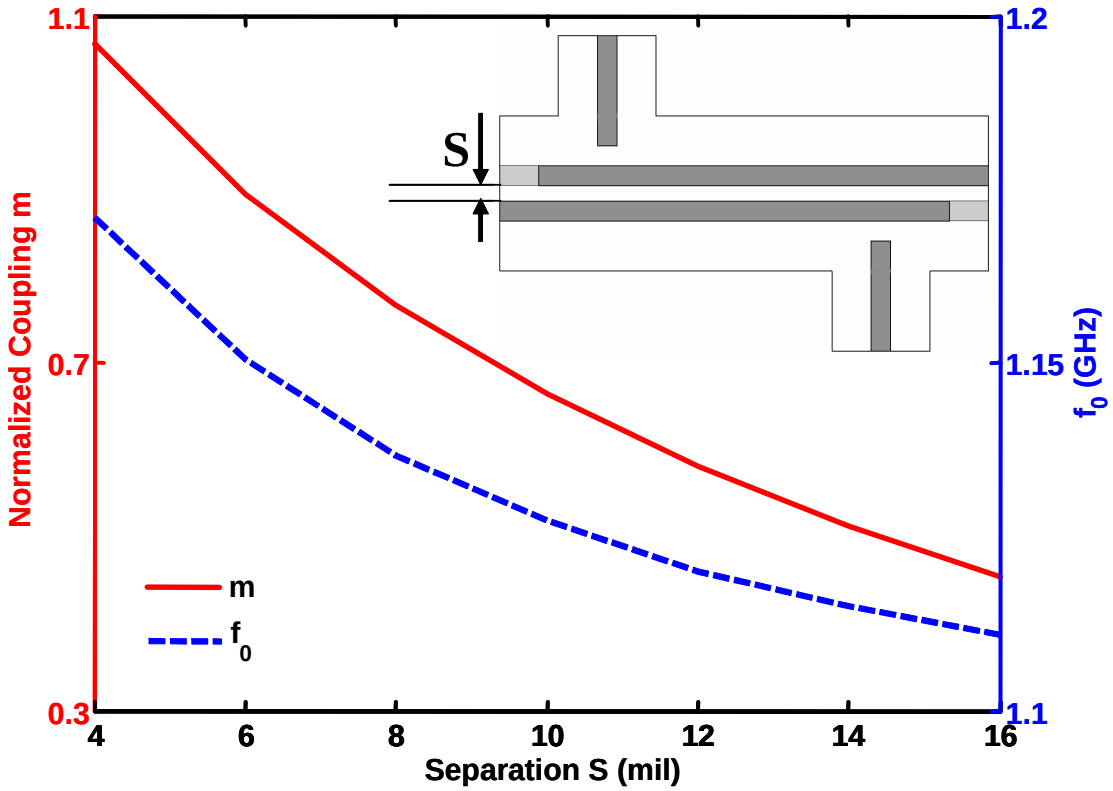

Figure 3.15: Inter-coupling curve between two resonators: normalized coupling m and loaded resonant frequency f_0 vs separation S.

inter-coupling m is given as

$$m = k\frac{f_0}{bw} \tag{3.12}$$

where f_0 is the center frequency of filter and bw is the bandwidth.

After the filter is assembled according to the calculated initial dimensions, the initial responses are simulated and presented in Fig. 3.16(a), which shows a good starting point for later optimization and tuning. MMM optimization and HFSS fine-tuning are then applied to improve the filter performance. The frequency responses of the final filter design are shown in Fig. 3.16(b). MMM simulation results with only TEM modes are also presented in Fig. 3.16(b), which

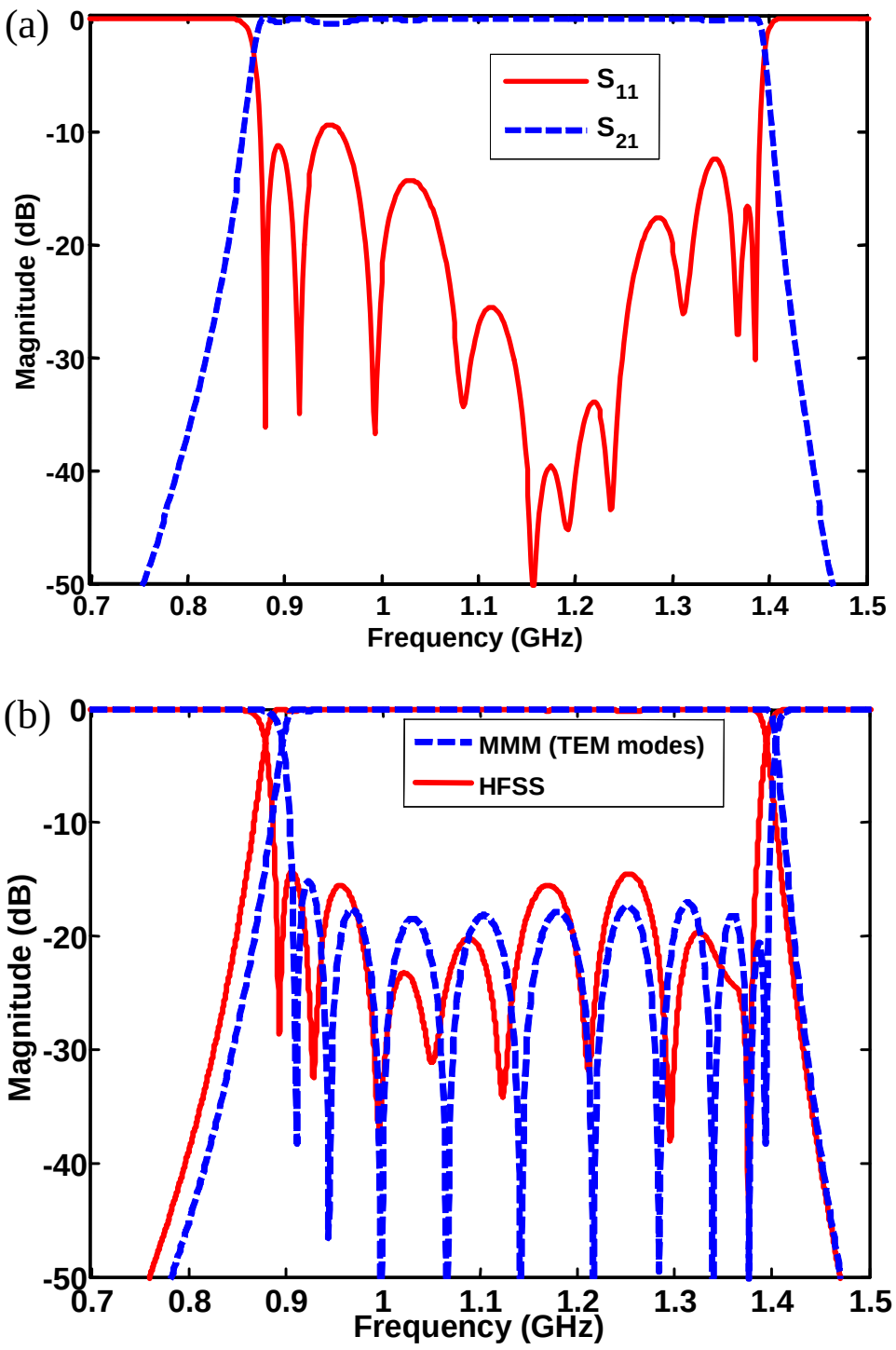

Figure 3.16: (a) Frequency response of filter example I with initial dimensions. (b) Simulated frequency response of filter example I with final dimensions by HFSS and MMM with only TEM modes.

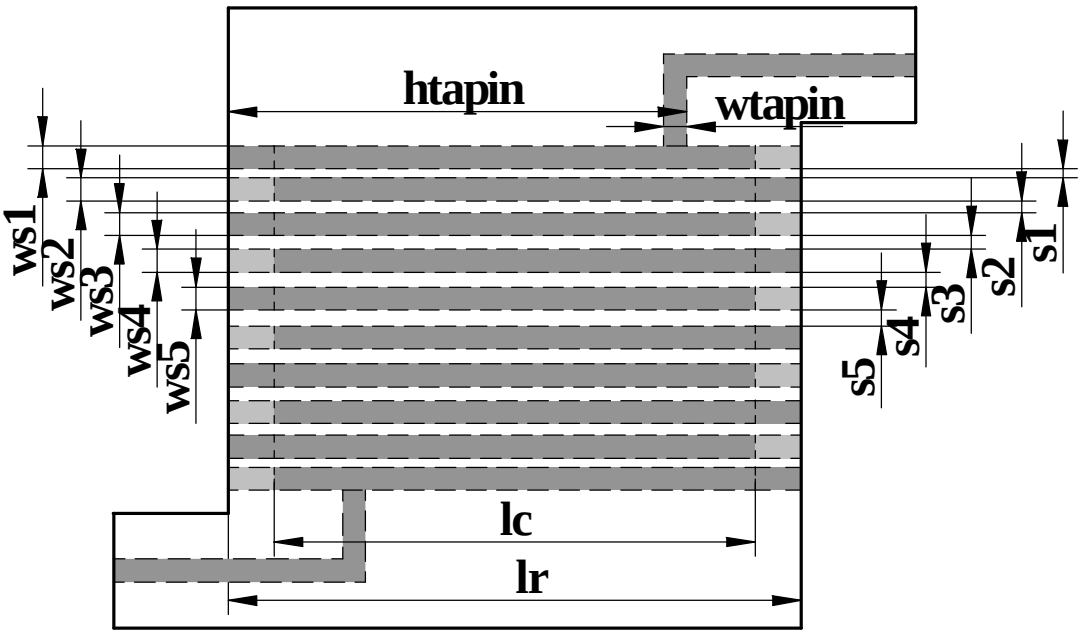

Figure 3.17: The final dimensions of filter example I: widths of the resonators (in mil): $ws1 = 21.2$, $ws2 = 23.1$, $ws3 = 21.4$, $ws4 = 20.2$, $ws5 = 19.8$. Separations between resonators (in mil): $s1 = 7.2$, $s2 = 11$, $s3 = 12.4$, $s4 = 13.1$, $s5 = 13.4$. Other dimensions (in mil): $lr = 500$, $lc = 420$, $htapin = 434$, $wtapin = 19$. Ports are $50ohm$ striplines. The filter is filled with a homogeneous dielectric material with $\varepsilon_r = 5.9$. The vertical dimensions shown in Fig. 3.11 are given in the context.

shows the feasibility of optimization by MMM (The frequency shift can be taken into account during the optimization). The final dimensions of the filter structure are given in the caption of Fig. 3.17.

The minimum return loss over the passband is about 15 dB because the non-adjacent couplings for such broadband filter are not avoidable and make it very difficult to achieve a return loss better than 15 dB. The upper stopband of this filter has clean spurious response up to the third harmonic. The final dimension of the whole filter box is about $500mil \times 515mils \times 59.28mil$, which is less than $\lambda/8 \times \lambda/8 \times h = 540mil \times 540mil \times 59.28mil$ at the center frequency 1.125 GHz.

This filter is manufactured in LTCC technology for testing. Fig. 3.18(a) shows the filter prototype and the arrangement of the measurement. Input and output ports of the filter are bent toward the same direction for the convenience to connect with other components. Transitions from $50Ohm$ microstrip lines to the tapped-in striplines are also added on the filter. J-probe launches and a Cascade Microwave Probe Station are used in the measurement. The measured response is shown in Fig. 3.19(a). The insertion loss at the center frequency is about 3 dB and at the higher band edge is about 6 dB. The wideband response shows that the spurious response starts around 3.6 GHz that is about three harmonics. A simulation by HFSS with lossy materials is also performed to investigate the response difference between the designed and manufactured filters. The employed parameters for loss are: finite conductivity $\sigma = 13100000\ S/m$ for conductor and loss tangent of 0.001 for ceramics. Both the simulated and measured responses are shown in Fig. 3.19(b). A good agreement is noticed except a frequency

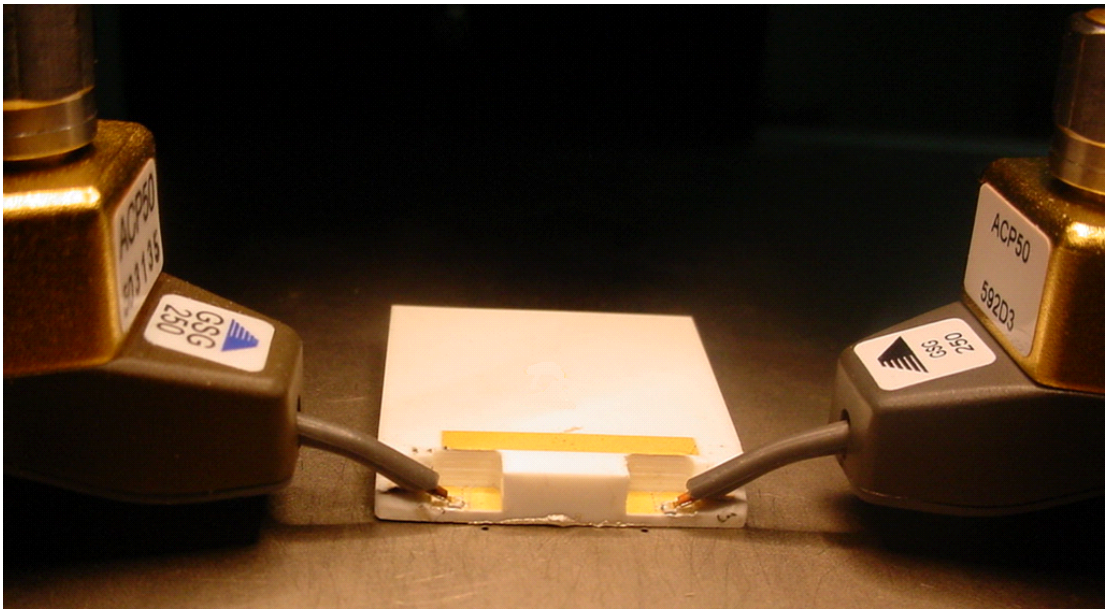

(a)

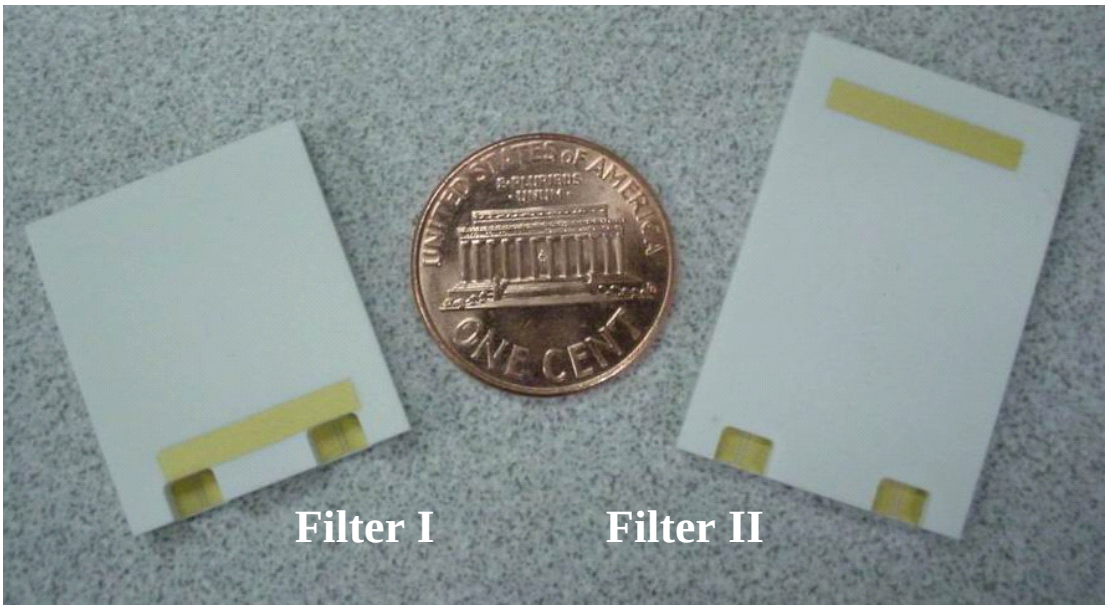

(b)

Figure 3.18: (a) Picture of the measurement arrangement. (b) Picture of the manufactured filters (example I and II). Filter II is slightly larger than Filter I.

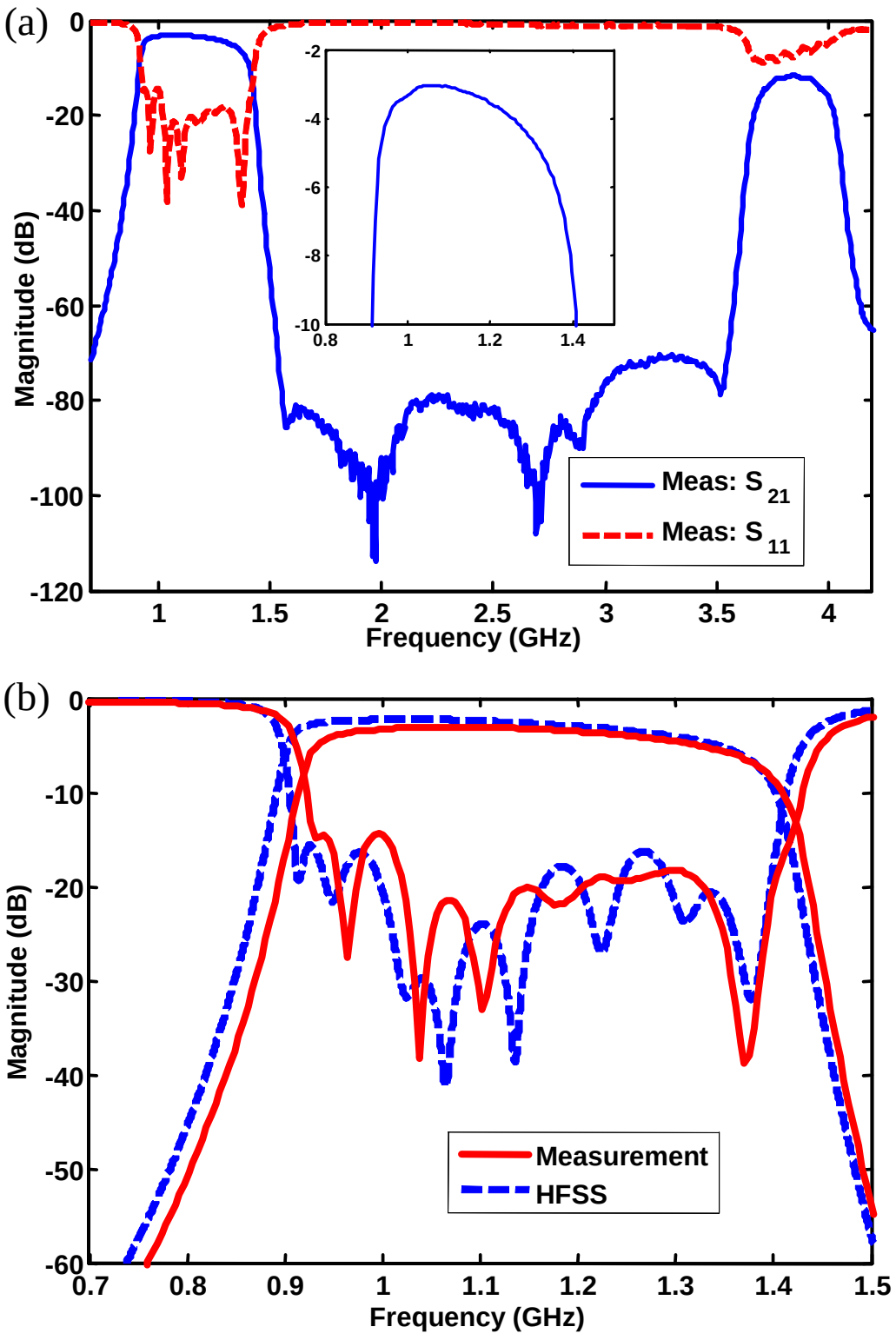

Figure 3.19: (a) Measured frequency response of filter I. (b) Comparison between the measurement and the simulated response by HFSS.

shift between them. The frequency shift is caused by the effects of the LTCC manufacturing procedure, such as vias, inhomogeneous ceramic layers, etc. (In HFSS simulation, solid walls and homogeneous materials are assumed.), which will be discussed later.

B. Design Example II

In design example I, one ceramic layer of thickness $ds = 3.74mil$ exists between the two strips of a resonator. To investigate the sensitivity of the filter with respect to ds and the effects of the LTCC manufacturing procedure on filter performance, a second design with larger ds is carried out for an odd-order interdigital filter. The filter requirements are identical with design example I, but a design of an eleven-pole filter is performed for this example. The stack-up option is different from example I. For this example, $h1 = 29.68mil$, $h2 = 37.08mil$, and $h = 63.02mil$. Definitions of $h1$, $h2$ and h are given as in Fig. 3.11. The separation between the two strips is $ds = h2 - h1 = 7.4mil$, which means that the physical length of the resonator will be longer than example I due to the relatively weaker coupling between two strips. The selected dimensions of the resonator are: $lr = 700mil$, $lc = 516mil$, and $ws = 20mil$.

The same design procedure as example I is followed for this design. The final dimensions of the filter structure are given in Table 3.2. The volume of the whole filter box is about $700mil \times 540mils \times 63.02mil$ that is larger than design example I. Fig. 3.18(b) shows both manufactured filters of example I and II. The measured response is shown in Fig. 3.20(a). The spurious response starts around 2.5 GHz that is about two harmonics. The reason that filter II has worse spurious

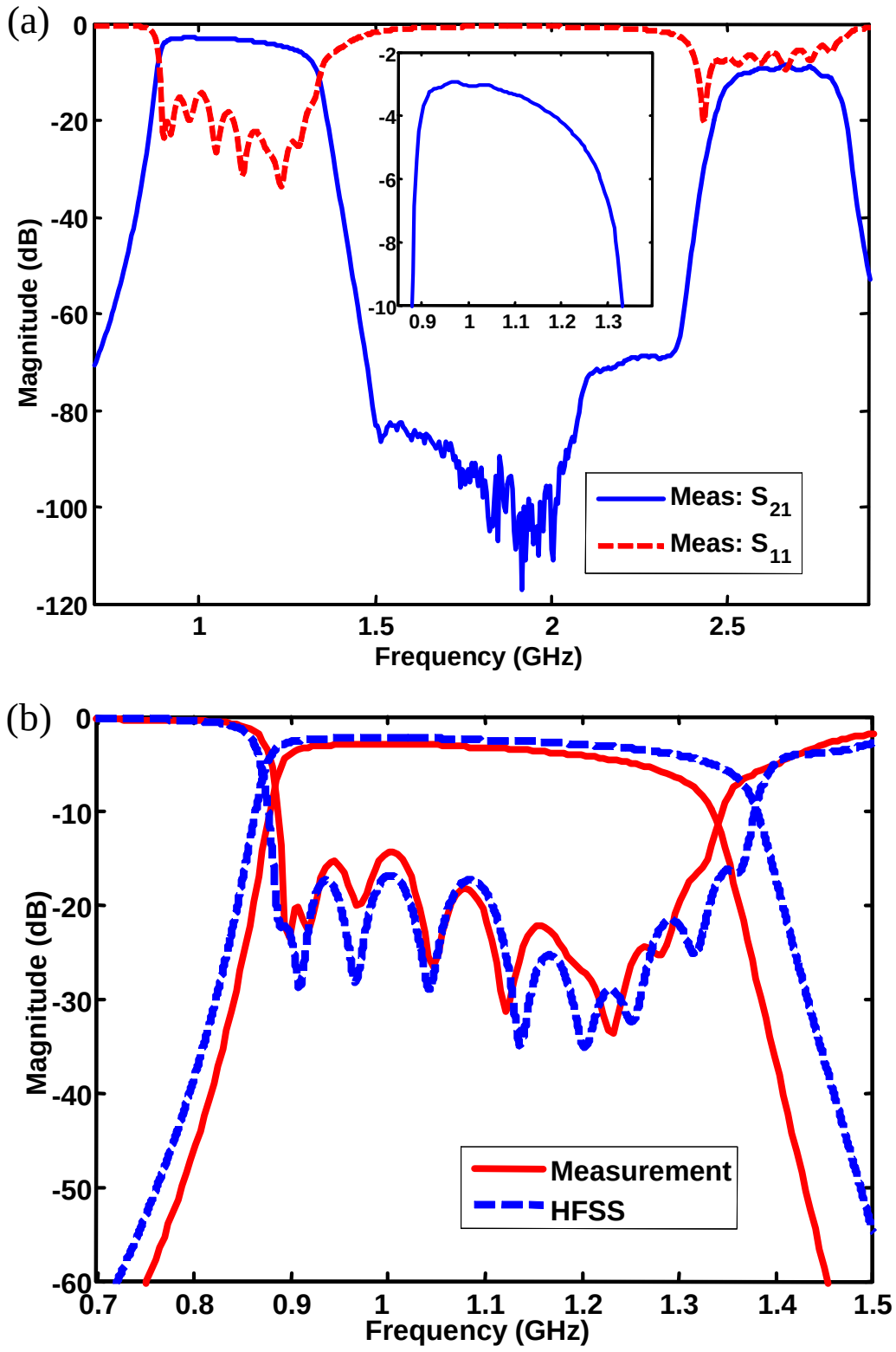

Figure 3.20: (a) Measured response of filter II. (b) Comparison between the measurement and the simulated response by HFSS.

Table 3.2: Final dimensions of filter example II. Variables have the similar definitions as in Fig. 3.17. All the dimensions are given in mil.

Variable	**Value**	**Variable**	**Value**	**Variable**	**Value**
$ws1$	20.4	$ws2$	20	$ws3$	20
$ws4$	20	$ws5$	20	$ws6$	20
$s1$	6.7	$s2$	10.8	$s3$	13.7
$s4$	14.7	$s5$	15.1	$wtapin$	19
lr	700	lc	516	$htapin$	568
$h1$	29.68	$h2$	37.08	h	63.02

performance than filter I is related to the resonator structure and dimensions. The first higher order resonating mode of the resonator is controlled by the introduced capacitive coupling between two strips. The stronger is the coupling, the further is the first higher order mode. Resonators in filter II have larger ds than filter I, and thus smaller capacitive coupling between strips, therefore, the first higher order resonating mode is closer to the center frequency which causes the spurious performance worse than filter I. The response comparison between the measurement and HFSS simulation is shown in Fig. 3.20(b). The measured bandwidth is slightly narrower than the simulated one, which is also due to the manufacturing effects.

In both design examples, the measured insertion loss is slightly larger than the simulated one. Two main reasons are responsible for that: i) vias in actual

structures might introduce more loss than the solid wall model in HFSS and ii) the loss tangent of the actual ceramic material is larger than 0.001.

C. Design Example III

A combline filter is also designed to show the feasibility of applying double-layer coupled stripline resonators for combline filter configuration as in Fig. 3.7(b). A design of six-pole filter with center frequency 1.1 GHz and 15% bandwidth is performed. The design procedure is exactly same as the previous two examples, except that different cross sections are used for MMM modeling. The filter structure and simulated frequency response are shown in Fig. 3.21.

3.2.5 LTCC Manufacturing Effects

The measured responses of example I and II are slightly different from the simulated ones, which is usually caused by the LTCC manufacturing effects. Shown in Fig. 3.22 is a draft of the physical realization of the designed filters in LTCC technology. Basically, the filled ceramic is placed layer by layer with fixed thickness of each layer. The horizontal walls and the resonator striplines inside the ceramic are implemented by metallization of gold. The vertical walls are realized by via fence of closely-placed vias. If the signal is communicating between different layers, vias are also applied to connect the signal lines. Such a manufacturing procedure will affect the filter performance from several points of views.

First, the via fence to realize the vertical walls of the filter will affect the resonator length, which can be observed from the zoom-in view in Fig. 3.22. Di-

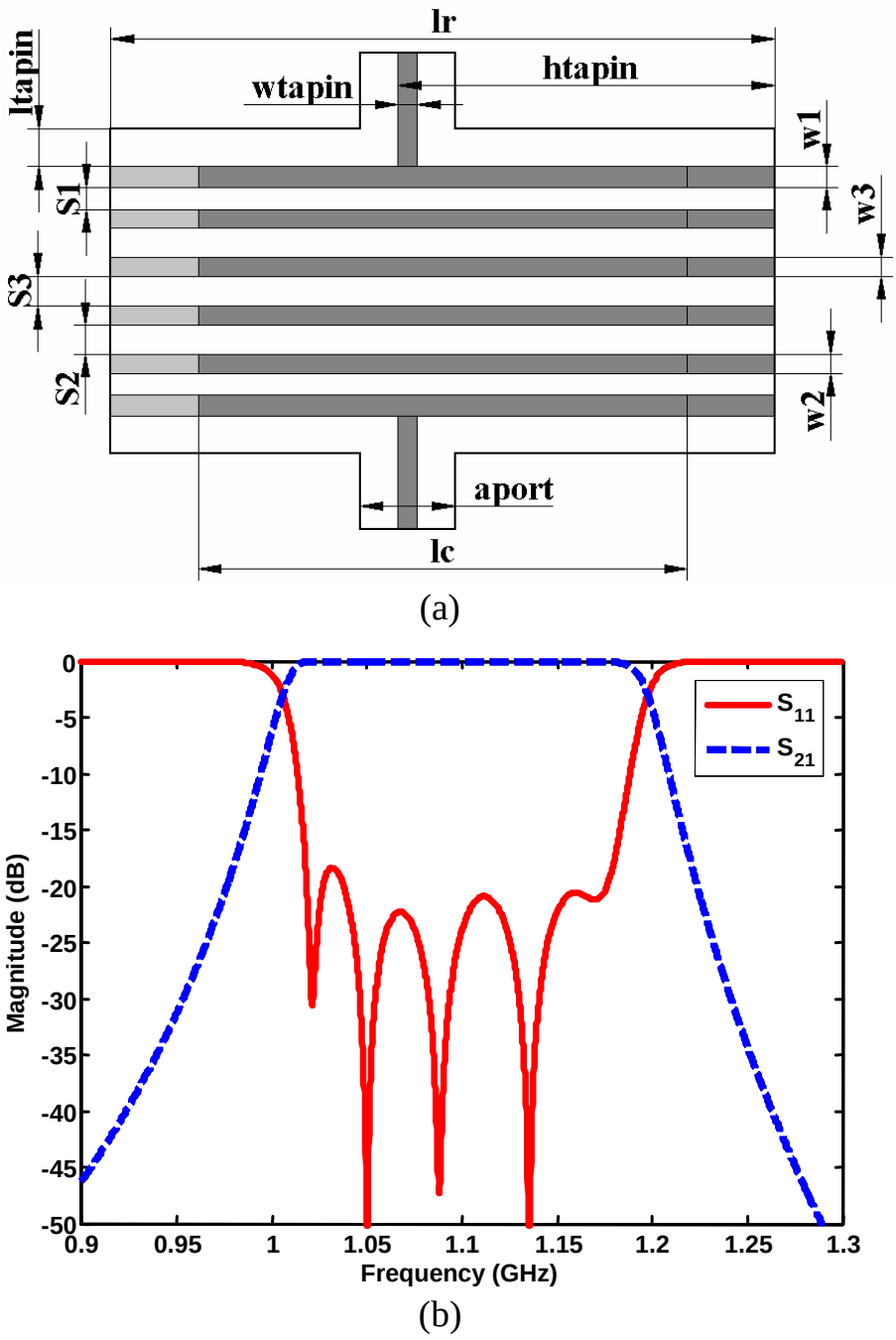

Figure 3.21: (a) Structure of combline filter example III. (b) Frequency response by HFSS. Filter dimensions: $h1 = 29.68mil$, $h2 = 37.08mil$, $h = 63.02mil$, (as in Fig. 3.11). $w1 = 21.8mil$, $w2 = 20mil$, $w3 = 20mil$, $s1 = 23.06mil$, $s2 = 30.6mil$, $s3 = 31.7mil$, $lr = 700mil$, $lc = 516mil$, $htapin = 322.7mil$, $wtapin = 20mil$, $aport = 100mil$.

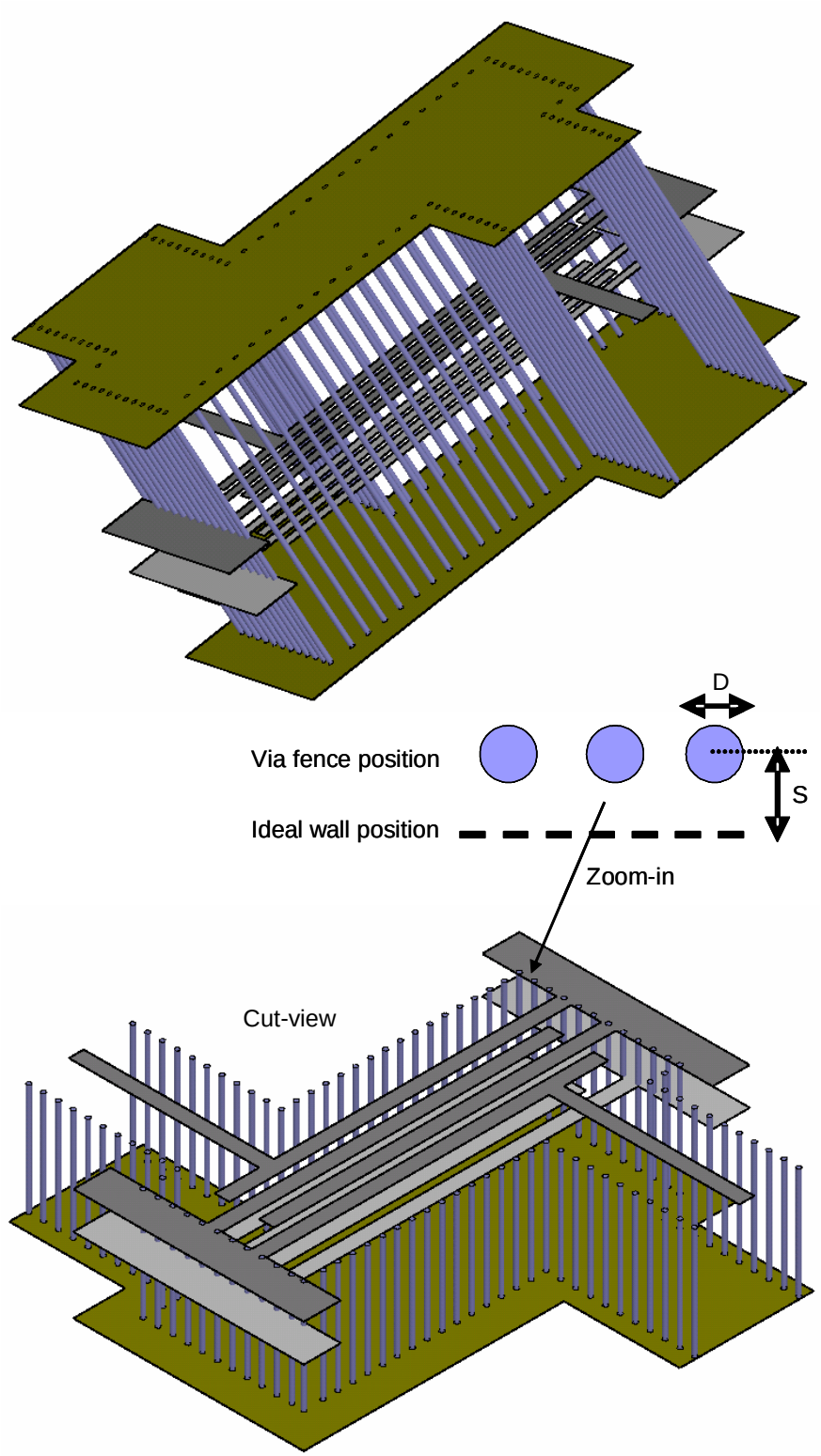

Figure 3.22: Draft of the physical realization of filters in LTCC technology.

ameter D of vias is about $6mil$. The distance between two vias should be selected appropriately to approximate the solid walls and also create an effective "pure resistance" environment (i.e. parasitic inductance and capacitance are counteracted.), which is usually decided experimentally. The via fence position relative to the ideal vertical wall position (S in Fig. 3.22) should be determined to have the manufactured resonator resonating at the same frequency as the ideal resonator, otherwise, the actual filter response will be shifted from the designed one. The optimum via fence position is about $S = D/4$.

Second, the thickness of gold metallization usually varies from $0.4mil$ to $0.6mil$. This effect will cause the variation of the vertical distance ds (as in Fig. 3.6) between two strips in a resonator, and thus the frequency shift of the resonators. The filters designed with smaller ds will be influenced more by this effect than those with larger ds since the variation occupies more percentage in smaller ds. This might be one of the reasons that the measured response of filter I is shifted from the desired center frequency.

Third, assembling the filled ceramic layer by layer causes the variation of the permittivity of different layers, i.e. the filled ceramic is not perfectly homogeneous. The relative permittivity can be from 4.7 to 6.3. This effect will cause the frequency shift and mainly influence all the couplings existing in the filters. The filters with larger ds will be affected more since larger ds means greater variation of the permittivity. This could be one of the reasons that filter II has narrower bandwidth than the designed one.

In the actual manufacture, several test pieces are usually manufactured and

measured first. The proper processing conditions to reduce the aforementioned effects are then determined according to the comparison between the measured response and the designed one. Once the processing conditions are found, the mass production of components can be performed with more than 95% yield.

3.3 Multiple-layer Coupled Resonator Filters

3.3.1 Introduction

In previous section, double-layer coupled stripline resonators have been successfully applied to design miniature and broadband filters. Nevertheless, for some applications where the size reduction is of primary importance, even smaller filters are desirable. A straightforward thinking is to extend the idea of the double-layer coupled resonators to multiple-layer coupled resonator structures. Stronger capacitive couplings can be introduced into a multiple-layer resonator structure to obtain a smaller size than the double-layer resonator structure. The implementation of multiple-layer resonator structures is realizable by using LTCC technology that has been discussed in previous section.

Recently, there has been increasing interest in multiple-layer bandpass filters to meet the challenges of size, performance and cost requirements [142–149]. However, in all the available multiple-layer filters, the multiple-layer structures have only been used to increase or affect the mutual couplings between single-layer resonators, while the size of single-layer resonators is still a main limitation

on the whole filter size. The multiple-layer resonators presented in this section is employed to significantly reduce the resonator size. Meanwhile, strong couplings between resonators can still be achieved for broadband filter designs.

In this section, the idea of generalized multiple-layer coupled resonators is discussed based on the circuit models as well as the full-wave numerical methods. Several possible multiple-layer resonator structures are presented, and two bandpass filter design examples using such structures are performed to validate the concept. Commercial software tool Sonnet [72], which is based on MoM, is employed to do the analysis and design in this section.

3.3.2 Possible Resonator Structures

Shown in Fig. 3.23 are some possible multiple-layer coupled resonator structures. Fig. 3.23(a) shows double- and triple-layer coupled stripline resonators. Each strip is grounded at one end and open at the other end. The ground ends of two adjacent strips are placed at opposite sides to create potential difference along the lines, and thus, a strong capacitive coupling between them. Fig. 3.23(b), (c) and (d) are double- and triple-layer coupled hairpin, folded stripline, and spiral resonators, respectively. Actually almost all the single-layer resonator structures can be extended to multiple-layer coupled resonator structures. The main idea is to create large potential differences, which lead to strong capacitive couplings, between any two adjacent single-layer structures inside the resonator. The coupling effects will then decrease the frequency value of the fundamental resonant mode.

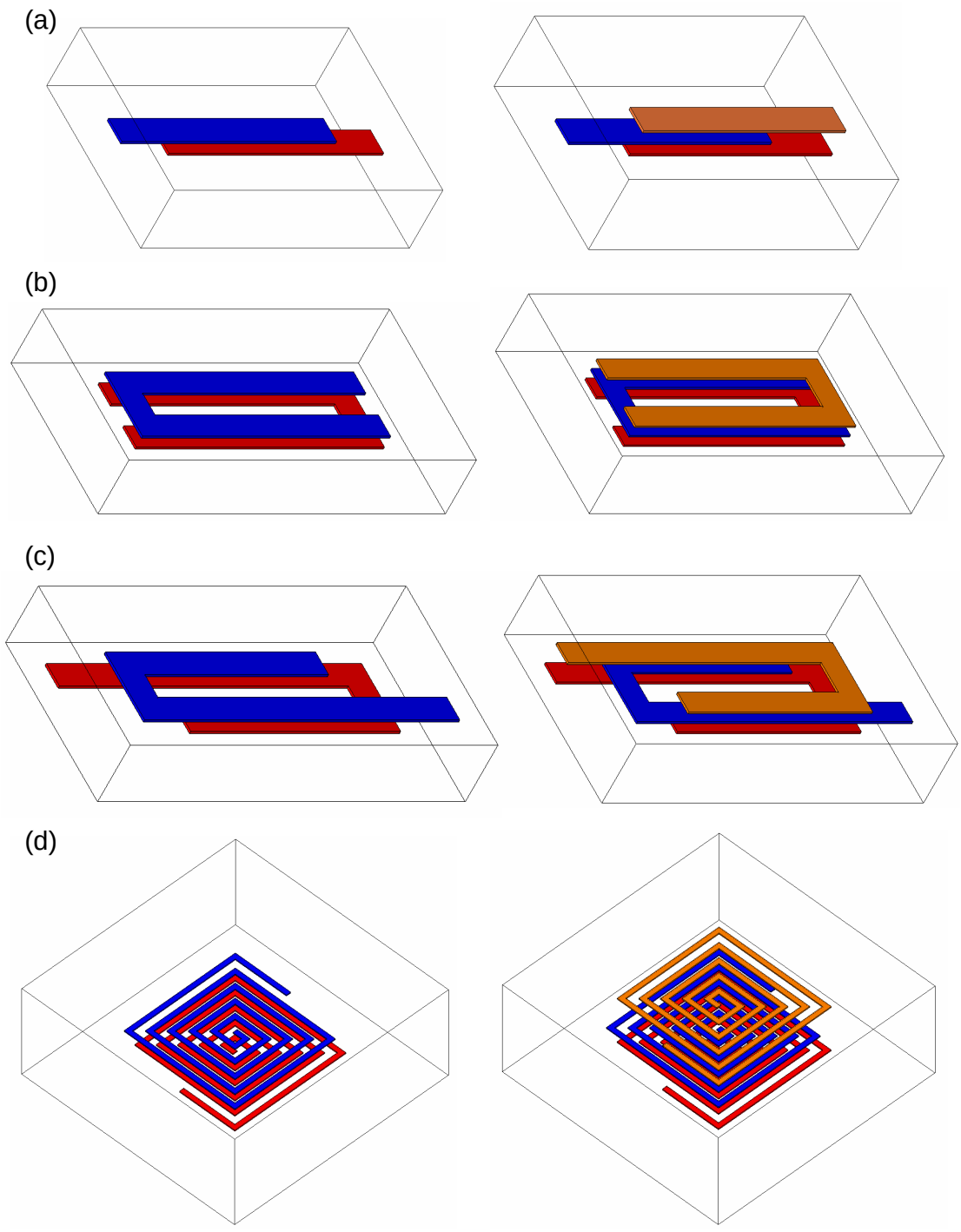

Figure 3.23: Possible multiple-layer coupled resonator structures. (a) Double and triple layer stripline resonators. Each strip is grounded at one end. (b) Double and triple layer hairpin resonators. (c) Double and triple layer folded stripline resonators. (d) Double and triple layer spiral resonators.

From the other point of view, the multiple-layer coupled resonators have shrunk size to realize a given resonant frequency point due to the capacitive couplings.

The straightforward intuition about the multiple-layer coupled resonators is that the greater the number of layers is used, the smaller the resonator size will be obtained. In order to know whether this intuition makes sense, three stripline resonators with different number of layers are analyzed in Sonnet to make comparisons. The structures are shown in Fig. 3.24, which are single-layer stripline resonator, double-layer coupled stripling resonator, and triple-layer coupled stripline resonator. They have identical substrate (material and height), identical enclosure box, and identical strip length. The double- and triple-layer resonators have the same overlap (coupled) length between two adjacent strips. To decide the resonant frequency of each structure numerically, two stripline ports are very weakly coupled to the resonators to excite the fundamental resonant mode (as shown in the geometry drawings of Fig. 3.24). The simulated S_{21} response is also shown in Fig. 3.24 for each resonator. The peak frequency points in the S_{21} responses correspond to the resonant frequency of each structure, which are 2.672 GHz, 1.383 GHz, and 1.123 GHz for single-layer, double-layer, and triple-layer resonator, respectively. According to the obtained result, it can be concluded that the resonant frequency becomes smaller with the more number of coupled layers (assuming other dimensions are identical) used in the multiple-layer resonators. It also verifies that the aforementioned intuition is correct.

The characteristics of multiple-layer coupled resonators can be summarized as: i) All the available single-layer planar resonator structures can be extended

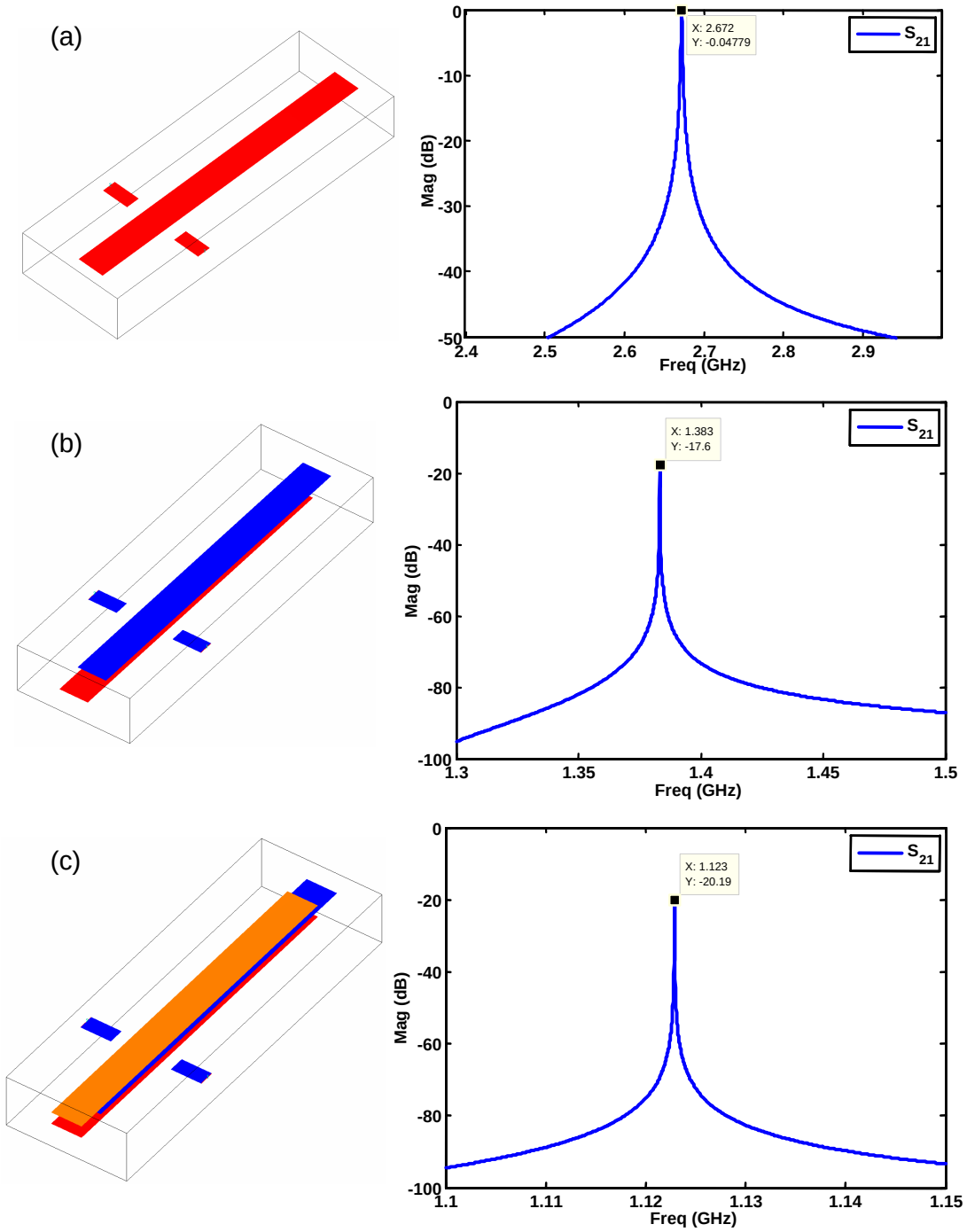

Figure 3.24: Comparison between resonators with different number of layers. (a) Single-layer stripline resonator. (b) Double-layer coupled stripline resonator. (c) Triple-layer coupled stripline resonator.

to multiple-layer resonator structures. ii) The size of multiple-layer resonator structures can be half the size or less than the original single-layer structure. The more the number of layers, the smaller the size of the resonator. iii) The coupling values between multiple-layer resonators will be almost the same order as between two equivalent single-layer resonators. iv) The filter topology realized with single-layer resonators can also be implemented with multiple-layer resonator structures. These characteristics make multiple-layer coupled resonators appropriate for miniature and broadband filter designs.

3.3.3 Equivalent Circuit Model

In order to understand the multiple-layer coupled resonators, the equivalent circuit model of the resonator is employed as shown in Fig. 3.25. Fig. 3.25(a) shows an equivalent LC loop circuit of a single-layer resonator. Basically, the fundamental resonant frequency f_0 is given as [2]:

$$f_0 = \frac{1}{2\pi\sqrt{L_0 C_0}} \tag{3.13}$$

Fig. 3.25(b) shows the equivalent circuit of a double-layer coupled resonator. Actually, the double-layer coupled resonator consists of two single-layer resonators that are coupled to each other by the electromagnetic fields in between (mainly electric field for this specific case.). Due to the coupling between the two single-layer resonators, the resonant frequencies of the double-layer resonator will be different from the single-layer ones. The circuit model can be used to find the resonant frequencies of the double-layer resonator approximately. For the natural

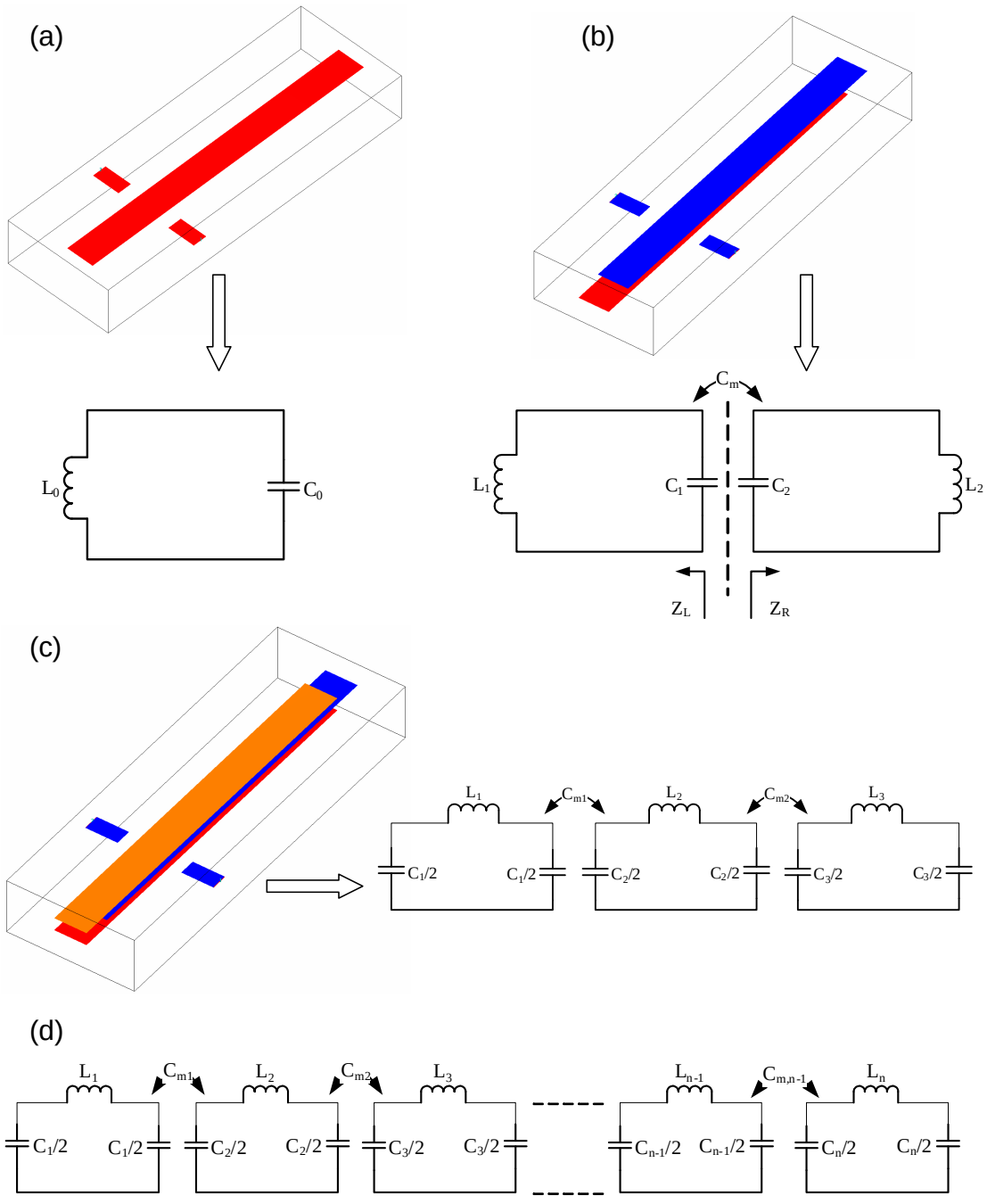

Figure 3.25: The equivalent circuit model of multiple-layer coupled resonators. (a) Single-layer resonator. (b) Double-layer coupled resonator. (c) Triple-layer coupled resonator. (d) Equivalent circuit of n-layer coupled resonator.

resonance of the circuit model in Fig. 3.25(b), the condition is

$$Z_L = -Z_R \tag{3.14}$$

where Z_L and Z_R are the input impedances looking at the left and the right of the reference plane (dotted line in Fig. 3.25(b)). This condition leads to an eigen-equation

$$\omega^4 \left(L_1 L_2 C_1 C_2 - L_1 L_2 C_m^2\right) - \omega^2 \left(L_1 C_1 + L_2 C_2\right) + 1 = 0 \tag{3.15}$$

The resonant frequencies can, therefore, be solved as

$$f_{1,2} = \sqrt{\frac{f_{01}^2 + f_{02}^2 \pm \sqrt{\left(f_{02}^2 - f_{01}^2\right)^2 + 4 f_{01}^2 f_{02}^2 k^2}}{2\left(1 - k^2\right)}} \tag{3.16}$$

where f_{01} and f_{02} are the unloaded resonant frequency of the two single-layer resonators, respectively. They are given by $f_{0i} = \frac{1}{2\pi\sqrt{L_i C_i}}$, $i = 1, 2$. k is the normalized coupling given by

$$k^2 = \frac{C_m^2}{C_1 C_2} \tag{3.17}$$

Usually the resonant frequencies of the two single-layer resonators are identical, i.e. $f_{01} = f_{02} = f_0$. Therefore, the two natural resonant frequencies of the double-layer resonator are

$$f_1 = \frac{f_0}{\sqrt{1+k}} \text{ and } f_2 = \frac{f_0}{\sqrt{1-k}} \tag{3.18}$$

Thus, if the coupling between two single-layer resonators is very strong, i.e. k is large, f_1 will be much smaller than f_0 and f_2 much larger than f_0. The fundamental resonant mode f_1 can then be used for filter designs to achieve a miniature size

since the whole area of the double-layer resonator is almost same as the single-layer resonator that actually has much higher resonant frequency than f_1.

Fig. 3.25(c) shows the equivalent circuit of a triple-layer coupled resonator. Essentially, it consists of three single-layer resonators coupled to each other, which is similar to the double-layer case. Three natural resonant frequencies will be generated due to the couplings between the three single-layer resonators. The mathematical derivation is similar as above, but more complicated. If the three single-layer resonators have the same unloaded resonant frequency f_0, one natural frequency of the triple-layer resonator will be much smaller than f_0, one will be around f_0, and one will be much larger than f_0.

A multiple-layer coupled resonator has the same behavior as the double- and triple-layer resonators. The equivalent circuit for an n-layer coupled resonator is shown in Fig. 3.25(d). Basically, n single-layer resonators are coupled to each other to generate n natural resonant frequencies, and the fundamental resonant mode will be used for miniature filter designs. If n is odd, one natural frequency will be always around the resonant frequency f_0 of the single-layer resonators. Others will be half smaller than f_0 and half larger than f_0. If n is even, the natural frequencies will be distributed about f_0, i.e. half smaller and half larger than f_0.

To demonstrate the validity of the above discussion about multiple-layer resonators, the natural resonant frequencies of three geometries in Fig. 3.24 are found by using Sonnet. The simulated responses are shown in Fig. 3.26 for each geometry. The peaks in the S_{21} responses correspond to the natural resonant

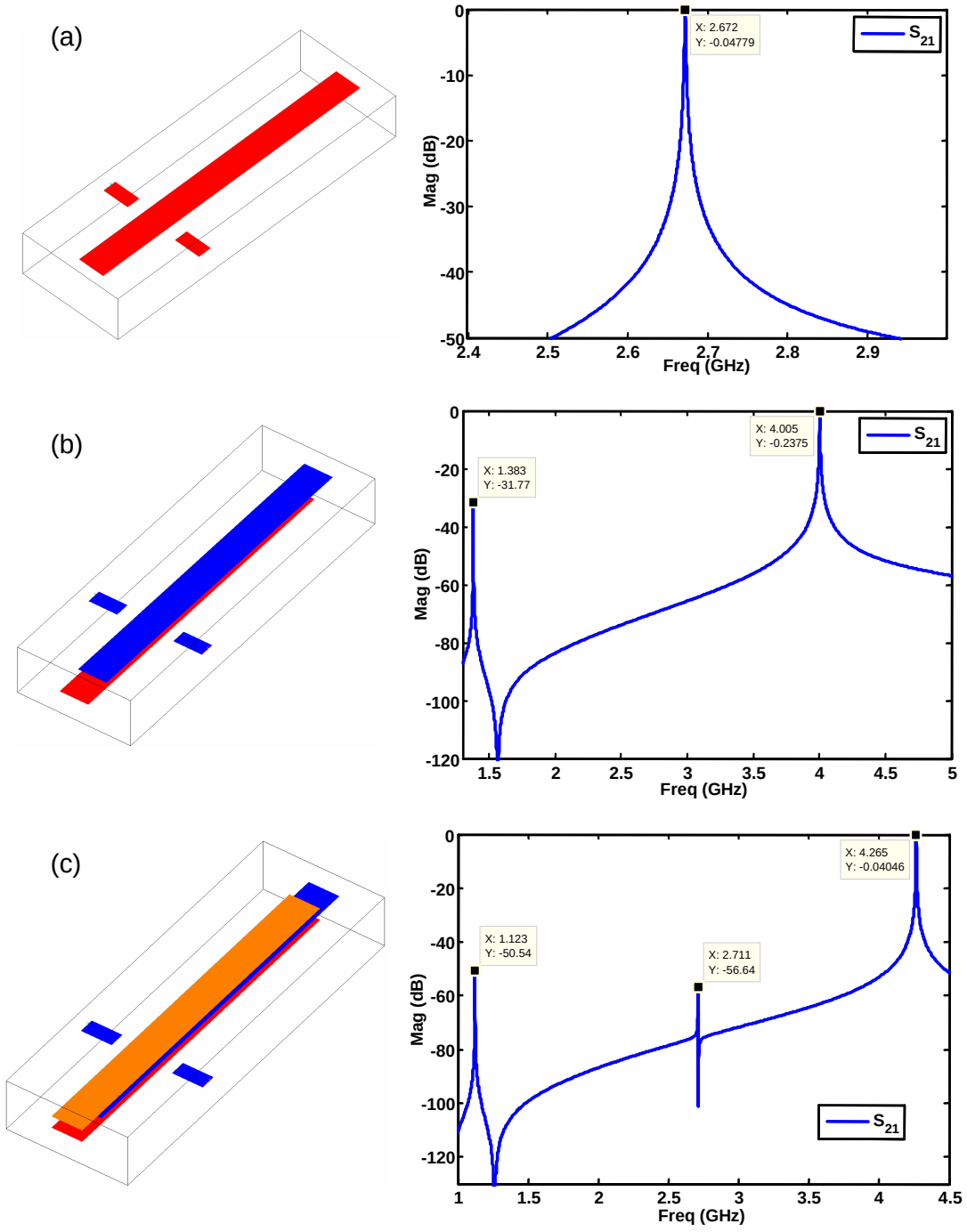

Figure 3.26: Natural resonant frequencies of multiple-layer coupled resonators. (a) Single-layer stripline resonator. (b) Double-layer coupled stripline resonator with two natural resonant frequencies. (c) Triple-layer coupled stripline resonator with three natural resonant frequencies.

frequencies of the resonators. The values are: 2.672 GHz for the single-layer resonator, 1.383 GHz and 4.005 GHz for the double-layer resonator, and 1.123 GHz, 2.711 GHz, and 4.265 GHz for the triple-layer resonator. These found values are consistent with the above discussions of multiple-layer resonators.

For a given center frequency of a filter design, the greater the number of layers used in a multiple-layer coupled resonator, the smaller the resonator size that can be obtained. However, the spurious performance will become worse with a greater number of layers because the second resonant mode will be closer to the fundamental resonant mode. It can be observed from Fig. 3.26(b) and (c): the triple-layer stripline resonator has a second resonant mode at 2.711 GHz, while the double-layer resonator has one at 4.005 GHz.

3.3.4 Filter Configuration

Many filter configurations can be realized by multiple-layer coupled resonators. The most commonly used ones are the so-called *combline* and *interdigital* configurations (as shown in Fig. 3.7 using double-layer resonators). They are extended structures from the single-layer combline and interdigital filters. In the multiple-layer filter structures, the strips (or single-layer structures) of one resonator are coupled to the strips at the same layer of another resonator. Therefore, the inter-coupling between two multiple-layer resonators is the combined couplings between the paired strips at each layer. The strong inter-coupling values are, thus, still achievable between the multiple-layer coupled resonators even though the size

(area) of the resonators is compact. Therefore, multiple-layer coupled resonators are appropriate for miniature and broadband filter designs.

Actually, other quasi-elliptic filter configurations realized by single-layer resonators are also able to be implemented by multiple-layer coupled resonators. However, the filter structures will be more complicated, which also makes the analysis and design more difficult. The mode matching method used in the previous section for double-layer resonator filters might not be an appropriate tool to analyze some multiple-layer resonator structures. FEM (in Ansoft HFSS) and MoM (in Sonnet) can, thus, be employed to perform the analysis and design. A systematic design methodology is then necessary to compensate the low efficiency of FEM and MoM. Two examples using MoM in Sonnet are given next to illustrate the design procedure.

In practice, three main factors are usually considered to decide the number of layers used in a resonator: filter size, filter bandwidth, and spurious performance. Generally, with more layers, the filter size will be smaller, achievable bandwidth will be narrower, and the spurious performance will be worse.

3.3.5 Triple-layer Coupled Stripline Resonator Filter

To demonstrate the feasibility of multiple-layer coupled resonator filters, the design of a six-order Chebyshev filter using triple-layer coupled stripline resonators is performed. The bandwidth is from 1.0 GHz to 1.27 GHz (~23% relative bandwidth). The return loss should be better than 18 dB in-band. The required

couplings are

$$\begin{aligned} R_{in} &= R_{out} = 1.10643 \text{ (276.61 MHz)} \\ M_{12} &= M_{56} = 0.88859 \text{ (222.15 MHz)} \\ M_{23} &= M_{45} = 0.62816 \text{ (157.04 MHz)} \\ M_{34} &= 0.59653 \text{ (149.13 MHz)} \end{aligned} \tag{3.19}$$

The coupling values in MHz are the actual couplings used in the design process, which are obtained by multiplying the normalized coupling values by the filter bandwidth. An interdigital configuration is employed to fulfill the filter (as shown in Fig. 3.30(a)). LTCC technology will be used to manufacture the filter. The LTCC parameters are: relative permittivity of ceramics $\varepsilon_r = 5.9$, thickness of metallization $ts = 0.4mil$, and thickness of each ceramic layer $tc = 3.74mil$.

The triple-layer coupled stripline resonator structure is shown in Fig. 3.27(a). The vertical dimensions are decided according to the desired stack option in LTCC. The heights of the three metallization layers as shown in Fig. 3.27(b) are: $h1 = 29.68mil$, $h2 = 37.08mil$, and $h3 = 44.48mil$, respectively. The height of the box is $h = 63.02mil$. The length lr of the box or resonator as shown in Fig. 3.27(c) is taken as a fixed value $480mil$. The width ws of each strip in the resonator is also fixed at $40mil$. Three strips in the resonator have the identical length ls. The center frequency of the filter is about 1.135 GHz. In order to obtain a resonator resonating at 1.135 GHz, the strip length ls is swept to find the right value. Basically, the resonator is weakly excited at the middle layer by two striplines. The S_{21} response is simulated in Sonnet to search for the resonant

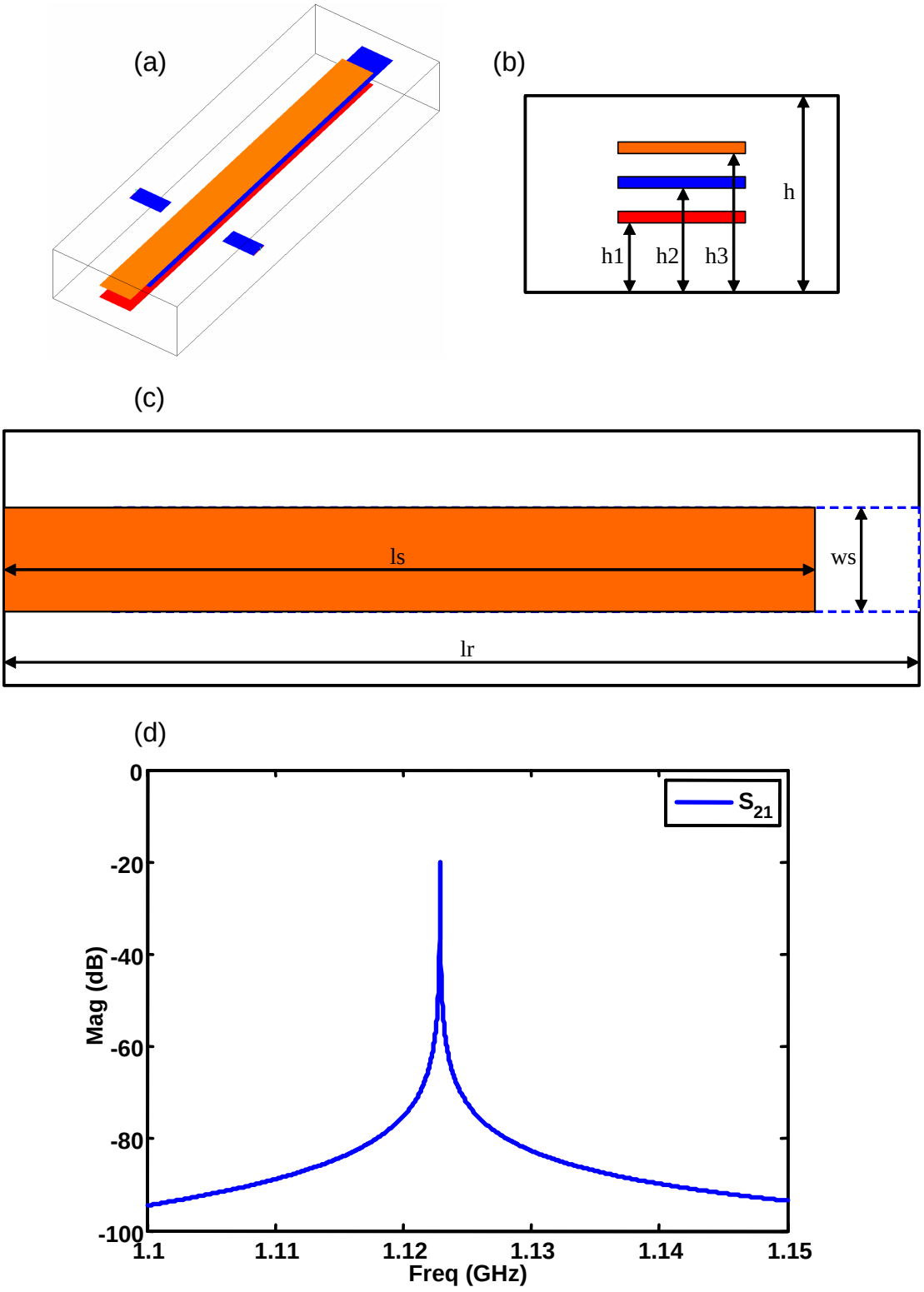

Figure 3.27: A triple-layer coupled stripline resonator (Drawings are not in scale). (a) 3D view with excitations. (b) End view. (c) Side view. (d) Typical S_{21} response.

frequency. A typical S_{21} response is shown in Fig. 3.27(d). The finally decided value of ls is $444mil$.

The external input and output couplings are provided by tapped-in 50-ohm striplines as shown in Fig. 3.28(a). The 50-ohm stripline can be tapped onto any of the three strips in one resonator. In this specific case, the middle strip of the resonator is used. A loop is constructed by the 50-ohm stripline and the middle strip of the resonator, which mainly provides the magnetic coupling to excite the resonator. Therefore, the larger the tapped-in position $htap$, the stronger the external coupling (because the loop is larger). The dimension $htap$ is swept to calculate the external coupling values by using (3.7). The obtained coupling curves are shown in Fig. 3.28(b): coupling value R vs $htap$, and the loaded frequency f_0 vs $htap$. It can be seen that R is linearly proportional to $htap$ and f_0 is almost constant. For this design, R should be about 276.61 MHz, and f_0 should be around 1.135 GHz. The value $htap$ found by interpolation is about $368mil$.

The inter-coupling structure is shown in Fig. 3.29(a), which is an interdigital configuration. The separation s between two resonators is swept to compute the coupling values and the loaded frequencies. The formulation (3.4) is used to calculate the coupling value M, while the loaded frequency is given by

$$f_0 = \sqrt{\frac{2f_1^2 f_2^2}{f_1^2 + f_2^2}} \approx \sqrt{f_1 f_2} \tag{3.20}$$

where f_1 and f_2 are the two peak frequency points of the simulated S_{21} response of the structure in Fig. 3.29(a). The obtained coupling curves are shown in Fig. 3.29(b): inter-coupling value M vs s and f_0 vs s. The values of s found

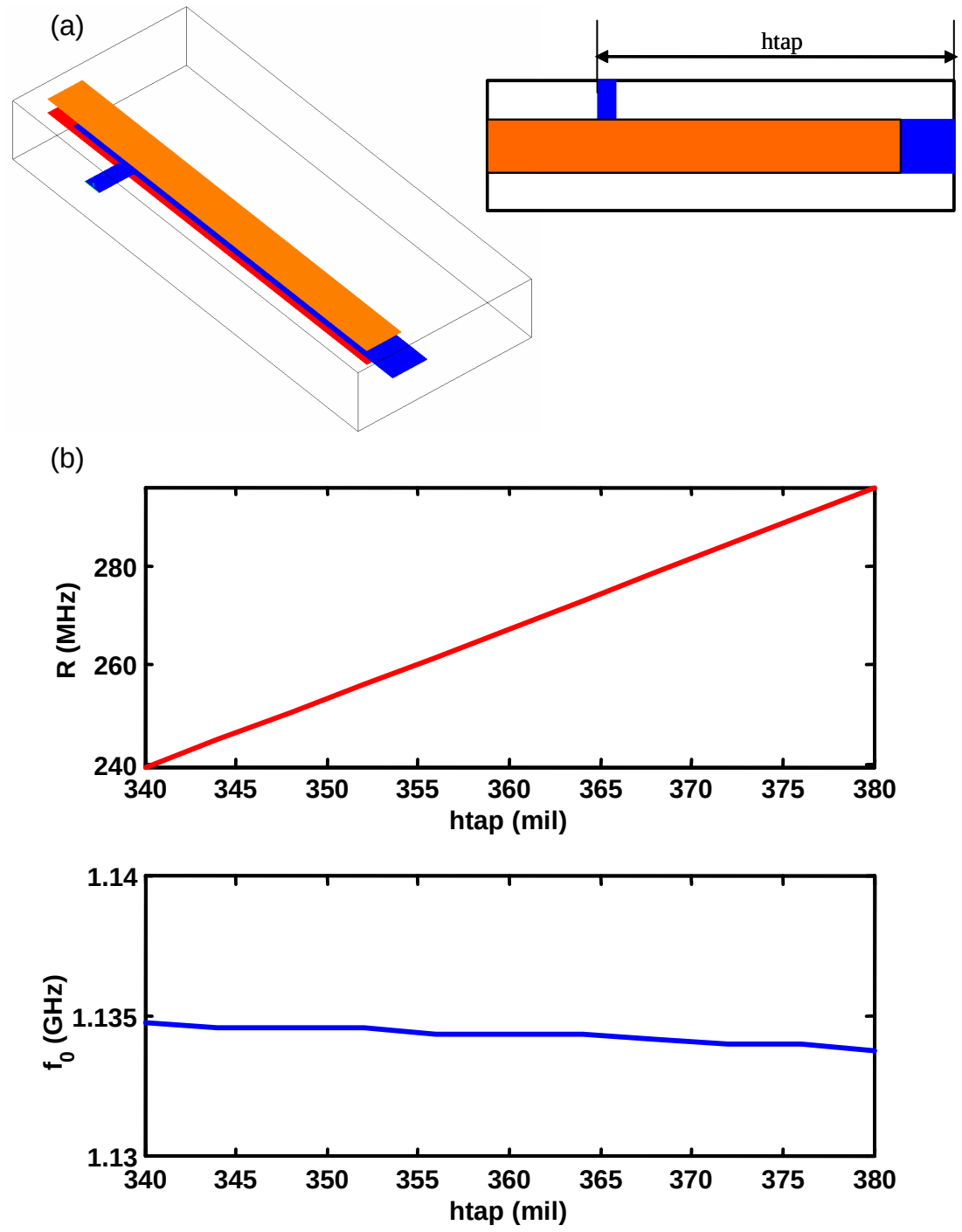

Figure 3.28: External coupling structure and computed coupling curves. (a) Tapped-in stripline external coupling structure. (b) External coupling curves with respect to the tapped-in position *htap*.

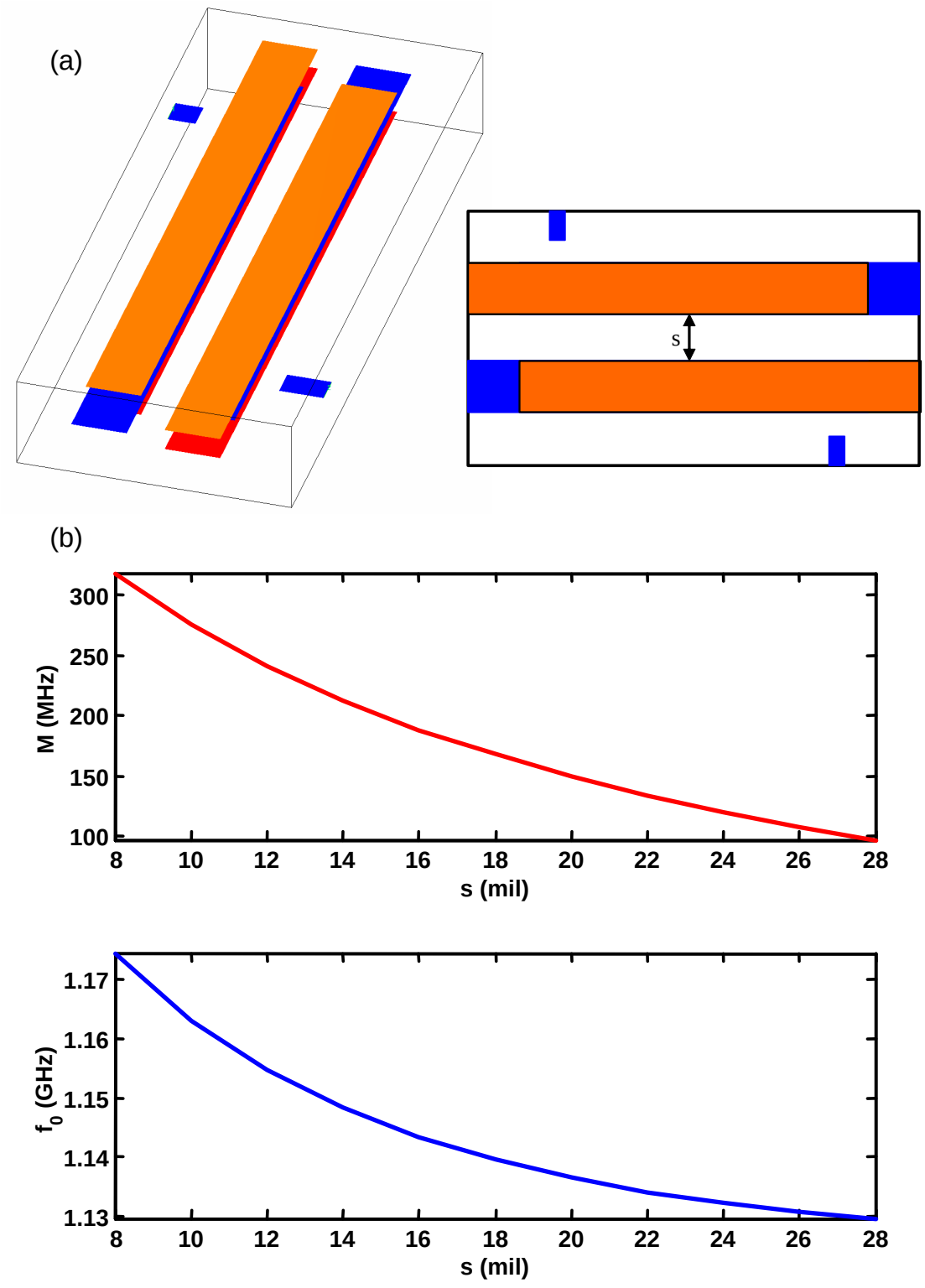

Figure 3.29: Inter-coupling structure and coupling curves. (a) Interdigital coupling structure between resonators. (b) Inter-coupling curves vs separation s.

by interpolation to provide the desired inter-couplings M_{12}, M_{23}, and M_{34} are $s1 = 13.3mil$, $s2 = 19.2mil$, and $s3 = 20.1mil$ (variables are defined in Fig. 3.30(b)), respectively. The loaded frequencies with respect to $s1$, $s2$, and $s3$ are 1.151 GHz, 1.138 GHz, and 1.136 GHz. These frequency values will be helpful for later tuning procedure.

The whole filter structure is assembled according to the obtained initial dimensions. Shown in Fig. 3.30 are the 3D and top views of the filter structure. The frequency response of this filter is simulated in Sonnet. It is well-known that uniform cells are used in Sonnet to perform the simulation. Therefore, in order to improve the simulation efficiency, integer values are taken for all the dimensions (Larger cells can, thus, be used in Sonnet). The used values of $s1$, $s2$, and $s3$ are 13, 19, and 20, respectively. The simulated response of the initial filter structure is shown in Fig. 3.31, which is a very good starting point for further tuning or optimization. The simulation time for this structure is about 18 minutes in a desktop PC with 3.0 GHz Pentium 4 CPU and 4 GB memory.

The filter dimensions need to be tuned or optimized to satisfy the requirements. The optimization speed is not acceptable since about 18 minutes are required for one single iteration. However, it is possible to tune the dimensions according to the calculated coupling curves, especially the loaded frequency curves. The loaded frequencies of the first and the second resonators are about 1.151 GHz, which is higher than the desired center frequency. The widths of these two resonators can be increased to tune the frequency down. The tuning step for all the dimensions is taken as 1 or 2 mil to keep the simulation efficiency. The

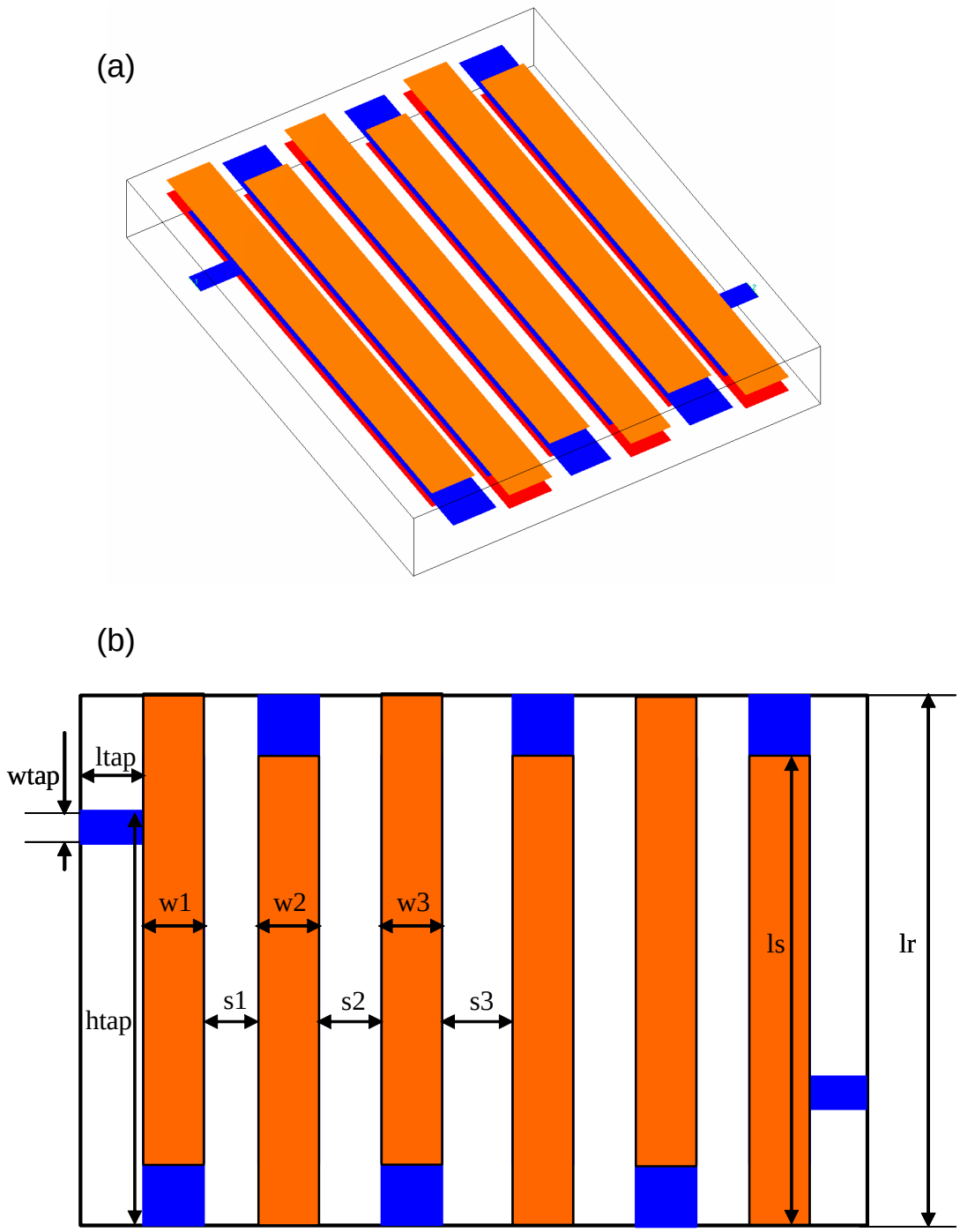

Figure 3.30: Filter structure using triple-layer coupled stripline resonators. The filter is flipped-symmetric and filled with homogeneous dielectric materials. (a) 3D view of the filter. (b) Top view of the filter with defined variables.

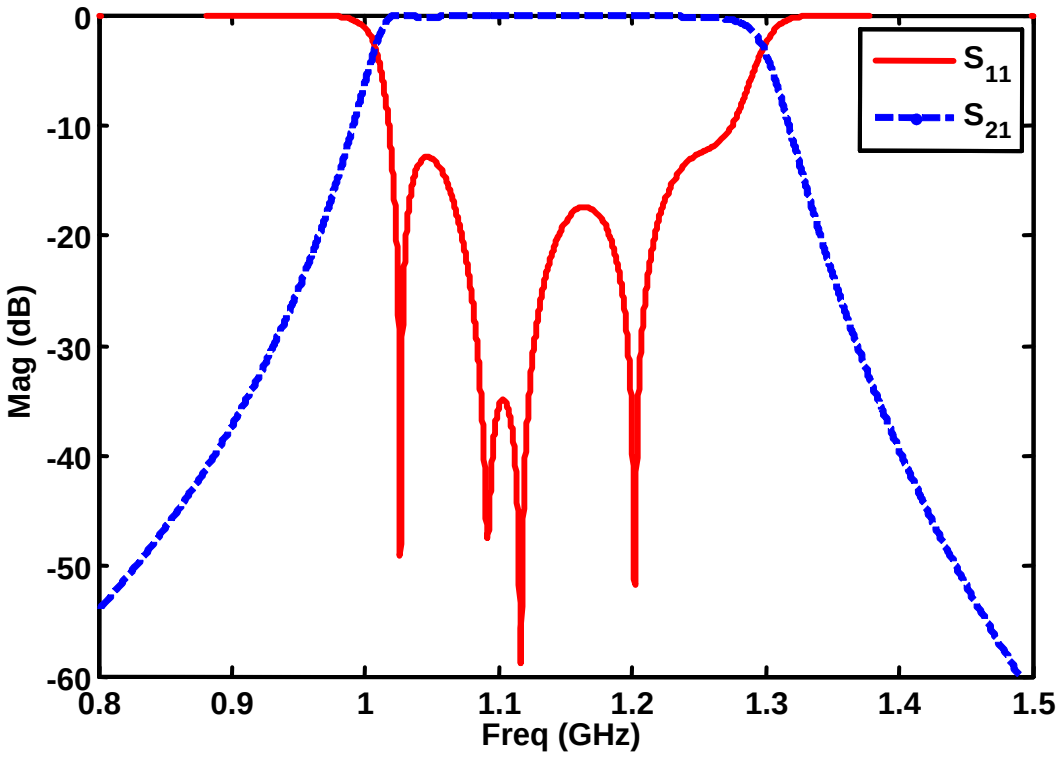

Figure 3.31: Frequency response of the initial filter structure by Sonnet.

other dimension to be tuned is the tapped-in position *htap*, because the external coupling will be affected by the dimension changing of the first resonator. The tuning procedure should always be guided by the solved coupling curves. The improved filter performance can be easily obtained after a few tuning steps. The parameter extraction method presented in [119] can also be employed to tune the filter. The frequency response of the final filter structure is shown in Fig. 3.32. Fig. 3.32(a) is the in-band response and Fig. 3.32(b) is the wide band response to show the spurious performance. The in-band return loss is larger than 19 dB. The spurious response is due to the higher order resonant modes of the resonator which are around 2.7 GHz and 4.25 GHz. The S_{21} spurious response around 2.7

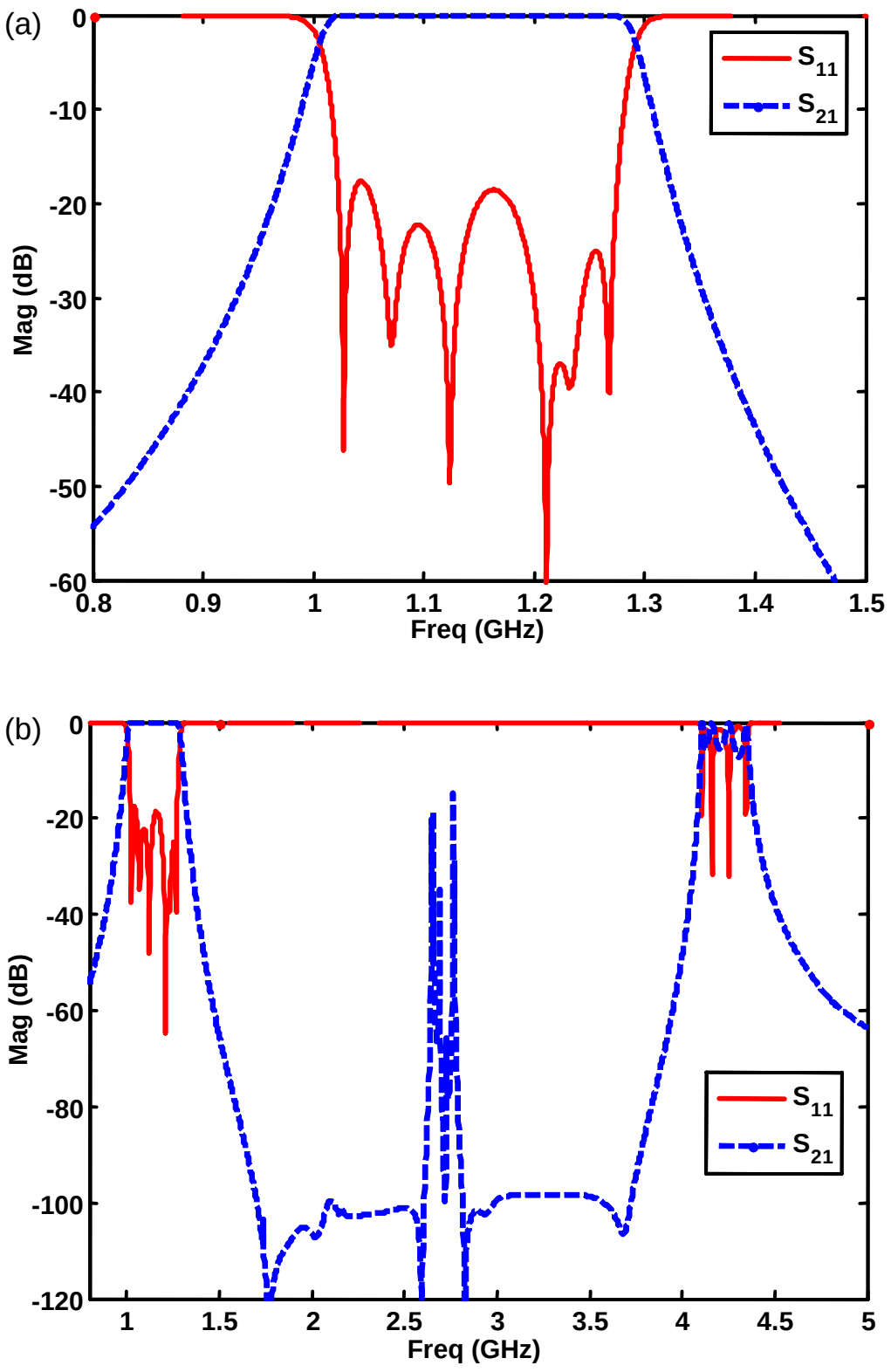

Figure 3.32: Frequency response of the final filter design by Sonnet. (a) In-band response. (b) Wide band response.

Table 3.3: Final dimensions of the triple-layer coupled stripline resonator filter as shown in Fig. 3.30. All the dimensions are given in mil. The thickness of metallization strips is 0.4 mil.

Variable	**Value**	**Variable**	**Value**	**Variable**	**Value**
$w1$	43	$w2$	43	$w3$	40
$s1$	13	$s2$	19	$s3$	20
$wtap$	20	$htap$	376	$ltap$	40
lr	480	ls	444	h	63.02
$h1$	29.68	$h2$	37.08	$h3$	44.48

GHz is suppressed below 20 dB because the employed external coupling structure excites the first higher order resonant mode very weakly. The final dimensions of the filter are given in Table 3.3.

3.3.6 Double-layer Coupled Hairpin Resonator Filter

In previously presented multiple-layer coupled stripline resonators, one end of the strips is shorted to ground, which usually requires using vias. The vias in a filter will introduce more loss, increase the cost, and degrade the performance. In order to avoid using vias in resonators, conventional single-layer hairpin resonator can be extended to a multiple-layer structure. The conventional hairpin resonator filters were introduced by Cristal et al [136] to meet the demand of small size and light weight bandpass filters. Further miniaturized hairpin resonator filters

were reported by Sagawa et al [150] for application to receiver front-end MICs. Single-layer hairpin resonators can be employed to realize combline, interdigital, pseudo-interdigital, and quasi-elliptic filter configurations [127, 130, 151, 152]. Essentially, a single-layer hairpin resonator is a symmetrically folded half-wavelength stripline resonator, where a virtual ground is created at the symmetric point on the stripline. The single-layer hairpin resonators can be easily extended to multiple-layer coupled hairpin resonators as shown in Fig. 3.23(c). One filter design example using double-layer coupled hairpin resonators is given next to show the feasibility.

The filter specifications are: the center frequency of 1.135 GHz, the passband bandwidth of 150 MHz (the relative bandwidth is about 13.22%), and the passband return loss of larger than 18 dB. A design of six-pole Chebyshev filter is performed. The normalized coupling values are identical as in (3.19). However, the actual coupling values are $R = 166MHz$, $M_{12} = 133.3MHz$, $M_{23} = 94.22MHz$, and $M_{34} = 89.48MHz$, which are smaller than the previous example due to the narrower bandwidth. The filter is designed for the same LTCC technology as before.

The structure of the employed double-layer coupled hairpin resonator is shown in Fig. 3.33(a). The vertical dimensions are $h1 = 29.68mil$, $h2 = 37.08mil$, and $h = 63.02mil$. The width and thickness of the metallization strip are $ws = 20mil$ and $ts = 0.4mil$. The distance between two arms in one resonator is taken as $wd = 40mil$. The length of the enclosure box lb is remained $80mil$ larger than the resonator length lr, i.e. $lb - lr = 80mil$ (resonator is placed in the middle

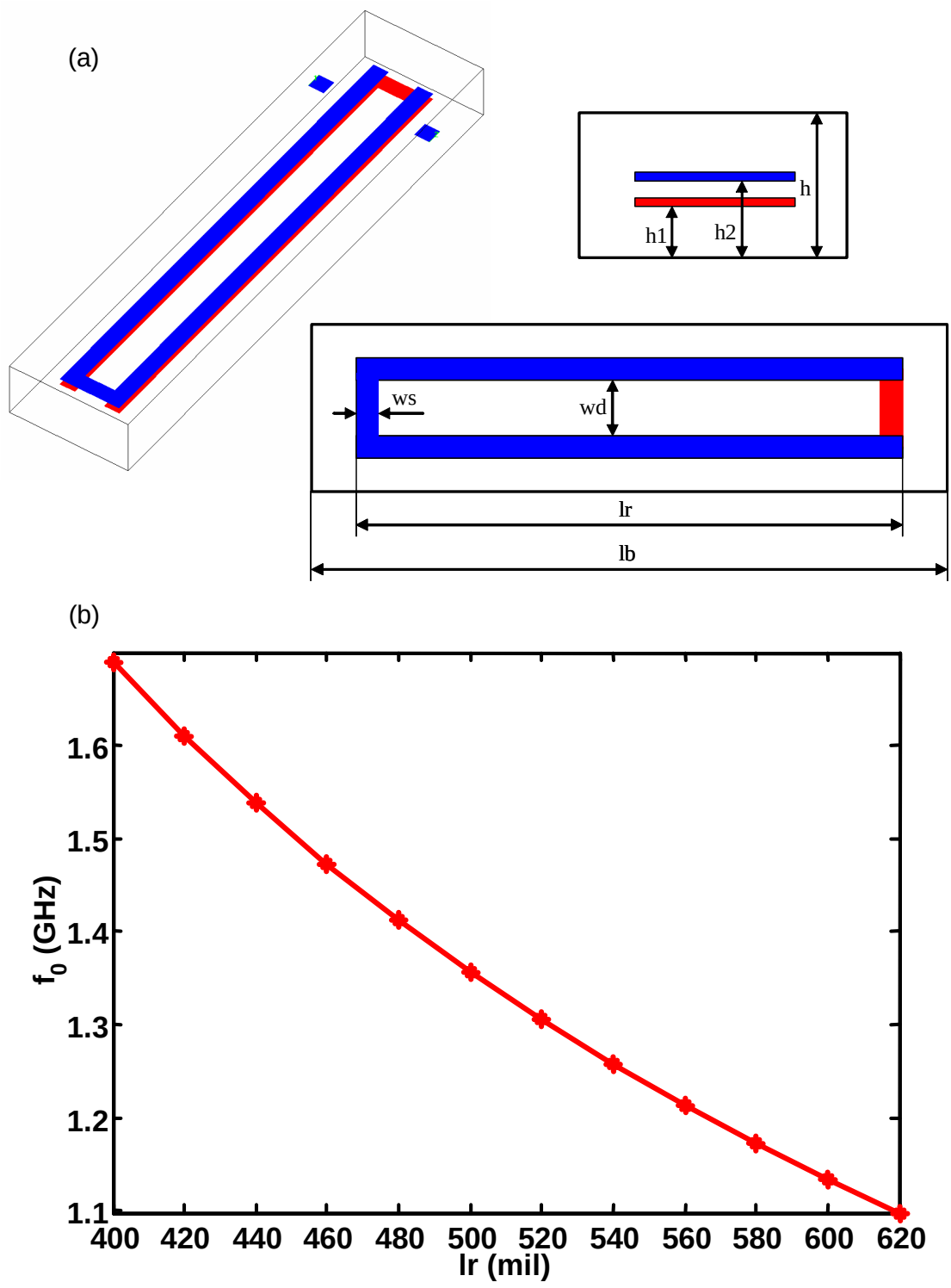

Figure 3.33: (a)Structure of double-layer coupled hairpin resonator (Filled with homogeneous dielectric material). (b) Resonant frequency f_0 with respect to the resonator length lr.

of the box). The resonator length lr is swept to search for the desired resonant frequency of 1.135 GHz. Shown in Fig. 3.33(b) is the calculated curve of the resonant frequency f_0 with respect to the resonator length lr. The value of lr is found to be $604mil$ by interpolation.

External couplings are also realized by tapped-in 50-ohm striplines as in previous examples. The tapped-in position $htap$ is swept to calculate the external coupling value R and the loaded resonant frequency f_0. The obtained coupling curves are shown in Fig. 3.34(a). To have a coupling value $R = 166MHz$, $htap$ is found to be $428mil$. However, the loaded resonant frequency f_0 is about 1.084 GHz that is smaller than the desired value of 1.135 GHz. The dimension wd is, therefore, decreased to increase the loaded resonant frequency f_0 and, meanwhile, remain the external coupling value R. The value of wd is taken as $28mil$ finally.

Two resonators are interdigitally coupled to each other as shown in the inset of Fig. 3.34(b). The calculation of inter-coupling value M and loaded frequency f_0 is following the same method presented before. The coupling curves are shown in Fig. 3.34(b). The values of the separation s for providing the desired inter-couplings are $s1 = 10.8mil$, $s2 = 16.4mil$, and $s3 = 17.3mil$ (variables defined in Fig. 3.35(a)). The loaded resonant frequencies are 1.135 GHz, 1.131 GHz, and 1.130 GHz, respectively.

The assembled filter structure is shown in Fig. 3.35(a). The initial dimensions are taken with the resolution of $0.5mil$ to gain the acceptable simulation speed in Sonnet. The used values of $s1$, $s2$, and $s3$ are 10.5, 16.5, and 17.5, respectively. The frequency response of the initial filter is shown in Fig. 3.35(b),

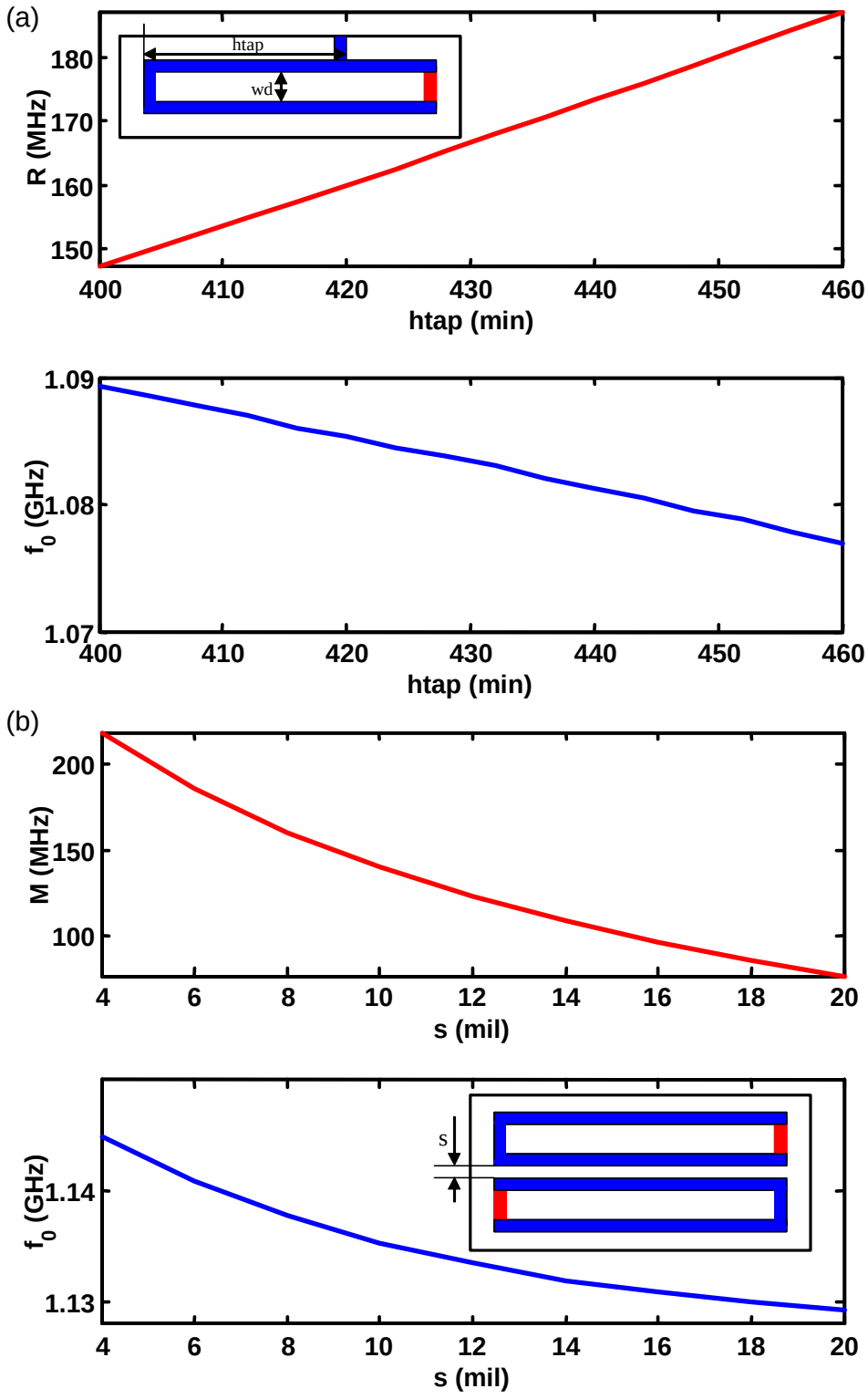

Figure 3.34: (a) External coupling curve of a tapped-in structure. (b) Inter-coupling curve between two double-layer coupled hairpin resonators.

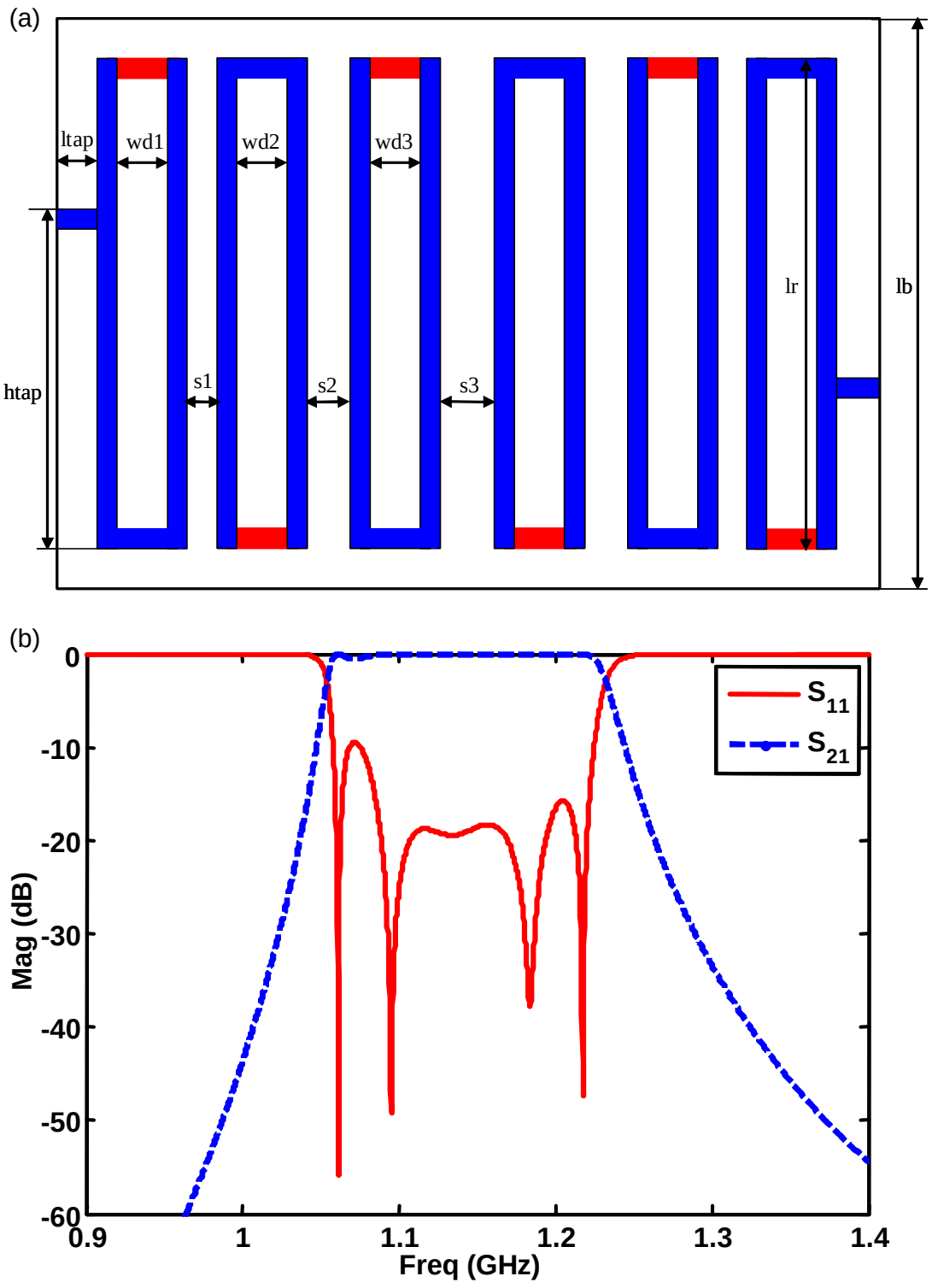

Figure 3.35: (a) A six-pole interdigital filter structure using double-layer coupled hairpin resonators. (b) The frequency response of the filter with initial dimensions.

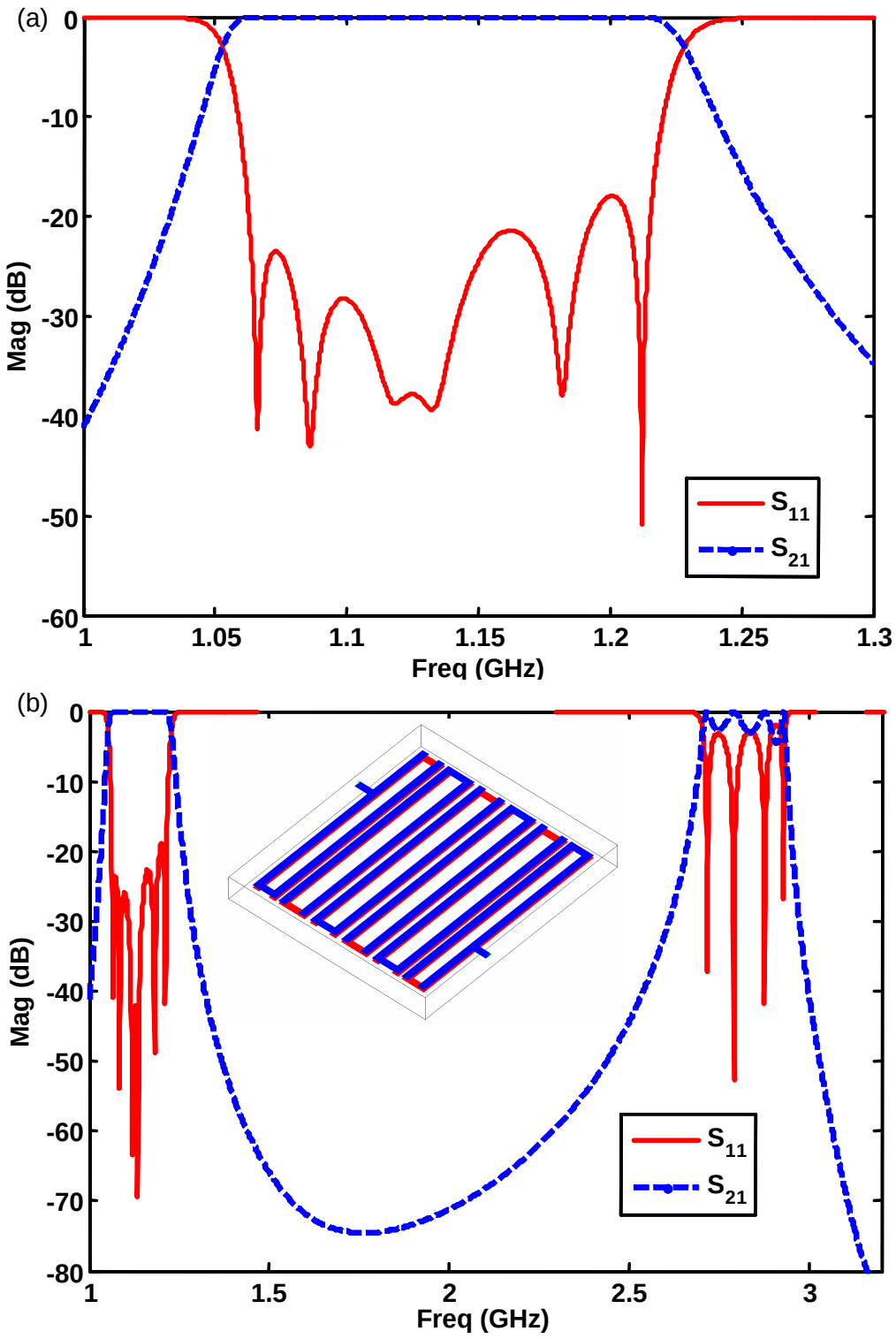

Figure 3.36: The frequency response of the final filter design using double-layer coupled hairpin resonators. (a) In-band response. (b) Wide band response.

Table 3.4: Final dimensions of the double-layer coupled hairpin resonator filter as shown in Fig. 3.35(a). All the dimensions are given in mil.

Variable	Value	Variable	Value	Variable	Value
$wd1$	30	$wd2$	42	$wd3$	40
$s1$	10.5	$s2$	16.5	$s3$	17.5
ws	20	$htap$	428	$ltap$	40
lr	604	lb	684		

which demonstrates a very good starting point for further tuning. The dimensions $wd1$ and $wd2$ are adjusted to modify the resonant frequencies of the first (and last) two resonators since the loaded frequencies of them are not around the center frequency. After a few tuning steps, an optimal filter response is obtained as shown in Fig. 3.36. The spurious response starts around 2.7 GHz. The final dimensions of the filter are given in Table 3.4.

3.4 Ridge Waveguide Coupled Stripline Resonator Filters

3.4.1 Introduction

High-performance communication systems have created the need for compact size, broad bandwidth, good quality, high selectivity, and easy-to-be integrated mi-

crowave filters and multiplexers. Planar filters are currently popular structures in integrated PCB circuits because of their small size and lower fabrication cost. The drawback of planar filters is their relatively-low quality factor. Waveguide filters have been recently applied in PCB circuits using LTCC technology for achieving higher quality factors. They are manufactured as multiple-layer structures to have high-integration level. LTCC ridge waveguide filter and multiplexer designs were presented in [61, 62, 141, 153]. The drawback of LTCC ridge waveguide filters is their relatively-large cross sections, especially their heights. Many ceramic layers are usually required to implement the ridge waveguide filters in LTCC technology, which will increase the cost and degrade the filter performance because the variation of the dielectric permittivity is increased with the number of ceramic layers. Therefore, new filter structures with more compact cross sections than ridge waveguides and better quality than planar structures need to be found for some integrated circuit systems.

The size of waveguide filters is mainly constrained by the cut-off frequency of their fundamental TE/TM mode, while planar filters do not have such constraint because TEM mode is their main operating mode (the size of planar filters is usually constrained by the resonator structures and the coupling mechanism). The idea is to use a TEM-mode resonator structure to gain a smaller filter cross section than other waveguide ones. New filter configurations using stripline resonators are presented in this section. The stripline resonators are coupled by ridge waveguide evanescent-mode sections to fulfill a bandpass filter and maintain the in-line topology (filter cross section remains same). The cross section of

the proposed filter configurations is much smaller than the aforementioned ridge waveguide filter structures, which makes them good choices for LTCC applications since only a few ceramic layers are usually required.

Two kinds of filter configurations using ridge waveguide coupled stripline resonators are discussed in this section. One configuration is for the classic Chebyshev filter topology. The design methodology is given and the spurious improvement with stepped impedance resonators is discussed. The other configuration is for the quasi-elliptic filter topology to obtain high frequency selectivity. All the designs are performed in MMM and verified by HFSS.

3.4.2 Chebyshev Filter Configuration and Design

A. Filter Configuration

The Chebyshev filter configuration is shown in Fig. 3.37(a) for LTCC applications. Basically the filter is constructed by stripline resonators coupled by ridge waveguide evanescent-mode sections. The size of the filter cross section is not limited by the cutoff frequency of stripline since the TEM mode of stripline is the propagating mode. Actually the filter cross section is mainly constrained by the ridge waveguide coupling sections. Usually the larger the cross section, the stronger the coupling. Therefore, for a broader bandwidth filter, a larger cross section will be required since strong couplings are needed. However, the cross section is always smaller than the classic ridge waveguide evanescent-mode filters [61, 62, 153] because all the modes of the ridge waveguides in this proposed filter

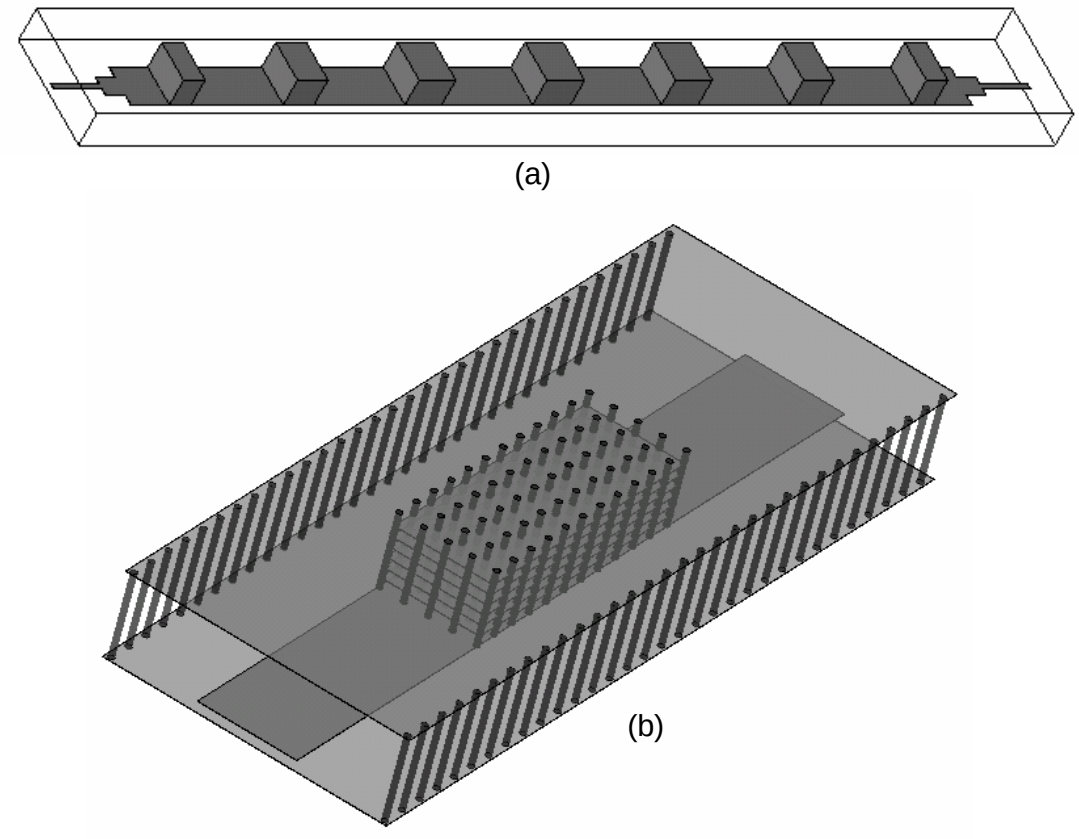

Figure 3.37: (a) Chebyshev filter configuration using ridge waveguide coupled stripline resonators for LTCC applications. (b) Draft of LTCC physical realization of a segment of the filter structure as shown in (a) (Stripline-Ridge-Stripline).

configuration are evanescent modes. Typically the filter cross section is about half the size of the ridge waveguide evanescent-mode filter for a 20% bandwidth filter. If filter bandwidth is smaller, the size of the cross section can be reduced more. Usually up to 40% bandwidth filter can be realized by the proposed filter configuration.

Fig. 3.37(b) is a draft showing how to manufacture the filter structure in LTCC technology. The horizontal walls of the ridge waveguides are constructed by

printing parallel planar conductors, while the vertical walls are realized by closely spaced metal vias. The stripline is implemented by one metallization layer. Thus, the filter can be embedded into multiple layer ceramics and integrated with other PCB circuits.

B. Filter Modeling in MMM

The full wave analysis of the proposed filter structure in Fig. 3.37(a) is carried out by means of rigorous mode matching method. Solid wall structures without vias are considered at the design stage (The filter is usually designed with sufficient margin with respect to the specifications to compensate the effects of the vias.). The mode matching analysis consists of three steps as discussed in Subsec. 1.2.3 (p. 11): i) Calculate the eigenmodes of all the waveguides involved. ii) Characterize each discontinuity by GSM. iii) Compute the complete filter response by cascading the GSMs of each discontinuity.

Two types of waveguides appear in the filter structure of Fig. 3.37(a): stripline and ridge waveguide. Their cross sections are shown in Fig. 3.38(a). The eigenmodes of stripline are classified as TEM, TE and TM modes, while the eigenmodes in ridge waveguide are classified as TE and TM modes. The eigenmodes of these two waveguides can be solved by the GTR technique discussed in Appendix A (p. 255). The typical electric field distribution of the fundamental TEM mode of a stripline cross-section is shown in Fig. B.1(a) (p. 269), while the fundamental TE mode of a single-ridge waveguide is shown in Fig. B.1(c).

Two types of waveguide discontinuities exist in the filter structure: stripline to stripline and stripline to ridge waveguide. The GSM of these two types of dis-

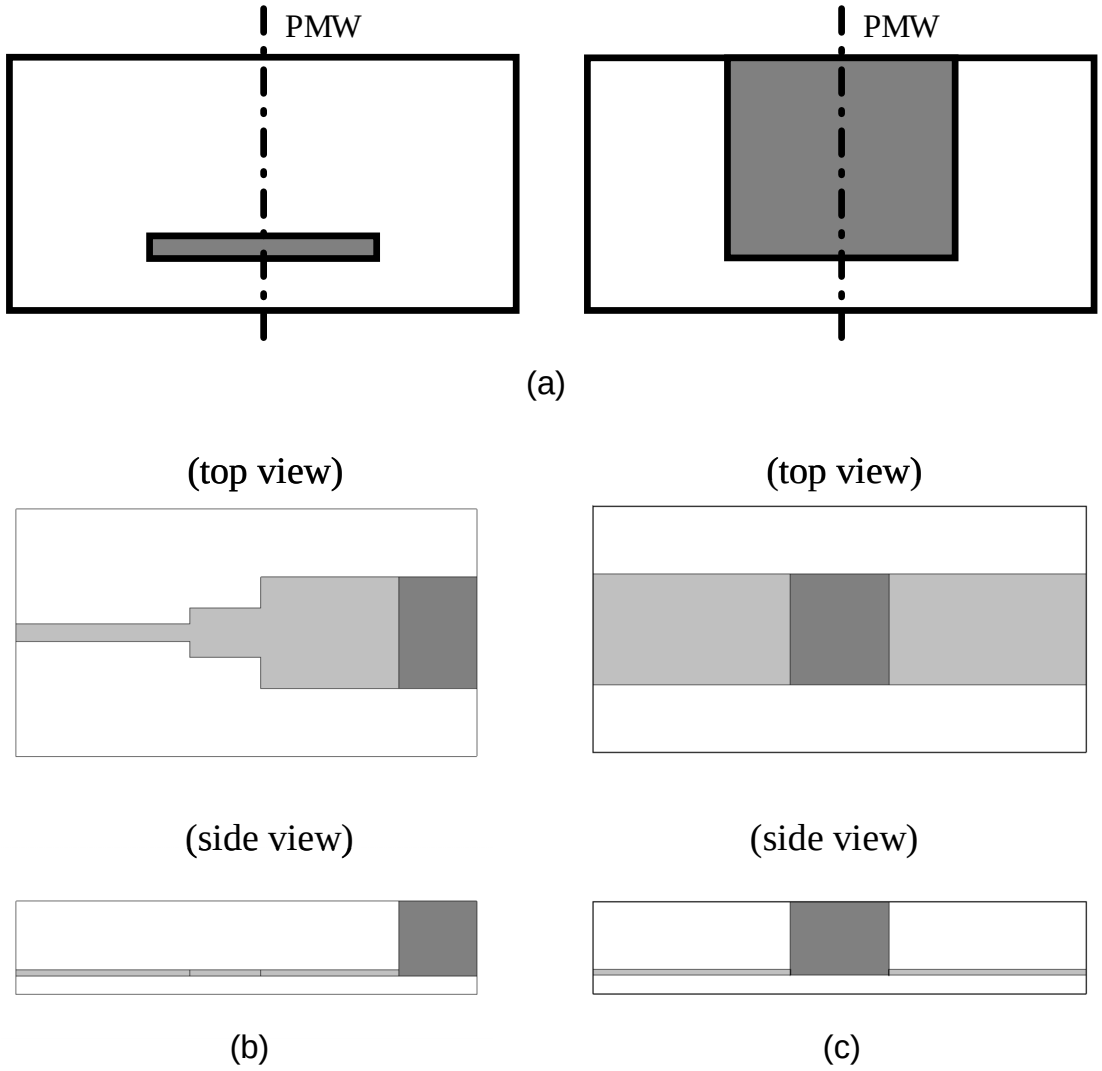

Figure 3.38: (a) Two types of cross sections that appear in the Chebyshev filter configuration: Stripline and Ridge waveguide. (b) Stripline tapped-in excitation for the external coupling. (c) Inter-coupling section between two stripline resonators by evanescent ridge waveguide.

continuities can be solved using the field matching procedure in Table 1.2 (p. 16). The coupling integrals $\mathbf{X}$ in Table 1.2 can be calculated based on the formulations in Appendix C (p. 271).

The GSM cascading is performed by using (1.2) to obtain the whole filter response. It is important to note that the filter has symmetry with respect to the middle plane along the overall length. Therefore, only the eigenmodes with PMW at the symmetric plane should be considered in the MMM analysis, which will significantly reduce the simulation time.

C. Filter Design Procedure

To design a filter with the proposed configuration as in Fig. 3.37(a), dimensions of the cross sections of stripline and ridge waveguide should be determined first according to the filter specifications, such as center frequency f_0 and pass-band bandwidth. Typically the cutoff frequency of the fundamental mode of the ridge waveguide can be chosen around $2f_0$ for $15\% - 20\%$ bandwidth filters, which will generate strong enough couplings between stripline resonators.

The filter design consists of two steps after the cross sections have been determined. The first step is to obtain the initial dimensions of the filter based on the impedance inverter method [1, 45, 154]. Physical realizations of the external couplings by stripline tapped-in excitation are shown in Fig. 3.38(b). The external coupling value can be calculated from the phase response of the reflection coefficient by (3.7). The inter-coupling sections between two stripline resonators are shown in Fig. 3.38(c). The GSM between the two discontinuities of stripline to ridge waveguide can be calculated by MMM. The impedance inverter is related

to the S-parameter by (3.6). The length of the ridge waveguide can be swept to find the dimensions for the required impedance inverter values. Phase information of the S-parameter should also be considered to adjust the stripline resonator lengths to compensate for loading effects.

The second step is the full wave optimization by MMM to obtain the optimum filter dimensions. Usually only the lengths of the resonators and coupling sections are optimized. By properly defining an objective function, the optimization of the filter performance can be done very efficiently using a gradient optimization method.

D. Filter Design Example

One filter is designed to show the feasibility of the proposed Chebyshev filter configuration. The requirements of the filter are: i) Passband: 8 – 10 GHz. ii) Minimum return loss: 22 dB. iii) Maximum insertion loss due to lossy materials: 2 dB. The relative bandwidth of the filter is about 22%. The parameters of the employed LTCC technology are: dielectric permittivity ε_r=5.9, thickness of one ceramic layer: 3.74 mil, and thickness of one metallization layer: 0.4 mil. The aforementioned design procedure is followed to design the filter. The dimensions of the cross sections of stripline and ridge waveguide are determined according to the filter requirements and the external couplings (Chosen dimensions as in Fig. 3.40(a)). Shown in Fig. 3.39 is the inter-coupling curve with respect to the length lr of the ridge waveguide coupling section. The initial filter dimensions are determined in terms of this coupling curve. Fig. 3.40 shows the optimized filter dimensions and the simulated response in MMM and HFSS. HFSS response

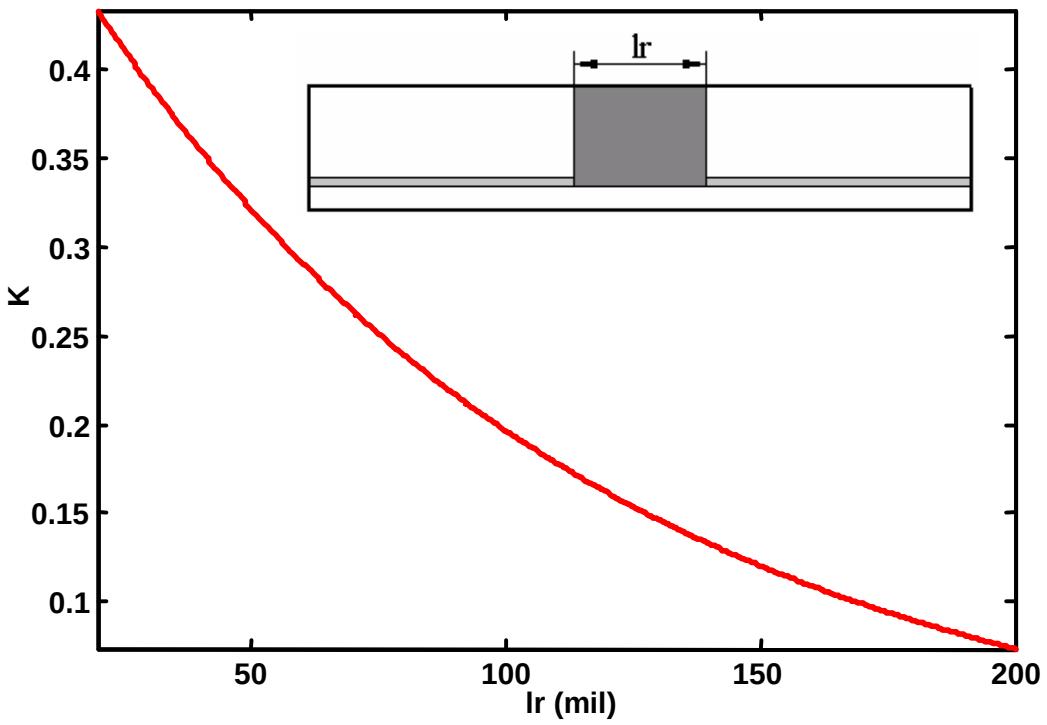

Figure 3.39: Inter-coupling values between stripline resonators with respect to the length lr of the ridge waveguide coupling section. Other dimensions are given in Fig. 3.40.

shows a very good agreement with MMM. To estimate the insertion loss of the filter, a HFSS simulation considering the finite conductivity $\sigma = 13100000$ S/m for conductor and loss tangent of 0.002 for dielectric is computed (These two typical values are supplied by Kyocera America, San Diego, CA 92123, USA). The response in Fig. 3.41 shows the insertion loss at the center frequency is about -1.35 dB. The unloaded quality factor Q is estimated to be around 150.

E. Spurious Performance Improvement

In some applications, better spurious response than the designed one as in Fig. 3.40(b) might be required. To improve the spurious performance, the con-

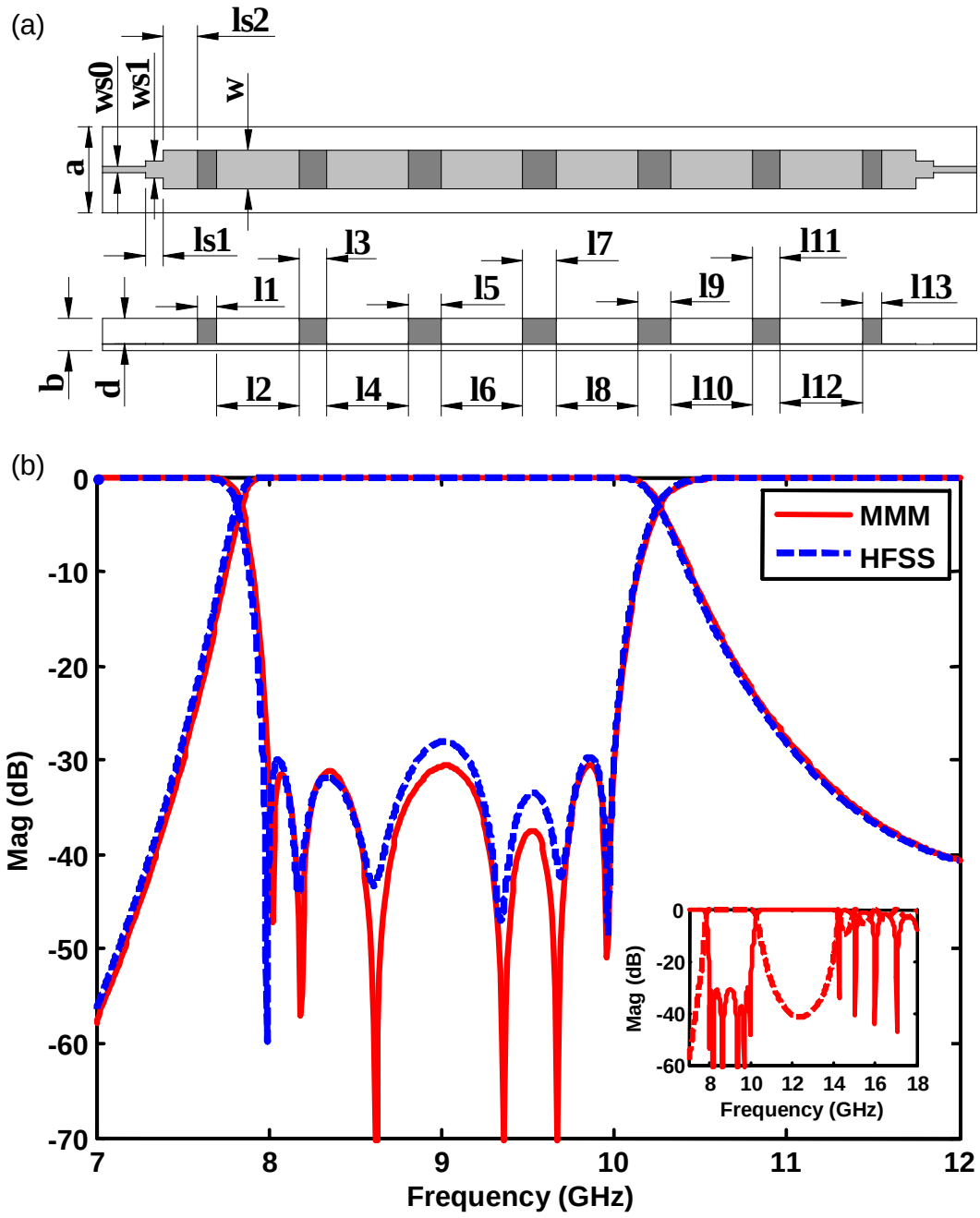

Figure 3.40: (a) Filter structure and dimensions. (b) Simulated frequency response by MMM and HFSS. Dimensions (in mil) of the filter are: $a = 100$, $b = 37.4$, $d = 29.92$, $ws0 = 7$, $ws1 = 20$, $w = 45$, $ls1 = 40.88$, $ls2 = 79.66$, $l1 = l13 = 44.73$, $l2 = l12 = 192.12$, $l3 = l11 = 63.37$, $l4 = l10 = 189.38$, $l5 = l9 = 76.25$, $l6 = l8 = 188.9$, $l7 = 78.92$.

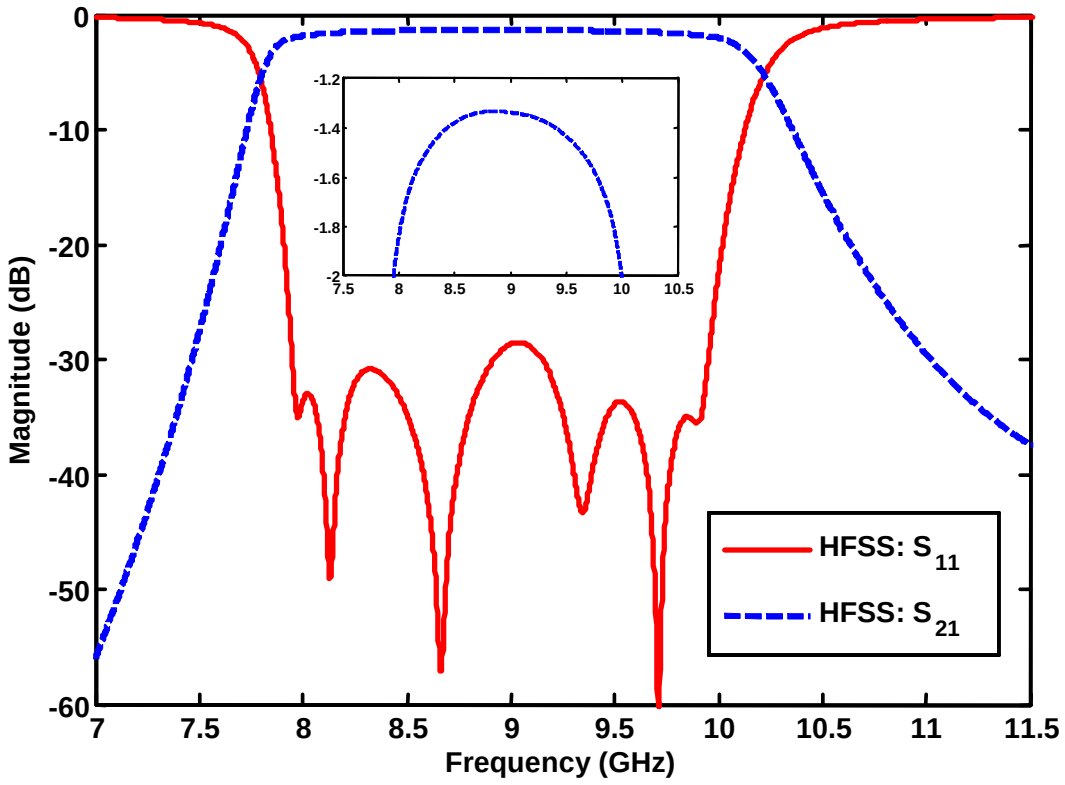

Figure 3.41: Frequency response with lossy material (conductivity $\sigma = 13100000$ S/m and loss tangent is 0.002).

cept of stepped impedance resonators (SIRs) can be applied [155–158]. Basically, a wider-strip lower-impedance stripline is introduced in the middle of the original stripline resonator (as in Fig 3.42(a)). This wider stripline will reduce the total length of the resonator to have a fundamental resonant mode at the center frequency f_0 because the field of this mode is concentrated around the middle of the resonator and this wider stripline introduces very strong coupling effect for it. While for the first higher order resonant mode, the field is very weak in the middle of the resonator and very strong close to the two ends. Therefore, the wider stripline will push the first higher order mode further away from f_0 since

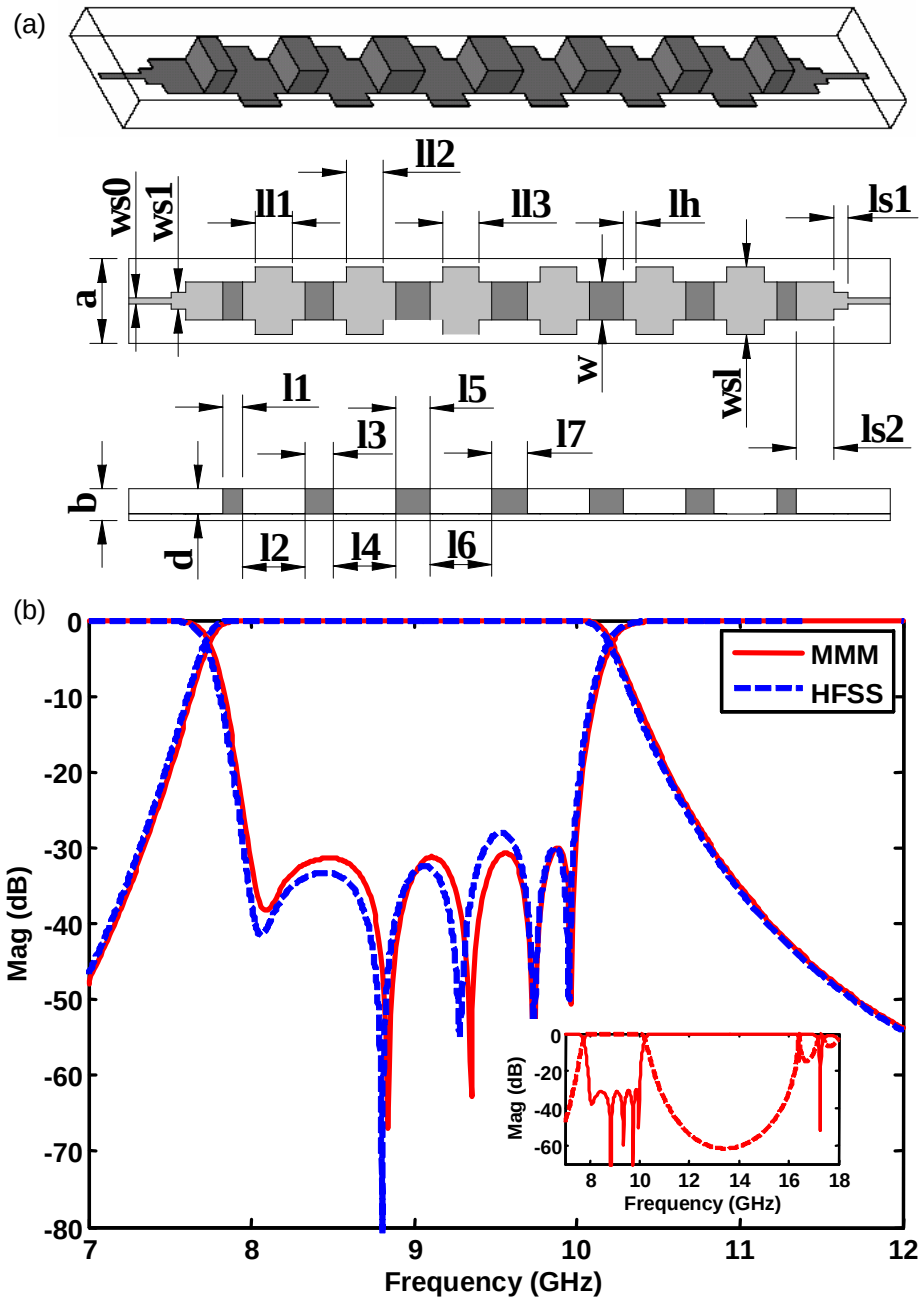

Figure 3.42: (a) Filter structure using SIRs. (b) Frequency response by MMM and HFSS. Filter dimensions (in mil) are: $a = 100$, $b = 37.4$, $d = 29.92$, $ws0 = 7$, $ws1 = 20$, $w = 45$, $wsh = 80$, $ls1 = 33.99$, $ls2 = 87.65$, $lh = 30$, $ll1 = 87.83$, $ll2 = 87.03$, $ll3 = 85.92$, $l1 = 46.33$, $l2 = 147.83$, $l3 = 66.99$, $l4 = 147.03$, $l5 = 80.4$, $l6 = 145.92$, $l7 = 84.26$. The length of narrow striplines in all the resonators are same as lh.

the length of the new resonator is shorter and the wider stripline introduces very week coupling effect on this mode.

The improved filter dimensions and responses are shown in Fig. 3.42. The spurious response is indeed improved. The spurious performance might be improved more if the ideas in [156–158] are applied here.

3.4.3 Quasi-Elliptic Filter Configuration and Design

A. Filter Configuration

The ridge waveguide coupled stripline resonators can also be employed in quasi-elliptic filter designs. The configuration of a canonical quasi-elliptic stripline resonator filter is shown in Fig. 3.43(a), which is used to realize a symmetric canonical filter topology as in Fig. 3.43(b). The filter configuration consists of two separated rows of ridge waveguide coupled stripline resonators, which correspond to the two rows in the filter topology. These stripline resonators are also coupled to the corresponding ones between the two rows by irises placed in the intermediate wall, which implement the cross couplings between two rows in the filter topology. The coupling mechanism will be discussed later. The filter configuration can also be built in LTCC technology as the Chebyshev one.

The filter configuration is symmetric about the middle yz plane and only implements the synchronous symmetric canonical filter topology (i.e. the filter response is symmetric about the center frequency). Therefore, resonators m and $2n - m + 1$ are identical, so are couplings M_{12} and $M_{2n-1,2n}$, etc.

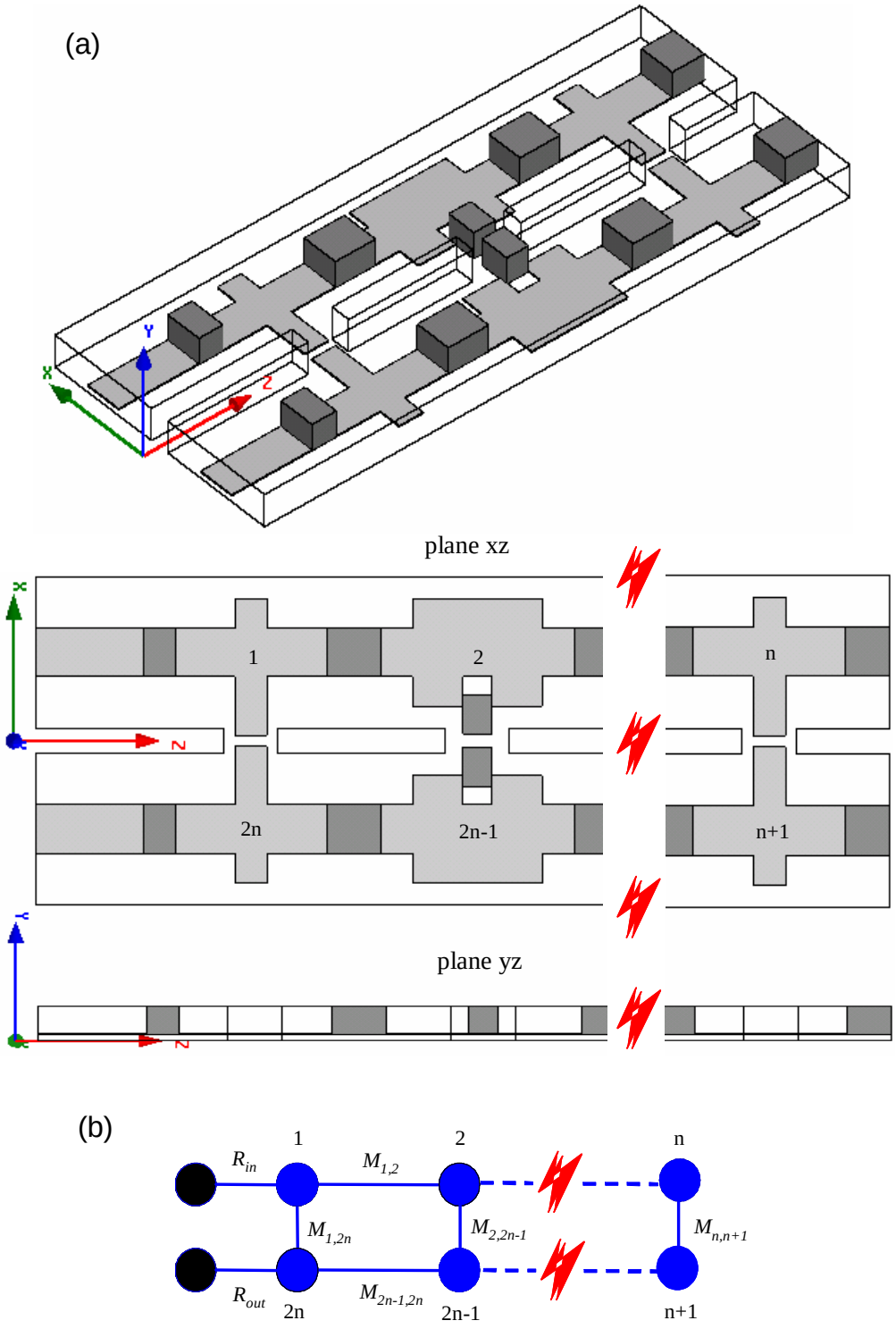

Figure 3.43: (a) Physical configuration of canonical filter topology using stripline resonators. (b) Canonical topology of $2n$ resonator symmetric quasi-elliptic filter.

B. Coupling Mechanism

The canonical filter topology as in Fig. 3.43(b) has adjacent couplings $M_{i,i+1}$ along the two rows and cross couplings $M_{i,2n-i+1}$ between the two rows (in some cases, some of $M_{i,2n-i+1}$ might be zero). The adjacent couplings $M_{i,i+1}$ are achieved by the ridge waveguide evanescent mode coupling sections between the stripline resonators, similar as the previously presented Chebyshev case. These adjacent couplings are mainly magnetic couplings and have positive signs. Cross couplings $M_{i,2n-i+1}$ include two types of couplings: electric coupling and magnetic coupling, which correspond to negative and positive sign couplings, respectively.

The realization of electric cross coupling is shown in Fig. 3.44(a). A small iris window is opened inside the separation wall at the center position of the stripline resonators. The broad sides of these two striplines are placed close to each other through this iris window. The electric coupling is provided by the interaction of the fringing fields of these two striplines. The coupling strength can be controlled by the coupled length of the two striplines and the separation space between them.

The realization of magnetic cross coupling is shown in Fig. 3.44(b). Ridge waveguides are sandwiched inside two stripline resonators first, and then coupled to each other through the iris window opened inside the separation wall. The ridge waveguide is to transform the TEM mode of stripline to TE/TM modes. The iris coupling is then mainly provided by the magnetic fields of the fundamental TE modes of the ridge waveguides. The coupling strength can be controlled by the size of the ridge waveguide and the separation between them. If very strong coupling

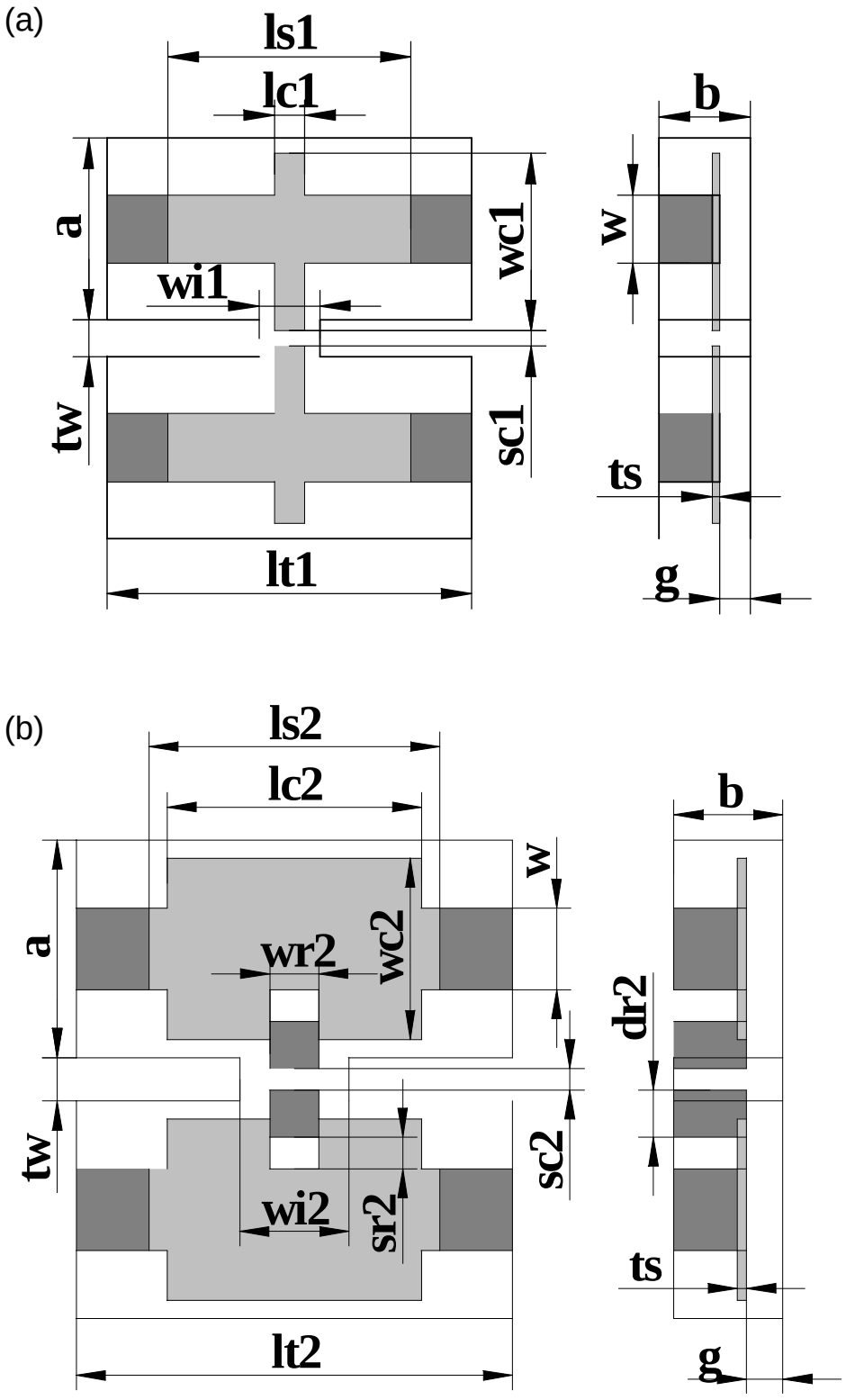

Figure 3.44: (a) Configuration of electric cross coupling. (b) Configuration of magnetic cross coupling.

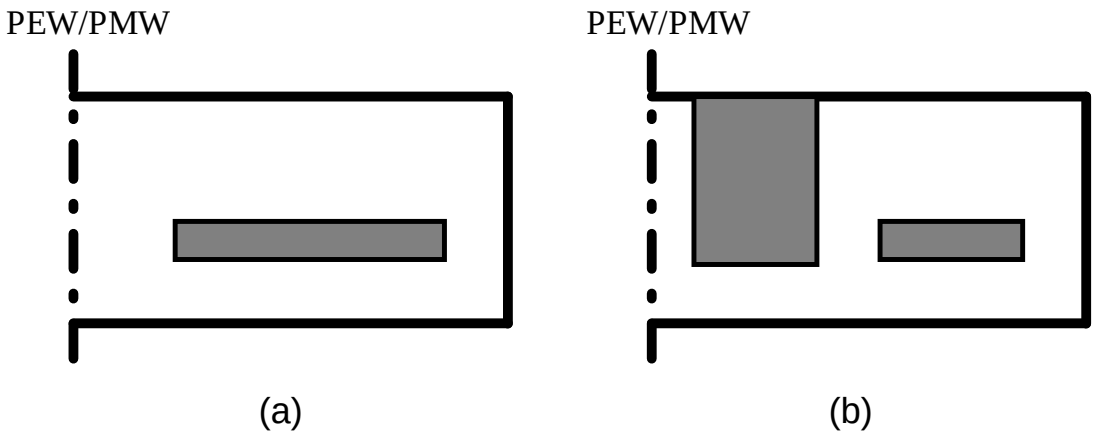

Figure 3.45: Two types of new cross sections in the canonical filter configuration. (a) Symmetric double stripline waveguide. (b) Symmetric double ridge-stripline waveguide.

is required, these two ridges can be connected together through the iris window.

C. Filter Modeling in MMM

The symmetry of the filter configuration is used to simplify the analysis in MMM (similar as the case of the filter in Fig. 3.10, p. 83). One half of the filter structure is analyzed twice with either PEW or PMW at the vertical symmetry yz plane. The GSMs of the half structure for the two cases can be obtained by MMM. Two reflection coefficients S_{11e} and S_{11m} of the fundamental mode from the input port are then extracted from the GSMs. S_{11e} and S_{11m} correspond to PEW and PMW at the symmetry plane yz, respectively. The scattering parameters of the fundamental mode of the whole filter structure is then calculated by using (3.9).

In addition to stripline and ridge waveguide, eigenmodes of two new waveguide cross sections in the half filter structure need to be solved. Their geometries are shown in Fig. 3.45. Both of them have PEW or PMW at one side wall. The

analysis method of these two cross sections is based on the GTR technique (see Appendix A, p. 255). Two kinds of TEM modes exist in these two cross sections: even TEM mode corresponding to PMW and odd TEM mode corresponding to PEW. The typical electric field distributions of the two TEM modes inside the cross section of Fig. 3.45(a) are shown in Fig. B.2(a) and (b) (p. 270). For the cross section in Fig. 3.45(b), the electric field distributions of two TEM modes and two TE modes are shown in Fig. B.2(c)–(e). The GSMs of each discontinuity can be calculated by using the formulations in Appendix C (p. 271).

D. Filter Design Procedure

The design procedure consists of two steps, similar to the Chebyshev case. In the first step, the initial dimensions of the filter are obtained according to the required coupling values. Basically each coupling value is matched with some physical dimensions. For external coupling R and adjacent couplings $M_{i,i+1}$, the impedance inverter method is used. The relationships between inverter K and normalized couplings $M_{i,i+1}$ and R are [3, 159]

$$\begin{aligned} K_{01} &= K_{2n,2n+1} = \sqrt{\frac{\pi}{2}\frac{bw}{f_0}R} \cdot \sqrt{\frac{f_0^2}{f_0^2 - f_c^2}} \\ K_{i,i+1} &= \frac{\pi}{2}\frac{bw}{f_0}M_{i,i+1} \cdot \frac{f_0^2}{f_0^2 - f_c^2} \end{aligned} \tag{3.21}$$

where f_0 and bw are center frequency and bandwidth of the filter. f_c is the cutoff frequency of the fundamental mode of the waveguide. In this presented case, f_c is zero. For cross couplings $M_{i,2n-i+1}$, the two resonant frequencies f_e and f_m (corresponding to a PEW and a PMW between two resonators, respectively) are computed for the structures in Fig. 3.44. Coupling value M in frequency unit

and loaded resonant frequency f_l are obtained as (extended from (3.5))

$$M = \frac{f_e^2 - f_m^2}{f_e^2 + f_m^2} \cdot f_l \text{ and } f_l = \sqrt{f_e f_m} \tag{3.22}$$

In the second step, the filter is analyzed and optimized using MMM to improve the performance and obtain an optimum design.

E. Filter Design Example

To demonstrate the feasibility of the proposed quasi-elliptic filter configuration, the design of a four-pole-two-zero filter with a center frequency of 9 GHz and bandwidth 900 MHz is performed. The minimum return loss is 22 dB. The equivalent circuit satisfying the specifications can be synthesized using the method presented in chapter 2. The synthesized prototype circuit has normalized external coupling $R = 1.15444$ and a coupling matrix

$$M = \begin{bmatrix} 0 & M_{12} & 0 & M_{14} \\ M_{12} & 0 & M_{23} & 0 \\ 0 & M_{23} & 0 & M_{34} \\ M_{14} & 0 & M_{34} & 0 \end{bmatrix} \tag{3.23}$$

with adjacent couplings $M_{12} = M_{34} = 0.9370$ and cross couplings $M_{23} = 0.7650$ and $M_{14} = -0.1026$.

The cross sections of the stripline resonators and ridge waveguides are chosen identical as the previous Chebyshev filter example since the center frequencies are identical. The length of the ridge waveguide coupling section is swept to find the dimension for the adjacent couplings M_{12} and M_{34}. The coupling curve is shown in Fig. 3.39. The coupling curves to determine the dimensions for cross

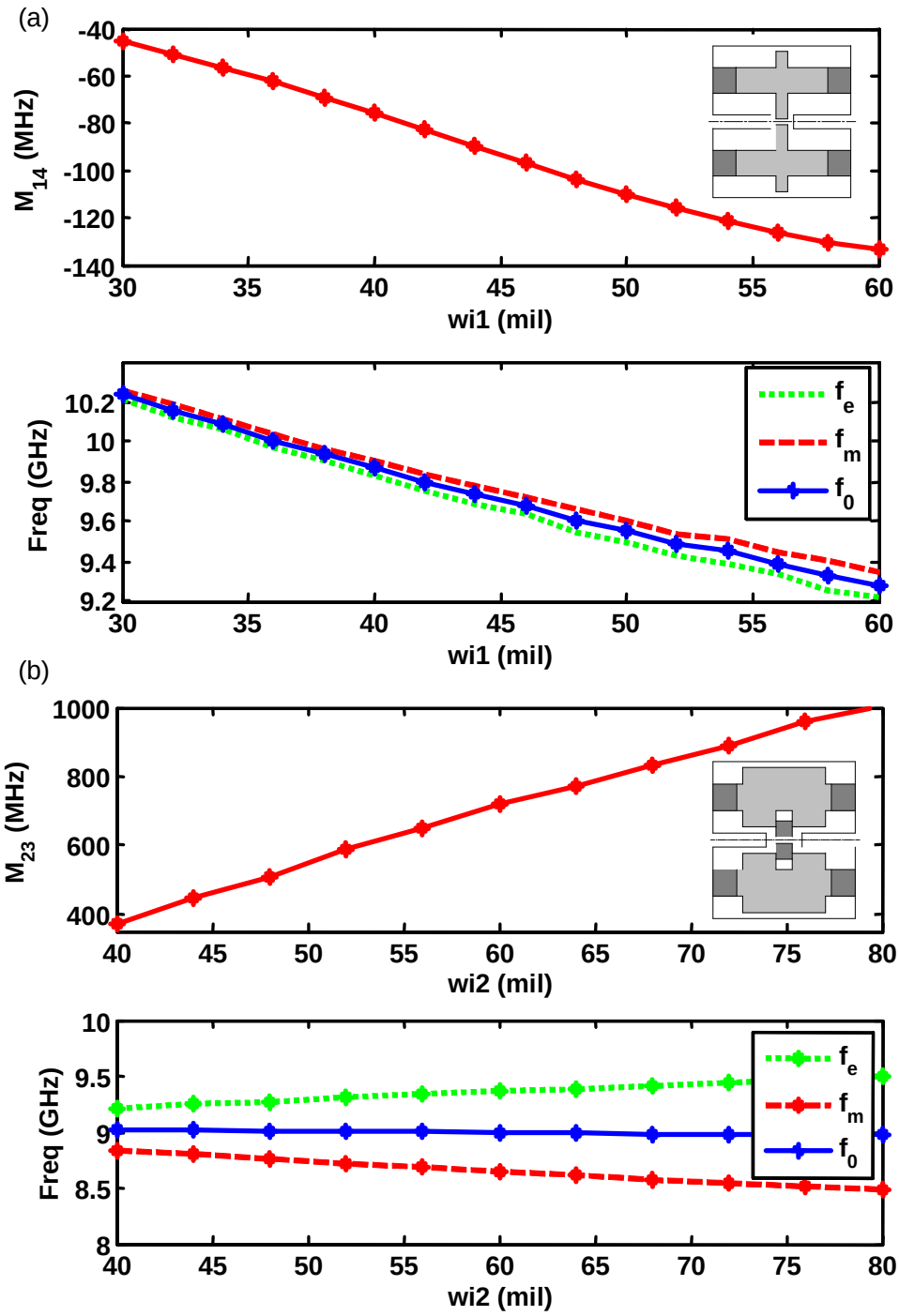

Figure 3.46: The cross coupling curves. (a) Electric cross coupling curve M_{14} and loaded frequency f_0 as a function of $wi1$ ($lc1 = wi1 - 20mil$). (b) Magnetic cross coupling curve M_{23} and loaded frequency f_0 as a function of $wi2$ ($wr2 = 0.45 \cdot wi2$). Other dimensions are shown in Table 3.5.

Table 3.5: Final dimensions of the quasi-elliptic stripline resonator filter as shown in Fig. 3.47(a). All the dimensions are given in mil.

Name	**Value**	**Name**	**Value**	**Name**	**Value**	**Name**	**Value**
a	100	b	37.4	w	45	g	7.48
$lr0$	20.93	$lr1$	110.8	$lr2$	40	$ls1$	144.47
$ls2$	218.43	$sc1$	10	$wi1$	51.99	$lc1$	31.99
$wc1$	97	$sc2$	12	$dr2$	23	$wi2$	61.31
$wr2$	27.59	$wc2$	80	$lc2$	178.51	$sr2$	10.5
ts	0.4	tw	24				

couplings M_{14} and M_{23} are shown in Fig. 3.46(a) and (b), respectively. To find the appropriate dimensions for coupling M_{14}, the length of resonator $ls1$ and the separation $sc1$ between two strips are determined first to have enough flexibility for achieving the required coupling value (Variables are defined in Fig. 3.47(a)). The width of iris window $wi1$ is then swept to obtain the coupling curve. The width of coupled strips $lc1$ is always fixed as $wi1 - 20mil$. The similar procedure is also applied to coupling M_{23}. Dimensions except $wi2$ and $wr2$ are firstly determined, and then $wi2$ is swept to calculate the couplings. The relationship between $wi2$ and $wr2$ is fixed as $wr2 = 0.45 \cdot wi2$.

The filter response with the initial dimensions is shown in Fig. 3.47(b), which demonstrates a very good starting point for further optimization. The optimized filter responses are shown in Fig. 3.48. The responses from ideal circuit

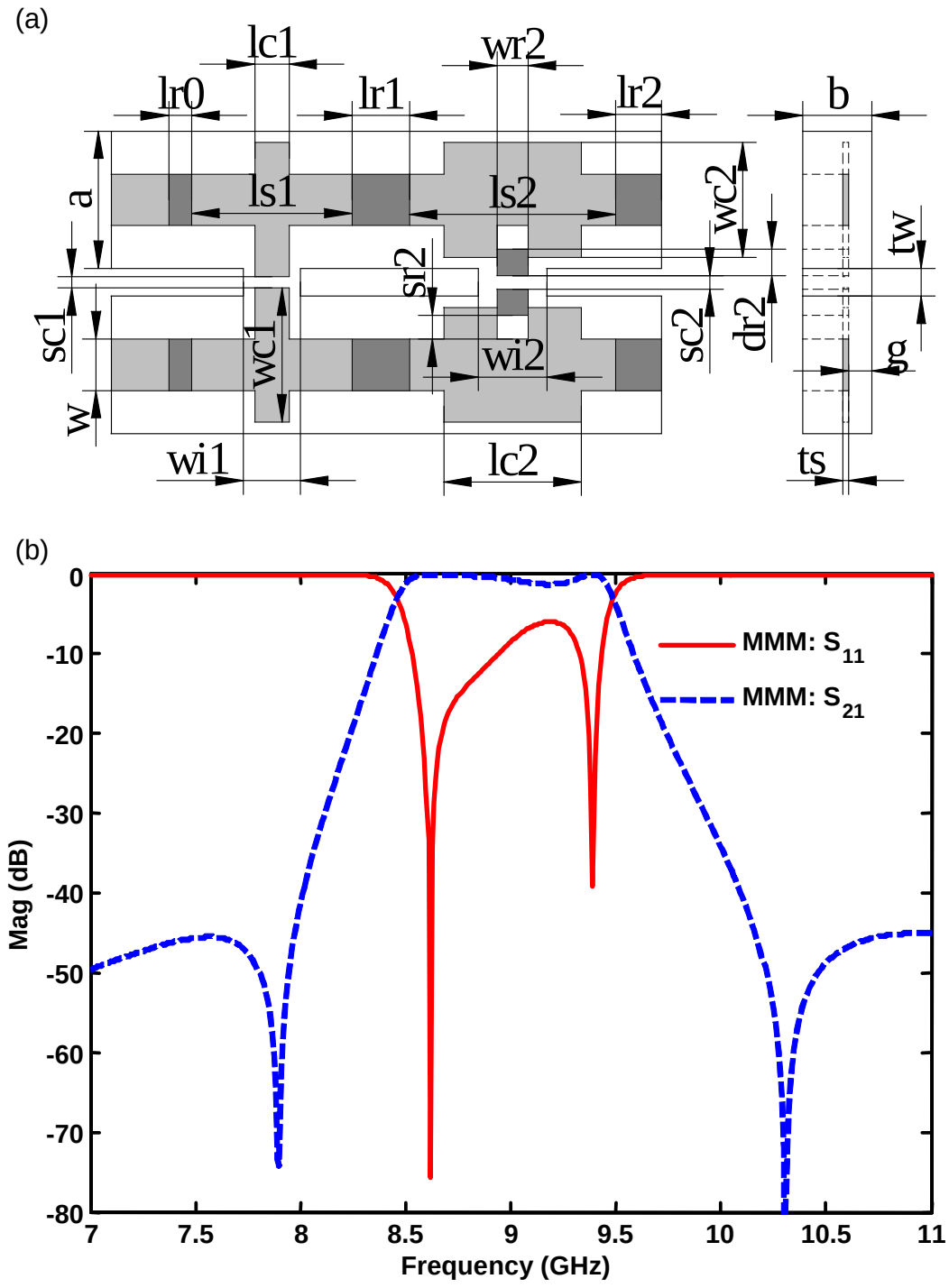

Figure 3.47: (a) The whole filter structure (Filled with LTCC ceramics $\varepsilon_r = 5.9$). (b) Simulated filter resonse by MMM with the initial dimensions.

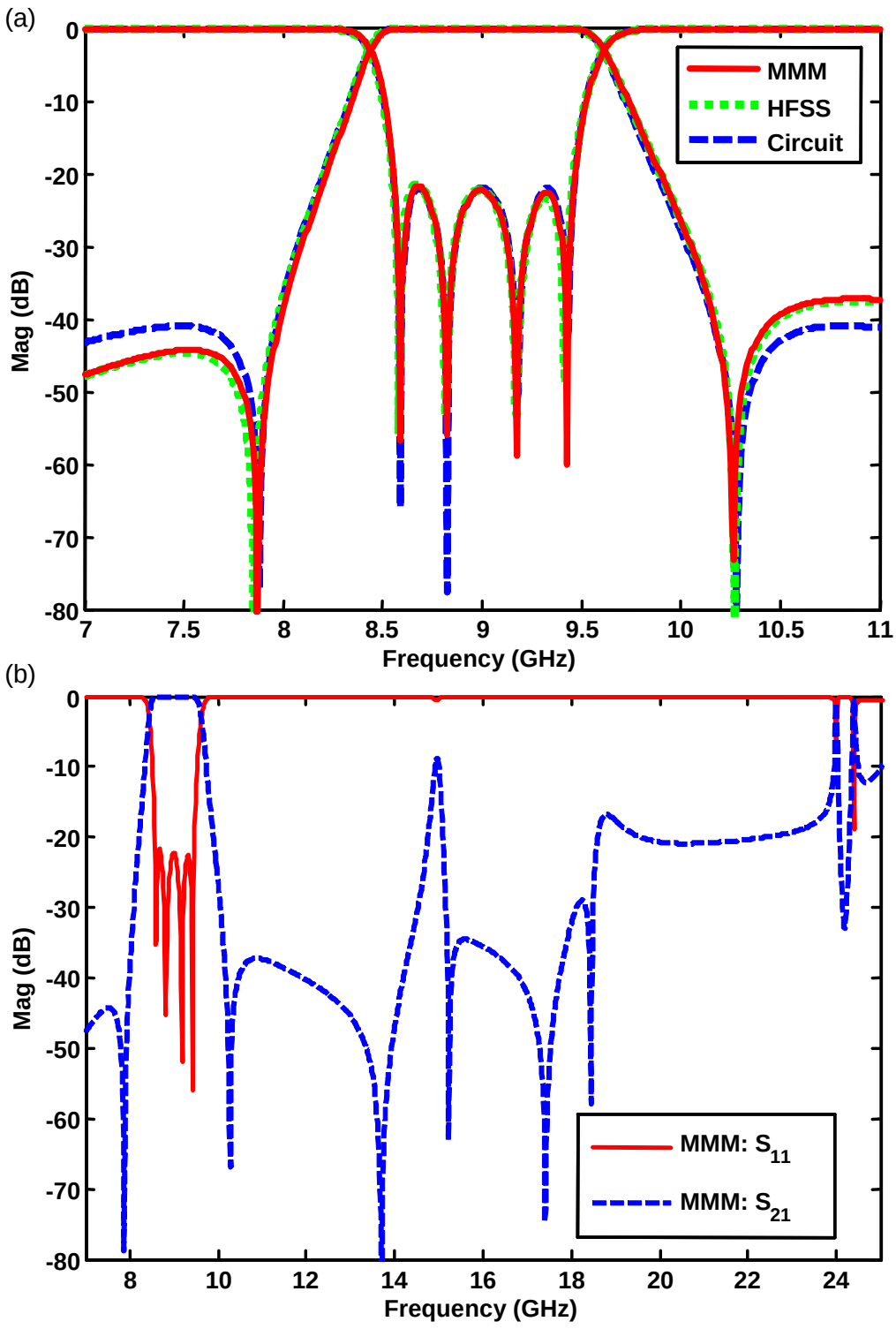

Figure 3.48: (a) Simulated frequency response of the final filter design by MMM and HFSS. Response obtained from ideal circuit model is also shown for comparison. (b) Wide band frequency response by MMM.

mode, MMM and HFSS are all shown in Fig. 3.48(a) for comparison. HFSS result shows a very good agreement with MMM. The wide band frequency response is shown in Fig. 3.48(b). The S_{21} spurious response around the second harmonic is suppressed below -10 dB by the stepped impedance resonators in the filter. The final filter dimensions are shown in Table 3.5.

3.5 Dual-mode Asymmetric Filters in Circular Waveguides

3.5.1 Introduction

High performance waveguide filters with high Q cavities may take up a significant physical volume, which is disadvantageous in many telecommunications and space applications. One method of size reduction is to exploit the existence of multiple degenerate modes in waveguide cavities. For example, one dual-mode cavity can be employed to implement two resonant circuits in one filter (Assuming the coupling between the two modes can be realized mechanically), such that the number of cavities required to realize an N-degree filter is reduced to $N/2$ (N is even) and, therefore, the physical filter volume is more compact than the filter realized by single-mode cavities (N single-mode cavities are required for an N-degree filter). Multiple-mode cavity filters were first reported by Lin in 1951 [160]. The concept was then extended to dual-, triple-, and quadruple-mode coupled cavity filters [161–164]. Since then, multiple-mode coupled cavity/resonator filters have been

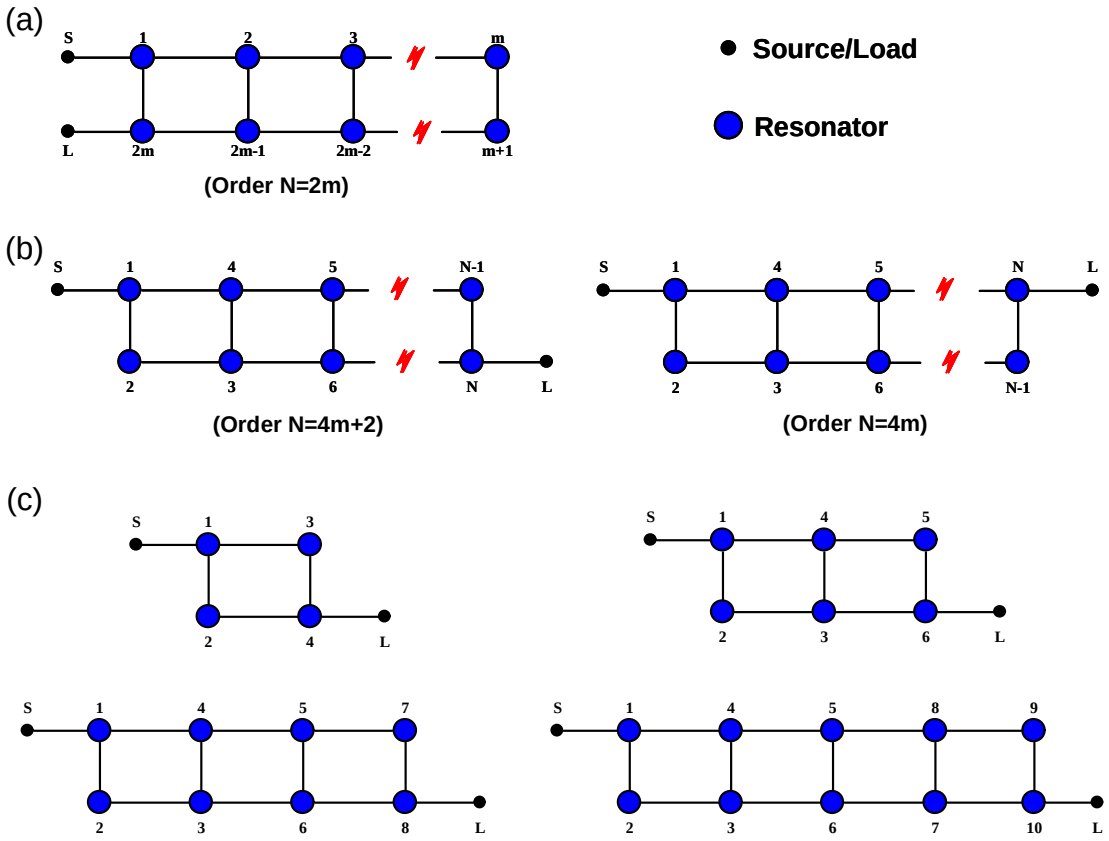

Figure 3.49: Network topologies applicable for dual-mode filter designs. (a) Canonical folded-network for symmetric transfer function. (b) Extended-box or longitudinal network for symmetric transfer function. (c) Extended-box or longitudinal network for asymmetric transfer function.

widely used for communications and satellite applications. Inside the multiple-mode cavities/resonators, dual-mode cavities/resonators are the most commonly used structures for microwave filter designs, especially for quasi-elliptic filter designs. In this section, only dual-mode cavity filters will be discussed.

An appropriate network topology must be synthesized first in order to design a dual-mode filter having quasi-elliptic transfer functions. For symmetric transfer functions, two types of topologies may be realized by dual-mode structures. one

type is the canonical folded-network topology as shown in Fig. 3.49(a). Any two resonators in one column (e.g. 1 and $2m$, m and $m+1$, etc.) can be implemented by one dual-mode cavity/resonator. The two rows/lines in this network topology are symmetric, which will simplify the hardware implementations of the couplings between two dual-mode cavities. However, one drawback of this topology is that the source and load of the filter will be in the same physical dual-mode cavity, which sometimes might not be practical. The other type is the extended-box or longitudinal topology as shown in Fig. 3.49(b), in which the source and load are at opposite ends. Even though this network topology is not symmetric, the produced frequency response is still symmetric about the center frequency. When the filter order $N = 4m + 2$, the source and load are in the same line/row, which means that they are exciting the same polarized mode of the dual-mode cavities. When the filter order $N = 4m$, the source and load are in different lines, which means that they are exciting two different polarized modes of the dual-mode cavities. The number of finite transmission zeros produced by this longitudinal topology is constrained by the number of resonators along the minimum path between source and load because each resonator along this minimum path corresponds to a transmission zero at infinity. Therefore, the maximum number of finite transmission zeros that can be generated by a longitudinal topology is given by [57]

$$N_{z,\max} = \begin{cases} \frac{N}{2} - 1 = 2m \text{ for } N = 4m + 2 \\ \frac{N}{2} = 2m \text{ for } N = 4m \end{cases} \tag{3.24}$$

The analytical synthesis procedure of the longitudinal topology for symmetric transfer functions is given in [88] for $N = 6, 8, 10, 12$, and 14. For higher order

filters, optimization procedure can be employed.

For asymmetric transfer function, the longitudinal topologies for $4th$, $6th$, $8th$, and $10th$ order filters as shown in Fig. 3.49(c) are appropriate for dual-mode realizations. The source and load are always in different lines. The maximum number of finite transmission zeros that can be produced by this type of topology is $(m-1)$ for a filter order of $N = 2m$, which can be seen through the afore-explained minimum path rule. The synthesis procedure of this kind of topology based on optimization method is given in [83].

Various dual-mode implementations of symmetric quasi-elliptic filters can be found in literature. In this section, in order to demonstrate the feasibility of dual-mode realization of asymmetric quasi-elliptic filters, a 4-pole filter with one transmission zero is synthesized and implemented by dual-mode circular waveguide cavities. The detailed design procedure and measurement results are given next. Similar structure and design procedure can also be applied for higher order dual-mode asymmetric filter designs.

3.5.2 Filter Parameters

A 4-pole-1-zero quasi-elliptic filter with bandwidth 35 MHz about the center frequency 3.38 GHz is designed. The minimum return loss within the pass band is required to be 22 dB. The maximum insertion loss within the passband is 0.3 dB. Two different solutions are possible according to the location of the transmission zero (one is within the lower stopband and the other one is within the upper stop-

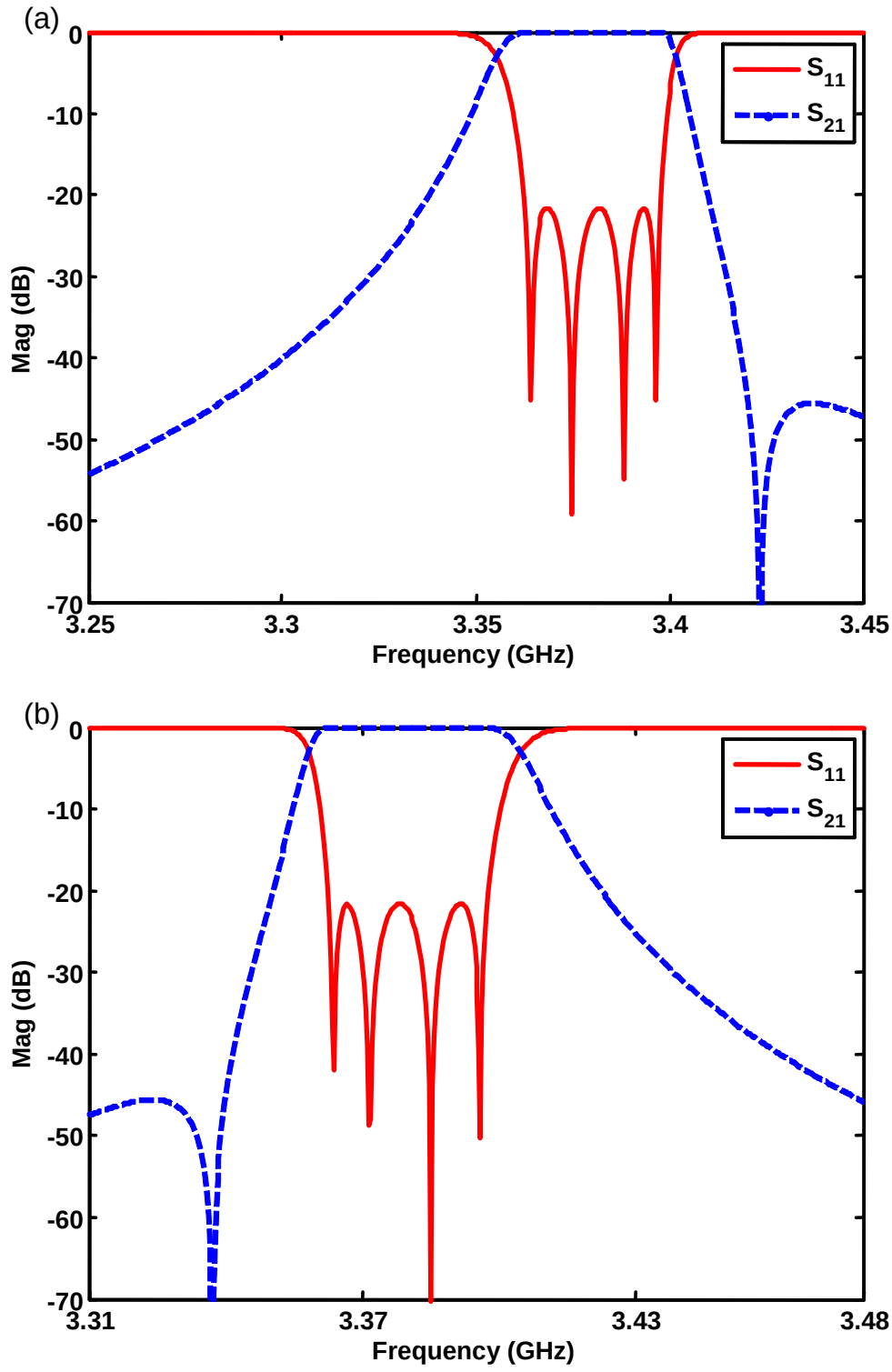

Figure 3.50: Ideal response of a 4-pole-1-zero asymmetric quasi-elliptic filter. (a) Transmission zero within the upper stopband. (b) Transmission zero within the lower stopband.

band.). The coupling matrices of the $4th$-order longitudinal topology as in Fig. 3.49(c) for these two solutions are given as

$$M_U = \begin{bmatrix} 0.0402 & 0.7673 & -0.5590 & 0 \\ 0.7673 & 0.5662 & 0 & 0.7673 \\ -0.5590 & 0 & -0.8582 & 0.5590 \\ 0 & 0.7673 & 0.5590 & 0.0402 \end{bmatrix}$$

$$M_L = \begin{bmatrix} -0.0402 & 0.7673 & -0.5590 & 0 \\ 0.7673 & -0.5662 & 0 & 0.7673 \\ -0.5590 & 0 & 0.8582 & 0.5590 \\ 0 & 0.7673 & 0.5590 & -0.0402 \end{bmatrix}$$

$$R_{in} = R_{out} = 1.1496 \tag{3.25}$$

where M_U is the solution for the filter with a zero within the upper stopband and M_L is for the filter with a zero within the lower stopband. The ideal frequency responses for these two cases are shown in Fig. 3.50(a) and (b), respectively. The location of transmission zero is only determined by the frequency offsets of the resonators, in other words, the signs of the self-coupling term M_{ii} in the coupling matrix. When the signs of all M_{ii} are changed to the opposite ones, the transmission zero will move to the opposite side of the stopband. The relationship between M_{ii} and the frequency offsets of resonators for narrow bandwidth filter is approximately given by

$$f_i \approx f_0 - \frac{1}{2} M_{ii} \cdot BW \tag{3.26}$$

where f_i is the shifted resonant frequency of each resonator. f_0 is the center frequency of the filter. M_{ii} is the normalized self-coupling coefficient. BW is the bandwidth of the filter. In practice, asymmetric quasi-elliptic filters are mostly used in the front end of the transmitter/receiver diplexers in base stations. The transmission zeros are, therefore, placed between the adjacent channels to obtain the high rejection to prevent the interference.

3.5.3 Physical Implementation

Dual-mode circular waveguide cavities operating with dual TE_{111} resonant modes are used to realize the synthesized ideal longitudinal network. The diagram of the implementation structure is shown in Fig. 3.51(a). The manufactured parts are shown in Fig. 3.51(b) and the assembled filter hardware is shown in Fig. 3.51(c). The external input and output couplings (R_{in} and R_{out}) are provided by the probes of SMA connectors. The two SMA connectors are positioned perpendicular to each other to excite the two polarizations of the TE_{111} resonant mode. Resonant frequencies (f_i) and cross couplings (M_{ij}, $i \neq j$) are adjusted by tuning screws, coupling screws and coupling iris as shown in Fig. 3.51(a) and (b). The tuning screws must be aligned with either of the SMA probes to modify the resonant frequency f_i, while the coupling screws must be placed at the position of 45 degrees from the tuning screws and the SMA probes to introduce the cross coupling between two orthogonal polarizations. In order to produce two cross couplings with different signs, the two coupling screws inside two consecutive cavities must

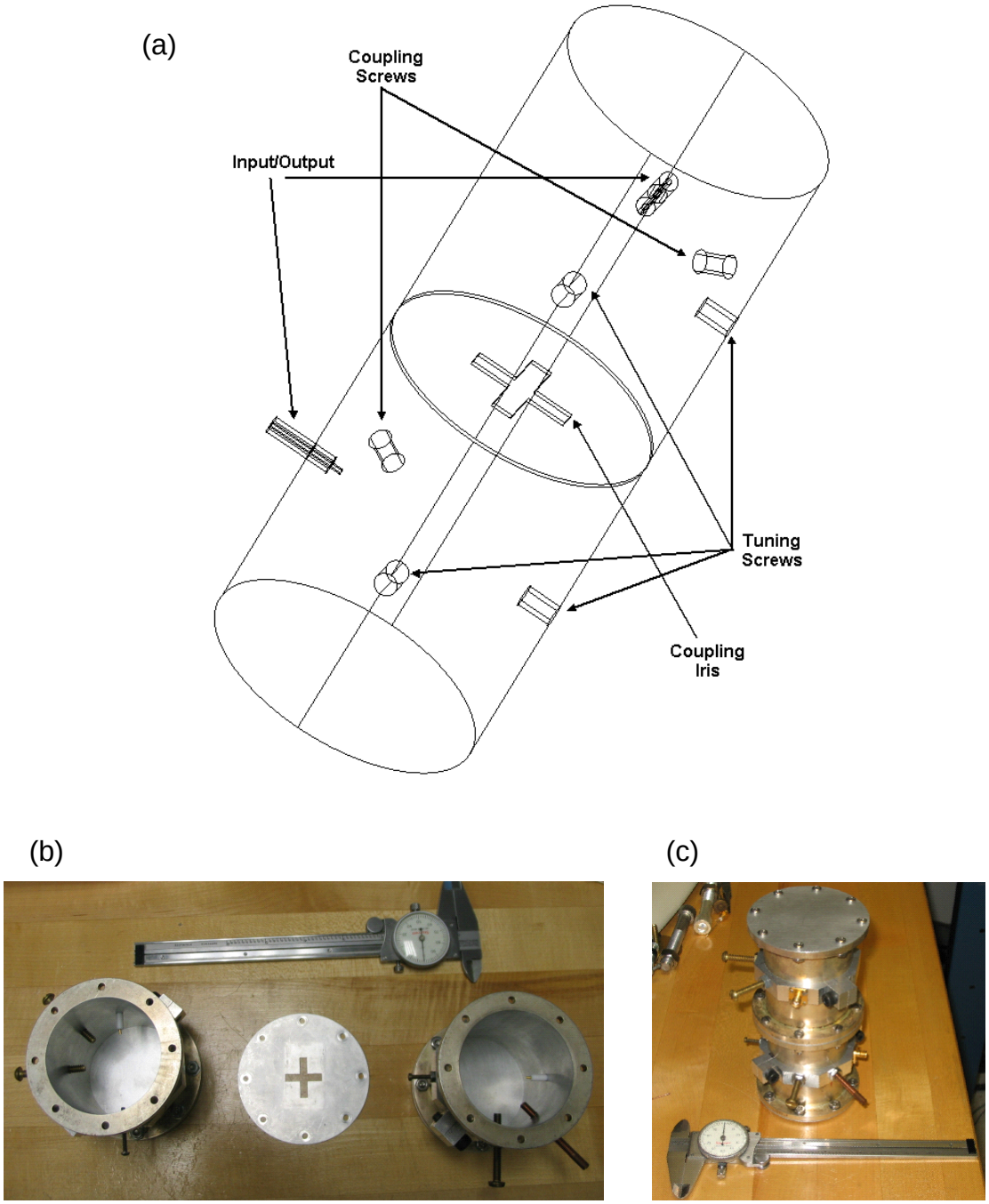

Figure 3.51: (a) The implementation structure for the $4th$-order longitudinal topology in dual-mode circular waveguide cavities. (b) The separated parts of the manufactured filter. (c) The assembled filter hardware.

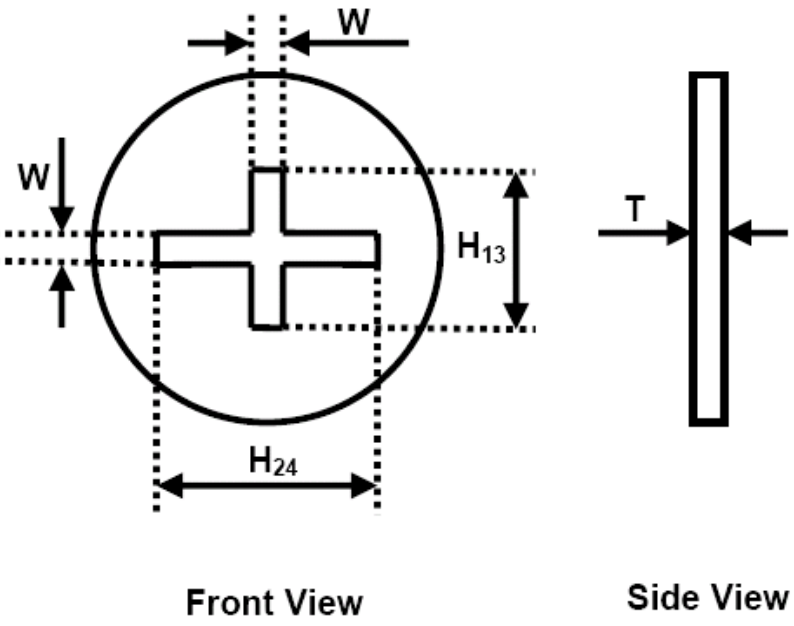

Figure 3.52: Front view and side view of the coupling iris.

be 180 degrees from each other in the ϕ-direction. The input/output SMA probes and all screws are positioned in the middle planes of the cavities where the electric field is maximum for TE_{111} resonant mode.

Two circular waveguide cavities with identical length are utilized to simplify the design because the resonant frequency of each resonant node can be achieved by adjusting the tuning screws. Two sets of dimensions need to be determined first for the manufacturing. One set is the cavity size: diameter and length. The other set is the size of the coupling iris (as shown in Fig. 3.52): thickness (T), width (W) and heights (H_{13}, H_{24}).

The filter is centered at 3.38 GHz. The four resonant frequencies which can be approximately calculated by (3.26) are slightly different from 3.38 GHz. Considering the effects of tuning screws and coupling screws on the cavity resonant

frequency, the cavity size should be chosen to have a higher TE_{111} resonant frequency than 3.38 GHz. The cavity size is finally selected to have a diameter of 2.4 inch and a length of 3.08 inch, which has a TE_{111} resonant frequency at about 3.46 GHz.

The dimensions of the coupling iris can be approximately decided by modeling the slot coupling structure between two identical cavities without considering the effects from the screws. Either MMM or FEM in HFSS is suitable for analyzing such structure. The iris thickness T and the identical width W of the two slots are chosen to be fixed ($T = 0.032$", $W = 0.1875$"). The height of each slot is then swept to search for H_{13} and H_{24} to have the coupling values of M_{13} and M_{24} (Assuming resonant node 1 and 2 are realized by one physical cavity, and node 3 and 4 are realized by the other cavity), respectively. The calculation method for the coupling values between two identical cavities is following the same way as before, i.e. using the two resonant frequency points f_e and f_m corresponding to PEW and PMW at the symmetric plane, respectively. The determined dimensions for H_{13} and H_{24} are 0.905" and 1.0", respectively.

3.5.4 Measurement Results

The manufactured filter hardware is shown in Fig. 3.51(b) and (c). A systematic tuning procedure is employed to find the optimum positions of all the screws. Each dual-mode cavity is tuned separately based on the phase response of S_{11} of the one-port network. The external input/output couplings and the resonant

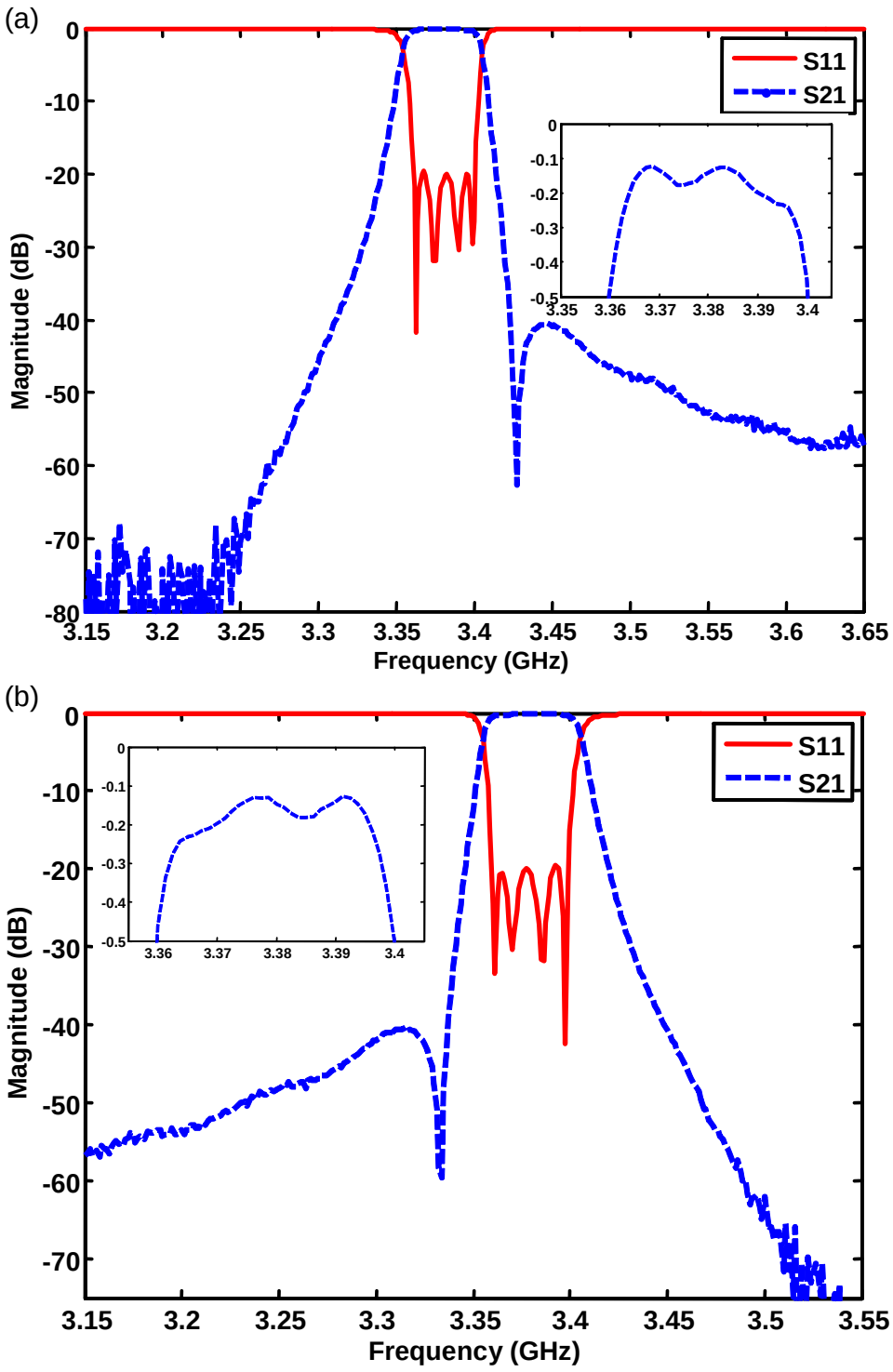

Figure 3.53: Measured filter responses of dual-mode circular wavguide filter. (a) Transmission zero within the upper stopband. (b) Transmission zero within the lower stopband.

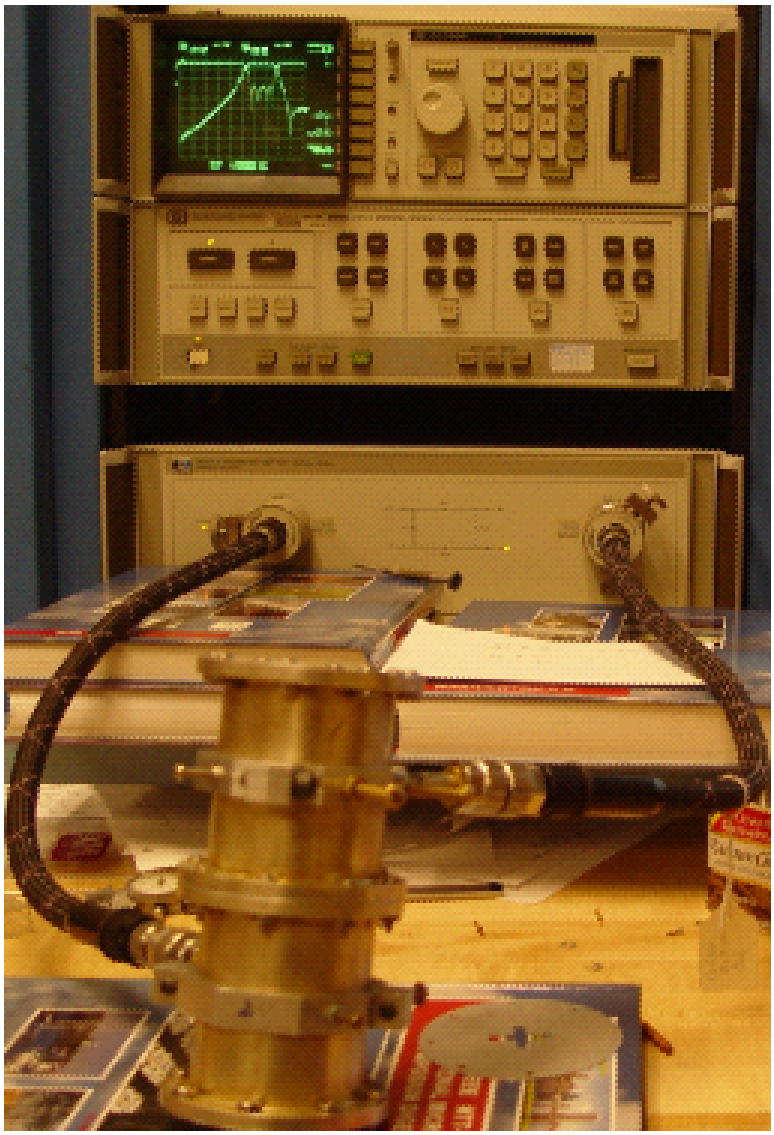

Figure 3.54: Photograph of the dual-mode circular waveguide cavity filter on the test bench.

frequencies f_1 and f_4 are achieved simultaneously first by tuning the lengths of the SMA probes inside the cavities. The cross couplings M_{12} (M_{34}) and the resonant frequencies f_1 and f_2 (f_3 and f_4) are then tuned based on the measured phase response of S_{11}, which is actually a parameter extraction procedure. The whole filter is then assembled to do the fine tuning until all the specifications have been

satisfied. The measured final filter responses are shown in Fig. 3.53(a) and (b) for the two different solutions with different transmission zero locations, respectively. The arrangement of the filter measurement is shown in Fig. 3.54 for one solution.

For higher order asymmetric quasi-elliptic filters, the tuning procedure will be much more difficult than the above presented one. The parameter extraction method based on optimization and the aforementioned space mapping method can then be employed to guide the tuning.

3.6 Dual-mode Quasi-Elliptic Filters in Rectangular Waveguides

3.6.1 Introduction

Dual-mode quasi-elliptic function filters are widely used in high-quality microwave filters and multiplexers due to their higher selectivity, smaller size and less mass than single mode coupled resonator filters [123, 161, 162, 165, 166]. The conventional approaches, e.g. dual-mode circular waveguide filter in previous section, to couple dual modes is by adding a coupling screw at 45° angle from the direction of the electric fields of the two dual modes. By changing the penetration of the coupling screw in the cavity, the coupling between the two dual modes can be adjusted. Although the tuning and coupling screws provide flexibility for optimizing the filter response, the tuning process is time consuming and makes the production of dual-mode filters expensive. Another drawback is that the power

handling capability of the filter is reduced due to the sharpness of the coupling and tuning screws. In order to avoid these aforementioned drawbacks, the screws must be completely removed from dual-mode filters and a precise and efficient design technique should be used to eliminate experimental tuning procedure.

With the progress in numerical techniques, researchers have been designing dual-mode filters in rectangular waveguide structures without any tuning requirement. For example, a section of evanescent-mode waveguide has been employed in [167] to replace the cross-shape coupling iris between the dual-mode pairs of the cavities. A waveguide with square-corner-cut is used to provide the dual-mode coupling in [159] and [168] instead of using coupling screws. All the structures can be rigorously analyzed in MMM, and thus, precise design of dual-mode quasi-elliptic filters using these coupling mechanisms are feasible.

However, the corner-cut structure in [159] and [168] requires long computation time due to the eigenmode searching procedure in MMM. If the dimensions of the corner-cut cross section are modified, the eigenmodes must be numerically calculated again in MMM, which will add excessive computation time. Besides, the power handling capability is still affected by the corner-cut structure in cavity. In this section, a new configuration for providing the cross coupling between the dual modes is proposed. Basically, an offset smaller waveguide is sandwiched inside the dual-mode square waveguide cavity, which will break the symmetry of the structure, as well as the orthogonality of the dual modes, to introduce couplings between the dual modes. To illustrate the application of the new coupling mechanism, a 4-pole-2-zero dual-mode rectangular waveguide cavity filter is de-

signed in MMM. The same design procedure can also be used to design higher order dual-mode filters.

3.6.2 Filter Configuration

Fig. 3.55(a) is the physical configuration of the dual-mode rectangular waveguide quasi-elliptic filters which can be used to implement the topologies shown in Fig. 3.49(b) and (c). The structure can be manufactured either in air-filled metallic form or in LTCC technology.

The input and output ports are standard rectangular waveguides, while the cavities are realized by square waveguides to support TE_{01} and TE_{10} degenerate modes. The external coupling is provided by the evanescent-mode iris between the port waveguide and the cavity. The input port waveguide only supports a single propagating mode (either TE_{10} or TE_{01}, depending on the placement of the waveguide) in the frequency range of interest, which will, therefore, only excite one polarization in the cavity. The output port waveguide excites either the same polarization (as shown in Fig. 3.55(a)) or the orthogonal dual mode depending on the filter order and filter topology as shown in Fig. 3.49(b) and (c).

In order to introduce the cross couplings between the dual modes in one cavity, a smaller waveguide is added into the middle of the cavity as shown in Fig. 3.55(b). The center of this small waveguide is offset from the center of the square waveguide for the cavity, thus, the double symmetry of the cavity is perturbed and a coupling will be generated between the two originally orthogo-

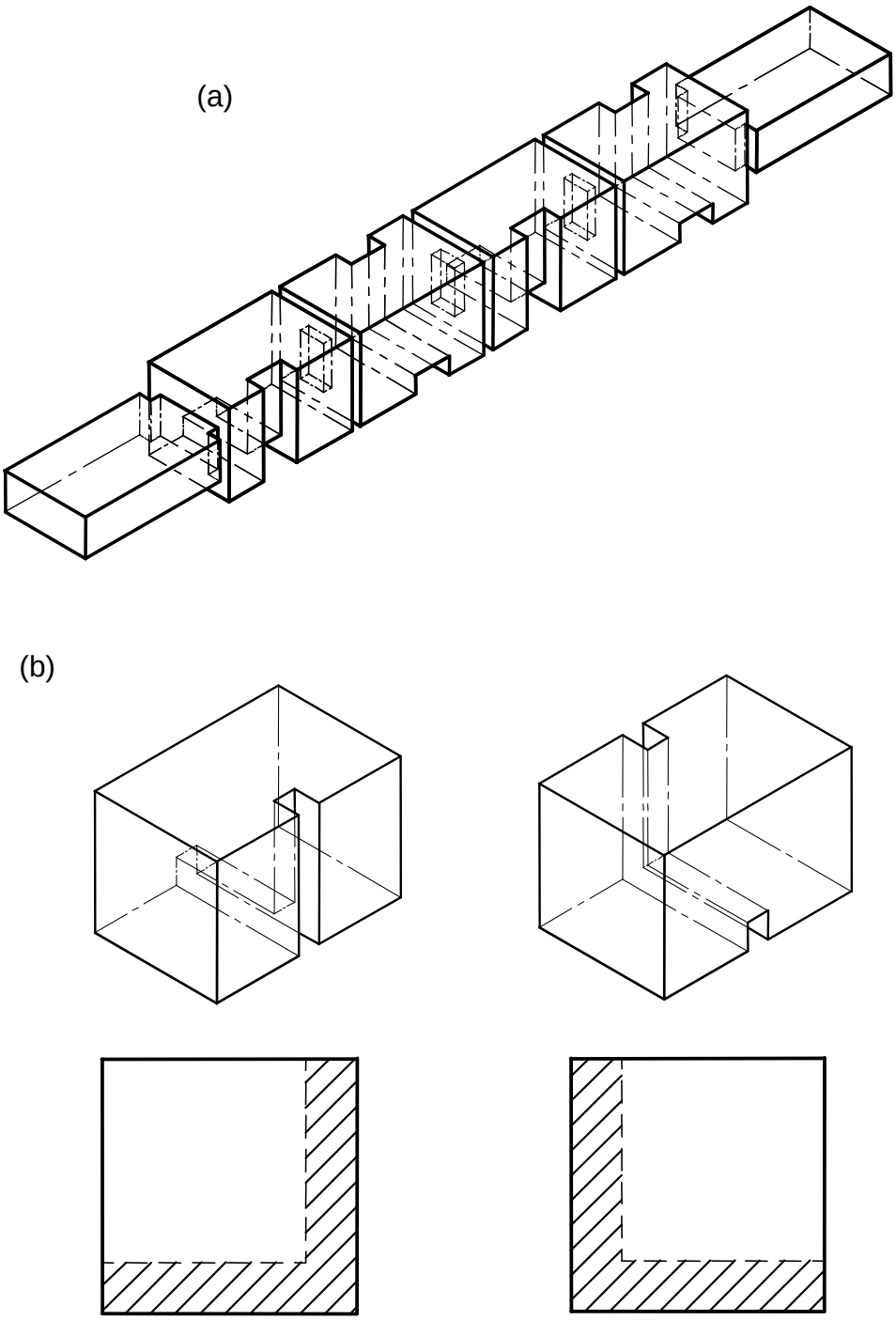

Figure 3.55: (a) Physical configuration of a rectangular waveguide quasi-elliptic function dual-mode filter. (b) Cross coupling mechanism between the dual modes.

nal dual modes. For symmetric quasi-elliptic function filters, all the resonators are synchronized at the center frequency, so this small waveguide will also be a square waveguide to have the same effect on the two polarizations. For asymmetric quasi-elliptic function filters, this small waveguide is usually not square to provide the different effects on the two polarizations because the resonators are not synchronized any more. The coupling values between the dual modes in one cavity can be controlled by adjusting the cross section and the length of the small waveguide, which dose not add excessive mode-searching computation time and provides flexibility in dual-mode coupling design. In quasi-elliptic filter designs, couplings with different signs are usually required. The small waveguides can be placed in opposite positions with respect to the square cavity (as shown in Fig. 3.49(b)) to provide cross couplings with different signs because the effects on the field distribution will introduce an equivalent 180° phase difference. The resonant frequencies of the dual resonant modes in one cavity are affected by the loading due to the coupling of the small waveguide and the lengths of the two separated square waveguides. Hence, it is very flexible to control the self-couplings and the cross-coupling in one cavity, which is especially important for asymmetric filter designs.

Evanescent-mode waveguides (i.e. the rectangular irises between cavities in Fig. 3.55(a)) are used to provide inter-couplings between dual-mode adjacent cavities. This structure has advantages compared to the cross-shape iris: i) Mode-searching procedure in MMM is avoided. ii) The numerical solution in MMM converges much faster because fewer modes are required. iii) The coupling is

much less sensitive to the dimensional tolerances. The coupling values can be controlled by adjusting the dimensions of the cross section and the thickness of the iris.

3.6.3 Filter Design Procedure

A. Design Parameters

The number of poles and transmission zeros is determined according to the given specifications. The coupling matrix is then synthesized for a chosen topology as in Fig. 3.49. The external coupling values and inter-coupling values are transformed to the equivalent impedance inverters using (3.21) which will be used later to decide the initial dimensions of the irises.

B. Design of Cavity and Irises

The dimensions (widths and heights) of the waveguides and cavities should be chosen first according to the frequency range of the filter. Usually, a standard waveguide is selected for the input and output ports, and the cross section of the square waveguide cavity is chosen equal to the width of the standard waveguide. In order to decide the dimensions (width, height and thickness) of input/output irises and the inter-cavity coupling irises, the scattering parameters obtained from MMM solution can be related to the impedance inverters by (3.6). The effect of the small waveguide in each cavity is neglected in this step.

C. Dual-mode Coupling Design

The small waveguide in each cavity causes the two degenerate orthogonal

modes to be split into two interacting resonant modes with two different resonant frequencies. An eigenmode solver in MMM can be used to obtain these two split frequencies. The coupling coefficient is simply given as

$$k = \frac{f_H^2 - f_L^2}{f_H^2 + f_L^2} \tag{3.27}$$

where f_H and f_L are the higher and lower frequency of the split degenerate resonant frequencies, respectively. This coupling equation is essentially same as (3.4).

D. Computer-aided Tuning and Optimization

The above design procedure neglects the effects of the coupling irises on the dual-mode cross couplings and the frequency dispersion of the junctions. To eliminate the degradations of the filter response due to these effects, computer-aided tuning or optimization should be applied to fine-adjust the filter dimensions. The computer-aided tuning is based on the parameter extraction procedure, which can usually be used for a low-order filter since only a few design parameters are involved. For high-order filters, the optimization procedure in MMM is employed since MMM is very efficient in solving such structures as in Fig. 3.55(a).

The MMM analysis only deals with step discontinuities between rectangular waveguides. The detailed formulations can be found in many textbooks [3, 10], and are not listed here. The filter structure does not have any symmetry, which means that all the eigenmodes should be used in the MMM analysis. A high number of modes might be needed to ensure the convergence of the solution, which may degrade the efficiency of MMM. An approximate solution based on curve fitting [169] or simple interpolation of the numerical solution can significantly reduce the

computation time and still yield very accurate results.

3.6.4 Design Example

A four-pole symmetric quasi-elliptic dual-mode filter is designed to demonstrate the feasibility. The center frequency of the filter is 8.5 GHz and the fractional bandwidth is 2% (170 MHz). The normalized coupling matrix and external coupling are given as

$$M = \begin{bmatrix} 0 & 1.0468 & 0 & -0.1364 \\ 1.0468 & 0 & 0.8380 & 0 \\ 0 & 0.8380 & 0 & 1.0468 \\ -0.1364 & 0 & 1.0468 & 0 \end{bmatrix}$$
$$R = 1.3764 \tag{3.28}$$

The input and output waveguide is chosen to be WR90 ($a \times b = 0.9 \times 0.4$ inch), and the width and height of the cavity waveguide are chosen to be $a \times a = 0.9 \times 0.9$ inch. In order to determine the dimensions of the input and output irises, the two-port network structure as shown in Fig. 3.56(a) is analyzed in MMM. The scattering parameter between the two discontinuities can be related to the impedance inverter by (3.6). Three dimensions of the iris can be modified to obtain the desired impedance inverter: width, height and thickness. To simplify the problem, the height of the iris is taken identical as WR90, i.e. $b = 0.4\ inch$. The thickness of the iris is fixed at $tio = 0.1\ inch$. The width of iris aio is swept to calculate the inverter values. The obtained coupling curves are shown in Fig. 3.56(b): the upper one is inverter values versus aio, and the lower ones are the

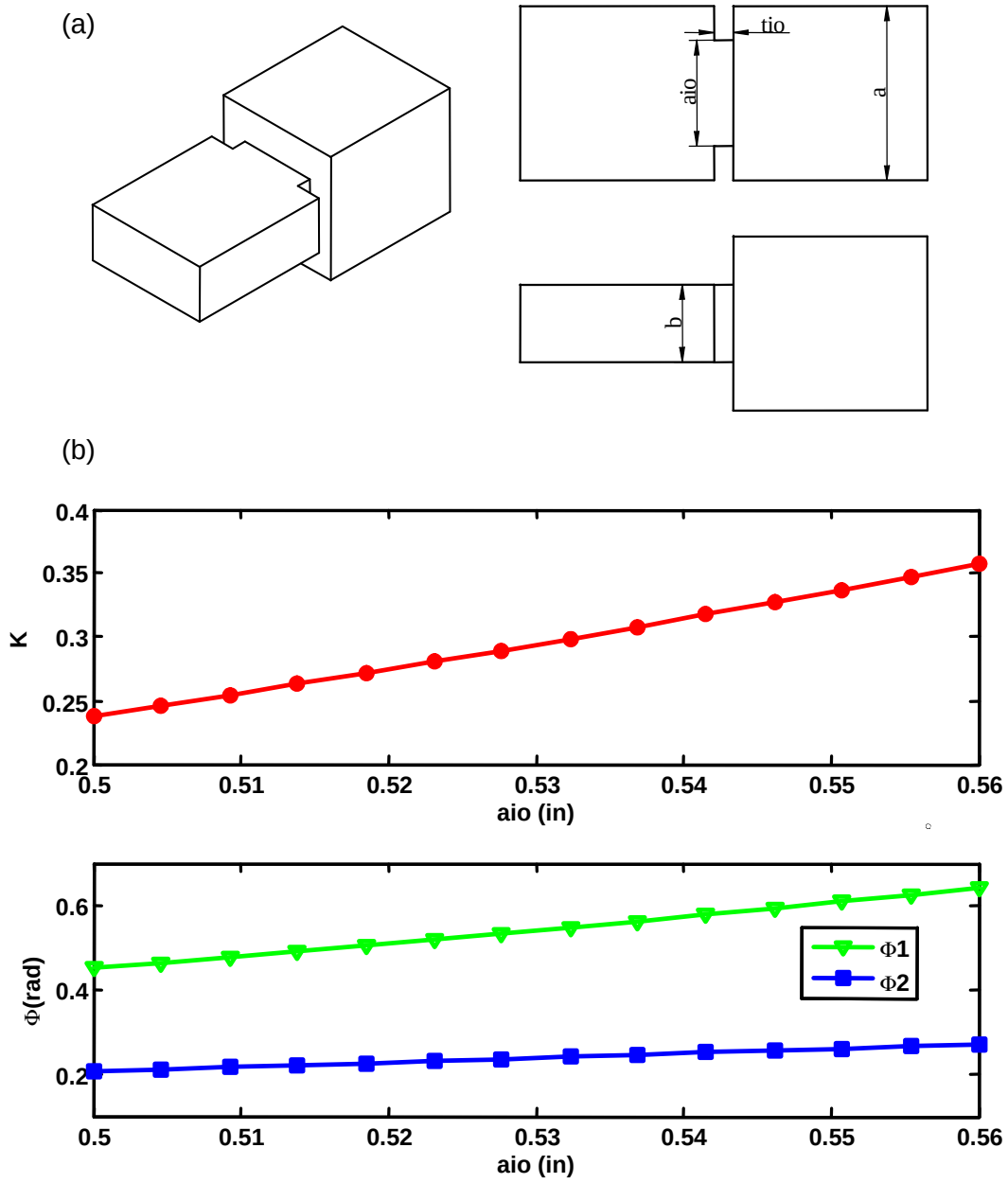

Figure 3.56: External coupling structure and calculated coupling curve. (a) Coupling structure and dimensions. (b) Coupling curves: k vs width of iris, and phase offsets vs width of iris.

phase offsets versus *aio*. The phase offsets are used later to adjust the cavity length. The value of *aio* is decided to be 0.546 *inch* by interpolation to have a desired inverter value 0.3270.

Two inter-coupling values M_{14} (or k_{14}) and M_{23} (or k_{23}) between the cavities are provided simultaneously by the evanescent-mode iris. The scattering parameters of the structure in Fig. 3.57(a) are calculated by MMM, and then related to the inverter values. Two sets of scattering parameters need to solve: one is corresponding to TE_{10} (H_{10}) mode, and the other one is corresponding to TE_{01} (H_{01}) mode. Therefore, the two inverter values k_{14} and k_{23} can be computed accordingly. There are three variables (width *air*, height *bir*, and thickness *tir*) to be determined for an iris to realize the coupling pairs. If one variable is chosen, the other two can be uniquely determined. Usually, the thickness of the iris is fixed because the width and height of the iris will each mainly affect one coupling value. In this case, the thickness is fixed at $tir = 0.1$ *inch*. The width *air* and height *bir* can be swept to calculate the inverter values k_{14} and k_{23}. The obtained curves are shown in Fig. 3.57(b). The values of *air* and *bir* are found to be 0.26 *inch* and 0.46 *inch*, respectively, to have the desired values of $k_{14} = 0.0163$ (corresponds to H_{10} mode) and $k_{23} = 0.1003$ (corresponds to H_{01} mode). A simple optimization procedure can also be used to find the values of *air* and *bir* to yield the required couplings for a given thickness. The objective function is constructed as

$$err = (k_{14}^c - k_{14}^d)^2 + (k_{23}^c - k_{23}^d)^2 \tag{3.29}$$

where (k_{14}^c, k_{23}^c) are the computed couplings and (k_{14}^d, k_{23}^d) are the desired ones.

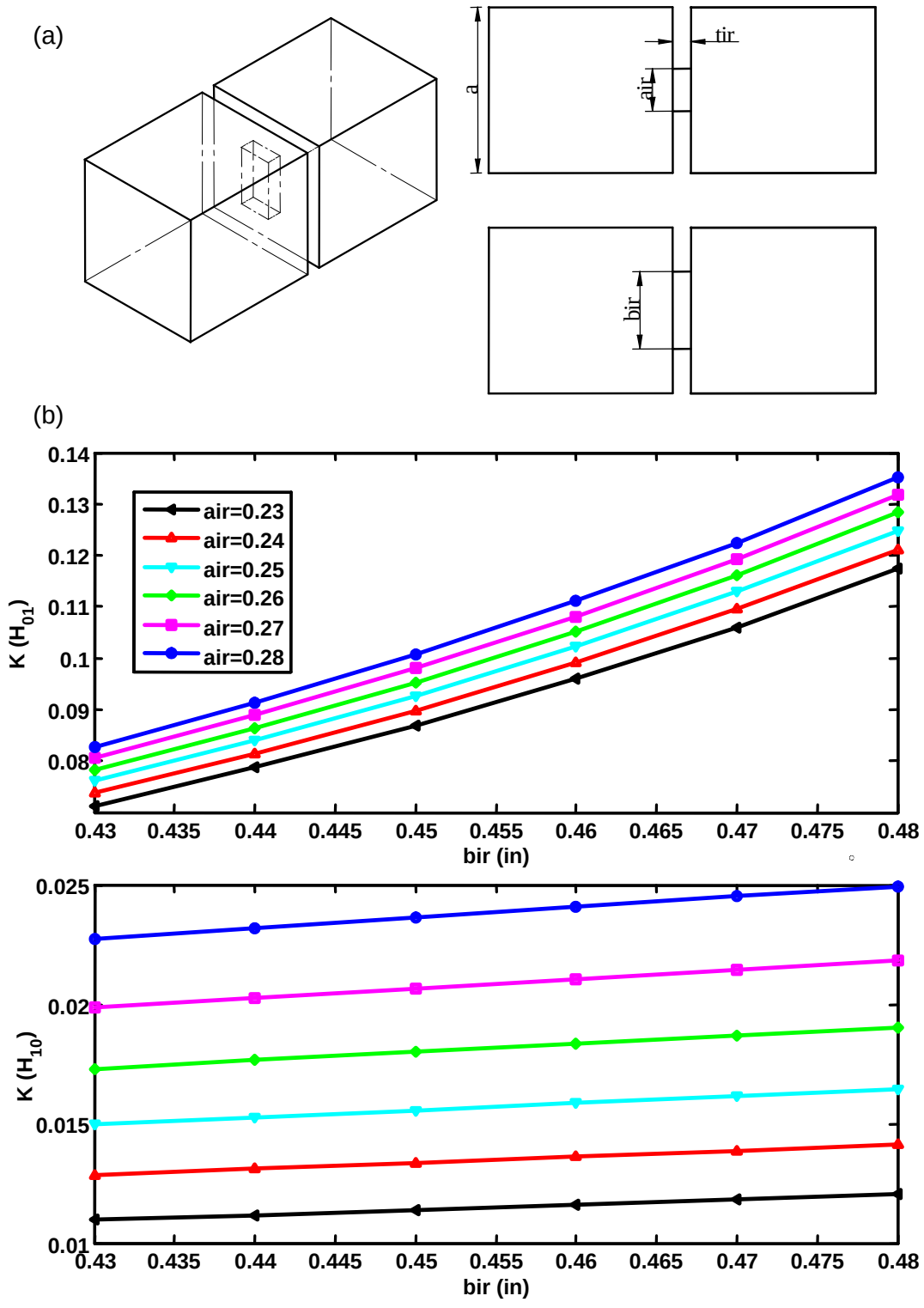

Figure 3.57: (a) Inter-coupling structure and dimensions. (b) Inter-coupling curves: inverter values vs cross sections of iris.

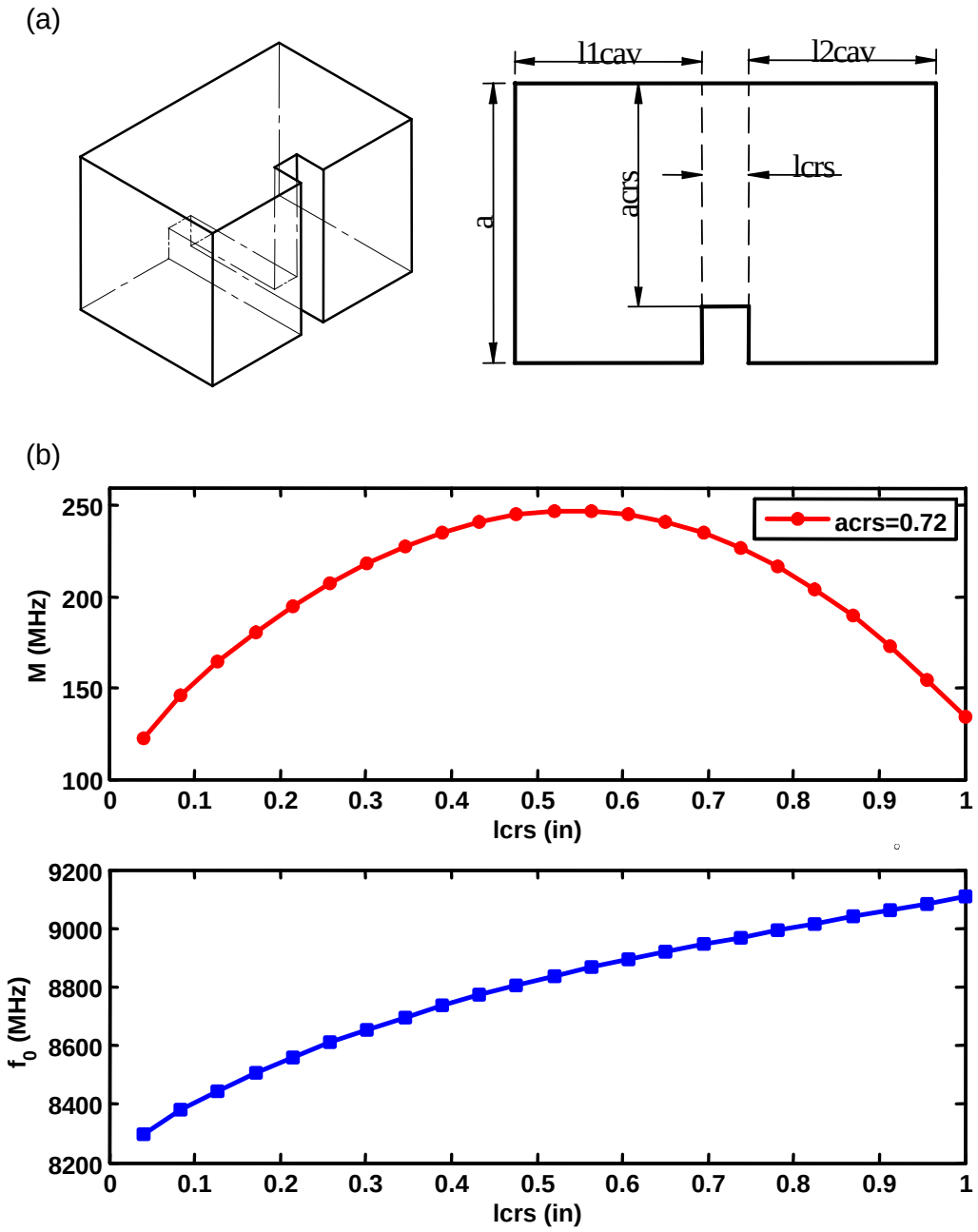

Figure 3.58: Cross coupling structure for dual-mode waveguide filter and the calculated coupling curves. (a) Coupling structure and dimensions. (b) Coupling curves: coupling value M and loaded frequency f_0 vs length of small waveguide $lcrs$.

Table 3.6: Final dimensions of the quasi-elliptic dual-mode filter as shown in Fig. 3.59. All the dimensions are given in inch.

Name	**Value**	**Name**	**Value**	**Name**	**Value**	**Name**	**Value**
a	0.9	b	0.4	aio	0.64	tio	0.107
$l1cav$	0.383	$lcrs$	0.372	$l2cav$	0.621	$acrs$	0.72
air	0.26	bir	0.47	tir	0.091		

The cross section of the small waveguide inside the cavity for the cross coupling is square since the filter is symmetric and resonators are synchronized at the center frequency of the filter. The coupling structure is shown in Fig. 3.58(a). The split degenerate modes are computed by an eigenmode solver using MMM. The coupling value is then obtained by (3.27). The width $acrs$ and length $lcrs$ of the small waveguide can be adjusted to produce the desired coupling value. To simplify the problem, the width $acrs$ is fixed at 0.72 $inch$, and the length $lcrs$ is swept to compute the coupling value. The total length of the cavity ($l1cav + lcrs + l2cav$) is also fixed at 1.35 $inch$ in this step. The calculated coupling curves are shown in Fig. 3.27(b). It can be seen that there is a maximum achievable dual-mode cross coupling for a length of small waveguide about 40% of the total cavity length. In order to have a desired coupling value of 178 MHz, the length of the small waveguide is found to be $lcrs = 0.17$ $inch$ by interpolation.

Shown in Fig. 3.59(a) is the filter response with the initial dimensions determined by the above procedure. The two transmission zeros are clearly generated.

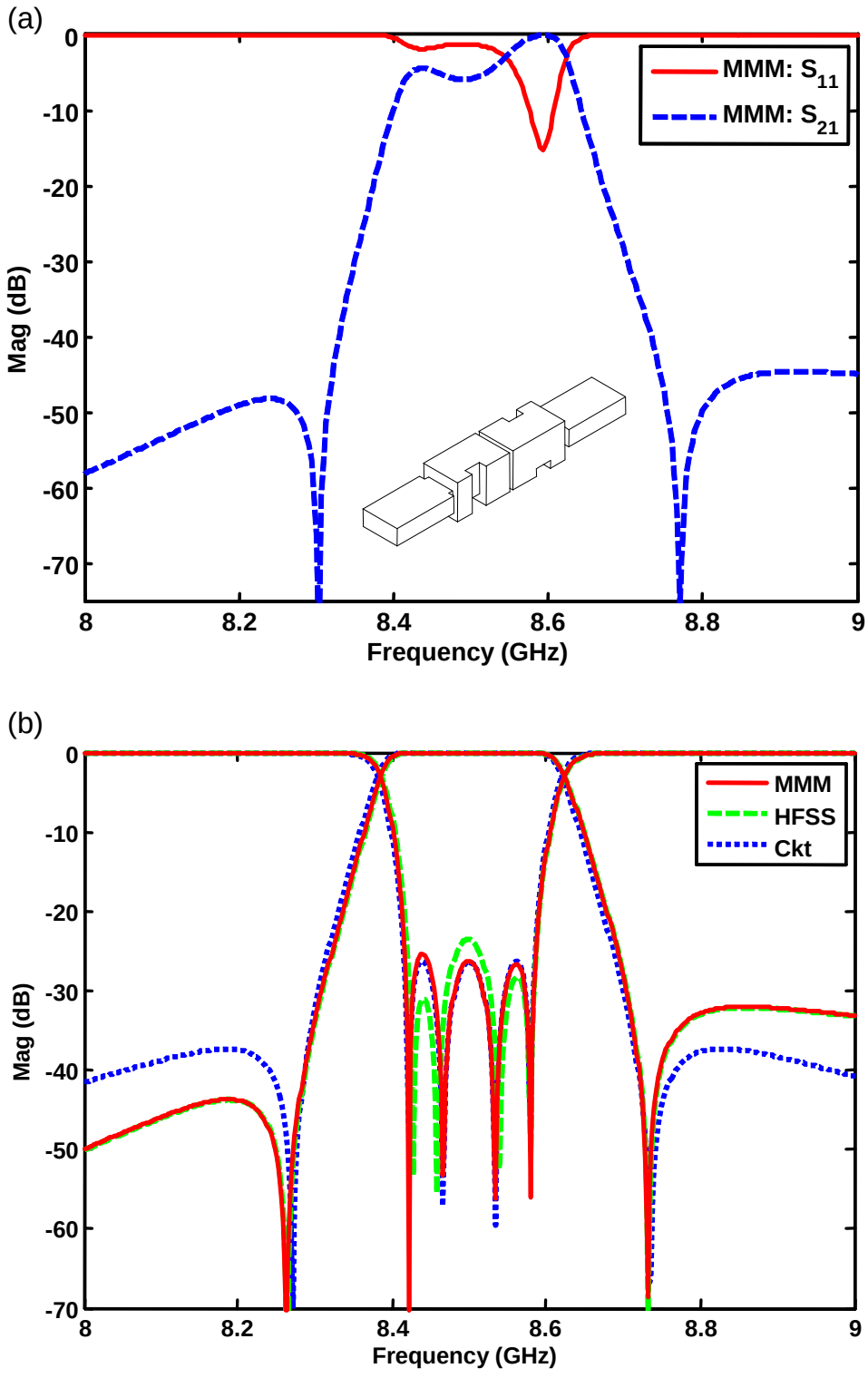

Figure 3.59: (a) Frequency response of the filter with initial dimensions. (b) Frequency responses of the ideal circuit model and the final filter structure in MMM and HFSS.

The center frequency and bandwidth are also very close to what is required. An optimization procedure in MMM is then applied to improve the filter performance. The frequency response of the final filter design is shown in Fig. 3.59(b) in MMM and HFSS. The response of the ideal circuit model is also shown in the figure. A very good agreement between them can be noticed. The final dimensions of the filter structure is shown in Table 3.6.

3.7 Systematic Tuning of Quasi-Elliptic Filters

3.7.1 Introduction

Quasi-elliptic function filters have wide applications in communication systems. They have important roles in the front end of the transmitter/receiver diplexers in wireless base stations because the high rejection of the filters is needed to prevent the interference between adjacent channels. The filter technologies that are currently being used in wireless base stations can be separated into two main categories: coaxial TEM cavity resonator filters [56, 57] and dielectric resonator (DR) filters [125, 170–176]. Even though coaxial TEM cavity filters have limited quality factor values, they offer the lowest cost design, wide tuning range, and excellent spurious-free performance, and are still being widely employed, particularly in wide bandwidth applications [58]. With increased demands for high performance wireless systems, dielectric resonator filters are emerging for wireless base stations because they have very low loss and high-temperature stability. However, the di-

electric resonator filters have higher cost than the coaxial TEM cavity filters and very poor spurious performance.

Quasi-elliptic filters using the above-mentioned two technologies usually require post-production adjustment procedure to obtain the desired filter response since a complete CAD of such filters based on numerical methods is not practical with available CAD tools. The post-production adjustment consists of two aspects: diagnosis and tuning. Diagnosis is to detect the components that are out of the tuning range of the tuning screws in a manufactured filter, e.g. one coupling value or one cavity frequency can not be achieved by adjusting the tuning screws. Usually, these failed components must be re-manufactured or replaced. Such faults typically originate from errors in the assembly, manufacturing, or even in the design. Tuning is to adjust and improve the filter response by means of the tuning screws, which often requires a skilled technician. Actually, the fault diagnosis and tuning are closely related problems. The diagnosis and tuning of multiple-coupled resonator quasi-elliptic filters are time-consuming and expensive. They can be very troublesome without the support of the computer. Therefore, the development of efficient algorithms for the computer aided diagnosis and tuning becomes an essential objective in order to improve the design efficiency and reduce the cost.

Many computer aided tuning methods have been published in the literature. Some of the algorithms are based on the optimization to extract the parameters of the coupling matrix [122, 177]. Such algorithms rely on pre-tuned filters whose frequency response is sufficiently close to the desired response. The possibility

to stuck in a local minimum and fail to converge to the desired coupling matrix is reduced. Some algorithms depend on the sensitivity analysis [178, 179]. A nearly linear relationship between the filter response and the depth of the tuning screws is employed. However, in practice, this linear dependence is restricted to small tuning ranges. Some other algorithms employing shorted circuit models do not estimate the filter parameters [180, 181], which make the fault diagnosis very difficult. Even though all the algorithms are based on a pre-tuned filter, they do not offer a diagnosis and tuning procedure to obtain a pre-tuned filter from an initially detuned filter after manufacturing and assembling.

In this section, a systematic tuning procedure of quasi-elliptic filters is discussed, which covers the whole process of developing a quasi-elliptic filter from scratch. The tuning procedure is especially useful for filters in coaxial TEM cavities and dielectric resonators since the full-wave CAD of such filters are not available nowadays. Filters in other technologies, e.g. waveguide and planar structures, can also be tuned on bench or in a numerical simulator based on a similar procedure. An example of an eight-pole asymmetric dielectric resonator filter is presented in this section to demonstrate the whole procedure.

3.7.2 Tuning Procedure

The systematic tuning procedure presented below was proven to be very efficient for the class of quasi-elliptic filters using the technologies of coaxial TEM cavities and dielectric resonators. Moreover, the principle can also be applied to other

realizations, in general, to all tunable filters that can be modeled by a coupling matrix. The systematic tuning procedure can be divided into four steps that will be discussed next.

1. CAD of Cavity and Coupling Structures

This step is actually not a bench tuning process, but it is a very important step to decide the manufacturing dimensions of the initial filter structure for tuning. Given the specifications of a filter, a filter topology is selected considering the filter performance, the mechanical feasibility and the tuning sensitivity. The coupling matrix, which will be used for realization and tuning, is then synthesized for this chosen filter topology. In order to determine the mechanical dimensions of the physical filter structure, the filter requirements and the coupling matrix should be related to the mechanical structures by full-wave numerical methods. In this step, one should try to make sure that all the filter parameters can be achieved by adjusting the tuning screws, in other words, all the filter parameters are inside the tuning range. Otherwise, post manufacturing will be required to fix or replace some elements in the filter, which will delay the developing time and increase the cost.

The physical cavity dimensions are determined according to the center frequency of the filter and the desired unloaded Q factor. For coaxial TEM cavities, the length of the cylinder rod and the capacitance loading from the tuning screw affect the resonant frequency. The size of the metallic enclosure has the influence on the unloaded Q factor. For dielectric resonators, the resonant frequency is mainly affected by the size of the ceramic puck and the depth of the tuning

disc. The unloaded Q is related to the loss tangent of the dielectric material and the size of the metallic enclosure. An eigenmode solver in MMM or FEM can be used to design the cavity dimensions. MMM is preferred because of its high efficiency. The MMM algorithms for solving the two cavity structures can be found in [44, 45, 154]. The tuning screw or disc should also be considered in the eigenmode solver to check the tuning range, which is especially important for asymmetric filter designs. The size of the cavity enclosure can be enlarged to improve the Q factor, however, this improvement diminishes as the size is increased. Therefore, an optimum enclosure size should be determined according to the computed Q factor and the filter size constraint.

The dimensions of the coupling structures are determined based on the bandwidth of the filter and the desired coupling values. Two kinds of couplings are usually required in quasi-elliptic filters: positive and negative couplings. The field distributions of the employed resonant mode of a cavity structure should be investigated, and the coupling mechanisms for positive and negative signs are created accordingly. For coaxial TEM cavities, iris coupling structure is often used for positive or magnetic couplings, while probe structure is normally used for negative or electric couplings [182]. For dielectric resonators, the coupling structures depend on the employed resonant modes and the filter topologies [57]. MMM and FEM are mostly used to design the coupling structures for these two technologies. The equation for computing coupling values has been presented before (p. 67). The coupling screws should also be included in the numerical simulator, e.g. HFSS, to make sure that the tuning range is enough to obtain the desired coupling values.

2. Fault Diagnosis

Filters in their initial state after manufacturing and assembling are strongly detuned. In order to check whether all the self-coupling and mutual-coupling values can be achieved by adjusting the tuning screws (or discs), a diagnosis procedure should be employed. If one coupling value is found not be able to be realized, one or more physical elements in the filter will then need to be fixed or replaced. The diagnosis procedure is, therefore, called fault diagnosis.

Precise parameter extraction is required to guarantee the accuracy of the diagnosis procedure. In [183], Hsu et al presented a computer-aided diagnosis method of cascaded (or in-line) coupled resonator filters. Basically, the phase of the reflection coefficient of short-circuit terminated networks is used to extract the inter-resonator couplings and the resonant frequencies of the resonators. The extracted parameters are always unique for the in-line coupled resonator structures. In order to apply this diagnosis method to a quasi-elliptic filter structure, the topology of the quasi-elliptic filter can be separated into many in-line paths consisting of coupled cavities. The phase responses of these one-port networks are then measured, and the self- and mutual-coupling values can be extracted using the method in [183]. The tuning screws are adjusted according to the differences between the extracted parameters and the desired parameters in the pre-synthesized coupling matrix. The cavities in each path should be included and tuned one by one according to the calculated ideal phase response to improve the efficiency. Once one or more parameters can not be achieved by the tuning screws, the corresponding fault physical elements can be easily identified.

In some cases, the filter topology consists of not only in-line paths, but also triplet or quadruplet loop paths. Most of the couplings in one loop path can be diagnosed first by breaking the loop into many smaller in-line paths except one connecting coupling. The optimization procedure can then be used to extract the parameters of the whole loop path. Usually, the ideal phase response can be calculated, and loaded onto the monitor of the instrument as a tuning reference. Once the measured response is close to the ideal one, the convergence of the optimization procedure will be guaranteed.

In the diagnosis procedure, the resonators outside the path of interest must be detuned using the tuning screws, i.e. setting the resonant frequencies of the corresponding resonators to values outside of the frequency range under consideration. The detuned resonators can create virtual short-circuit terminations at the plane of the coupling irises or other coupling structures, which are necessary for the applicability of the diagnosis algorithm.

3. Tuning of Sub-filters

After the fault diagnosis procedure, all the mutual-couplings are tuned very close to the desired coupling values, and the tuning screws have enough tuning ranges. A sequential tuning procedure as in [121] can be applied to obtain a pre-tuned filter. Basically, the whole filter is tuned gradually through the sub-filters, i.e. beginning with all resonators being strongly detuned, one resonator after the other is tuned. Thus, for a filter of degree n, one gets a sequence of n sub-filters, the sub-filter i being characterized by $n - i$ tuned and i detuned resonators. Tuning at each step aims to minimize the deviation between the ideal

and actual sub-filter response or parameters.

Usually, tuning from two ports of the filter individually provides the possibility to tune a certain number of sub-filters using the input reflection coefficients S_{11} and the remaining sub-filters using the output reflection coefficients S_{22}. This increases the overall accuracy of the tuning procedure. Better performances are obtained by minimizing the number of additional resonators to be tuned from one port providing unperceptive variations on the phase response. These resonators are usually coupled to other resonators by means of very weak couplings. Therefore, a good criterion is tuning half a filter by means of S_{11} and the remaining sub-filters by means of S_{22}.

In practice, the ideal phase response of each sub-filter, which can be calculated using the pre-synthesized coupling matrix, can be used as a reference to guide the tuning and improve the efficiency. Usually, only the resonators need to be tuned in this step since the mutual-couplings are already very closely tuned. In very rare cases, if one desired sub-filter response can not be obtained by any means, a parameter extraction method can then be applied to determine the parameters of the corresponding tuned part of the sub-filter, which is actually a second diagnosis procedure. The parameter extraction of the sub-filters is based on the optimization procedure. The optimized parameters must be constrained inside a small variations from the desired values, which assures that the converged parameter values are the correct solutions.

The frequency response of the final sub-filter, i.e. the whole filter, using the sequential tuning procedure is sufficiently close to the desired response. For

filters of moderate degree and complexity, an additional fine tuning procedure even becomes unnecessary. For high degree ($\geq$ 8) filters with highly complex topologies, the response is usually good enough for one to use the available fine tuning techniques.

4. Fine Tuning

The pre-tuned filter after step 3 may require fine tuning procedure to improve the performance. Usually, a skilled technician can easily finish the fine tuning if the pre-tuned filter response is very close to the desired response. In some cases, the filter responses might be very sensitive to the parameters or the tuning screws. Some fine tuning techniques based on parameter extraction or space mapping can then be employed to guide the tuning.

3.7.3 Filter Tuning Example

A quasi-elliptic eight-pole bandpass filter realized by single $TE_{10\delta}$ mode of dielectric resonators with two finite transmission zeros in the left stopband is designed and tuned to demonstrate the tuning procedure. The filter possesses a center frequency of 868.1 MHz and a fractional bandwidth of 0.86% (7.5 MHz). The ideal filter response is shown in Fig. 3.60, and a Cul-De-Sac topology (as the inset of Fig. 3.60) is synthesized. The equal ripple frequency point for the left stopband is at 863.95 MHz. The unloaded Q value used in the circuit model to estimate the loss is taken as 20000 that is a typical value of the employed dielectric resonators. This filter is used as the transmit filter in a transceiver diplexer for wireless base

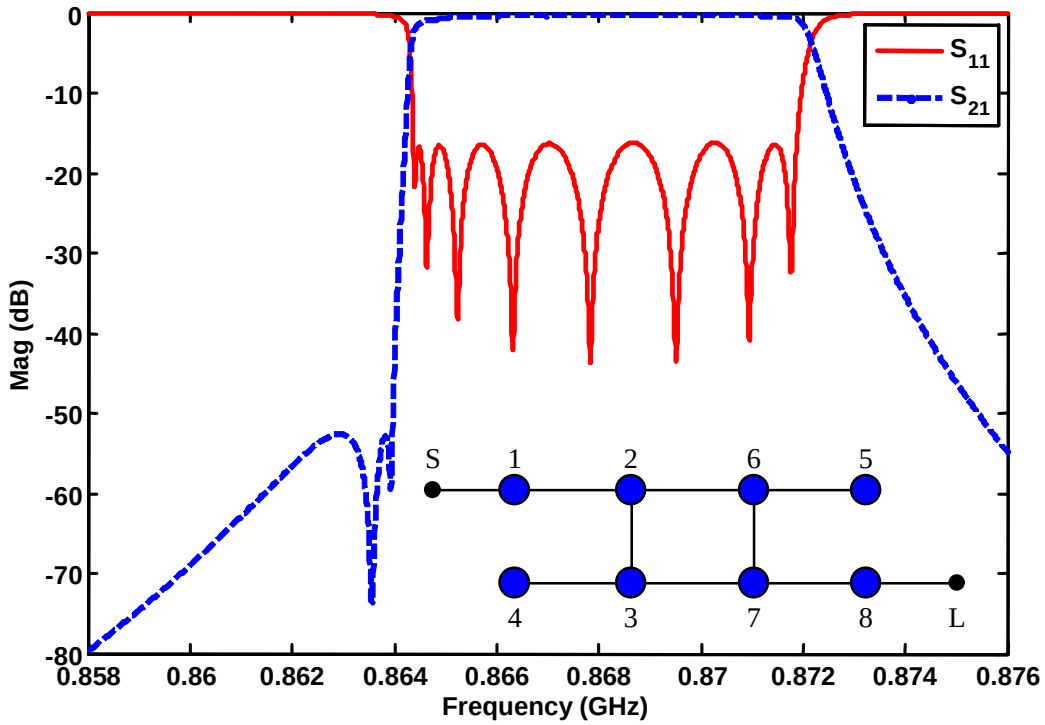

Figure 3.60: The ideal response of a quasi-elliptic eight-pole filter with two finite transmission zeros. The filter is synthesized in Cul-De-Sac topology.

station. The synthesized coupling matrix M is given as

$$\begin{bmatrix}
-0.0140 & 0.7577 & 0 & 0 & 0 & 0 & 0 & 0 \\
0.7577 & -0.0158 & 0.4036 & 0 & 0 & 0.4036 & 0 & 0 \\
0 & 0.4036 & 0.1832 & 0.1693 & 0 & 0 & -0.4036 & 0 \\
0 & 0 & 0.1693 & 0.9483 & 0 & 0 & 0 & 0 \\
0 & 0 & 0 & 0 & 0.2903 & 0.6903 & 0 & 0 \\
0 & 0.4036 & 0 & 0 & 0.6903 & -0.2239 & 0.4036 & 0 \\
0 & 0 & -0.4036 & 0 & 0 & 0.4036 & -0.0158 & 0.7577 \\
0 & 0 & 0 & 0 & 0 & 0 & 0.7577 & -0.0140
\end{bmatrix}$$

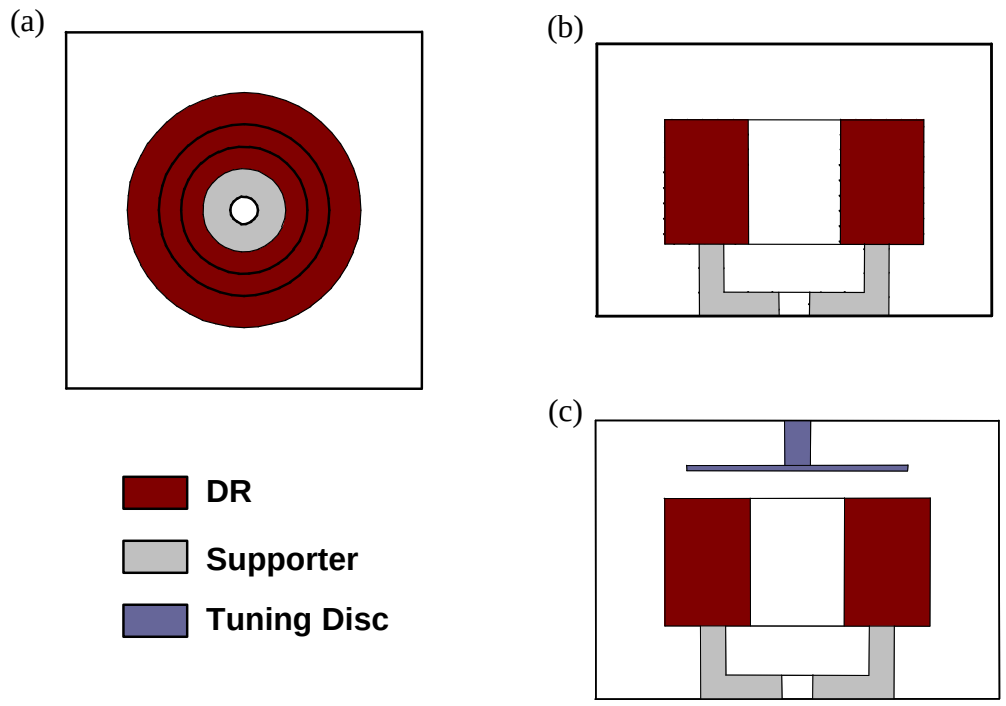

Figure 3.61: Dielectric resonator structure. (a) Top view. (b) Side view. (c) Dielectric resonator with tuning disc.

The external input and output coupling $R = 0.8222$. There is only one negative mutual coupling (M_{37}) in this filter, which will simplify the implementation. However, Cul-De-Sac topology is well-known to be very sensitive to the parameters since it consists of very few cross couplings between resonators. For this specific filter, 0.5% tolerance is required for most of the parameters in the coupling matrix. Without the computer aided diagnosis procedure, it will be very difficult to achieve such a stringent accuracy requirement.

A dielectric resonator needs to be designed to have a resonant frequency of $TE_{01\delta}$ mode around 868.1 MHz. The resonator structure is shown in Fig. 3.61. A ceramic disk is placed on a dielectric supporter inside a rectangular conductive

enclosure. Shown in Fig. 3.61(c) is the resonator structure with a tuning disc inside. The tuning disc could be metallic or ceramic. For a metallic tuning disc, the resonant frequency is increased with the increasing depth inside the enclosure. While for a ceramic tuning disc, an opposite behavior can be noticed. In this presented filter, metallic tuning discs are used. The dielectric resonator is firstly designed without the tuning disc in MMM. The tuning disc is then included to check the tuning range in HFSS to assure that all the shifted frequencies of the resonators can be achieved.

The external coupling can be achieved by a curved probe or a straight wire, as shown in Fig. 3.62(a) and (b), respectively, since the electric field is along the ϕ-direction. If the spacing between the wire and the ceramic disc is identical, the curved probe structure will have a shorter length than the straight wire to realize a given coupling value. However, it is more difficult to analyze and manufacture the curved probe structure than the straight one. A curved probe structure is employed in the presented filter and analyzed in HFSS.

The positive couplings can be realized by either an iris coupling structure as in Fig. 3.62(c) or a curved probe structure as in Fig. 3.62(d). In the iris coupling structure, the magnetic fields along the axial direction are coupled to each other through the iris between two resonators, which corresponds to a positive coupling value. In the curved probe structure, the electric fields along the ϕ-direction are coupled through the probe. An extra 180° phase offset is introduced by the asymmetrically bent probe structure, which makes the structure correspond to a positive coupling value. The negative couplings can be realized by either a

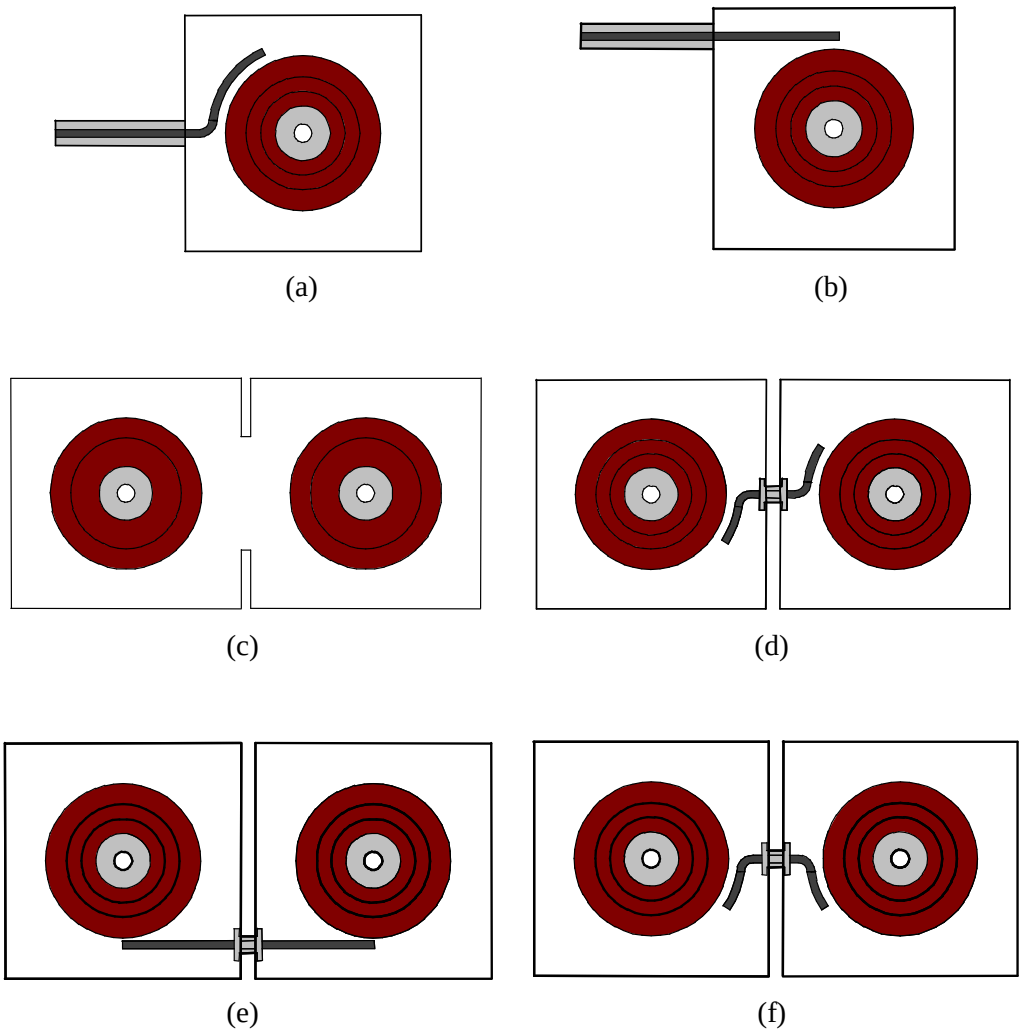

Figure 3.62: The coupling structures for dielectric resonator filters. (a) A curved probe for external coupling. (b) A straight wire for external coupling. (c) Iris coupling structure for positive coupling. (d) Curved probe structure for positive coupling. (e) Straight wire structure for negative coupling. (f) Curved probe structure for negative coupling.

straight wire as in Fig. 3.62(e) or a curved probe as in Fig. 3.62(f). Both of the coupling structures are electric couplings. Coupling structures as in Fig. 3.62(c) and (f) are employed in the presented filter for the positive and negative couplings, respectively. HFSS is used to design the dimensions for each coupling. The tuning screws are also included in the analysis to check the tuning range. It must be pointed out that the sign of these coupling structures might be changed for a triplet structure because of the phase offset of the field. The detailed discussion can be found in [170].

The filter topology is separated into several in-line paths to perform the diagnosis. The detailed diagnosis procedure is given as below.

1. The in-line path L-8-7-3-4 is diagnosed first. The probe coupling structure for the negative coupling M_{37} is in this path and should be tuned at the first step because the probe has very strong effect on the self-couplings of resonator 3 and 7. All the resonators are detuned at the beginning, and added one after the other according to the order in the path. The phase response of S_{22} for path L-8, L-8-7, L-8-7-3, and L-8-7-3-4 are shown in Fig. 3.63(a), (b), (c), and (d), respectively. After this step, the output coupling and the inter-couplings between resonator 8, 7, 3 and 4 can be achieved very accurately, and the positions of the coupling screws and probe should be locked.

2. Continuing from step 1, resonator 4 is detuned, and path L-8-7-3-2 is diagnosed. The sub-path L-8-7-3 has been tuned in step 1, therefore, only

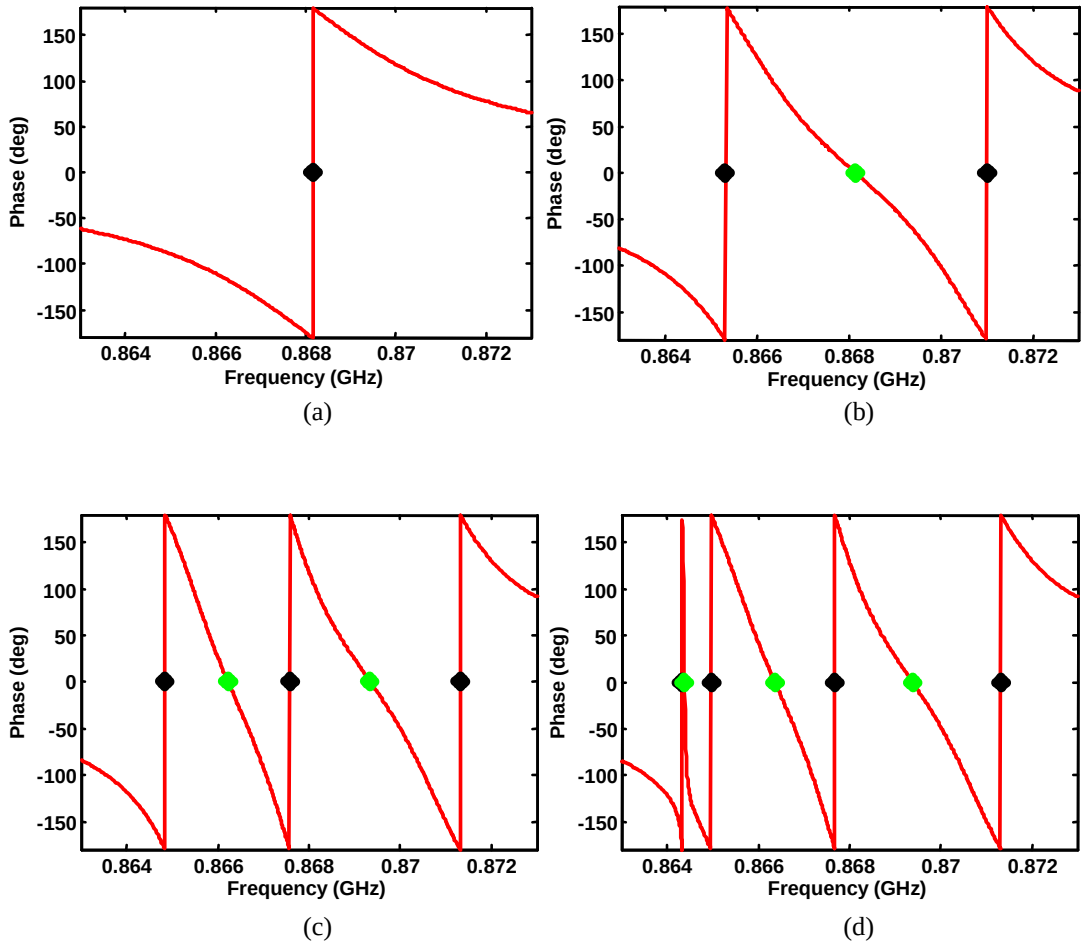

Figure 3.63: The phase of the reflection coefficient of the in-line diagnosis path. (a) Path L-8. (b) Path L-8-7. (c) Path L-8-7-3. (d) Path L-8-7-3-4.

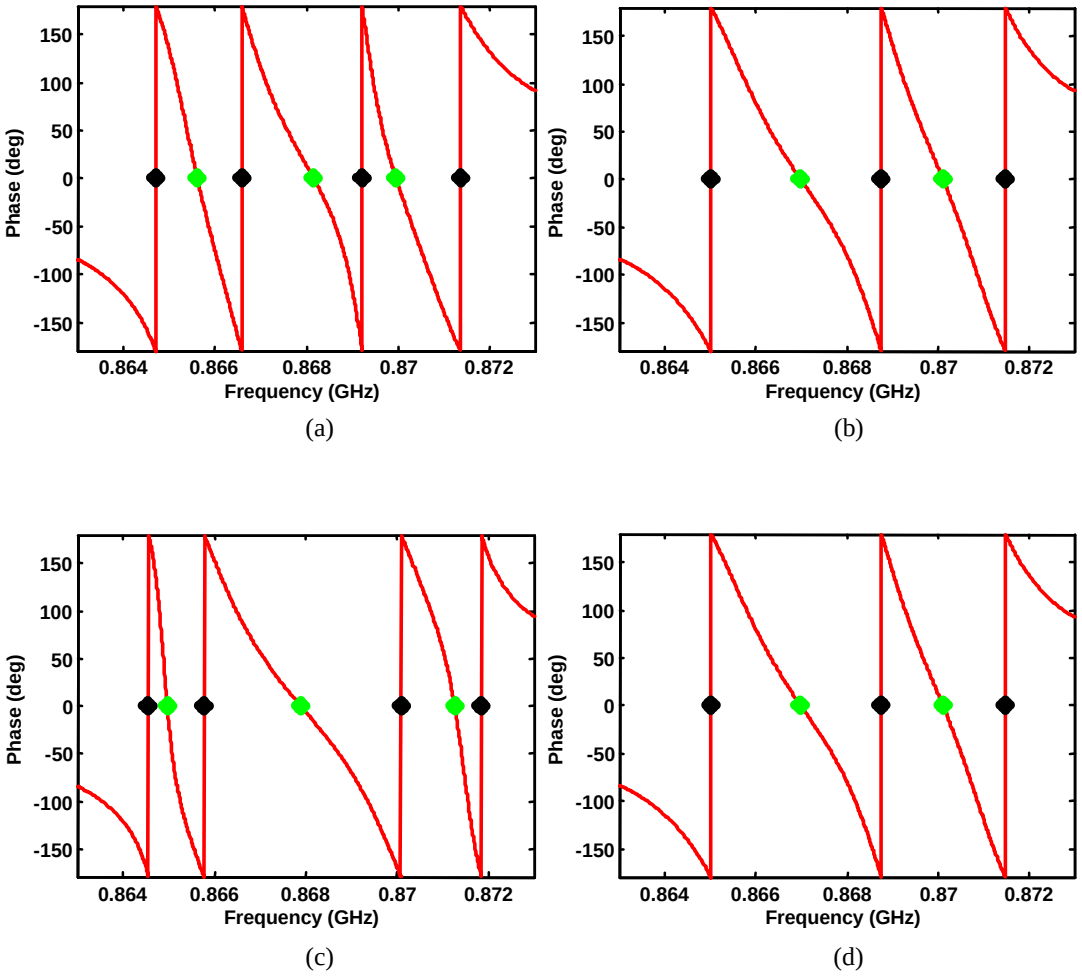

Figure 3.64: The phase of the reflection coefficient of the in-line diagnosis paths. (a) Path L-8-7-3-2. (b) Path L-8-7-6. (c) Path L-8-7-6-5. (d) Path S-1-2-6.

coupling M_{23} and resonator 2 and 3 need to be tuned at this step. The phase response of S_{22} for path L-8-7-3-2 is shown in Fig. 3.64(a). The coupling M_{23} can be achieved very accurately after this step.

3. Continuing from step 2, resonator 2 and 3 are detuned, and path L-8-7-6-5 is diagnosed. The sub-path L-8-7 has been tuned in step 1. The resonator 6 and 5 are included one by one. The phase response of path L-8-7-6 and L-8-7-6-5 are shown in Fig. 3.64(b) and (c), respectively. The couplings of M_{67} and M_{56} are achieved very accurately after this step.

4. Continuing from step 3, resonator 7 and 5 are detuned, and path S-1-2-6-5 is diagnosed. The phase response of S-1 and S-1-2 are identical as L-8 and L-8-7, respectively. The phase response of L-1-2-6 and L-1-2-6-5 are shown in Fig. 3.64(d) and Fig. 3.64(a), respectively. The input coupling and couplings between resonator 1, 2, and 6 can be tuned very accurately after this step.

After the four steps of the diagnosis procedure, all the couplings in the filter structure are tuned very close to the desired values. A sequential tuning procedure of the sub-filters is then applied to align the filter. Four sub-filters are tuned sequentially, namely S-1-2-6-5, S-1-2-6-5-3, S-1-2-6-5-3-4, and S-1-2-6-5-3-4-7. The phase response of these sub-filters are shown in Fig. 3.65. Actually, only the resonators are needed to be tuned because all the mutual-couplings have been achieved very close to the desired values after the diagnosis procedure.

The frequency response of the pre-tuned filter after the sequential tuning

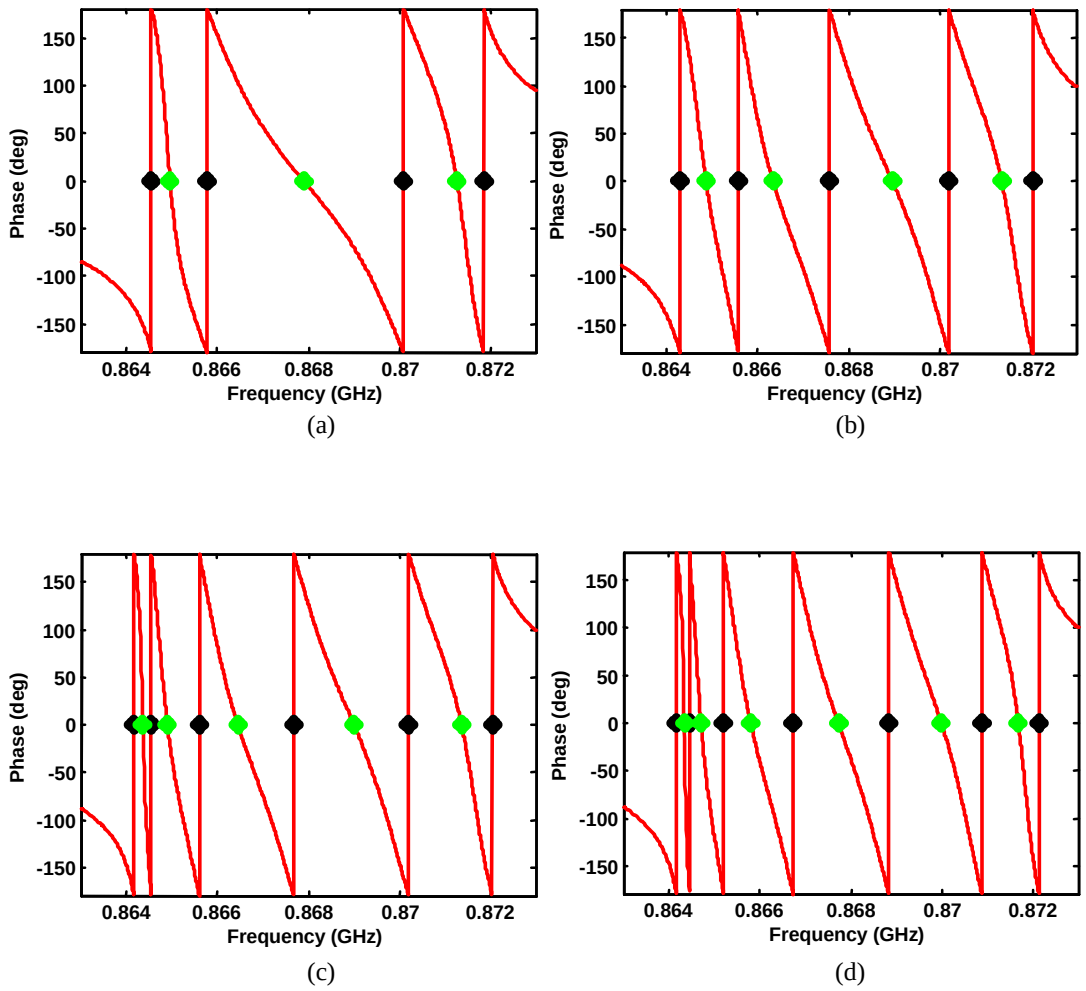

Figure 3.65: The phase response of the sub-filters in the filter structure. (a) Sub-filter path S-1-2-6-5. (b) Sub-filter path S-1-2-6-5-3. (c) Sub-filter path S-1-2-6-5-3-4. (d) Sub-filter path S-1-2-6-5-3-4-7.

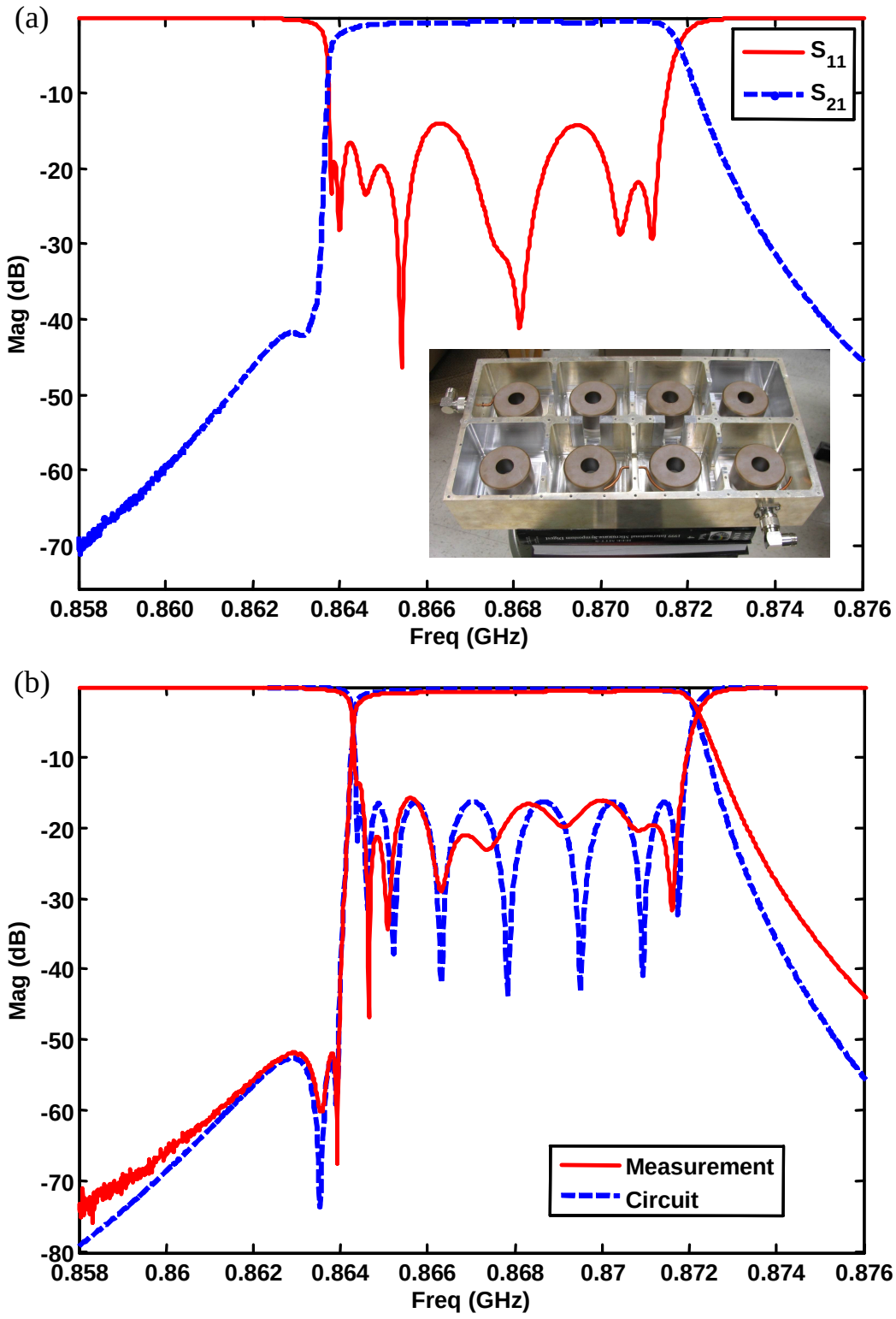

Figure 3.66: (a) The measured response of the pre-tuned filter. (b) The measured response of the fine-tuned filter.

procedure is shown in Fig. 3.66(a). The in-band response is very close to the desired one, but the left stopband performance needs to be improved more. The resonators 3, 4, 5 and 6, and the couplings between them are fine tuned to improve the filter performance because these resonators are strongly offset from the center frequency of the filter. After several iterations, the final tuned filter response is obtained and shown in Fig. 3.66(b). The measured response is also compared with the ideal circuit response in Fig. 3.66(b). A very good agreement can be noticed. The physical filter structure is shown as the inset of Fig. 3.66(a).

The presented filter example validates the feasibility of the systematic tuning procedure for quasi-elliptic filters. The filters realized in other technologies can also be tuned in a similar procedure as the presented dielectric resonator filter.

Chapter 4

Microwave Multiplexer Designs

4.1 Design Methodology

4.1.1 General Theory

The purpose of a multiplexer is to divide the frequency band into a number of channels, which may be contiguous (adjacent in the frequency band) or separated by guard bands. Practical applications using multiplexers include multi-carrier communications satellite repeater, antenna feeding system, wireless base station, and power combiner, etc. Obviously, in order to obtain multiplexing performance one can not just connect arbitrarily selected filters in shunt or series and expect the multiplexer to work. The immittance of one channel filter might have a strong degrading effect on the performance of the others [184]. The literature on theories of multiplexer synthesis is quite extensive. An overview of these theories is discussed next.

A fundamental multiplexer theorem was present by Grayzel [185] in 1969, which states that it is always possible to design a contiguous multiplexer having arbitrary bandwidths. However, the Grayzel theory is just a concept, and unsuitable for any practical application in its original form. In practice, two types of multiplexers are most commonly used. One type has the property that the interacting channel filters are directly connected (all in series or all in parallel) through a common junction without additional immittance compensation networks. The other type is using immittance compensation networks in the multiplexer, e.g. manifold multiplexers. For multiplexers in series or parallel form, a general direct analytical design process is presented in [186]. Basically, independent doubly terminated filters are developed for each individual channel first, and formulas for modifications to parameters associated with the first two resonators are derived to match the multiplexer. The main limitation of these formulas is that the channels may not be spaced too closely in frequency. In [187], an extended general design procedure is presented for multiplexers having any number of channel filters, with arbitrary degrees, bandwidths, and inter-channel spacings. Commencing with the closed-form expressions for element values in doubly terminated channel filters, this multiplexer design process modifies all of the elements in each channel filter in turn by optimization, and preserves a match at the two points of perfect transmission closes to the band edges of each channel filter, while taking into account the frequency dependence across each channel.

For multiplexers using immittance compensation networks, manifold multiplexers are widely used in practical applications. General design procedures of

manifold multiplexers can be found in [188] and [189]. Basically, the design process also commences from doubly terminated channel filters. The channel filters are connected to a manifold junction with physical separations or phase shifters in between. The spacings or the phase shifters between channels not only serve to separate the filters physically, but also compensate the filter interactions. Actually, the phase shifters are sufficient to compensate the multiplexer to such an extent that contiguous channeling cases are even designable. Closed formulas and computer optimization process can be found in [188] and [189], respectively.

When the channels of the multiplexer are contiguous, i.e. adjacent channels have attenuation characteristics that typically cross over at 3 dB points, singly terminated filter prototypes are usually employed [1, 190–192]. The typical responses of the input admittance and scattering parameters of a singly terminated quasi-elliptic filter are shown in Fig. 4.1. The real part of the filter input admittance has an equal ripple property about the value of 1 within the passband of the filter, and are all zeros outside the passband (as shown in Fig 4.1(a)). Therefore, the singly terminated filters in a contiguous multiplexer are easier to compensate than their doubly terminated counterpart because the condition on the input admittance of the multiplexer is more closely satisfied by singly terminated filters. The condition is given by [185]

$$\begin{aligned} Y(s) &= \sum_{i=1}^{n} Y_i(s) = 1 \implies \\ \sum_{i=1}^{n} \mathrm{Re}\left[Y_i(s)\right] &= 1 \quad \text{and} \quad \sum_{i=1}^{n} \mathrm{Im}\left[Y_i(s)\right] = 0 \end{aligned} \tag{4.1}$$

where $Y(s)$ is the input admittance of a contiguous multiplexer consisting of n

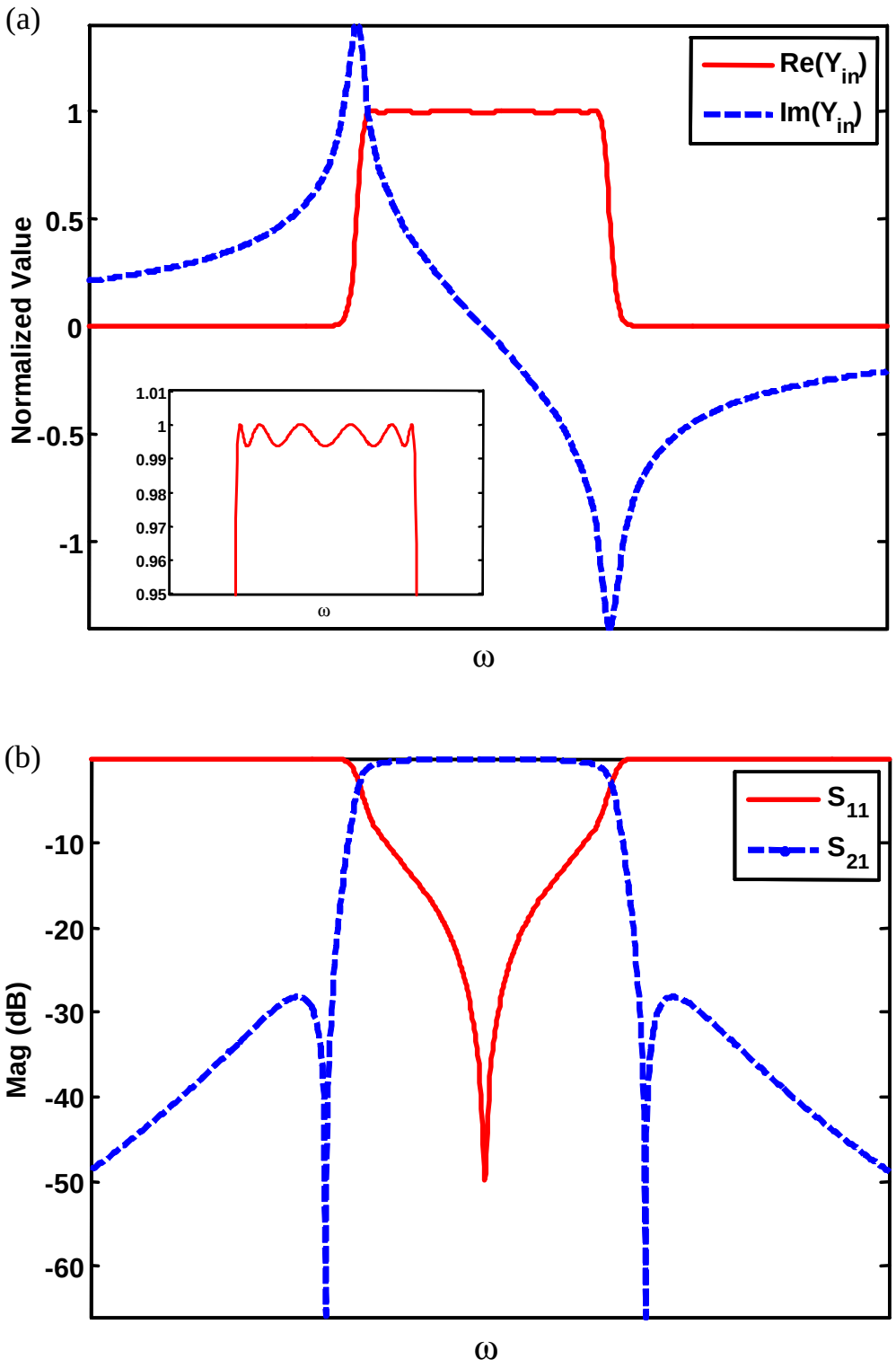

Figure 4.1: The typical response of a singly terminated quasi-elliptic filter. (a) Real and imaginary parts of input admittance Y_{in}. (b) S-parameters.

channels, and $Y_i(s)$ is the input admittance of the ith channel filter. For multiplexer designs based on singly terminated filters, dummy channels are usually required to imitate absent channels at the edges of the total multiplexer bandwidth, thus forming an additional annulling network for the compensation of the channel interactions.

4.1.2 Full-Wave CAD in MMM

The above-discussed theories are based on single-mode network representations and can only provide approximate results. It is desirable to apply rigorous numerical methods for the reliable CAD of the complete multiplexer structures. In all of the available numerical methods, MMM is well-known for its high efficiency and accuracy, and is widely employed for waveguide multiplexer designs. The analyzable configurations and the general design procedure of multiplexers in MMM are discussed next.

Usually, waveguide multiplexers can be decomposed as several key building blocks, namely waveguide junctions and filters. Possible waveguide junctions include E- and H-plane T-junctions, E- and H-plane bifurcations, E- and H-plane multi-furcations, and ridge waveguide T-junctions, etc [3, 153]. It should be noted that a manifold structure is actually composed of cascaded T-junctions. In some cases, a compensation structure, e.g. a conductor block, can also be added to these junctions to obtain better performance. Waveguide filters might be inductive window bandpass filters, corrugated waveguide filters, E-plane metal-insert

filters [43], and ridge waveguide bandpass filters, etc. All these key building blocks can be analyzed in MMM by several different techniques discussed before.

The general design procedure of a multiplexer in MMM can be divided into three main steps [3, 193, 194]. Firstly, the channel filters are designed individually using the techniques presented in previous chapter to meet the required specifications of each channel. The filters might be doubly or singly terminated depending on the frequency spacings between the channels. If doubly terminated filters are used in a multiplexer design, the stopband attenuation levels of one channel filter over the passbands of other channels will be improved around 6 dB after the filter is added to the multiplexer (due to the power division between the in-band and out-of-band channels). This property, sometimes, can be considered to reduce the orders of the channel filters. After this step, all the channel filters will be characterized by the GSMs solved in MMM.

Secondly, the waveguide junctions are designed and analyzed in MMM. Usually, a homogeneous power splitter structure is desired for the junctions. Some compensation structures are also often added in the junctions to have more degrees of freedom to match the filter loads. The GSMs of the channel filters are then cascaded with the GSMs of the junctions to obtain the multiplexer response at the initial state. A few parameters can be tuned in this step to improve the multiplexer performance. For example, the lengths of the connecting waveguides between filters and junctions, and the dimensions of the compensation structures in junctions, etc. This tuning procedure is very efficient since the GSMs (normally, using the GSMs just corresponding to the fundamental modes is accurate

enough at this step) of the filters (and sometimes the junctions) do not need to be recalculated again.

The third step is a full-wave optimization procedure. A high computation effort, especially for multiplexers with many channels, is required in this step since the whole multiplexer needs to be re-analyzed in each iteration. The parameters to be optimized should be included gradually to speed up the convergence. Mostly, the desired multiplexer performance can be obtained by optimizing only the first few dimensions (close to the junction) in the channel filters. In some cases, e.g. a manifold multiplexer, if a good match has been achieved in the second step, namely each channel can be identified clearly from the multiplexer response and has an acceptable in-band return loss for optimization, then the channel filters can be optimized one after the other to speed up the procedure. During the optimization of one channel filter, the GSMs of other components only need to be calculated once. The dimensions of the junctions and the connecting waveguides should not be changed during the optimization of each filter, otherwise, the compensation effect will be destroyed. Some other techniques to improve the efficiency of the optimization procedure can be found in [195–197].

4.1.3 Hybrid CAD

For some multiplexers, the channel filters might not possibly be analyzed by MMM, e.g. a multiplexer consisting of a manifold junction and many dielectric resonator filters. The channel filters may need to be tuned on bench or designed

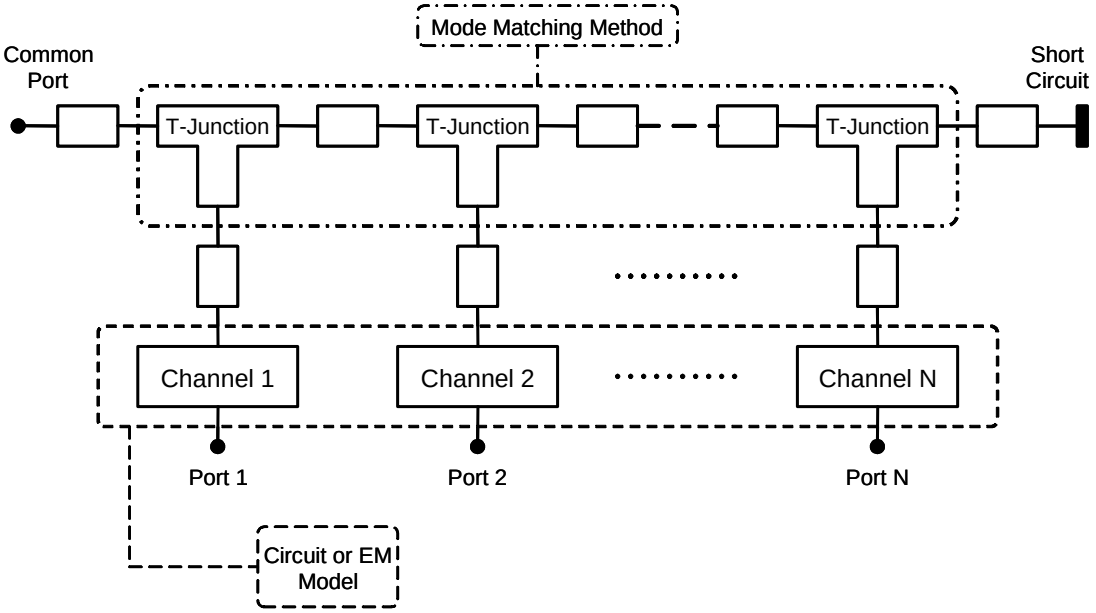

Figure 4.2: A hybrid CAD model of a manifold multiplexer. The channel filters may be represented by circuit models or S-parameters from an EM simulator.

in other full-wave electromagnetic simulation tools. A hybrid CAD procedure can then be applied to design these multiplexers. Shown in Fig. 4.2 is an example of a manifold multiplexer model that can be designed by a hybrid approach. The general design procedure can be divided into four main steps [198].

Firstly, the manifold junction, which usually comprises many waveguide T-junctions, is analyzed in MMM, and the GSM of it is calculated and stored. The lumped elements or the coupling matrices of the channel filters (doubly or singly terminated) are synthesized by the well-known methods according to the channel specifications. The GSM (in fundamental mode) of the manifold junction and the circuit models of the filters are then cascaded together to give a coarse model of the multiplexer. The lengths of the connecting waveguides/ transmission lines and the circuit elements of the filters are optimized to obtain the desired multiplexer

performance. After the optimization, the updated circuit elements or the coupling matrix of each channel filter are extracted out and stored.

Secondly, each channel filter is designed separately according to the extracted coupling matrix from the previous step (The frequency response is normally not an optimum filter response). In this step, the filters can be either designed in an EM simulator or tuned on bench to match the updated filter response. Some special technique, like space mapping method, is often combined with the EM tools to perform the filter design since other numerical methods are not so efficient as MMM. After this step, the scattering parameters of each channel filter are obtained and stored.

Thirdly, the S-parameters of the channel filters from the second step are cascaded with the GSM of the manifold to check the multiplexer response (the optimized connecting waveguide lengths from the first step should be used). A second optimization procedure may be performed to improve the performance. But this time, only the connecting waveguide lengths should be optimized. The channel filters may also be tuned again if the desired multiplexer performance can not be achieved by the optimization. Therefore, it is actually an iterative process in this step.

Fourthly, the manifold junction (also the filters if they are designed by EM tools in previous steps) is manufactured and assembled with the filters to realize the multiplexer. A fine tuning procedure may be needed to achieve the requirements. Nevertheless, it usually takes a very short time if the previous steps are successfully accomplished.

4.1.4 Multiport Network Synthesis

For multiplexers in an integrated structure, i.e. the complete network is formed exclusively by coupled resonators, an exact coupling matrix synthesis method is desired since the implementation and tuning procedure are dependent on the coupling matrix. Many efforts have been made in the past on this topic [199, 200]. However, most of the approaches used today are based on optimization. Recently, a virtually exact analytical synthesis approach was presented in [201] for diplexers. Basically, the rational polynomials of a diplexer are obtained by an iteration process. The polynomials for each channel filter are then derived accordingly, and the general method discussed in chapter 2 is used to synthesize the coupling matrix. Another analytical method was presented in [202], in which the rational polynomials of multiplexers are generated through the Cauchy method [203]. At this point, the exact synthesis of multiport networks, namely multiplexers, is still a very active research topic.

4.2 Wideband Ridge Waveguide Divider-type Multiplexers

4.2.1 Introduction

The development of millimeter-wave communications and transceiver technology has created the need for compact, wideband, high-performance diplexers and multiplexers. Usually, waveguide multiplexers are the most suitable choices to achieve

these requirements. Previous waveguide multiplexer designs consist of E- and H-plane manifold multiplexers, E- and H-plane T-junction multiplexers, E- and H-plane divider-type multiplexers [3], and Ridge waveguide T-junction multiplexers [153, 204], etc. However, rectangular waveguide junctions are usually not applicable for wideband multiplexer designs because of the limited mono-mode frequency range of rectangular waveguides. Ridge waveguides have much wider mono-mode frequency range than rectangular waveguides, which makes them an appropriate choice for wideband multiplexer designs. A wideband diplexer design using ridge waveguide T-junction has been presented in [204]. The disadvantage of ridge waveguide T-junction multiplexers is that the physical size, especially the total area, is large and the physical layout makes it very difficult to integrate them inside a system.

In this section, novel ridge waveguide divider junctions are presented for wideband multiplexer designs. A wideband match at the common port can be easily achieved for these junctions. Diplexers and multiplexers using such junctions usually occupy a small area and provide a convenient layout for high-integration. These diplexer or multiplexer designs are mostly applicable for LTCC applications since they can be integrated underneath other components on a circuit board. The LTCC realization procedure of ridge waveguide structures has been discussed before (see sec. 3.4, p. 132). Analysis and design of the ridge waveguide divider junctions can be completely performed in MMM.

Two design examples, one diplexer and one triplexer, using ridge waveguide divider junctions are given in this section to validate the concept. Both de-

signs have very wide fractional bandwidth, 95% for the diplexer and 50% for the triplexer. Ridge waveguide evanescent-mode bandpass filters are employed for all the channel filters. The diplexer and triplexer are designed to be manufactured in LTCC technology. Multiplexer designs in metallic form using the presented junctions are also possible.

4.2.2 Ridge Waveguide Divider Junction

Waveguide junctions are very important components in many microwave applications, especially in multiplexer designs. These junctions are usually lossless reciprocal three ports, and all three ports can not be matched simultaneously [2]. However, in multiplexer applications, it is often desirable to have the junction with one of its ports well matched over a wide frequency band [204], i.e. low reflection from the common port. Fig. 4.3(a) shows a simple ridge waveguide divider junction. Basically, a common port of single ridge waveguide is connected to an intermediate double ridge waveguide, and then to two separated output ports of single ridge waveguides. Many modes, mainly the fundamental mode, of the double ridge waveguide are excited by the fundamental mode of the common port ridge waveguide. These modes will then excite the fundamental mode of the two output ridge waveguides. This structure is expected to have a power divider performance because most of the power transmitted to the double ridge waveguide almost equally splits into the two output waveguides. The typical performance of this simple junction structure is shown in Fig. 4.3(b), which is indeed a power

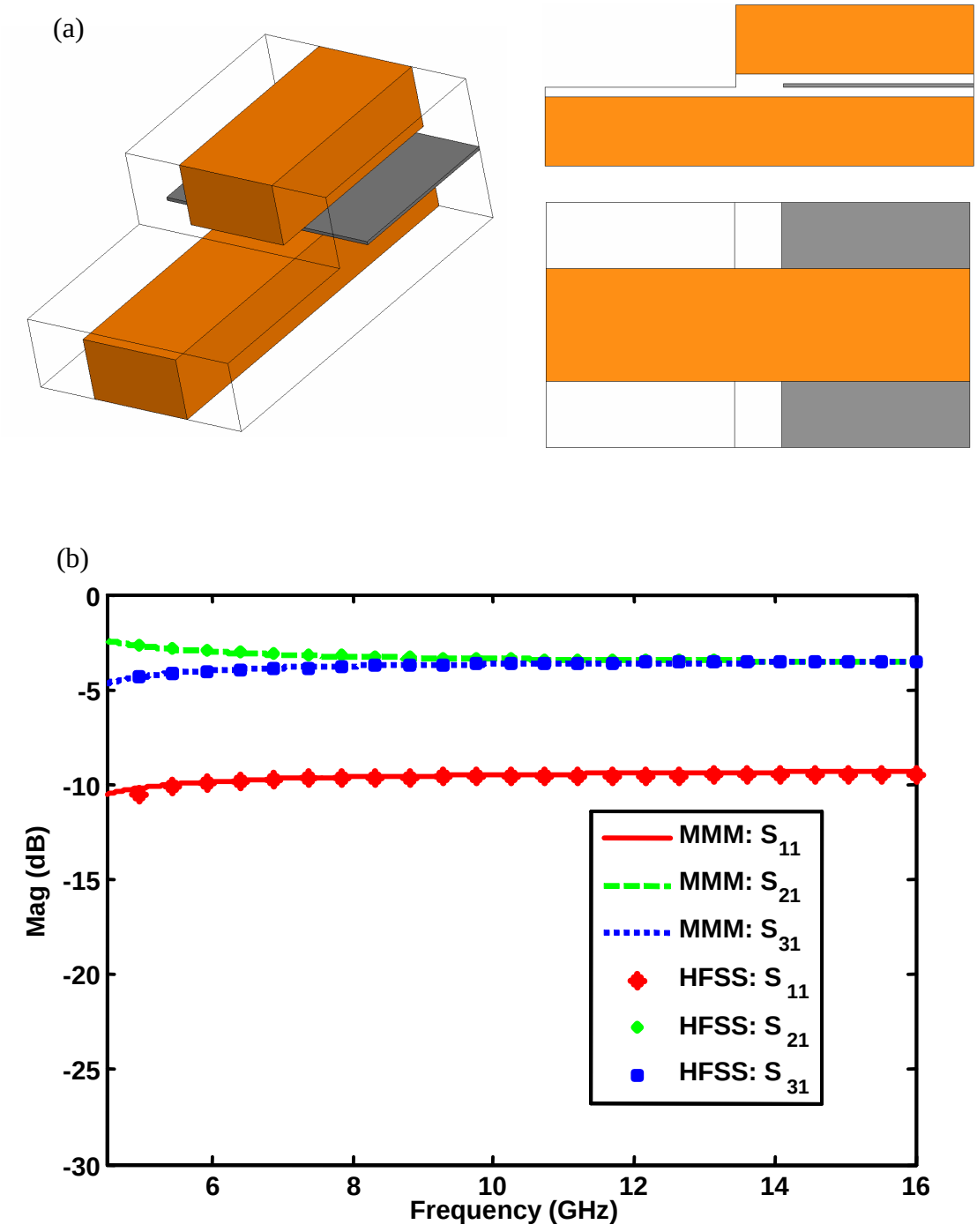

Figure 4.3: (a) Structure of a simple ridge waveguide divider junction. (b) A typical magnitude response of the junction.

divider. However, the performance of the common port matching is limited, which is mainly due to the discontinuity between the common port ridge waveguide and the double ridge waveguide.

In order to improve the junction performance, a matching transformer is introduced between the common port and the double ridge waveguide. The new junction structure is shown in Fig. 4.4(a). The transformer is used to relax the abrupt discontinuity in the simple junction and compensate the power reflection from the double ridge waveguide. To design a junction as in Fig. 4.4(b), an analysis and optimization procedure by MMM is applied. The eigenmodes of each ridge waveguide are found by the GTR technique (see Appendix A, p. 255). The discontinuities between waveguides are characterized as GSMs solved by MMM (using the formulations in Appendix C, p. 271). The frequency response of the whole junction is obtained by GSM cascading. In the analysis, the three-port junction can be represented as a generalized two-port network (see [35], p. 37), which is convenient to cascade the junction with other channel filters for multiplexer analysis. The optimization goal of the junction is to have small reflection coefficient from the common port and almost equal transmission coefficients to the two output ports. Shown in Fig. 4.4(b) is the response of the optimized junction, which shows a very good wideband performance. Responses by HFSS are also given in Fig. 4.3(b) and 4.4(b) to show the agreement with MMM. For both junction structures, usually the shorter the double ridge waveguide, the better the performance. This length can be set as the achievable minimum length of the employed manufacture technology.

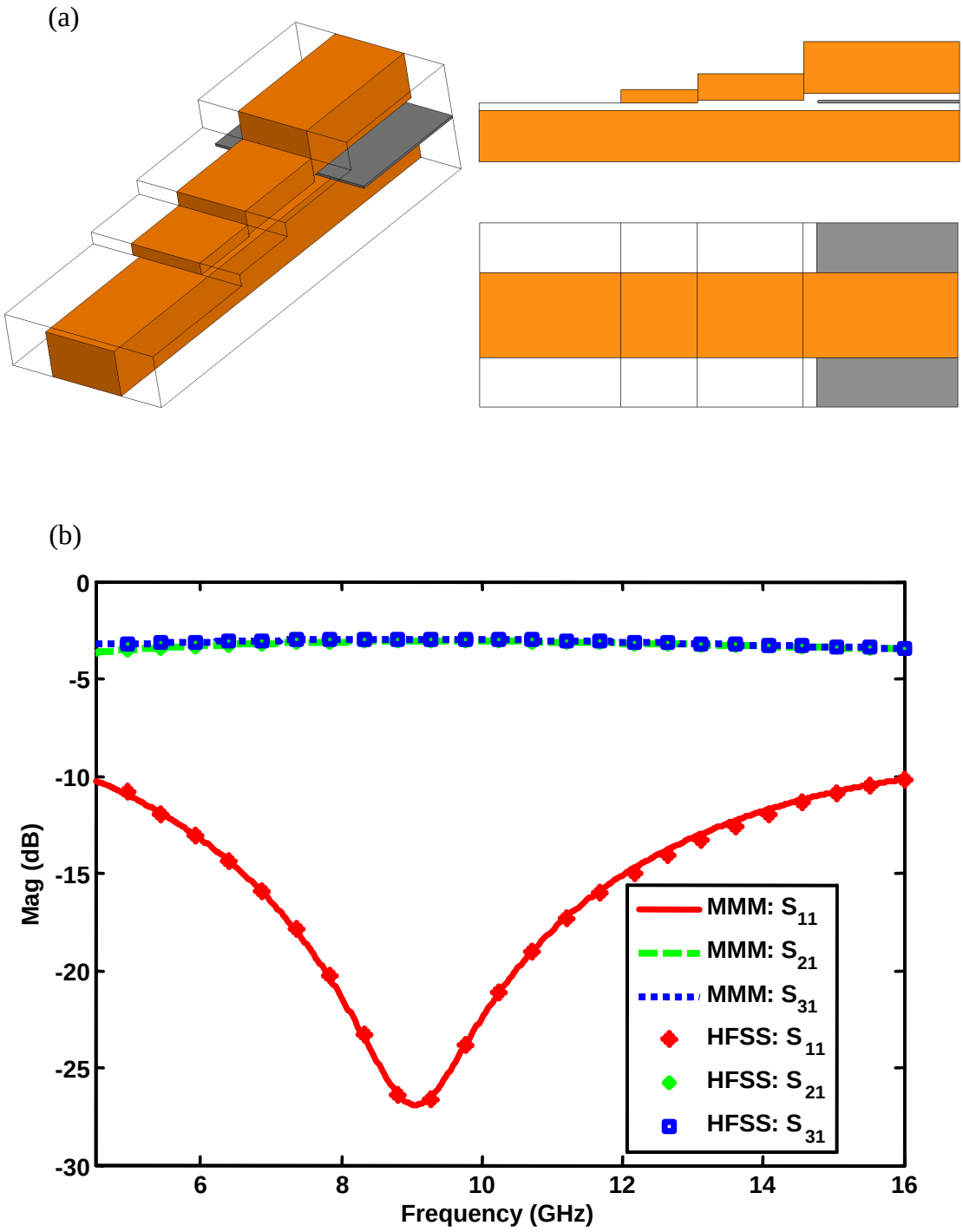

Figure 4.4: (a) Structure of a ridge waveguide divider junction with an embedded matching transformer. (b) Typical magnitude response of the improved divider junction.

4.2.3 Ridge Waveguide Channel Filters

Ridge waveguide evanescent-mode filters are appropriate for the channel filters in a multiplexer using the above-presented junctions. A typical filter structure is shown in Fig. 4.5(a). Basically, the resonators in the filter are realized by the ridge waveguide sections. The inter-couplings between ridge waveguide resonators are provided by the empty rectangular waveguides that have the same enclosure as the ridge waveguides (as shown in Fig. 4.5(b)). Over the filter passband all the modes of the rectangular waveguides are evanescent, i.e. cutoff frequencies are larger than the filter upper band edge. Therefore, these evanescent waveguides are behaving like inductors that provide the mutual inductive couplings between the resonators. This type of filters is taking advantage of the wide fundamental mode operation bandwidth and low cutoff frequency of ridge waveguide [205, 206]. They have drawn considerable attention because of their compact size, low loss, wide bandwidth and wide spurious-free stopband range [61, 207–209].

The filter design procedure is similar as the design methodology discussed before (sec. 3.1, p. 3.1). The cross section of the ridge waveguide is determined first according to the passband range of the desired filter. Usually, the cutoff frequency of the fundamental mode should be 20% or more below the lower passband edge, and the first higher order mode should be much higher than the upper passband edge. The initial lengths of ridge waveguides and evanescent waveguides are then decided based on the k-inverter method [1, 45]. Equation (3.6) can be used to solve the coupling values from the S-parameter of a coupling section be-

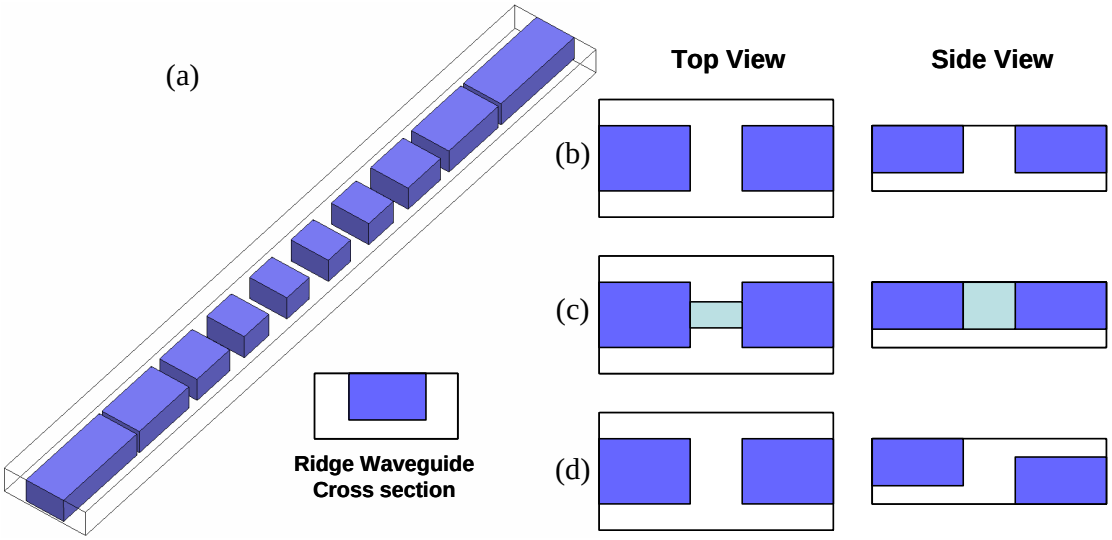

Figure 4.5: (a) A typical ridge waveguide evanescent-mode filter. (b) Coupling by evanescent rectangular waveguide. (c) Coupling by evanescent narrow ridge waveguide. (d) Coupling between flipped ridge waveguides by evanescent rectangular waveguide.

tween resonators. Finally, the full-wave optimization in MMM (using GTR as in Appendix A and C) are employed to obtain the desired filter performance.

In large bandwidth filters ($\geq$ 40%), the required couplings, especially the input and output couplings, are so strong that the lengths of the evanescent waveguides are diminished to impractical levels for manufacturing. In order to avoid this problem, a coupling mechanism using narrow ridge waveguide as shown in Fig. 4.5(c) can be used. The narrow ridge coupling sections are less evanescent than the empty rectangular waveguides, so that the coupling length must be enlarged for a given coupling value. Therefore, the coupling lengths can be managed large enough for manufacturing by selecting proper narrow ridge sections (i.e. appropriate widths). A 100% bandwidth filter using narrow ridge coupling sections

can be found in [210]. Another coupling mechanism for solving the problem is shown in Fig. 4.5(d). Two *interdigital* ridge waveguides are coupled through an evanescent waveguide. The coupling strength of this structure is similar as the narrow ridge coupling structure. This type of coupling arrangement is usually used for some filters in which the input and output ridge waveguides are required to be *flipped* to each other for the sake of connection with other components. Such a filter is given in the later triplexer example.

4.2.4 Input and Output Transitions

The ports of the junctions and filters presented above (also the multiplexers given later) are ridge waveguides that can not be connected to other components in a system or measured on bench. A transition from ridge waveguide to other components must be designed. For LTCC applications, a transition is usually made from ridge waveguide to 50-ohm stripline as shown in Fig. 4.6(a). In air-filled metallic waveguide structures, a transition can be made from ridge waveguide to standard coaxial connectors as shown in Fig. 4.6(b) (Note: for wideband applications, a transition from ridge waveguide to standard rectangular waveguide is not possible because multiple modes will exist in the rectangular waveguide). The transition design procedure starts from the Chebyshev multi-section matching transformer [2] for knowing the number of sections and the impedances in each section. The intermediate stripline sections are then designed according to the impedance values, and the length of each section is about quarter wavelength

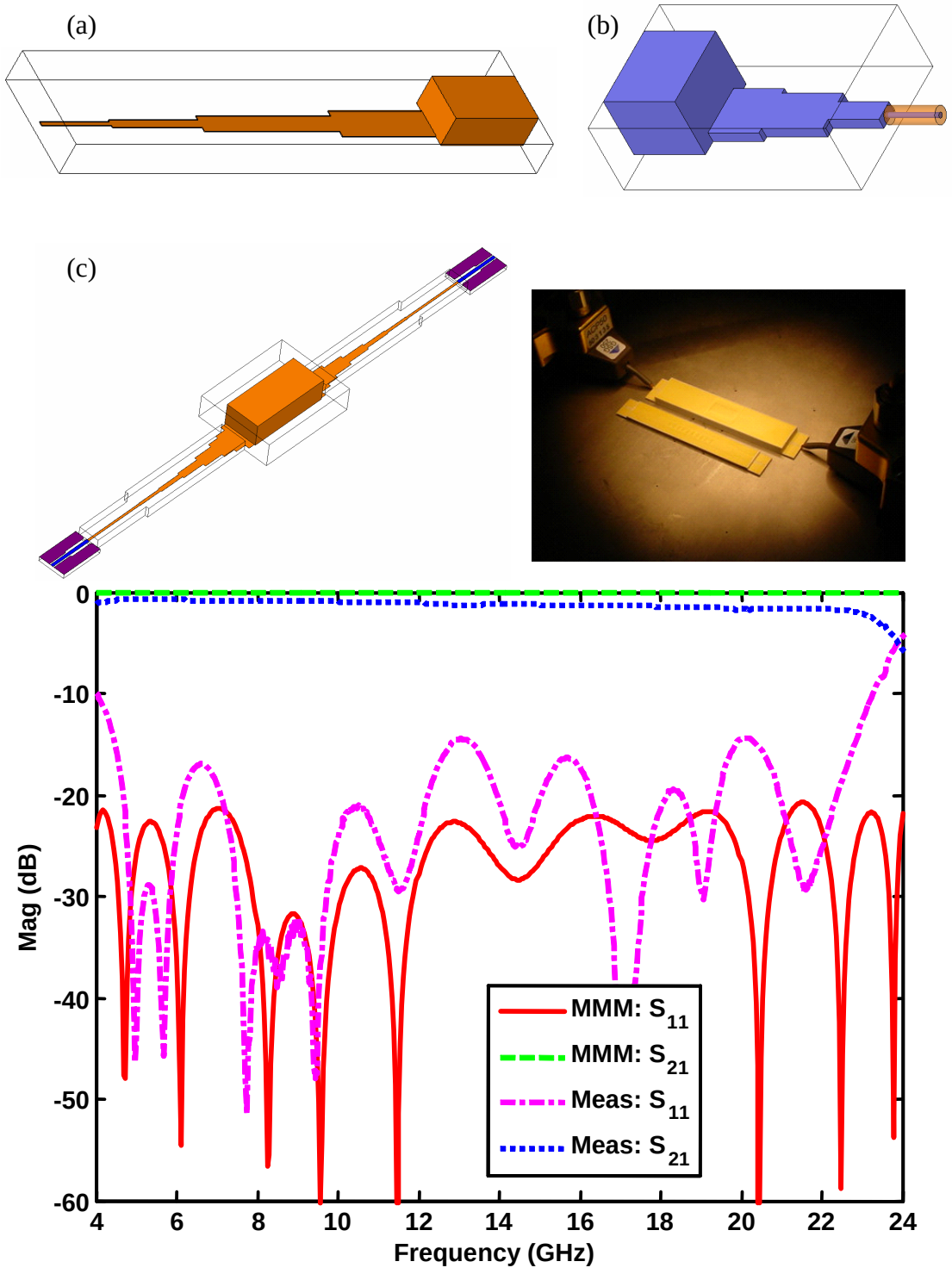

Figure 4.6: (a) A transition from ridge waveguide to 50 ohm stripline in LTCC. (b) A transition from ridge waveguide to SMA connector. (c) Simulation and measurement results of a back-to-back transition in LTCC.

at the center frequency. A full-wave optimization in MMM (using GTR as in Appendix A and C) is then applied to acquire the desired transition performance.

Extreme wideband transitions can be designed using the structures as in Fig. 4.6(a) and (b). Shown in Fig. 4.6(c) is an example of transition for LTCC application. The fractional bandwidth is about 140% (4 to 24 GHz). The transition is connected back to back, and two coplanar lines are connected to the input and output striplines for measurement. A Cascade probe station is used to measure the response. Even though the performance is degraded by LTCC manufacturing effect, it is still acceptable for the specific application.

4.2.5 Diplexer Design Example

A wideband diplexer is designed to demonstrate the feasibility of using ridge waveguide divider junctions for multiplexer designs. The specifications are given in Table 4.1. The relative bandwidth of the whole diplexer is about 95%. Channel filter 1 has relative bandwidth of about 31% and channel filter 2 has about 33%. The diplexer is designed based on LTCC technology. The relative permittivity of dielectric material is 5.9. The thickness of each dielectric layer is 3.74 mil and the thickness of metallization is 0.4 mil. The diplexer height must be integer multiples of dielectric layers.

The junction as in Fig. 4.4(a) is employed for this diplexer design. Its response as in Fig. 4.4(b) shows very good performance through the whole diplexer frequency band.

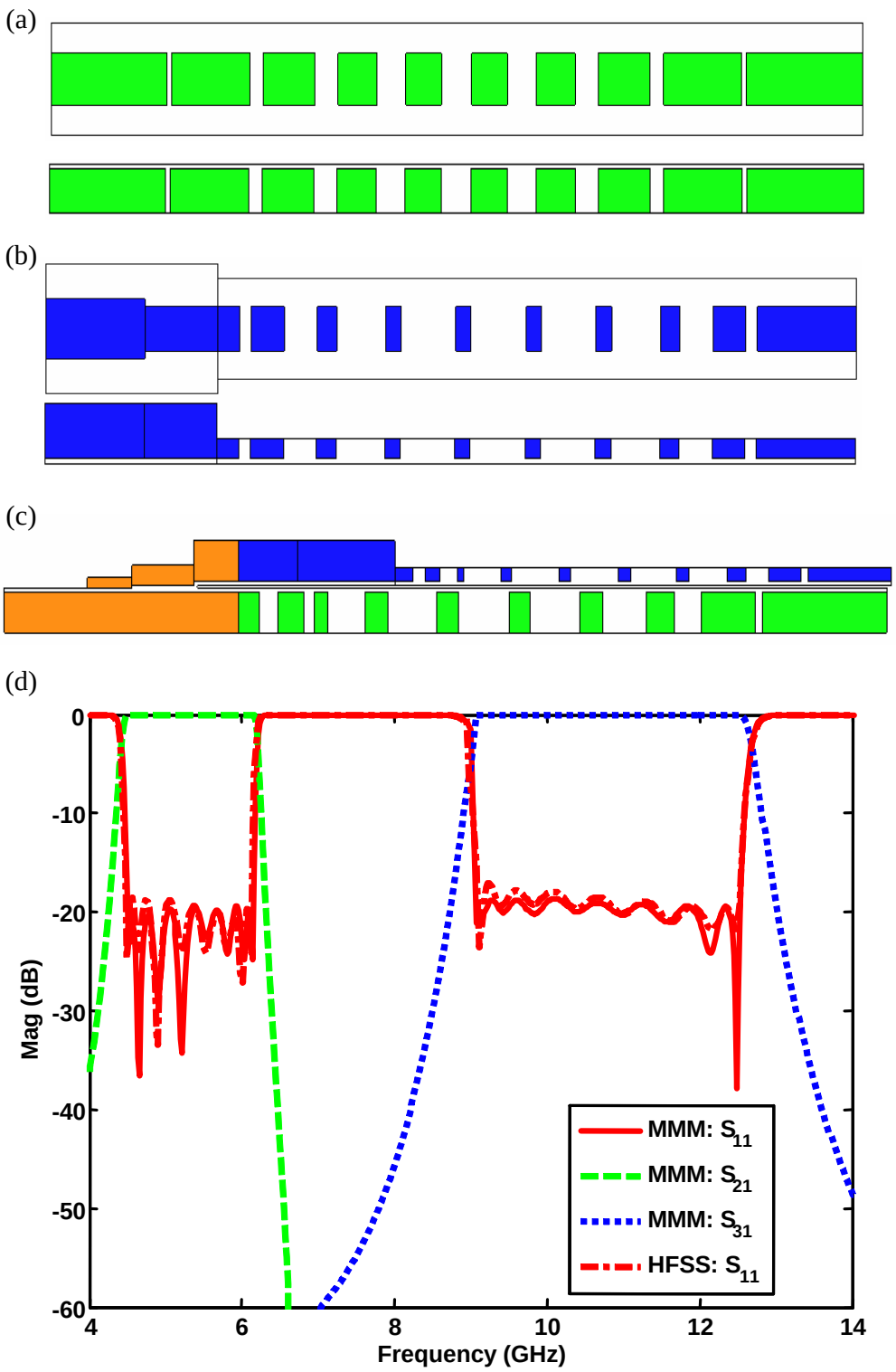

Figure 4.7: (a) Structure of channel filter 1. (b) Structure of channel filter 2 including transformer in-front. (c) Diplexer structure and simulated response in MMM and HFSS.

Table 4.1: The specifications of a wideband diplexer.

Channel	Passband (GHz)	Return Loss (dB)	Isolation (dB)
1	4.5 – 6.15	≥ 18	≥ 60
2	9.0 – 12.5	≥ 18	≥ 60

Channel filter 1 and channel filter 2 are ridge waveguide evanescent-mode bandpass filters. Shown in Fig. 4.7(a) and Fig. 4.7(b) are the top and side views of filter 1 and filter 2, respectively. The cross sections of the ridge waveguides employed by these two filters are different due to the difference of the center frequencies of the filters. Filter 1 uses the same ridge waveguide as the junction output waveguide, while filter 2 uses a smaller one since it has a higher center frequency. A matching transform is, therefore, added between the junction and filter 2 to connect them, which is also shown in Fig. 4.7(b). These two filters are initially chosen as 8-pole doubly terminated Chebyshev filters.

Shown in Fig. 4.7(c) is the side view of the diplexer structure. The optimized junction and channel filters are connected together to have the initial design of the diplexer. The response of the diplexer is computed by cascading the GSMs of the junction and filters (using (1.2) since the junction is characterized as a generalized two-port network). If the higher order resonant modes of channel filter 1 do not exist inside the passband of channel filter 2, the initial diplexer response (only adjusting the connection waveguide lengths) will be a very good starting point for optimization. If it is not the case, the higher order resonant modes of channel

Table 4.2: The specifications of a wideband triplexer design using ridge waveguide divider junctions.

Channel	Passband (GHz)	Return Loss (dB)	Isolation (dB)
1	6.0 – 6.6	≥ 20	≥ 60
2	7.6 – 8.4	≥ 20	≥ 60
3	9.0 – 10	≥ 20	≥ 60

filter 1 must be managed to move out of the passband of channel filter 2.

The optimization procedure in MMM is applied to improve the diplexer performance. The lengths of ridge waveguide resonators and coupling sections of each filter are optimized. The final diplexer response is shown in Fig. 4.7(d). The S_{11} response by HFSS shows a very good agreement with MMM. The housing dimensions of the whole diplexer are about $width \times height \times length = 260mil \times 168.3mil \times 2130mil$.

4.2.6 Triplexer Design Example

A wideband triplexer example is designed by cascading two diplexers using ridge waveguide divider junctions. The specifications are given in Table 4.2. The relative bandwidth of the whole triplexer is 50% and each channel filter is about 10%. The triplexer is also designed to be manufactured in LTCC technology. The LTCC parameters are identical as the ones for the previous diplexer design.

The presented ridge waveguide divider junction is a three-port network com-

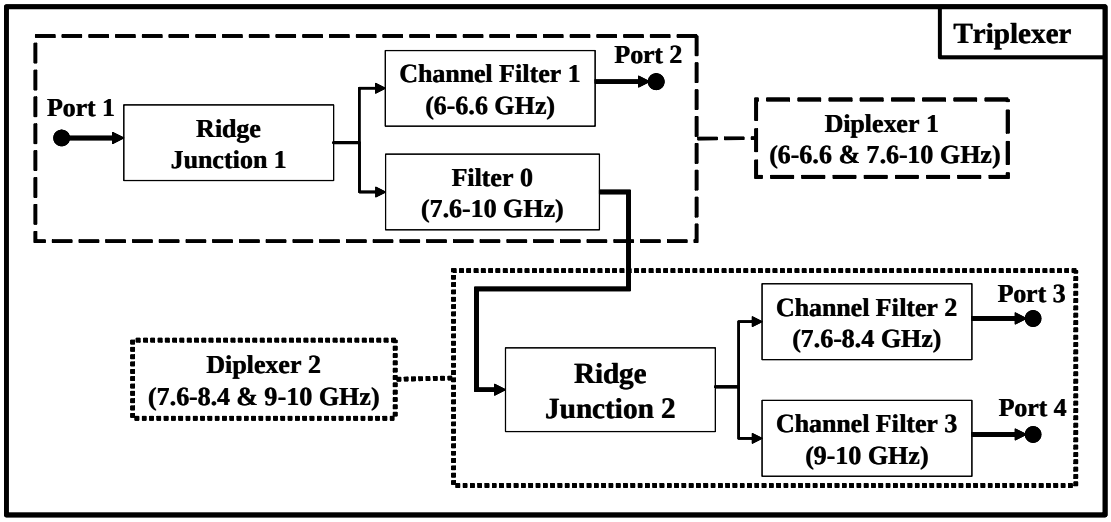

Figure 4.8: Triplexer configuration by cascading two diplexers using ridge waveguide divider junctions.

ponent which is proper for diplexer design. To make a triplexer design with such junctions, the configuration as in Fig. 4.8 is proposed. Basically, two diplexers using ridge waveguide divider junctions, diplexer 1 and diplexer 2, are cascaded together to fulfill the triplexer. The two channels of diplexer 1 are: 6.0 – 6.6 GHz and 7.6 – 10.0 GHz, with the second channel covering the whole frequency band of channel filter 2 and 3 of the triplexer. Diplexer 2 consists of two channels that are identical as channel filter 2 and 3 of the triplexer. A triplexer is, therefore, expected if well designed diplexer 1 and diplexer 2 are cascaded together. The second channel filter of diplexer 1 is named as filter 0 in Fig. 4.8 for later discussion. This configuration of triplexer maintains the advantage of compactness and is appropriate for system integration.

Fig. 4.9(a) shows the structure of diplexer 1 which consists of filter 0 (bottom branch) and filter 1 (top branch). Fig. 4.10(a) shows the structure of diplexer 2

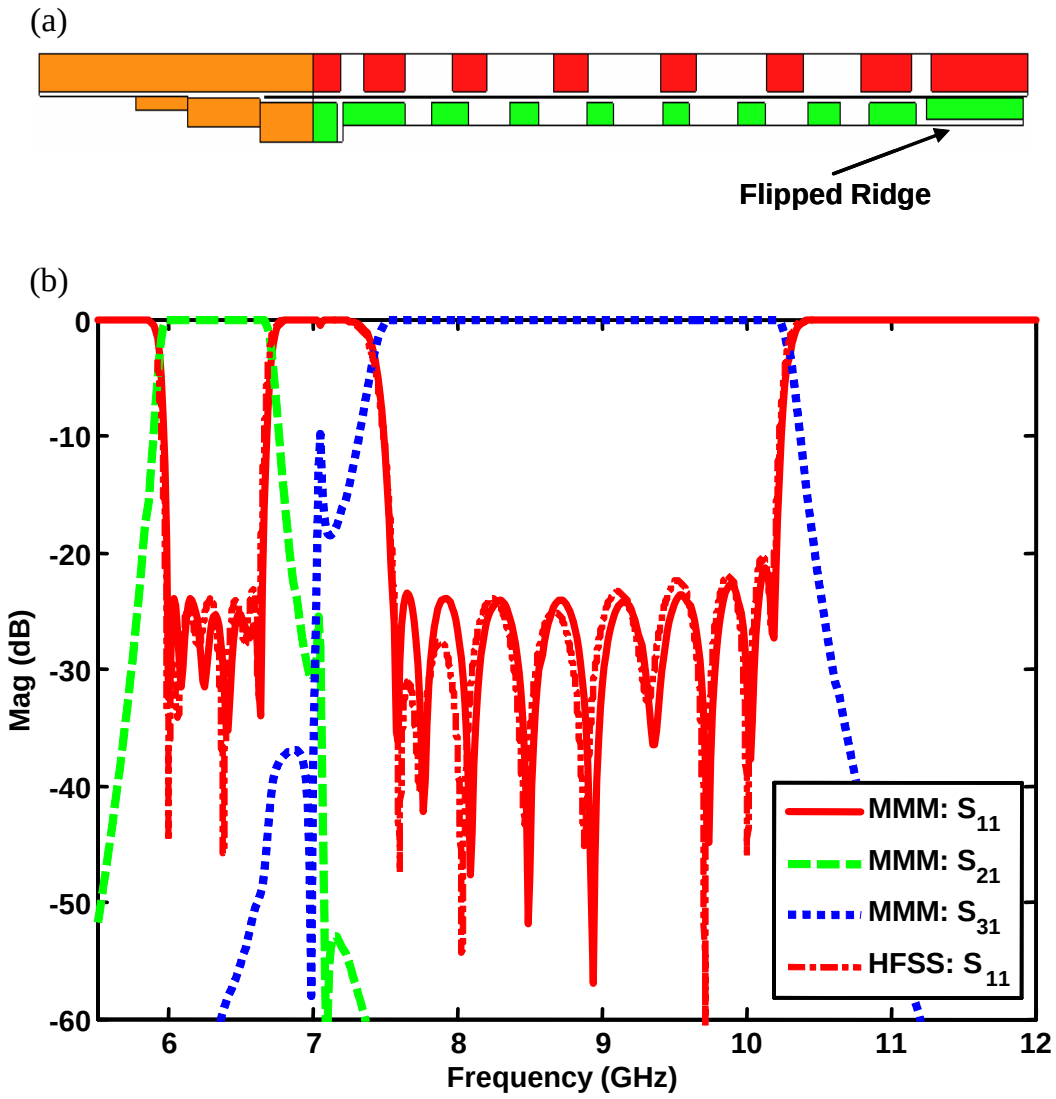

Figure 4.9: (a) side view of diplexer 1 for the triplexer design. (b) Simulated response of diplexer 1 by MMM and HFSS.

which consists of filter 2 (top branch) and filter 3 (bottom branch). All the filters are ridge waveguide evanescent-mode bandpass filters. The output waveguide of filter 0 is a flipped ridge waveguide (as in Fig. 4.9(a)) with respect to other ridge waveguide resonators inside the filter (i.e. the *interdigital* coupling arrangement is used to realize the output coupling). The purpose by doing this is to be able

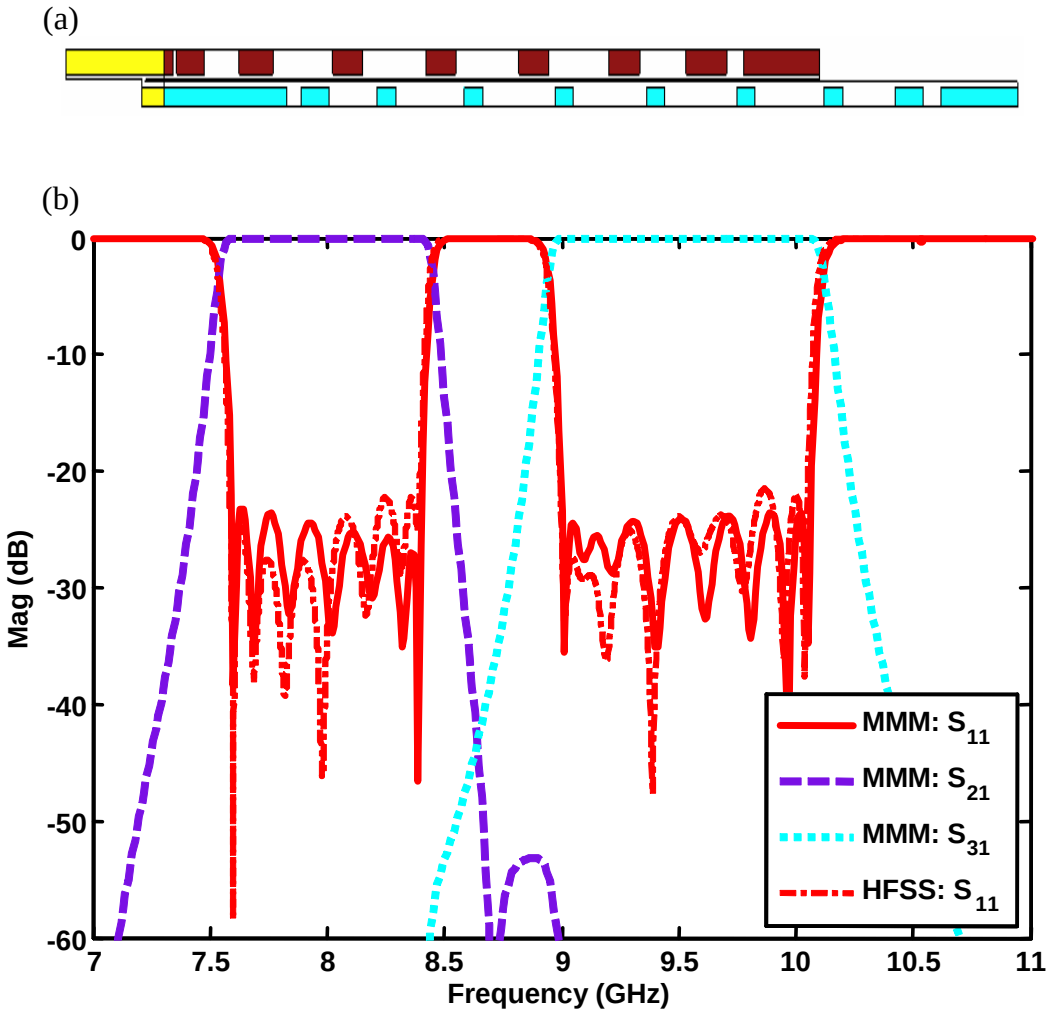

Figure 4.10: (a) Side view of diplexer 2 for the triplexer design. (b) Simulated response of diplexer 2 by MMM and HFSS.

to connect it with diplexer 2 (otherwise, two diplexers will be overlapped). The design procedure of the two diplexers is similar as the previous diplexer example. Fig. 4.9(b) and Fig. 4.10(b) are the simulated responses by MMM and HFSS for diplexer 1 and 2, respectively. HFSS response shows very good agreement with MMM for both designs.

The triplexer is realized by cascading the two designed diplexers together.

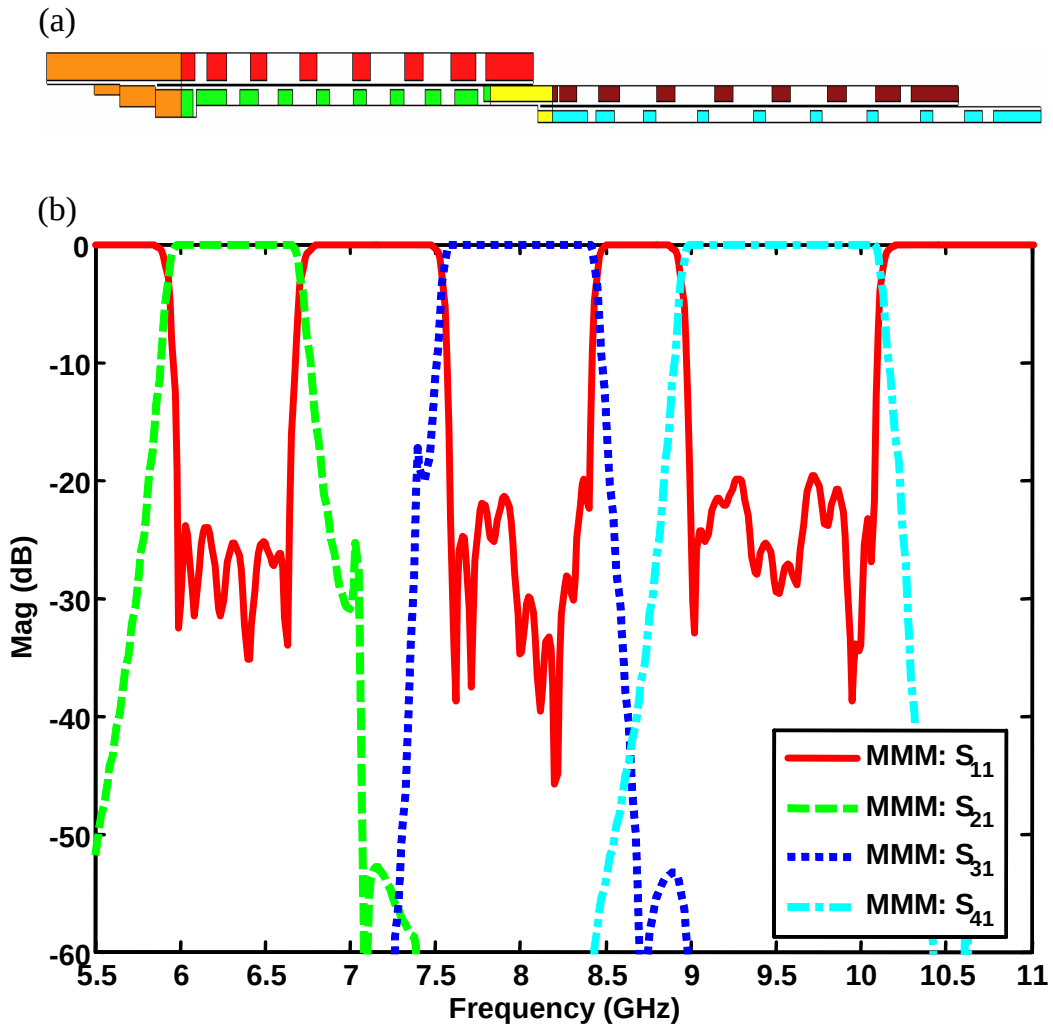

Figure 4.11: (a) Side view of the triplexer structure fulfilled by two cascaded diplexers. (b) Simulated response in MMM.

The side view of the triplexer structure is shown in Fig. 4.11(a). Usually the triplexer response will satisfy the requirements if the two diplexers are well designed. It is possible that the performance is slightly worse than the requirements. In this case, the connection waveguides between components can be optimized to improve the performance. There is usually no need to change other dimensions. The simulated triplexer response by MMM is shown in Fig. 4.11(b), which satis-

fies all the desired requirements. The housing dimensions of the whole triplexer are about:$width \times height \times length = 200mil \times 149.6mil \times 4276mil$.

4.3 Waveguide Multiplexers for Space Applications

4.3.1 Introduction

Multiplexers for space applications, e.g. satellite payload system, are desired to have good performance in four aspects. Firstly, the lowest possible insertion loss is desired in each channel filter, especially in the transmitting channel, to obtain optimal efficiency with the limited power of the spacecraft or satellite. Secondly, The lowest possible mass and compact size are sought due to the high launch cost of a payload. Thirdly, the highest possible power handling capability is aimed in order to include more carriers in the transmitting channel and avoid the multipaction discharge. Fourthly, the largest possible working temperature range is wanted to overcome the severe environmental condition in space. In order to achieve an optimum solution concerning these decisive deign goals, the manifold multiplexing technique is most commonly used [3].

A modern satellite payload system usually requires three different type of multiplexers: the diplexing or multiplexing antenna feed system, the input multiplexer (IMUX) to split the carriers into the power amplifiers (usually traveling wave tubes), and the output multiplexer (OMUX) to combine the carriers into the

transmitting channel. In this section, the diplexer and multiplexer for antenna feed system are discussed and designed. In order to limit the experimental expense, a complete CAD procedure is employed to design these multiplexers with the considerations of insertion loss, mass and volume, multipaction effect, and temperature drifting. More importantly, the manufacturing tolerance has been taken into account at the design step, and therefore, the designed multiplexers need not be tuned after the manufacture.

Two frequency bands are normally used in satellite TV system: C band and Ku band. In this section, two multiplexers at the Ku band are designed for the antenna feeding in a satellite payload system that is used to receive the *uplink* signal and transmit the amplified *downlink* signal. The complete design procedure and necessary considerations related to the above-mentioned design goals are demonstrated through these two multiplexer examples.

4.3.2 Multiplexer Configuration and Modeling

Metallic waveguides are used in the multiplexer structures in order to achieve low insertion loss and high power handling capability. Waveguide E-plane T-junctions as shown in Fig. 4.12(a) are employed to fulfill a manifold and connect the channel filters. Compared with the typical manifold multiplexer, the multiplexers in this section use a slightly different configuration as shown in Fig. 4.12(b). The channel filters are sequentially connected to the T-junctions of the manifold according to their center frequencies. Instead of a short circuit at the opposite end of

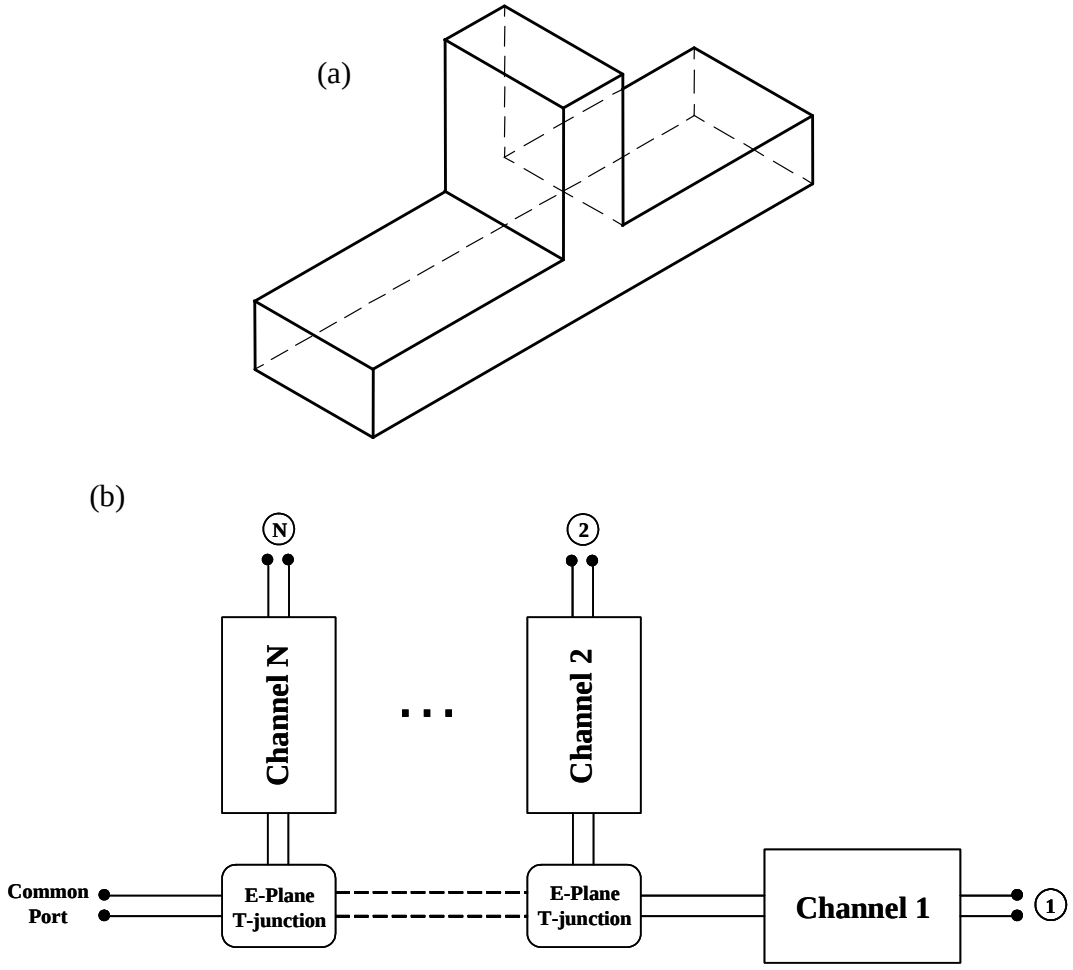

Figure 4.12: (a) E-plane waveguide T-junction. (b) Multiplexer configuration.

the common port (one typical arrangement of normal manifold multiplexers), one channel filter is connected there to avoid using one more T-junction in the manifold. In Fig. 4.12(b), the center frequencies of channel filter 1 to N are in ascending order from the lowest value to the highest one. Therefore, channel filter 1 is usually for the transmitting channel since the downlink frequencies are smaller than the uplink ones.

A stepped impedance waveguide lowpass filter structure as shown in Fig.

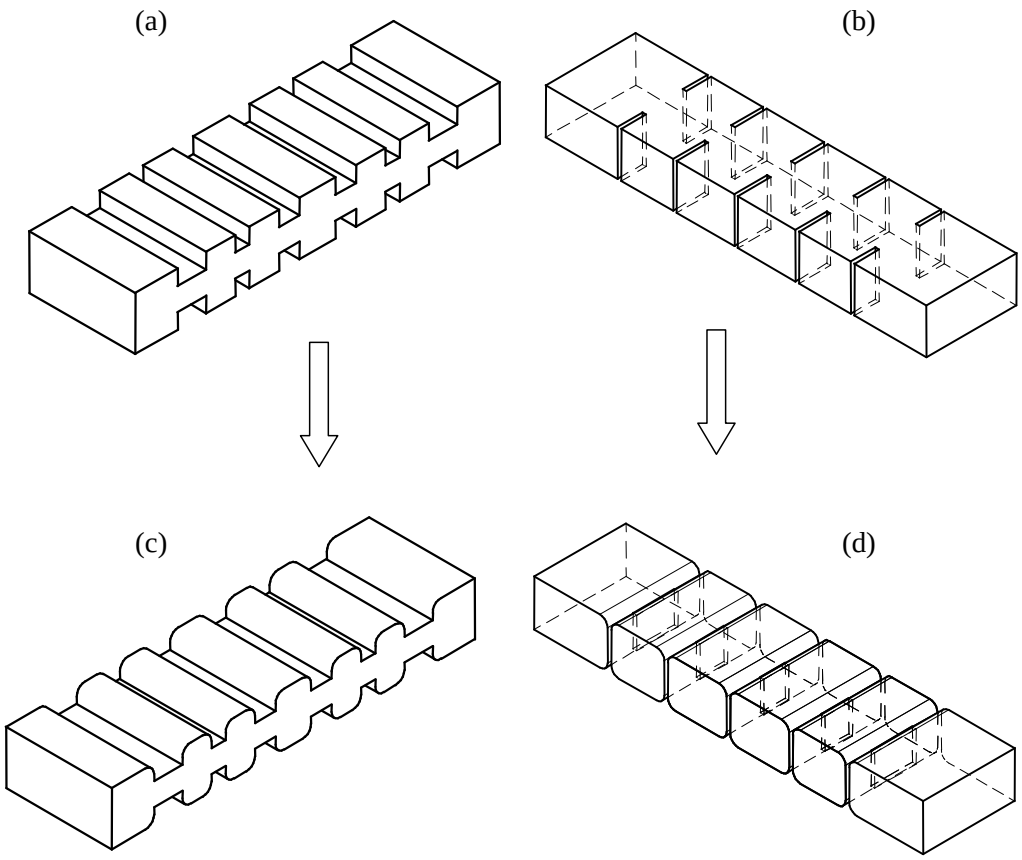

Figure 4.13: The filter structures employed in the multiplexers. (a) Stepped impedance waveguide lowpass filter. (b) Waveguide inductive window bandpass filter. (c) Waveguide lowpass filter with E-plane round corners. (d) Waveguide bandpass filter with E-plane round corners.

4.13(a) is employed for the transmitting channel because such lowpass filter structures usually have better insertion loss performance and higher power handling capability than other waveguide bandpass filter structures. Basically, two waveguides with different heights (impedances) are used to represent the inductors and capacitors in a lowpass filter. It is possible to use a lowpass filter for the transmitting channel because the transmitting channel is usually sitting in the lowest frequency

range of a multiplexer. An inductive window waveguide bandpass filter structure as shown in Fig. 4.13(b) is used for the receiving channels in a multiplexer. Basically, waveguide resonators are coupled through the iris windows in between [1].

The multiplexers using the E-plane T-junctions and the two types of filter structures can be manufactured as one integrated element by the split-block housing fabrication procedure, i.e. the whole multiplexer structure is split into two halves along the symmetric plane (magnetic wall). The multiplexers are expected to operating correctly right after the manufacturing, which means that tuning screws are not needed in the physical structures. However, in reality, the round corners resulting from the manufacturing process are not avoidable due to the finite tool radius. This corner problem is not serious for multiplexers at low frequency bands, but it becomes critical as the operating frequency band moves to millimeter-wave frequency, e.g. Ku band in this section, since the dimensions of the multiplexers are now comparable with the round corners. To overcome this corner problem, modified filter structures, as shown in Fig. 4.13(c) and (d), are used instead of the ideal ones as in Fig. 4.13(a) and (b). In the two modified filter structures, E-plane round corners are included in the designs. The performance of manufactured multiplexers using such modified filters can be maintained almost identical as the designed one. The modified filters also allow the use of relatively large radius tools, which can reduce the manufacturing difficulty and lower the cost.

The E-plane T-junction can be modeled in MMM using either the three-

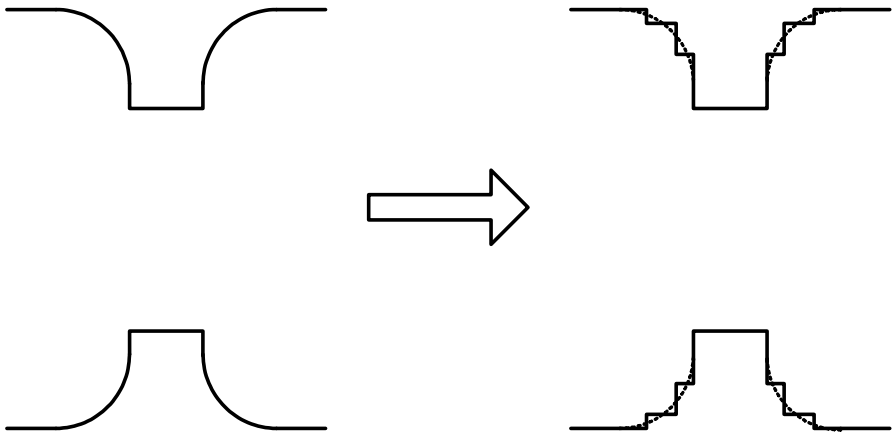

Figure 4.14: Approximation of round corner by waveguide steps for analysis.

plane matching method [211] or the GAM method discussed before. The GAM method is employed in this section (Detailed formulations can be found in [10, 35], and are not listed here.) since the three-plane matching method has the disadvantage that only one mode is considered in the vertical arm of the junction. The filters having round corners can be modeled in MMM with approximated structures for the corners. The E-plane round corners are discretized as a number of waveguide steps, as shown in Fig. 4.14, such that the round corner discontinuity can be regarded as a cascade of several waveguide steps connected by waveguide sections with different heights. Usually, the more steps are used, the more accurate result will be obtained. However, the simulation speed will be slower with the more number of steps. Typically, using $3 - 5$ steps is an appropriate choice. It should be noted that the number of modes used in MMM to analyze these waveguide steps is a very important factor to obtain a converged result. If too few or too many modes are used in the analysis, the result will not be converged correctly. In practical design, the result solved in MMM can be compared with the result

from other numerical methods, e.g. HFSS, and the number of modes employed in MMM can be determined accordingly. The formulations used in MMM program for a waveguide step discontinuity can be found in [3, 10, 35].

The lowpass filter is designed using the stepped-impedance lowpass filter theory [2]. The port waveguide dimensions, width a_0 and height b_0, are decided first according to the operating frequency range and the interface to other components. The height dimensions, b_h and b_l, of the high-z and low-z waveguides (they have the same width as the port waveguide) are then determined based on the power handling consideration and the stopband rejection requirement. The initial lengths of the waveguides are given as

$$l_h = \frac{Lb_0}{\beta_h b_h} \text{ and } l_l = \frac{Cb_l}{\beta_l b_0} \tag{4.2}$$

where L and C are the inductances and capacitances in the circuit model of the lowpass filter, respectively. l_h and l_l are the corresponding lengths of the high-z and low-z waveguides. β_g, $g = (h, l)$, is the propagating constant of the waveguide at the cutoff frequency f_0 of the lowpass filter, which is given as

$$\beta_g = \frac{2\pi\sqrt{f_0^2 - f_{c,g}^2}}{c} \tag{4.3}$$

where $f_{c,g}$ is the cutoff frequency of the fundamental mode of the waveguides. c is the speed of light in vacuum. Finally, the optimization procedure in MMM is applied to acquire the desired filter performance. Once round corners are included in the lowpass filter, the frequency response will be shifted slightly higher. The lengths of the high-z waveguides can be tuned longer to compensate the shifting effect. A second optimization procedure may be needed too.

The bandpass filter is designed based on the k-inverter method [1]. The round corner approximated by the waveguide steps should be included in the MMM analysis to calculate the inverter values. Optimization is also required to improve the filter performance. The analysis and optimization of the whole multiplexer in MMM have been discussed before, and are ignored here.

4.3.3 Multipaction Consideration

The transmitting filter in a multiplexer can suffer malfunctions if multipaction discharges are present during its life cycle. Multipaction discharge is a resonant vacuum discharge which is actually an avalanche caused by secondary electron emission [212, 213]. Primary electrons accelerated by microwave fields can impact a surface and release a larger number of secondary electrons, which may in turn be accelerated and impact a surface again to release even more electrons. Hence, a resonant discharge occurs. Multipaction phenomena can dissipate substantial amounts of energy fed into microwave structures. It can detune a microwave signal and heat the surface, possibly increasing noise levels and perhaps causing damage. In some circumstances, multipaction may even induce vacuum breakdown. For satellite application, a multipaction discharge can lead to a failure in the whole satellite transponder. The space hardware, e.g. multiplexer in this section, needs to be extensively tested against multipaction before launch, which is usually a very expensive task. Sometimes, a device may have to be redesigned and tested until a free of multipaction performance is achieved.

In order to reduce development time and cost, it is necessary to assess the multipaction risk in the devices before actual manufacturing and testing. A lot of efforts have been made towards the accurate modeling and prediction of multipaction risk in high power satellite components. In [214] and [215], an approximate method based on circuit models was developed for the calculation of the peak voltage inside bandpass filters and multiplexers. More recently, the voltage magnification factor (VMF) was introduced to estimate the multipaction risk [216]. The VMF is calculated provided that the electromagnetic fields are accurately known inside the structure. The method using VMF to estimate the multipaction threshold in a structure is discussed next.

Given a designed component, the electromagnetic analysis using numerical methods, e.g. HFSS, is used to find the peak voltage inside the structure. The VMF can be calculated as

$$VMF(f) = \frac{V_{peak}(f)}{V_{in}^{+}(f)} \tag{4.4}$$

where V_{peak} is the total peak voltage at the multipaction analysis plane, and V_{in}^{+} is the peak forward voltage at the input port. The multipaction threshold P_m is then calculated using the equation

$$P_m = \frac{V_{th}^2(f)}{2Z_0(f)VMF^2(f)} \tag{4.5}$$

where V_{th} is the peak threshold voltage of multipaction discharge which can be calculated using the multipaction susceptibility curve generated by ESA [217]. Z_0 is the impedance of the employed transmission structure, i.e. waveguide in this

section. The multipaction margin M_m can, therefore, be estimated as

$$M_m = \begin{cases} 10\log(\frac{P_m}{P_i}), \text{ for single carrier devices} \\ 10\log(\frac{P_m}{N^2 P_i}), \text{ for multiple carrier devices} \end{cases} \tag{4.6}$$

where P_i is the desired peak power of each carrier. N is the number of carriers in a multi-carrier device. Usually, the margin is expected to be larger than 6 dB or 3 dB to obtain a free of multipaction device.

However, the above method is not applicable in some cases for multi-carrier devices. Another method is proposed to calculate the maximum permissible power per carrier based on *20-gap-crossing-rule* [218]. The rule states: *as long as duration of multi-carrier peak and mode order gap are such that no more than 20 gap crossings can occur, during the multi-carrier peak, the design may be considered safe with regards to multipaction even though the multipaction threshold may be exceeded from time to time.* This is because the multipaction discharges are so short that the generated noise and harmonics have no effects on system performance.

In this section, a waveguide stepped impedance lowpass filter is employed for the transmitting channel in a multiplexer. It is possible to estimate the multipaction margin of such a filter with a stand-alone waveguide structure since there is no resonating cavity in the filter. The estimation is actually performed in a multipaction calculator [219] created by Strijk in ESA/ESTEC that can be used to perform single- and multi-carrier multipaction analysis on parallel gap, microstrip, stripline, coaxial and waveguide components.

The multipaction threshold is dependent on the surface material. Four typ-

Table 4.3: The specifications of a Ku band diplexer. All the interface waveguides should be WR75. 12 carriers are operating in the diplexer with the power of each at 85 W. Isolation means channel to channel rejection level. TR represents the operating temperature range.

Ch. #	Passband (GHz)	IL (dB)	RL (dB)	Isolation (dB)	TR ($^{\circ}C$)
1	11.7 – 12.2	≤ 0.14	≥ 20.8	≥ 55 in Ch. 2	-40 to 140
2	14.0 – 14.5	≤ 0.14	≥ 20.8	≥ 70 in Ch. 1	-40 to 140

ical materials are usually employed in reality, and they are given in an ascending order of the multipaction threshold as: Aluminum, Copper, Silver, and Gold. Aluminum is normally preferred for the hardware manufacturing because of its light weight and low cost. In order to improve the power handling capability of Aluminum, a chromium free conversion coating process called Alodine can be used to treat the Aluminum. The multipaction threshold of a surface after Alodine finishing is much larger than Copper and slightly smaller than Silver. The multiplexers designed in the section will be manufactured in Aluminum and treated by Alodine process.

4.3.4 Diplexer Example

A diplexer at Ku band is designed to demonstrate the design procedure. The specifications of the diplexer are given in Table 4.3. All the interface waveguides must be WR75 (0.75×0.375 inch). The diplexer is expected to handle simulta-

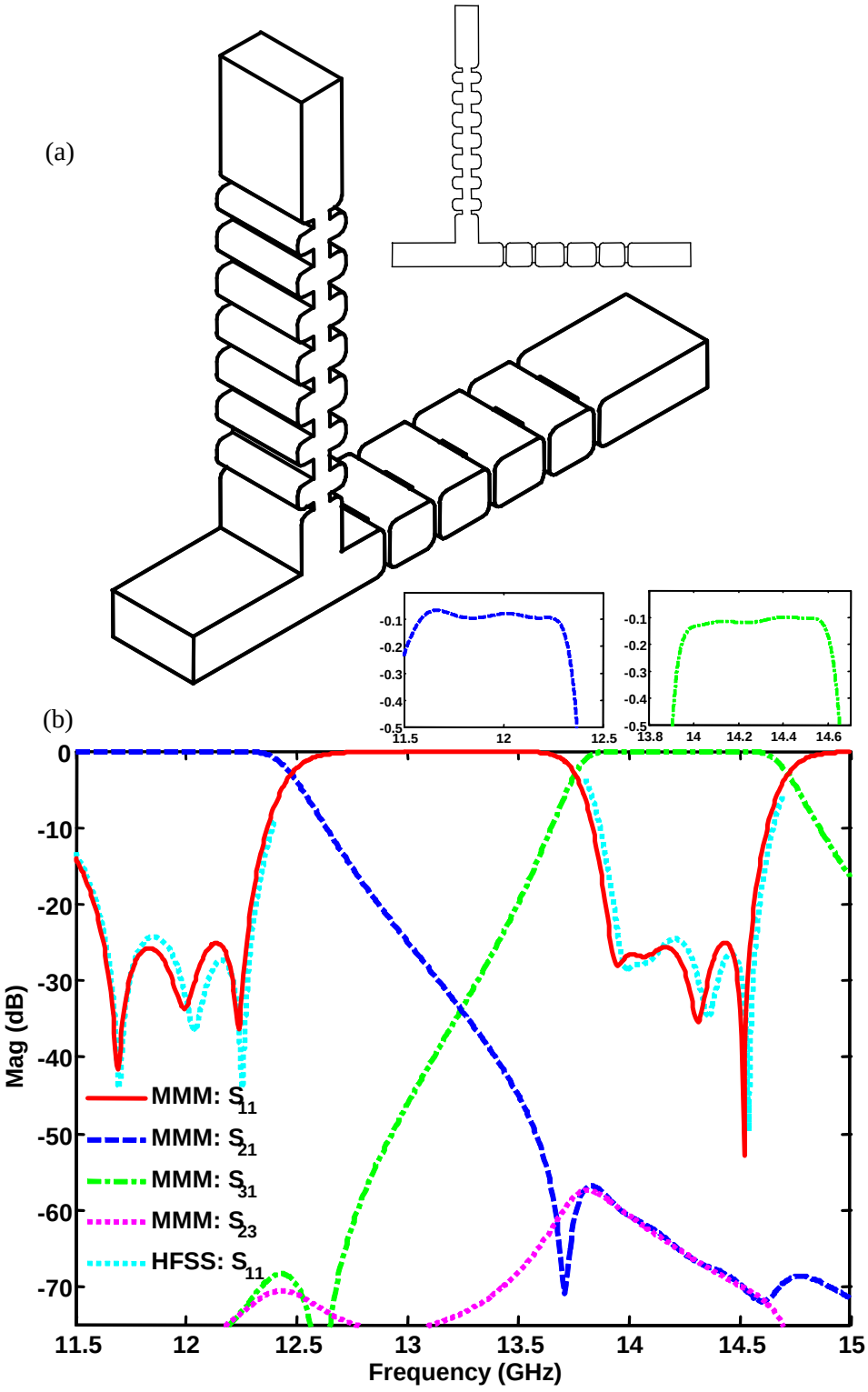

Figure 4.15: (a) The Ku-band diplexer structure. (b) The simulated diplexer response in MMM and HFSS.

neously RF power of 12 carriers with each at 85 W. In single carrier analysis, the transmitting filter should have a multipaction margin larger than 3 dB. In multiple carrier analysis, 6 dB or greater margin between the 20-gap-crossing multipaction power and the applied power levels should exist.

In order to compensate the effect of the temperature drifting, the designed filter bandwidths are enlarged 100 MHz wider than the required bandwidths, i.e. the channel passbands are designed to be: 11.65 – 12.25 GHz and 13.95 – 14.55 GHz. A 3 dB or more margin for return loss and isolation is achieved between the designed filters and the required ones to compensate the possible performance degrading due to the manufacturing tolerance.

For the waveguide lowpass filter, the height of the low-z waveguide is determined according to the requirement of the multipaction margin. The height should be selected as the lowest possible value to reduce the filter volume. By using the tool of multipaction calculator, the height of the low-z waveguide is decided to be 0.15 inch to have a 3.36 dB multipaction margin with Alodine surface finishing. The height of the high-z waveguide is determined to be 0.45 inch to achieve a 60 dB isolation in the receiving band with a 15-order lowpass filter. A 4-order bandpass filter is used for the receiving filter to achieve a 73 dB isolation in the transmitting band.

The designed filter structure is shown in Fig. 4.15(a). The simulated responses of the diplexer in MMM and HFSS are shown in Fig. 4.15(b). A good agreement can be noticed. This diplexer is being made of Aluminum. To estimate the insertion loss of each channel, a HFSS simulation is performed with the con-

Table 4.4: The specifications of a Ku band triplexer. The interface waveguides are: WR62 for the common port and Ch. 3; WR75 for Ch. 1 and 2. Isolation means channel to channel rejection level. TR represents the operating temperature range.

Ch. #	Passband (GHz)	IL (dB)	RL (dB)	Isolation (dB)	TR ($^{\circ}C$)
1	11.7 – 12.2	≤ 0.14	≥ 20.8	≥ 40 in Ch. 2&3	-40 to 140
2	14.0 – 14.5	≤ 0.14	≥ 20.8	≥ 40 in Ch. 1&3	-40 to 140
3	17.3 – 17.8	≤ 0.14	≥ 20.8	≥ 40 in Ch. 1&2	-40 to 140

sideration of the loss from Aluminum (the conductivity of Aluminum is taken as $\sigma = 33000000\ S/m$). The insertion loss responses for both channels are also shown in Fig. 4.15. The insertion loss for the transmitting (receiving) channel is less than 0.1 dB (0.14 dB) over the whole passband, which satisfies the requirement.

4.3.5 Triplexer Example

The specifications of the triplexer example is given in Table 4.4. The interface waveguides are: WR62 (0.622×0.311 inch) for the common port and channel filter 3; WR75 for channel filter 1 and 2. Therefore, two WR62 E-plane T-junctions are used in this triplexer. For channel filter 1 and 2, one port waveguide is taken as WR62 to connect with the T-junction, while the other port is WR75 for the output. For channel filter 3, both ports are WR62. Enough margins should be also gained during the design step for the temperature compensation, the multipaction

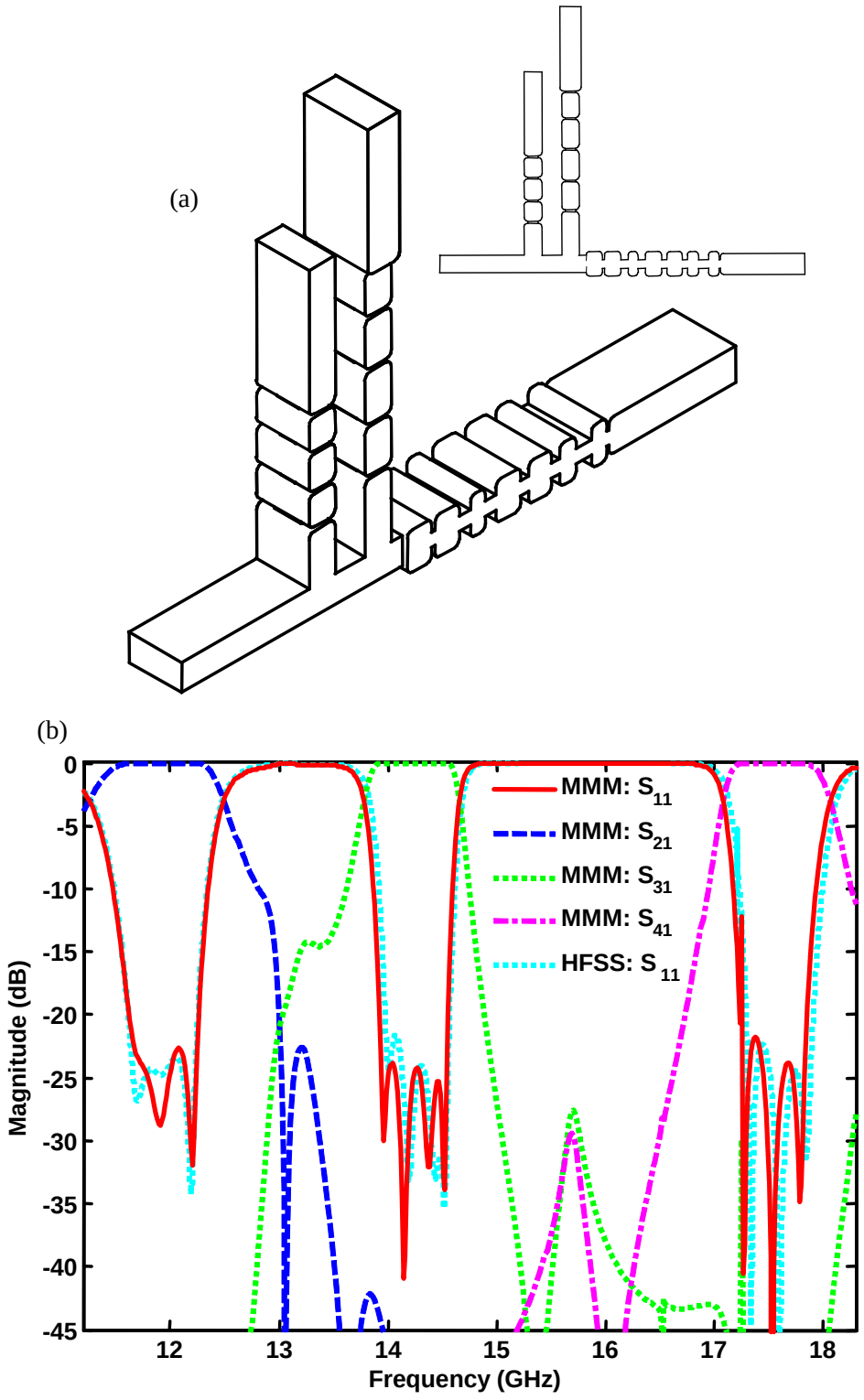

Figure 4.16: (a) The Ku-band Triplexer structure. (b) The simulated responses in MMM and HFSS.

margin, the return losses, and the channel to channel isolations.

The channel filter 1 and 2 can be designed with the same waveguide for both ports first. One port is then replaced by the required interface waveguide, which usually degrades the filter performance. Optimization can be applied again to achieve the desired filter requirements. The designed triplexer structure and simulated responses are shown in Fig. 4.16(a) and (b), respectively. A good agreement can be seen between the responses from MMM and HFSS.

4.4 LTCC Multiplexers Using Stripline Junctions

4.4.1 Introduction

With the development of the LTCC technology, it is desirable to integrate all the components of a microwave system into one single circuit board. The microwave passive components, e.g. filters and multiplexers, are usually placed underneath other active components due to their bulk size. Stripline structures are the most common choices for microwave passive components in a circuit board because of their practical features, namely compact size, wide applicable frequency range, easy processing in LTCC, and convenient connection with active elements [220]. A major drawback of stripline structures is the high loss, which is very critical for filters and multiplexers. Nevertheless, stripline and waveguide structures can be combined together for the realizations of filters and multiplexers to improve the insertion loss, e.g. ridge waveguide coupled stripline resonator filters presented in

Sec. 3.4 (p. 132).

In this section, novel multiplexer/diplexer configurations using stripline junctions are presented. They are applicable to LTCC applications and can be integrated easily with other components. A good insertion loss performance is also able to be achieved. Such multiplexers can be rigorously designed in MMM, which guarantees their performance after the manufacturing in LTCC (In practice, it is no possible to tune a LTCC component.). A diplexer example is designed in this section to show the validity of the concept.

4.4.2 Multiplexer Configuration

Two types of stripline junctions can be employed for the multiplexer structure: stripline bifurcation junction and stripline manifold junction as shown in Fig. 4.17(a) and (b), respectively. Stripline bifurcation junction is appropriate for a diplexer design with relatively broad bandwidth ($> 30\%$) and high integration requirement, while stripline manifold junction is a good choice for multiplexer designs with relatively narrow bandwidths ($< 20\%$). A transformer is usually required in the bifurcation junction to improve the matching. These two junctions can be modeled by MMM with the theories of GSM and GAM, respectively [35].

Ridge waveguide coupled stripline resonator filters are used for the channel filters in a multiplexer to gain a good insertion loss performance. Shown in Fig. 4.17(c) is a typical filter structure. Compared with the filter structure in Fig. 3.37(a) (p. 135), the external couplings of the filter in Fig. 4.17(c) are provided

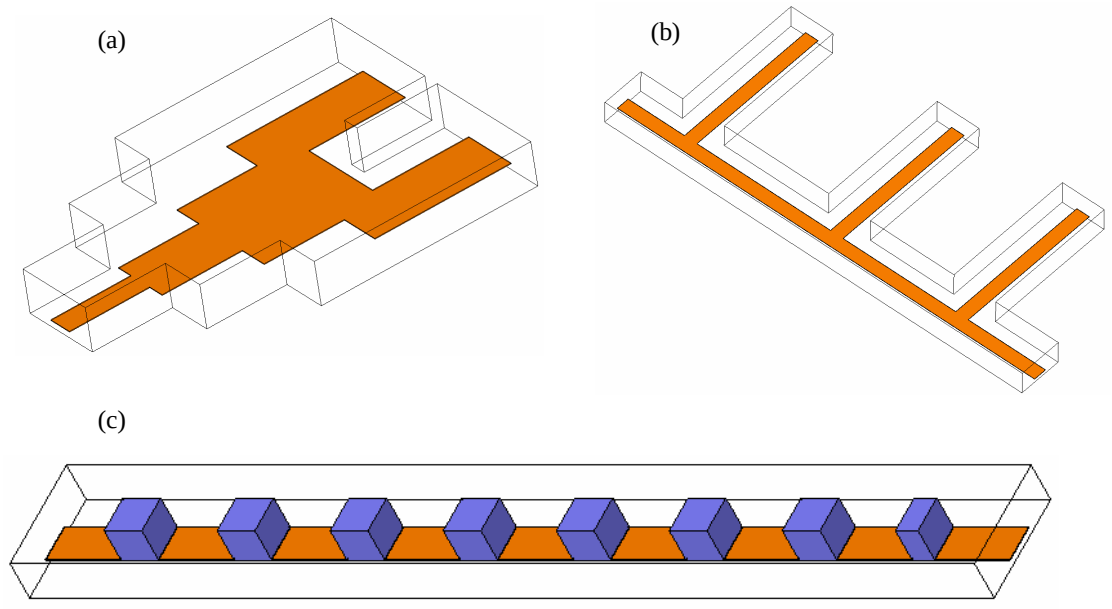

Figure 4.17: (a) Stripline bifurcation junction. (b) Stripline manifold junction composed of stripline T-junctions. (c) Ridge waveguide coupled stripline resonator filter.

by ridge waveguide coupling sections instead of tapped-in structures. Even though the filter bandwidth is relatively narrower than before, a better multiplexing performance will be obtained once the filter is connected to the junction.

The multiplexer modeling is performed in MMM by cascading the GSMs of the junctions and filters (using GTR as in Appendix A and C). The detailed discussion has been given before, and is ignored here.

4.4.3 Diplexer Example

A diplexer example is designed to validate the concept. The specifications are given in Table 4.5. The relative bandwidth of the whole diplexer is about 32%. The relative bandwidths of the two channel filters are about 12% and 10%, re-

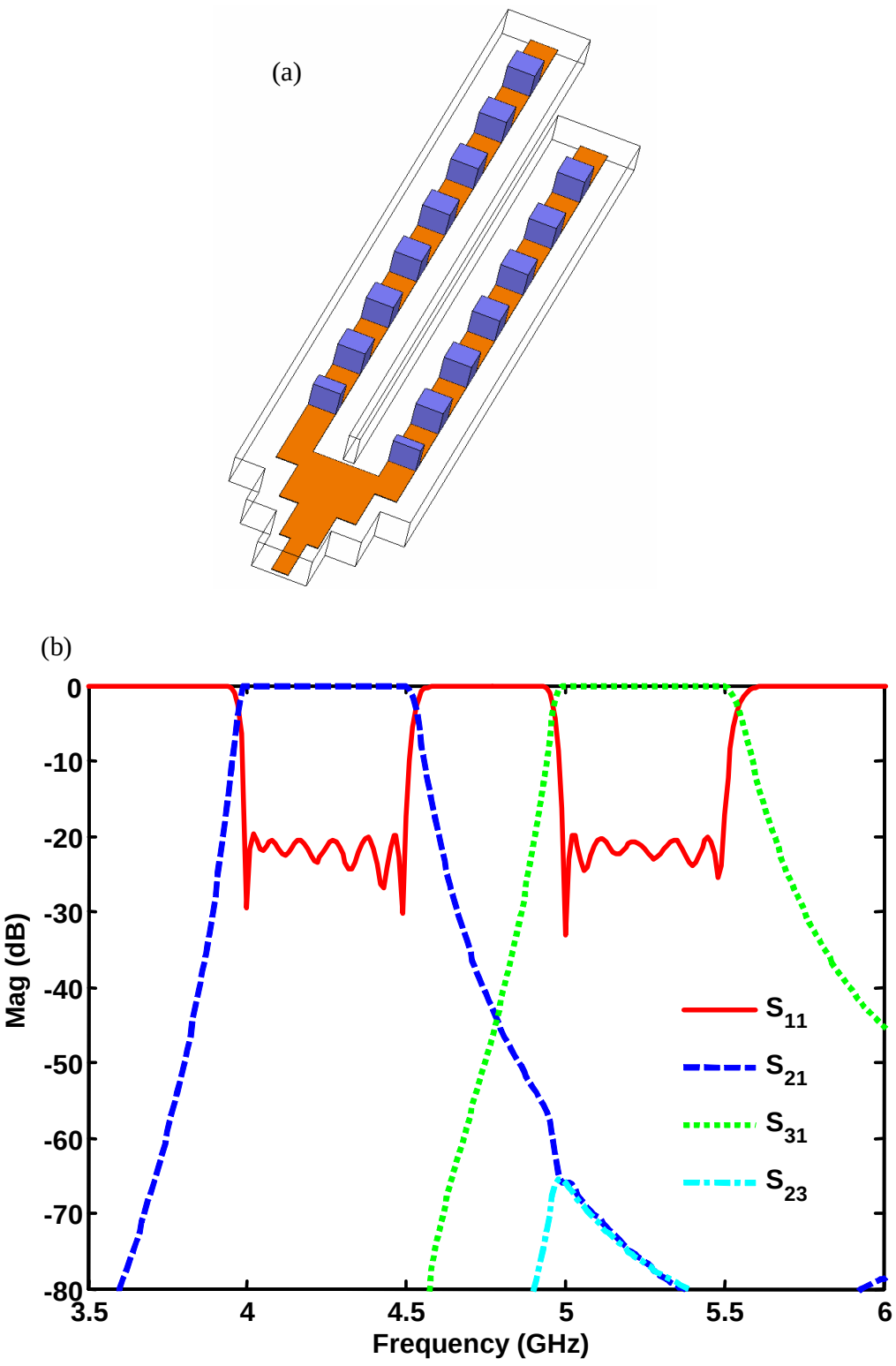

Figure 4.18: (a) Diplexer structure. (b) Simulated responses in MMM.

Table 4.5: The specifications of a diplexer using stripline bifurcation junction in LTCC technology.

Channel	Passband (GHz)	Return Loss (dB)	Isolation (dB)
1	4 – 4.5	≥ 20	≥ 50 in Ch. 2
2	5 – 5.5	≥ 20	≥ 50 in Ch. 1

spectively. This diplexer is expected to be realized in LTCC technology. The LTCC parameters are: relative permittivity of ceramic $\varepsilon_r = 5.9$, thickness of metallization $ts = 0.4mil$, and thickness of each ceramic layer $tc = 3.74mil$.

The designed diplexer structure is shown in Fig. 4.18(a). A stripline bifurcation junction is employed. The two channel filters are implemented as seven- and six-order bandpass filters, respectively. The simulated response by MMM of the designed diplexer is shown in Fig. 4.18(b), which satisfies all the requirements.

4.5 Wideband Diplexer Using E-plane Bifurcation Junction

4.5.1 Design Task and Diplexer Configuration

One wideband diplexer, in which one channel filter is in K band and the other one is in Ka band, is desired to be designed and manufactured in metallic waveguide structures. A compact configuration that is suitable for quasi-planar printed cir-

Table 4.6: The specifications of a wideband diplexer using E-plane bifurcation junction.

Channel	Passband (GHz)	Return Loss (dB)	Isolation (dB)
1	19 – 23	≥ 18	≥ 50 in Ch. 2
2	29.5 – 31	≥ 18	≥ 50 in Ch. 1

cuit technology is required for this diplexer. The detailed specifications are given in Table 4.6. The relative bandwidth of the whole diplexer is about 50%. The two channel filters have relative bandwidths of about 20% and 7%, respectively. A standard waveguide WR34 (0.34×0.17 inch) must be used for all three ports of the diplexer.

A waveguide junction structure must be selected first to satisfy two conditions: wideband common-port matching and compact size suitable for integration. An E-plane bifurcation junction as shown in Fig. 4.19(a) is an appropriate choice. The advantages of such a junction include [3]: i) a very good matching can be achieved over a wide frequency band. ii) It is compact, low-cost, and can be used in quasi-planar printed components. iii) It is appropriate for E-plane split-block housing fabrication. iv) the transformer is less complicate and easier to design than H-plane junctions owing that the waveguide division plane is an electric wall for the fundamental mode. The designed junction response is shown in Fig. 4.19(b), which demonstrates a power divider performance and a very good matching at the common port over the whole operating frequency band.

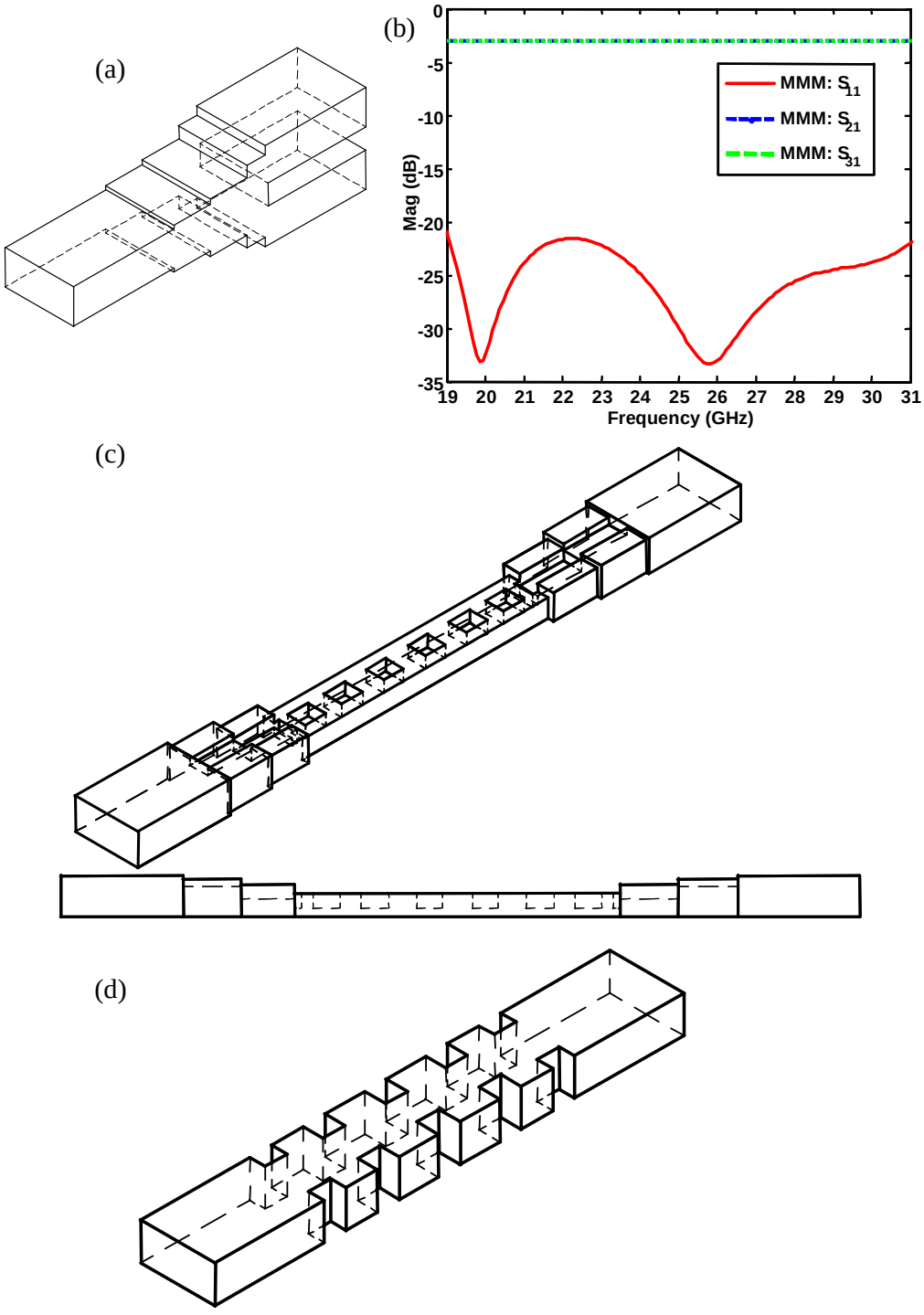

Figure 4.19: (a) E-plane waveguide bifurcation junction. (b) Simulated response of the junction. (c) Ridge waveguide filter structure with transformers. (d) Iris coupled waveguide filter structure.

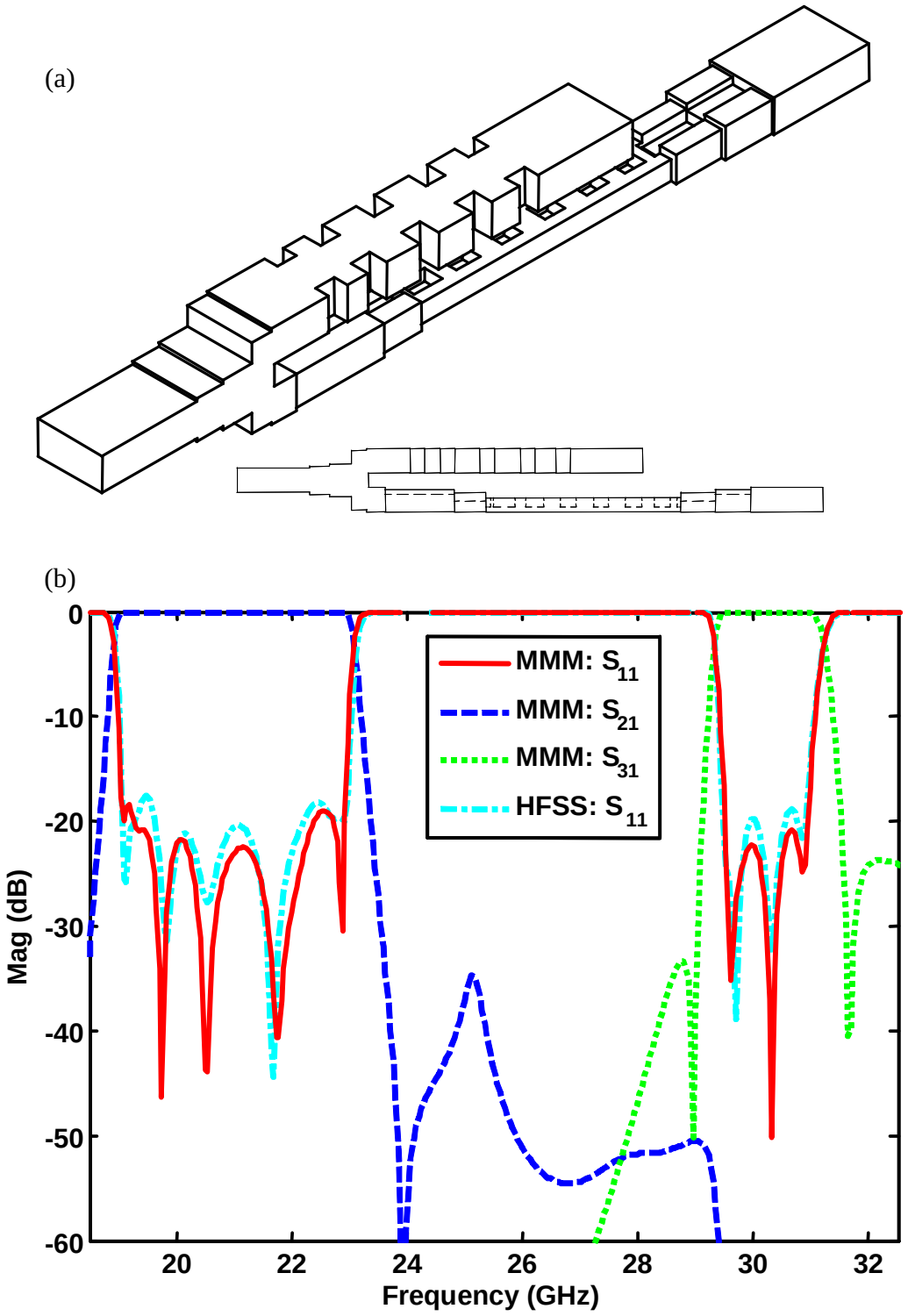

Figure 4.20: (a) The diplexer structure. (b) Simulated responses in MMM and HFSS.

A large separation exists between the passbands of the two channel filters. The stopband spurious response of channel filter 1 must be clean (>50 dB rejection) inside the passband of channel filter 2. If a bandpass filter is used for channel filter 1, the higher order harmonic resonant modes must be outside the passband of the channel filter 2, otherwise, a *stop notch* will be generated in channel filter 2. In order to have a broad bandwidth along with acceptable spurious performance, a ridge waveguide evanescent-mode bandpass filter as shown in Fig. 4.19(c) is employed to implement channel filter 1 because available rectangular waveguide filters are unlikely to achieve the requirements. Two transformers from ridge waveguide to rectangular waveguide are also included in the filter structure for the sake of connection with the above junction. An iris coupled rectangular waveguide filter as shown in Fig. 4.19(d) is applied to realize channel filter 2.

4.5.2 Results

MMM is used to analyze and optimize each element and the whole diplexer. The formulations for E-plane bifurcation junction and waveguide step discontinuities can be found in [3, 10]. Actually, the E-plane bifurcation junction can be characterized as a generalized two-port network to simplify the analysis (see [35], p. 37). The ridge waveguide filter can be modeled by using the GTR technique as discussed in Appendix A and C. The designed diplexer structure is shown in Fig. 4.20(a). The simulated diplexer responses in MMM and HFSS are shown in Fig. 4.20(b), from which a good agreement can be noticed.

Chapter 5

Conclusions and Future Research

5.1 Conclusions

This dissertation has been devoted to the description of novel filter and multiplexer structures, the modeling and design of microwave components using numerical methods, the miniaturized realization of filters and multiplexers, and the systematic tuning of quasi-elliptic filters. The motivation is to develop optimum designs of microwave filters and multiplexers to meet continuously more demanding specifications. Several practical examples have been presented in this dissertation and proved to be successful to reach this goal.

Modern communication systems have created the need for multiple-band quasi-elliptic filters. An iteration procedure has been derived in Chapter 2 to obtain the polynomial expressions of the optimum multiple-band quasi-elliptic transfer function (i.e. the approximation procedure), from which different network topologies can be synthesized through the well-known synthesis methods.

The approximation procedure is generalized and effective for any number of passbands and stopbands in a multiple-band filter function. A powerful building-block technique has also been presented in Chapter 2 in order to synthesize versatile topologies. The effectiveness and powerfulness of the technique are evidenced by the given examples.

The generalized design methodologies of microwave filters and multiplexers have been discussed in Chapter 3 and 4. The modeling and design procedure can be applied to any structure, regardless of the geometry of the problems. Several novel filter and multiplexer designs have been presented to achieve the miniaturization and wideband performance, namely double- and multiple-layer coupled resonator filters, ridge waveguide coupled stripline resonator filters and multiplexers, and ridge waveguide divider-type multiplexers. Some other filters and multiplexers have been developed for high power applications, which are dual-mode filters in circular and rectangular waveguides ,and waveguide multiplexers using bifurcation, T- and manifold junctions. A systematic tuning procedure has also been created for the development of quasi-elliptic filters. The feasibility has been validated by a dielectric resonator filter example.

5.2 Future Research

This dissertation has concentrated on describing the modeling and design of microwave and millimeter-wave filters and multiplexers. Future research work of interest includes:

- Rigorous CAD of single- and multiple-band quasi-elliptic filters, especially the asymmetric filters, in waveguide and planar structures.
- Harmonic multiple-band filter designs with multiple-layer coupled resonator structures.
- Spurious performance improvement by using SIR technology in ridge waveguide and rectangular waveguide filters.
- Computer aided tuning of single- and multiple-band quasi-elliptic filters in coaxial TEM cavity and dielectric resonator technologies.
- Tunable filters in coaxial TEM cavity and dielectric resonator technologies.
- Multiple-mode filter designs in waveguide and dielectric resonator technologies.
- Multiport network synthesis and its application in diplexer and multiplexer designs.
- Miniaturization of waveguide filters and multiplexers in LTCC technology to achieve high quality.

Appendix A

Generalized Transverse Resonance (GTR) Technique[1]

A.1 Introduction

In this dissertation, many non-canonical waveguide geometries have been employed to design filters and multiplexers in mode matching method (MMM). Some of the waveguide cross-sections are shown in Fig. 1.4 (p. 13). One necessary step in MMM is to solve the eigenmodes and eigenfields of waveguide cross-sections. The modes of canonical waveguides, namely rectangular, circular, coaxial circular, and elliptical, can be obtained by analytical method [10, 12]. However, the modes of non-canonical waveguides need to be solved by approximated numerical methods. In this dissertation, the generalized transverse resonance (GTR) technique

[1] The formulations in this appendix have been presented in the Ph.D. thesis of Dr. J. A. Ruiz-Cruz [35]. They are repeated here just for completeness.

is used to acquire the modes of the used non-canonical waveguides.

The GTR is a well-known technique used to analyze waveguide cross-sections that can be segmented into rectangular coordinates. The literature in GTR is very extensive, and its theory and applications can be found in many references [14, 35, 45, 46, 49–51]. The complete GTR formulations for TEM, TE and TM modes have been detailedly presented in [35]. Nevertheless, the formulations are repeated again in this appendix since some new structures in this dissertations are analyzed by the GTR.

A.2 Problem Statement

It is well-known that the electromagnetic field in homogeneous waveguide can be described in terms of TEM, TE and TM modes. The theory of waveguides is well established and reported in many textbooks [7, 13]. The properties of TEM, TE and TM modes are summarized in Table A.1. The field of a TEM, TE or TM mode can be derived from a scalar potential Φ that is the solution of Laplace or Helmholtz equation with appropriate boundary conditions. Therefore, the objective is to find the cutoff wavenumber k_c of the modes and the associated scalar potential Φ. Once Φ is solved, the components of the eigenfield can be easily obtained by using the basic gradient operations in Table A.1.

In order to solve the eigenmodes and eigenfields of the non-canonical waveguides

[2]For a waveguide with $P+1$ conductors (each one with contour C_p), P TEM modes exist. The boundary conditions are $\Phi_m = \upsilon_{m,p}$ on C_p, $p = 1, 2, ..., P$. $\upsilon_{m,p}$ is a constant potential.

Table A.1: Properties of TE (h), TM (e) and TEM (o) modes of a homogeneous waveguide cross section [10, 35].

Property	Electric Field	Magnetic Field
Transv. Field	$\mathbf{E}_t = \sum_m \left(a_m e^{-\gamma_m z} + b_m e^{\gamma_m z}\right) \mathbf{e}_m$	$\mathbf{H}_t = \sum_m \left(a_m e^{-\gamma_m z} - b_m e^{\gamma_m z}\right) \mathbf{h}_m$
Modal vectors	$\mathbf{e}_m = \begin{cases} \sqrt{Z_m}\nabla_t \Phi_m \times \mathbf{u}_z, & \text{h} \\ \sqrt{Z_m}\nabla_t \Phi_m, & \text{e/o} \end{cases}$	$\mathbf{h}_m = \begin{cases} \sqrt{Y_m}\nabla_t \Phi_m, & \text{h} \\ \sqrt{Y_m}\mathbf{u}_z \times \nabla_t \Phi_m, & \text{e/o} \end{cases}$
Orthog.	$\int_S \mathbf{e}_m \cdot \mathbf{e}_n dS = 0$	$\int_S \mathbf{h}_m \cdot \mathbf{h}_n dS = 0$
Normliz.	$Y_m \int_S \mathbf{e}_m \cdot \mathbf{e}_m dS = 1$	$Z_m \int_S \mathbf{h}_m \cdot \mathbf{h}_m dS = 1$
Scalar potent.	On cross-section S: $\begin{cases} \nabla_t^2 \Phi_m + k_{c,m}^2 \Phi_m = 0, & \text{TE and TM} \\ \nabla_t^2 \Phi_m = 0, & \text{TEM} \end{cases}$	
Bound. cond.	On contour C: $\begin{cases} \nabla_t \Phi_m \cdot \mathbf{u}_n = 0 & \text{TE} \\ \Phi_m = 0 & \text{TM} \\ \nabla_t \Phi_m \cdot \mathbf{u}_t = 0 & \text{TEM}^2 \end{cases}$	
Propag. const.	$\gamma_m = \begin{cases} \sqrt{k_{c,m}^2 - \omega^2 \mu\varepsilon} & \text{TE or TM} \\ j\omega\sqrt{\mu\varepsilon} & \text{TEM} \end{cases}$	
Wave imped.	$Z_m = \begin{cases} \frac{j\omega\mu}{\gamma_m} = \frac{jk\eta}{\gamma_m} & \text{TE modes} \\ \frac{\gamma_m}{j\omega\varepsilon} = \frac{\gamma_m \eta}{jk} & \text{TM modes} \\ \sqrt{\frac{\mu}{\varepsilon}} & \text{TEM modes} \end{cases}$	

as shown in Fig. 1.4, a generic waveguide cross-section as shown in Fig. A.1(a) is considered. The generic structure consists of a cascade of M parallel-plate regions along the x-direction. Rectangular conductors, which create subregions in one region, may exist in some of the parallel-plate regions, e.g. region m in Fig. A.1(a). Each top and bottom wall may have different boundary conditions, namely PEW or PMW, according to the symmetry of the geometries. This generic cross-section is a generalized waveguide, and all the non-canonical waveguides in this dissertation are special cases of it.

The GTR is used to characterize the generic waveguide cross-section in A.1(a). Basically, the generic structure can be represented as a generalized transverse network as shown in Fig. A.1(b). Each parallel-plate region is considered as multiple-electric-port transmission lines. The discontinuity (D_m in Fig. A.1(b)) between two parallel-plate regions is characterized by GSM. The two terminal ends are either short or open circuit depending on the symmetry of the structure. Therefore, the generalized transverse network in Fig. A.1(b) is actually a resonant network, and its resonant condition will provide the cutoff wavenumber k_c of each eigenmode of the waveguide structure.

Therefore, the problem can be stated as: *Given a non-canonical waveguide that can be segmented into many parallel-plate regions, a generalized transverse resonance network needs to be created to represent the structure, and the natural resonant condition is used to solve the eigenmodes and eigenfields of the waveguide.* The detailed formulations for characterizing the discontinuities and creating the resonance network are given next.

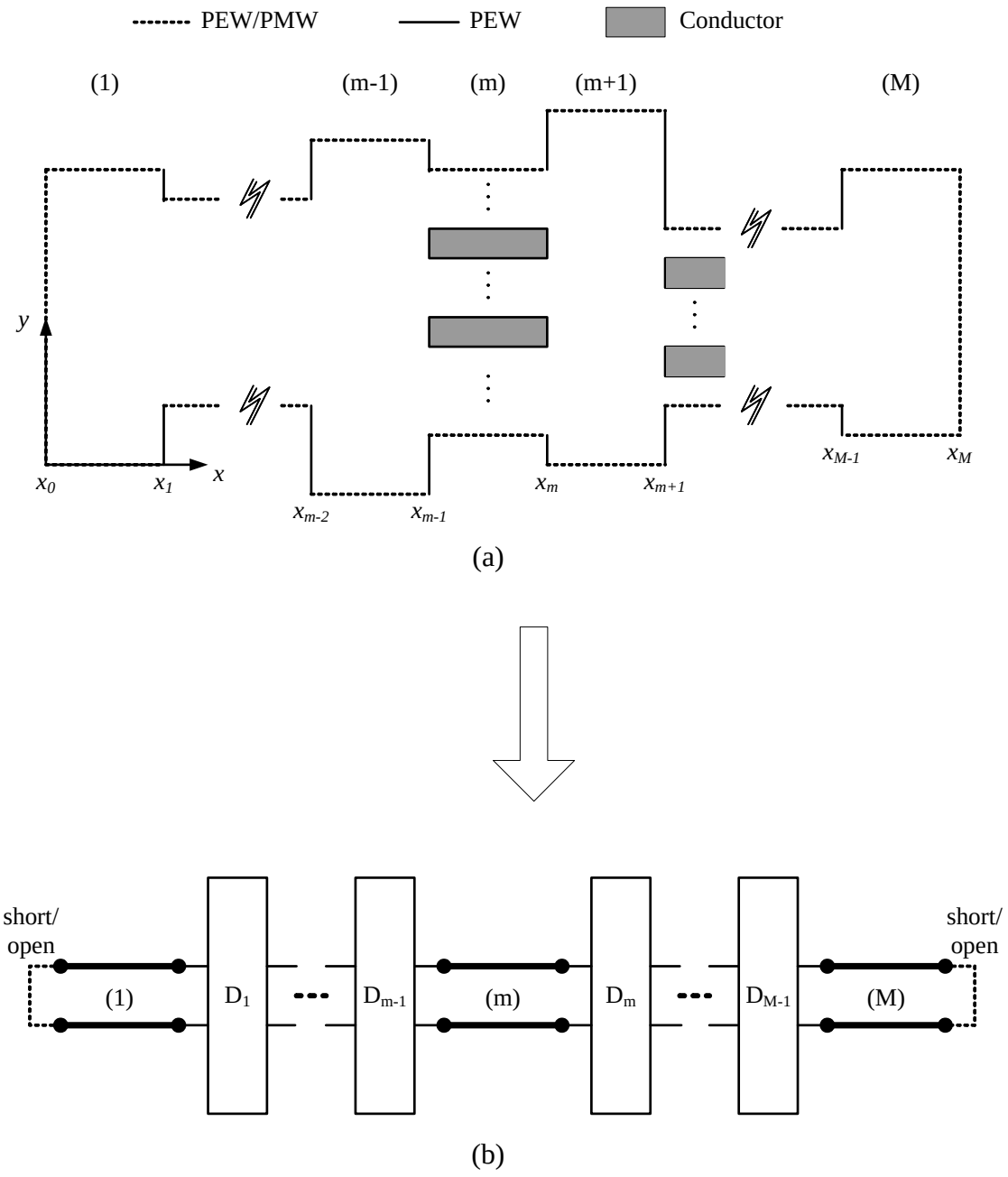

Figure A.1: (a) Generic waveguide cross-section that can be characterized by GTR. (b) Generalized equivalent transverse network of the generic cross-section. D_m represents the discontinuity between two parallel-plate regions. D_m is characterized by GSM.

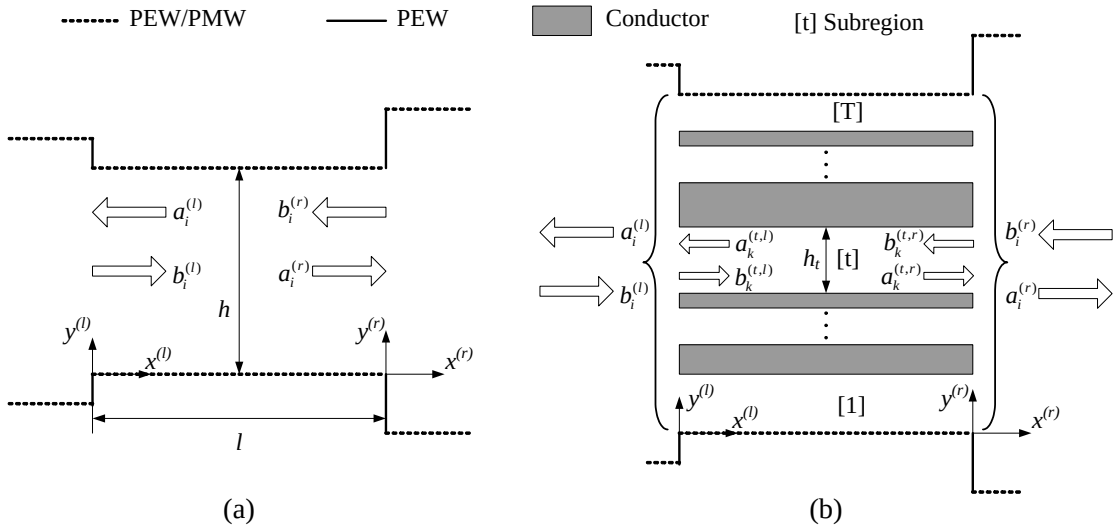

Figure A.2: (a) One single-parallel-plate region with two reference systems. (b) One multi-parallel-plate region consisting of T subregions.

A.3 Field Expansion in Parallel-plate Region

The scalar potential Φ of each mode of the generic structure in Fig. A.1(a) has a local series representation $\Psi^{(m)}$ defined inside each parallel-plate region m:

$$\Phi = \begin{cases} \Psi^{(1)} & x \in [x_0, x_1] \\ \vdots & \\ \Psi^{(m)} & x \in [x_{m-1}, x_m] \\ \vdots & \\ \Psi^{(M)} & x \in [x_{M-1}, x_M] \end{cases} \tag{A.1}$$

The series for Ψ in one parallel-plate region as shown in Fig. A.2(a) are written as the followings:

- TEM

$$\Psi = \psi_0(y) + \sum_{i=1}^{N} \left(a_i^{(l)} e^{+\gamma_{xi} x^{(l)}} + b_i^{(l)} e^{-\gamma_{xi} x^{(l)}} \right) \psi_i(y) \tag{A.2a}$$

$$= \psi_0(y) + \sum_{i=1}^{N} \left(a_i^{(r)} e^{-\gamma_{xi} x^{(r)}} + b_i^{(r)} e^{+\gamma_{xi} x^{(r)}} \right) \psi_i(y) \tag{A.2b}$$

- TE

$$\Psi = \sum_{i=1}^{N} \left(-a_i^{(l)} e^{+\gamma_{xi} x^{(l)}} + b_i^{(l)} e^{-\gamma_{xi} x^{(l)}} \right) \psi_i(y) \tag{A.3a}$$

$$= \sum_{i=1}^{N} \left(a_i^{(r)} e^{-\gamma_{xi} x^{(r)}} - b_i^{(r)} e^{+\gamma_{xi} x^{(r)}} \right) \psi_i(y) \tag{A.3b}$$

- TM

$$\Psi = \sum_{i=1}^{N} \left(a_i^{(l)} e^{+\gamma_{xi} x^{(l)}} + b_i^{(l)} e^{-\gamma_{xi} x^{(l)}} \right) \psi_i(y) \tag{A.4a}$$

$$= \sum_{i=1}^{N} \left(a_i^{(r)} e^{-\gamma_{xi} x^{(r)}} + b_i^{(r)} e^{+\gamma_{xi} x^{(r)}} \right) \psi_i(y) \tag{A.4b}$$

The series have been truncated to N terms for computational purpose. The signs of the amplitudes have been chosen in such a way to acquire similar formulations in the field-matching procedure. Two coordinate systems (see Fig. A.2) are used in the formulations: l-system and r-system. The amplitudes in these two systems are related by

$$a_i^{(r)} = b_i^{(l)} e^{-\gamma_{xi} l} \text{ and } a_i^{(l)} = b_i^{(r)} e^{-\gamma_{xi} l} \tag{A.5}$$

In matrix form (grouping the amplitudes a_i and b_i in column vectors),

$$\mathbf{a}^{(r)} = \boldsymbol{\Upsilon} \mathbf{b}^{(l)} \text{ and } \mathbf{a}^{(l)} = \boldsymbol{\Upsilon} \mathbf{b}^{(r)} \tag{A.6}$$

Table A.2: Basis functions for TEM, TE and TM modes.

B.C.		**TE**		**TEM and TM**	
$y=0$	$y=h$	$\varphi_i(y)$	k_{yi}	$\varphi_i(y)$	k_{yi}
PEW	PEW	$\frac{1}{\sqrt{\epsilon_{i1}}}\cos(k_{yi}y)$	$\frac{(i-1)\pi}{h}$	$\sin(k_{yi}y)$	$\frac{i\pi}{h}$
PEW	PMW	$\cos(k_{yi}y)$	$\frac{(2i-1)\pi}{2h}$	$\sin(k_{yi}y)$	$\frac{(2i-1)\pi}{2h}$
PMW	PEW	$\sin(k_{yi}y)$	$\frac{(2i-1)\pi}{2h}$	$\cos(k_{yi}y)$	$\frac{(2i-1)\pi}{2h}$
Note: $\epsilon_{mn} = \begin{cases} 2 & m=n \\ 1 & m\neq n \end{cases}$					

where

$$\boldsymbol{\Upsilon} = diag\left[e^{-\gamma_{xi}l}\right]_{i=1,\ldots,N} \tag{A.7}$$

The basis function $\psi_i(y)$ is determined according to the boundary conditions on the top ($y=h$) and bottom ($y=0$) walls: PEW or PMW. The basis function can be written as

$$\psi_i(y) = \gamma_{xi}^{-1/2}\sqrt{\frac{2}{h}}\varphi_i(y),\ \gamma_{xi} = \sqrt{k_{yi}^2 - k_c^2} \tag{A.8}$$

The trigonometric function φ_i and the y-wavenumber k_{yi} are defined in Table A.2. For the TEM modes, k_c is always zero.

The linear function $\psi_0(y)$ in (A.2) is given by

$$\psi_0(y) = \alpha y + \beta,\ \alpha = \frac{v^{(t)} - v^{(b)}}{h} \text{ and } \beta = v^{(b)} \tag{A.9}$$

where $v^{(t)}$ and $v^{(b)}$ are the potential values at the top and bottom walls, respectively.

The term *multi-parallel-plate* region is used to refer one parallel-plate region having multiple conductors inside (see region m in Fig. A.1(a)). In a multi-parallel-plate region as shown in Fig. A.2(b), there are T parallel-plate subregions. In each subregion t, the function Ψ can be expanded in a series formally identical to (A.2), (A.3), and (A.4) for TEM, TE, and TM modes, respectively. The amplitudes of each subregion can be grouped together as one set of amplitudes for the multi-parallel-plate region:

$$\begin{aligned}
\mathbf{a}^{(l)} &= \left[\mathbf{a}^{(1,l)}, \cdots, \mathbf{a}^{(t,l)}, \cdots \mathbf{a}^{(T,l)}\right]^t, \ \mathbf{a}^{(t,l)} = \left[a_1^{(t,l)}, \cdots, a_{N_t}^{(t,l)}\right]^t \\
\mathbf{b}^{(l)} &= \left[\mathbf{b}^{(1,l)}, \cdots, \mathbf{b}^{(t,l)}, \cdots \mathbf{b}^{(T,l)}\right]^t, \ \mathbf{b}^{(t,l)} = \left[b_1^{(t,l)}, \cdots, b_{N_t}^{(t,l)}\right]^t \\
\mathbf{a}^{(r)} &= \left[\mathbf{a}^{(1,r)}, \cdots, \mathbf{a}^{(t,r)}, \cdots \mathbf{a}^{(T,r)}\right]^t, \ \mathbf{a}^{(t,r)} = \left[a_1^{(t,r)}, \cdots, a_{N_t}^{(t,r)}\right]^t \\
\mathbf{b}^{(r)} &= \left[\mathbf{b}^{(1,r)}, \cdots, \mathbf{b}^{(t,r)}, \cdots \mathbf{b}^{(T,r)}\right]^t, \ \mathbf{b}^{(t,r)} = \left[b_1^{(t,r)}, \cdots, b_{N_t}^{(t,r)}\right]^t
\end{aligned} \tag{A.10}$$

where N_t is the truncated number of terms for each subregion. The amplitudes in the two coordinate systems are related by (A.6), where the matrix $\boldsymbol{\Upsilon}$ is now constructed by the subregions

$$\boldsymbol{\Upsilon} = diag\left[\boldsymbol{\Upsilon}^{(t)}\right]_{t=1,\ldots,T}, \ \boldsymbol{\Upsilon}^{(t)} = diag\left[e^{-\gamma_{xi}^{(t)} l}\right]_{i=1,\ldots,N_t} \tag{A.11}$$

Therefore, a multi-parallel-plate region can be considered to be a generalized parallel-plate region, whose mathematical operations are similar to a single parallel-plate region.

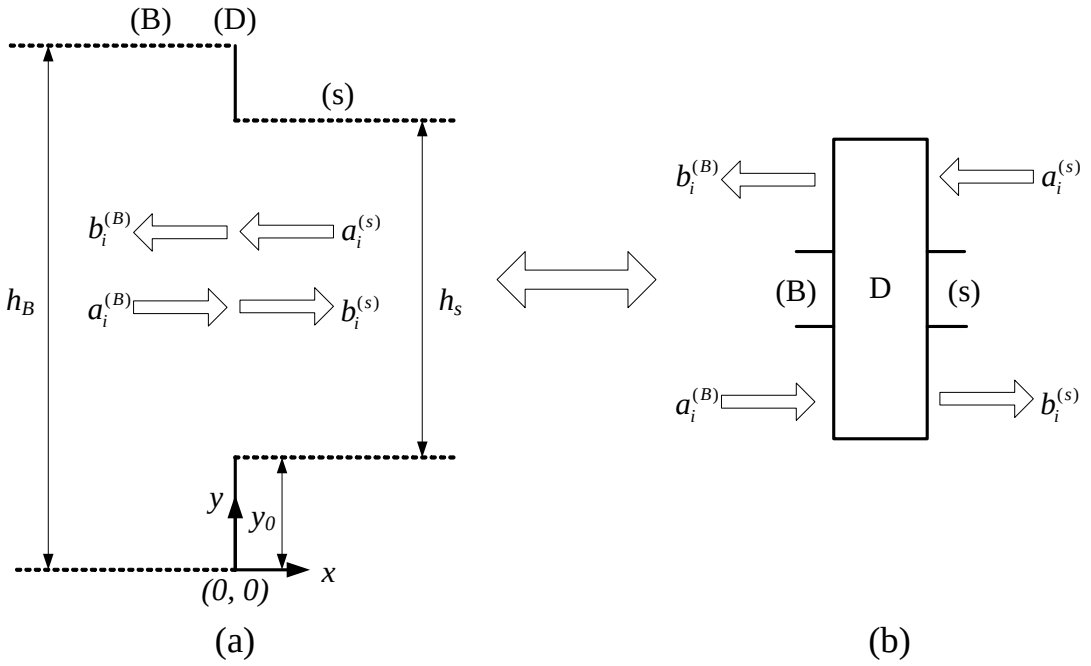

Figure A.3: (a) Basic discontinuity between two parallel-plate regions. A simplified reference system is used. (b) An equivalent block model. The discontinuity is represented by GSM_x.

A.4 Field Matching Between Regions

Once Ψ has been determined satisfying the boundary conditions at the top and bottom walls, the next step is to fulfill the electric and magnetic field boundary conditions at the interface between regions. One typical interface between two regions (B) and (s) is shown in Fig. A.3. A simplified reference system is used here. The boundary conditions at the interface ($x = 0$) are given by

$$\begin{aligned}
\mathbf{u}_x \times \left(\mathbf{e}^{(B)} + e_z^{(B)}\mathbf{u}_z\right) &= \begin{cases} 0, & y \in [0, y_0] \cup [y_0 + h_s, h_B] \\ \mathbf{u}_x \times \left(\mathbf{e}^{(s)} + e_z^{(s)}\mathbf{u}_z\right), & y \in [y_0, y_0 + h_s] \end{cases} \\
\mathbf{u}_x \times \left(\mathbf{h}^{(B)} + h_z^{(B)}\mathbf{u}_z\right) &= \mathbf{u}_x \times \left(\mathbf{h}^{(s)} + h_z^{(s)}\mathbf{u}_z\right), \; y \in [y_0, y_0 + h_s]
\end{aligned} \tag{A.12}$$

After applying the above boundary conditions to TEM, TE and TM modes, the resultant systems are given as

- TEM modes

$$\begin{cases} \mathbf{f} + \left(\mathbf{a}^{(B)} + \mathbf{b}^{(B)}\right) = \mathbf{X}^t \left(\mathbf{a}^{(s)} + \mathbf{b}^{(s)}\right) \\ \mathbf{X}\left(\mathbf{a}^{(B)} - \mathbf{b}^{(B)}\right) = \left(-\mathbf{a}^{(s)} + \mathbf{b}^{(s)}\right) \end{cases} \tag{A.13}$$

where

$$\begin{aligned} [X_{ij}] &= \sqrt{\frac{\gamma_{xj}^{(B)}}{\gamma_{xi}^{(s)}}} \frac{2}{\sqrt{h_B h_s}} \int_{y=y_0}^{y_0+h_s} \varphi_i^{(s)}(y-y_0)\varphi_j^{(B)}(y)dy \\ [f_j] &= \frac{\alpha^{(s)}}{k_{yj}^{(B)}} \sqrt{\frac{2}{k_{yj}^{(B)} h_B}} \left(\varphi_j^{(B)}(y_0) - \varphi_j^{(B)}(y_0+h_s)\right) \end{aligned}$$

- TE and TM modes

$$\begin{cases} \left(\mathbf{a}^{(B)} + \mathbf{b}^{(B)}\right) = \mathbf{X}^t \left(\mathbf{a}^{(s)} + \mathbf{b}^{(s)}\right) \\ \mathbf{X}\left(\mathbf{a}^{(B)} - \mathbf{b}^{(B)}\right) = \left(-\mathbf{a}^{(s)} + \mathbf{b}^{(s)}\right) \end{cases} \tag{A.14}$$

where

$$\begin{aligned} [X_{ij}] &= \sqrt{\frac{\gamma_{xi}^{(s)}}{\gamma_{xj}^{(B)}}} \frac{2}{\sqrt{h_B h_s}} \int_{y=y_0}^{y_0+h_s} \varphi_i^{(s)}(y-y_0)\varphi_j^{(B)}(y)dy, \text{ TE mode} \\ [X_{ij}] &= \sqrt{\frac{\gamma_{xj}^{(B)}}{\gamma_{xi}^{(s)}}} \frac{2}{\sqrt{h_B h_s}} \int_{y=y_0}^{y_0+h_s} \varphi_i^{(s)}(y-y_0)\varphi_j^{(B)}(y)dy, \text{ TM mode} \end{aligned}$$

The resultant systems can be written in matrix format as

$$\underbrace{\begin{bmatrix} \mathbf{b}^{(B)} \\ \mathbf{b}^{(s)} \end{bmatrix}}_{\mathbf{b}} = \underbrace{\begin{bmatrix} \mathbf{X}^t\mathbf{J}\mathbf{X} - \mathbf{I}_B & \mathbf{X}^t\mathbf{J} \\ \mathbf{J}^t\mathbf{X} & \mathbf{J} - \mathbf{I}_s \end{bmatrix}}_{\mathbf{GSM}_x} \underbrace{\begin{bmatrix} \mathbf{a}^{(B)} \\ \mathbf{a}^{(s)} \end{bmatrix}}_{\mathbf{a}} + \underbrace{\begin{bmatrix} \mathbf{c}^{(B)} \\ \mathbf{c}^{(s)} \end{bmatrix}}_{\mathbf{c}} \tag{A.15}$$

where

$$\begin{aligned} \mathbf{J} &= 2(\mathbf{I}_s + \mathbf{X}\mathbf{X}^t)^{-1}, \ \mathbf{I} \text{ is identity matrix} \\ \mathbf{c}^{(B)} &= \frac{1}{2}\left(\mathbf{X}^t\mathbf{J}\mathbf{X} - 2\mathbf{I}_B\right)\mathbf{f}, \ \mathbf{c}^{(s)} = \frac{1}{2}\mathbf{J}\mathbf{X}\mathbf{f} \end{aligned} \tag{A.16}$$

Therefore, each interface can be characterized by $\mathbf{GSM}_x$ for TE and TM modes ($\mathbf{c}$ is null). For TEM modes, a vector $\mathbf{c}$ is generated. The $\mathbf{GSM}_x$ and $\mathbf{c}$ for a interface between multi-parallel-plate regions can be obtained similarly as the above procedure. The only difference is that the matrix $\mathbf{X}$ and vector $\mathbf{f}$ are composed of blocks from each subregion.

A.5 Characteristic System

With the matrix characterization of every basic discontinuity in Fig. A.3(b), the complete matrix representation of the problem as shown in Fig. A.1(b) can be obtained by means of cascading of the characterizations of each discontinuity. The $\mathbf{GSM}_x$ ($\mathbf{S}^{(T)}$) that relates the amplitudes at $x = x_0$ and $x = x_M$ can be easily computed to obtain the total characterization of the structure:

$$\underbrace{\begin{bmatrix} \mathbf{b}_1^{(T)} \\ \mathbf{b}_2^{(T)} \end{bmatrix}}_{\mathbf{b}^{(T)}} = \underbrace{\begin{bmatrix} \mathbf{S}_{11}^{(T)} & \mathbf{S}_{12}^{(T)} \\ \mathbf{S}_{21}^{(T)} & \mathbf{S}_{22}^{(T)} \end{bmatrix}}_{\mathbf{S}^{(T)}} \underbrace{\begin{bmatrix} \mathbf{a}_1^{(T)} \\ \mathbf{a}_2^{(T)} \end{bmatrix}}_{\mathbf{a}^{(T)}} + \underbrace{\begin{bmatrix} \mathbf{c}_1^{(T)} \\ \mathbf{c}_2^{(T)} \end{bmatrix}}_{\mathbf{c}^{(T)}} \tag{A.17}$$

where

$$\begin{cases} \mathbf{b}_1^{(T)} = \mathbf{a}^{(1,l)} & \mathbf{b}_2^{(T)} = \mathbf{a}^{(M,r)} \\ \mathbf{a}_1^{(T)} = \mathbf{b}^{(1,l)} & \mathbf{a}_2^{(T)} = \mathbf{b}^{(M,r)} \end{cases} \tag{A.18}$$

In order to obtain the characteristic equation for the whole system (see Fig. A.1), the conditions at the lateral walls (PEW or PMW) are applied:

$$\begin{bmatrix} \mathbf{b}^{(1,l)} \\ \mathbf{b}^{(M,r)} \end{bmatrix} = \underbrace{\begin{bmatrix} \mathbf{\Gamma}_L & \mathbf{0} \\ \mathbf{0} & \mathbf{\Gamma}_R \end{bmatrix}}_{\mathbf{\Gamma}} \begin{bmatrix} \mathbf{a}^{(1,l)} \\ \mathbf{a}^{(M,r)} \end{bmatrix}, \quad \mathbf{\Gamma}_L, \mathbf{\Gamma}_R = \begin{cases} -\mathbf{I}, \text{ PEW} \\ +\mathbf{I}, \text{ PMW} \end{cases} \tag{A.19}$$

The characteristic system is therefore represented by

$$\left(\mathbf{\Gamma}^{-1} - \mathbf{S}^{(T)}\right) \mathbf{a}^{(T)} = \mathbf{c}^{(T)} \tag{A.20}$$

For TEM modes, the solution of this characteristic system provides the amplitudes at the lateral walls, while for TE and TM modes, a mode can exist only if

$$\det\left(\mathbf{\Gamma}^{-1} - \mathbf{S}^{(T)}\right) = \det\left(\mathbf{\Gamma}^{-1} - \mathbf{S}^{(T)}(k_c)\right) = 0$$

The real roots of the above characteristic equation are the cutoff wavenumber k_c of the modes. These roots can be solved by Muller method [114] for real argument functions. Once k_c is known for each mode, the amplitudes in each region can be obtained by an iterative procedure of de-cascading.

Appendix B

Eigenfield Distribution of Waveguides

In this appendix, the eigenfield distribution of some non-canonical waveguides used in this dissertation is demonstrated. All the waveguide cross-sections are characterized by the GTR technique. Shown in Fig. B.1(a) is the electric field distribution of the TEM mode of stripline. This structure has been used in all of the LTCC filter designs. Fig. B.1(c) and (d) are the fundamental TE modes of single and double ridge waveguides, respective. They have been used in ridge waveguide filter and junction designs. Fig. B.1(e) shows two TEM modes of a multiple-stripline structure that has been used in the double-layer coupled stripline resonator filters. There are actually 20 TEM modes in this structure. Fig. B.2 shows the field distributions of the cross sections used in the ridge waveguide coupled stripline elliptic filters.

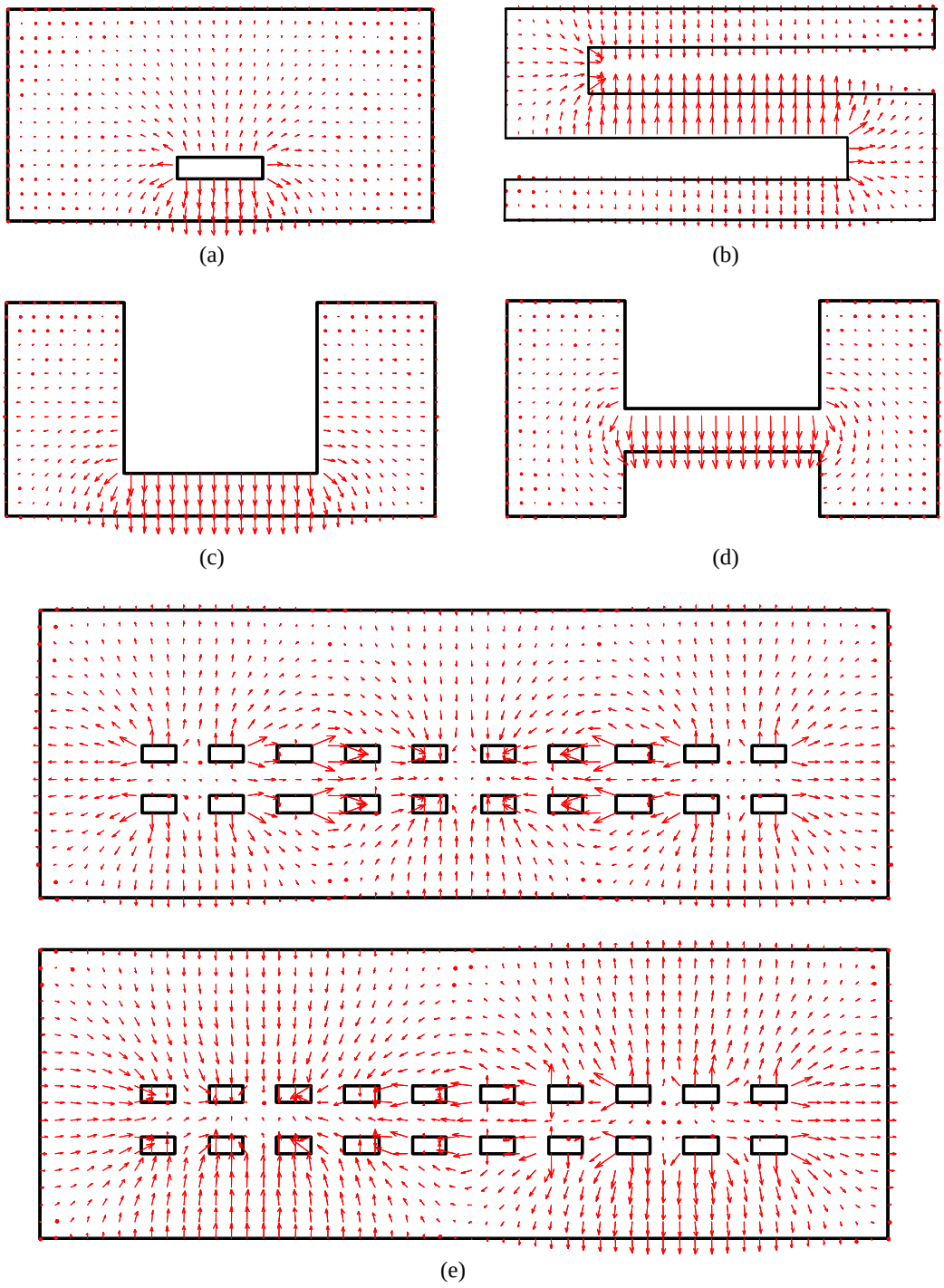

Figure B.1: Electric field distribution of waveguides. (a) TEM mode of stripline. (b) Fundamental mode of coupled-ridge. (c) Fundamental mode of single ridge. (d) Fundamental mode of double ridge. (e) Two TEM modes of multiple-stripline (totally 20 TEM modes exist).

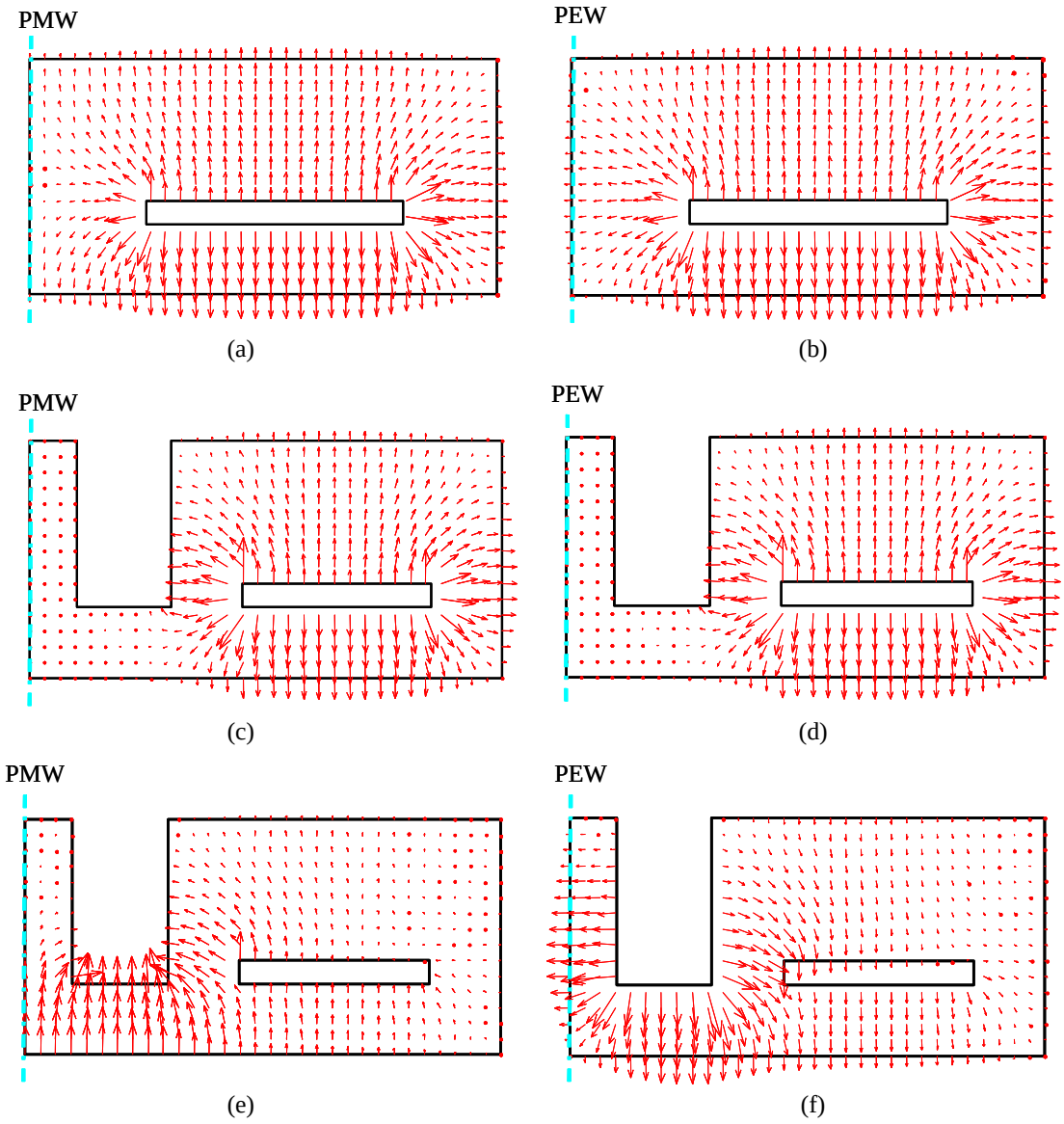

Figure B.2: Electric field distribution of waveguides. (a) TEM mode with PMW of coupled stripline. (b) TEM mode with PEW of coupled stripline. (c) TEM mode with PMW of ridge-stripline. (d) TEM mode with PEW of ridge-stripline. (e) The first TE mode with PMW of ridge-stripline. (f) The first TE mode with PEW of ridge-stripline.

Appendix C

Coupling Integrals between Waveguides[1]

In the application of the mode matching technique between waveguides (one large and one small in the most general case), it is usually necessary to calculate the coupling integrals between the modes of the waveguides (e.g. matrix $\mathbf{X}$ in Table 1.2, p. 16). Two types of inner products need to be computed if the scalar potential Φ is used to evaluate the coupling integral, which are

$$X_1 = \iint_S \nabla_t \Phi_1 \cdot \nabla_t \Phi_2 dS, \;\; X_2 = \iint_S \nabla_t \Phi_1 \cdot \nabla_t \Phi_2 \times \mathbf{u}_z dS \tag{C.1}$$

where Φ_1 and Φ_2 are two modes belonging to two different waveguides. The surface S usually coincides with the area of the small waveguide cross-section. It is worth noting that the coupling integral between a TEM/TM mode of the small waveguide with a TE mode of the large waveguide is always equal to zero.

[1] The formulations in this appendix have been presented in the Ph.D. thesis of Dr. J. A. Ruiz-Cruz [35] before.

In this appendix, the coupling integral between two waveguides characterized by GTR (see p. 255) is formularized. The surface S of the discontinuity between two GTR waveguides can be decomposed into non-intersecting rectangular domains R_k as

$$S = \underset{k}{\cup} R_k \tag{C.2}$$

and then the inner product is given by

$$X_1 = \sum_k X_{1,R_i},\ X_2 = \sum_k X_{2,R_k}$$

where X_{1,R_k} and X_{2,R_k} are the local inner products evaluated over domain R_k.

In each domain R (index k is ignored), the local representation Ψ of the scalar potential Φ of the modes can be written as

$$\Psi = \sum_{i=1}^{N} \left(A_{pi} e^{+\gamma_i x} + A_{ni} e^{-\gamma_i x} \right) f_i(y) + \alpha y + const \tag{C.3}$$

where the x-coordinate has been transformed to the local system of domain R (The transformed coefficients are counted into A_{pi} and A_{ni}). A_{pi} and A_{ni} are also related to the amplitudes in (A.2), (A.3) and (A.4) in terms of normalization constants and sign changes.

Assuming that the bottom ($y = 0$) of domain R has an offset y_0 with respect to the the corresponding parallel-plate region in the waveguide, the function in y is then given as $f_i(y) = \varphi_i(y + y_0)$. For TE and TM modes, $\alpha = 0$. In the following discussions, domain R is assumed to have a width w and a height h.

The inner product $X_{1,R}$ and $X_{2,R}$ over domain R are then evaluated as

$$X_{1,R} = \iint_R \nabla_t \Psi_1 \cdot \nabla_t \Psi_2 dS,\ X_{2,R} = \iint_R \nabla_t \Psi_1 \cdot \nabla_t \Psi_2 \times \mathbf{u}_z dS \tag{C.4}$$

The partial derivatives of (C.3) are calculated as

$$\begin{aligned}\frac{\partial \Psi}{\partial x} &= \sum_{i=1}^{N} \gamma_i \left(A_{pi} e^{+\gamma_i x} - A_{ni} e^{-\gamma_i x} \right) f_i(y) \equiv \Psi_x \\ \frac{\partial \Psi}{\partial y} &= \alpha + \sum_{i=1}^{N} \left(A_{pi} e^{+\gamma_i x} + A_{ni} e^{-\gamma_i x} \right) f_i'(y) \equiv \alpha + \Psi_y \end{aligned} \tag{C.5}$$

Thus, the following equations can be written:

$$\begin{aligned}\Psi_{1x} &= \sum_{i=1}^{N_1} \gamma_i^{(1)} \left(A_{pi}^{(1)} e^{+\gamma_i^{(1)} x} - A_{ni}^{(1)} e^{-\gamma_i^{(1)} x} \right) f_i^{(1)}(y) \\ \Psi_{1y} &= \sum_{i=1}^{N_1} \left(A_{pi}^{(1)} e^{+\gamma_i^{(1)} x} + A_{ni}^{(1)} e^{-\gamma_i^{(1)} x} \right) f_i^{(1)'}(y) \\ \Psi_{2x} &= \sum_{j=1}^{N_2} \gamma_j^{(2)} \left(A_{pj}^{(2)} e^{+\gamma_j^{(2)} x} - A_{nj}^{(2)} e^{-\gamma_j^{(2)} x} \right) f_j^{(2)}(y) \\ \Psi_{2y} &= \sum_{j=1}^{N_2} \left(A_{pj}^{(2)} e^{+\gamma_j^{(2)} x} + A_{nj}^{(2)} e^{-\gamma_j^{(2)} x} \right) f_j^{(2)'}(y) \end{aligned} \tag{C.6}$$

Equation (C.4) can then be calculated through the following identities

$$\begin{aligned}\nabla_t \Psi_1 \cdot \nabla_t \Psi_2 &= \Psi_{1x}\Psi_{2x} + \Psi_{1y}\Psi_{2y} + \alpha_1 \Psi_{2y} + \alpha_2 \Psi_{1y} + \alpha_1 \alpha_2 \\ \nabla_t \Psi_1 \cdot \nabla_t \Psi_2 \times \mathbf{u}_z &= \Psi_{1x}\Psi_{2y} - \Psi_{1y}\Psi_{2x} + \alpha_2 \Psi_{1x} - \alpha_1 \Psi_{2x} \end{aligned} \tag{C.7}$$

and

$$\begin{aligned}\Psi_{1x}\Psi_{2x} &= \sum_{i=1}^{N_1} \sum_{j=1}^{N_2} \gamma_i^{(1)} \gamma_j^{(2)} \left(A_{pi}^{(1)} e^{+\gamma_i^{(1)} x} - A_{ni}^{(1)} e^{-\gamma_i^{(1)} x} \right) \cdot \\ &\quad \left(A_{pj}^{(2)} e^{+\gamma_j^{(2)} x} - A_{nj}^{(2)} e^{-\gamma_j^{(2)} x} \right) f_i^{(1)}(y) f_j^{(2)}(y) \\ \Psi_{1y}\Psi_{2y} &= \sum_{i=1}^{N_1} \sum_{j=1}^{N_2} \left(A_{pi}^{(1)} e^{+\gamma_i^{(1)} x} + A_{ni}^{(1)} e^{-\gamma_i^{(1)} x} \right) \cdot \\ &\quad \left(A_{pj}^{(2)} e^{+\gamma_j^{(2)} x} + A_{nj}^{(2)} e^{-\gamma_j^{(2)} x} \right) f_i^{(1)'}(y) f_j^{(2)'}(y) \\ \Psi_{1x}\Psi_{2y} &= \sum_{i=1}^{N_1} \sum_{j=1}^{N_2} \gamma_i^{(1)} \left(A_{pi}^{(1)} e^{+\gamma_i^{(1)} x} - A_{ni}^{(1)} e^{-\gamma_i^{(1)} x} \right) \cdot \\ &\quad \left(A_{pj}^{(2)} e^{+\gamma_j^{(2)} x} + A_{nj}^{(2)} e^{-\gamma_j^{(2)} x} \right) f_i^{(1)}(y) f_j^{(2)'}(y) \end{aligned}$$

$$\Psi_{1y}\Psi_{2x} = \sum_{i=1}^{N_1}\sum_{j=1}^{N_2}\gamma_j^{(2)}\left(A_{pi}^{(1)}e^{+\gamma_i^{(1)}x}+A_{ni}^{(1)}e^{-\gamma_i^{(1)}x}\right)\cdot \left(A_{pj}^{(2)}e^{+\gamma_j^{(2)}x}-A_{nj}^{(2)}e^{-\gamma_j^{(2)}x}\right)f_i^{(1)'}(y)f_j^{(2)}(y) \tag{C.8}$$

Therefore, $X_{1,R}$ and $X_{2,R}$ can be obtained by calculating the integral of each term in (C.7) over domain R. All the integrals are analytical since only exponential and trigonometric functions are involved. For example,

$$\iint_R \Psi_{1x}\Psi_{2x}dS = \sum_{i=1}^{N_1}\sum_{j=1}^{N_2}\gamma_i^{(1)}\gamma_j^{(2)}\cdot \begin{bmatrix} A_{pi}^{(1)}A_{pj}^{(2)}\int_{x=0}^{w}e^{(+\gamma_i^{(1)}+\gamma_j^{(2)})x}dx - A_{pi}^{(1)}A_{nj}^{(2)}\int_{x=0}^{w}e^{(+\gamma_i^{(1)}-\gamma_j^{(2)})x}dx \\ -A_{ni}^{(1)}A_{pj}^{(2)}\int_{x=0}^{w}e^{(-\gamma_i^{(1)}+\gamma_j^{(2)})x}dx + A_{ni}^{(1)}A_{nj}^{(2)}\int_{x=0}^{w}e^{(-\gamma_i^{(1)}-\gamma_j^{(2)})x}dx \end{bmatrix}\cdot \int_{y=0}^{h}f_i^{(1)}(y)f_j^{(2)}(y)dy \tag{C.9}$$

Other integral terms can be computed in similar procedures, and are not listed here.

Bibliography

[1] G. L. Matthaei, L. Young, and E. M. T. Jones, *Microwave Filters, Impedance-Matching Networks and Coupling Structures*. Boston: Artech House, 1980.

[2] D. M. Pozar, *Microwave Engineering*. New York: John Wiley, 1998.

[3] J. Uher, J. Bornemann, and U. Rosenberg, *Waveguide Components for Antenna Feed Systems*. Boston: Artech House, 1993.

[4] M. Williamson, *The Communications Satellite*. Bristol and New York: Adam Hilger, 1990.

[5] D. Roddy, *Satellite Communications*. New York: McGraw-Hill, 2006.

[6] A. A. Oliner, "Historical perspectives on microwave field theory," *IEEE Trans. Microw. Theory Tech.*, vol. 32, pp. 1022–1045, Sept. 1984.

[7] N. Marcuvitz, *Waveguide Handbook*. New York: McGraw-Hill, 1951.

[8] C. Montgomery, R. Dicke, and E. Purcell, *Principles of Microwave Circuits*. London: IEE Electromagnetic waves series 25, 1987.

[9] R. Levy and S. Cohn, "A history of microwave filter research, design, and development," *IEEE Trans. Microw. Theory Tech.*, vol. 32, pp. 1055–1067, Sept. 1984.

[10] G. Conciauro, M. Guglielmi, and R. Sorrentino, *Advanced modal analysis: CAD techniques for waveguide components and filters*. John Wiley, 1999.

[11] J. D. G. Swanson and W. J. R. Hoefer, *Microwave Circuit Modeling Using Electromagnetic Field Simulation*. Boston, London: Artech House, 2003.

[12] P. Morse and H. Feshbach, *Methods of Theoretical Physics*. McGraw-Hill, 1953.

[13] R. E. Collin, *Field Theory of Guided Waves*. New York: IEEE Press, 1991.

[14] T. Itoh (editor), *Numerical Techniques for Microwave and Millimeter-Wave Passive-Structures*. New York: John Wiley, 1989.

[15] R. F. Harrington, *Field Computation by Moment Methods*. New York: Macmillan, 1968.

[16] R. Sorrentino, "Planar circuits, waveguide models, and segmentation method," *IEEE Trans. Microw. Theory Tech.*, vol. 33, pp. 1057–1066, Oct. 1985.

[17] F. Arndt, R. Beyer, J. M. Reiter, T. Sieverding, and T. Wolf, "Automated design of waveguide components using hybrid mode-matching/numerical EM building-blocks in optimization-oriented CAD frameworks-state of the art and recent advances," *IEEE Trans. Microw. Theory Tech.*, vol. 45, pp. 747–760, May 1997.

[18] F. Arndt, J. Brandt, V. Catina, J. Ritter, I. Rullhusen, J. Dauelsberg, U. Hilgefort, and W. Wessel, "Fast CAD and optimization of waveguide components and aperture antennas by hybrid MM/FE/MoM/FD methods-state-of-the-art and recent advances," *IEEE Trans. Microw. Theory Tech.*, vol. 52, pp. 292–305, Jan. 2004.

[19] R. Beyer and F. Arndt, "Efficient modal analysis of waveguide filters including the orthogonal mode coupling elements by an MM/FE method," *IEEE Microwave Guided Wave Lett.*, vol. 5, pp. 1–3, Jan. 1995.

[20] *Wasp-Net*. Bremen, Germany: Microwave Innovation Group.

[21] *Microwave Wizard*. Bremen, Germany: Mician GbR.

[22] G. Mur, "Finite difference method for the solution of electromagnetic waveguide discontinuity problem," *IEEE Trans. Microw. Theory Tech.*, vol. 22, pp. 54–57, Jan. 1974.

[23] A. Taflove and S. Hagness, *Computational Electromagnetics: The Finite-Difference Time-Domain Method*. Norwood, MA: Artech House, 2000.

[24] W. K. Gwarek, "Analysis of arbitrarily shaped two-dimensional microwave circuits by Finite-Difference Time-Domain method," *IEEE Trans. Microw. Theory Tech.*, vol. 36, pp. 738–744, Apr. 1988.

[25] S. Haffa, D. Hollmann, , and W. Wiesbeck, "The finite difference method for S-parameter calculation of arbitrary three-dimensional structures," *IEEE Trans. Microw. Theory Tech.*, vol. 40, pp. 1602–1610, Aug. 1992.

[26] P. P. Silvester and R. L. Ferrari, *Finite Elements for Electrical Engineers*. New York: Cambridge University Press, 1996.

[27] J. Webb and S. Parihar, "Finite element analysis of H-plane rectangular waveguide problems," *IEE Proc.*, vol. 133 pt. H, pp. 91–94, Apr. 1986.

[28] M. Koshiba and M. Suzuki, "Application of the Boundary-Element method to waveguide discontinuities," *IEEE Trans. Microw. Theory Tech.*, vol. 34, pp. 301–307, Feb. 1986.

[29] C. Christopoulos, *The Transmission-Line Modeling Method TLM.* New York: IEEE Press, 1995.

[30] P. B. Johns, "A symmetrical condensed node for the TLM method," *IEEE Trans. Microw. Theory Tech.*, vol. 35, no. 4, pp. 370–377, 1987.

[31] G. Conciauro, P. Arcioni, M. Bressan, and L. Perregrini, "Wideband modeling of arbitrarily shaped H plane waveguide components by the 'Boundary Integral-Resonant Mode Expansion method'," *IEEE Trans. Microw. Theory Tech.*, vol. 44, pp. 1057–1066, July 1996.

[32] P. Arcioni, M. Bressan, G. Conciauro, and L. Perregrini, "Wideband modeling of arbitrarily shaped E plane waveguide components by the 'Boundary Integral-Resonant Mode Expansion method'," *IEEE Trans. Microw. Theory Tech.*, vol. 44, pp. 2083–2092, Nov. 1996.

[33] J. M. Reiter and F. Arndt, "A Boundary Contour Mode-Matching method for the rigorous analysis of cascaded arbitrarily shaped H-plane discontinuities in rectangular waveguides," *IEEE Microwave Guided Wave Lett.*, vol. 2, pp. 403–405, Oct. 1992.

[34] J. M. Reiter and F. Arndt, "Rigorous analysis of arbitrarily shaped H- and E-plane discontinuities in rectangular waveguides by a full-wave Boundary Contour Mode-Matching method," *IEEE Trans. Microw. Theory Tech.*, vol. 43, pp. 796–801, Apr. 1995.

[35] J. A. R. Cruz, *Contribution to the CAD of Microwave-Millimeterwave Passive Devices by Mode-Matching Techniques.* PhD thesis, Univ. Politécnica de Madrid, Madrid, Spain, 2005.

[36] T. Itoh, "Analysis of microstrip resonators," *IEEE Trans. Microw. Theory Tech.*, vol. 22, pp. 946–952, 1974.

[37] A. Wexler, "Solution of waveguides discontinuities by modal analysis," *IEEE Transactions on Microwave Theory and Techniques*, vol. 15, pp. 508–517, 1967.

[38] P. J. B. Clarricoats and K. R. Slinn, "Numerical method for the solution of waveguide discontinuity problems," *Electronic Letters*, pp. 226–227, 1966.

[39] S. W. Drabuwitch, "Multimode antennas," *Microwave Journal*, vol. 9, pp. 41–51, 1966.

[40] W. Menzel and I. Wolff, "A method for calculating the frequency-dependent properties of microstrip discontinuities," *IEEE Trans. Microw. Theory Tech.*, vol. 25, pp. 107–112, Feb. 1977.

[41] J. Bornemann and F. Arndt, "Modal-S-matrix design of optimum stepped ridged and finned waveguide transformers," *IEEE Trans. Microw. Theory Tech.*, vol. 35, pp. 561–567, June 1987.

[42] H. Patzelt and F. Arndt, "Double-plane steps in rectangular waveguides and their application for transformers, irises, and filters," *IEEE Trans. Microw. Theory Tech.*, vol. 82, pp. 771–776, May 1982.

[43] J. Dittloff and F. Arndt, "Computer-aided design of slit-coupled H-plane T-junction diplexers with E-plane metal-insert filters," *IEEE Trans. Microw. Theory Tech.*, vol. 36, pp. 1833–1840, Dec. 1988.

[44] C. Wang, *Modeling of conductor, dielectric loaded resonators, filters and double ridge waveguide T-junctions*. PhD thesis, University of Maryland, College Park, MD, USA, 1997.

[45] Y. Rong, *Modeling of combline coaxial, ridge waveguide filters and multiplexers*. PhD thesis, University of Maryland, College Park, MD, USA, 1999.

[46] Y. Rong and K. A. Zaki, "Characteristics of generalized rectangular and circular ridge waveguides," *IEEE Trans. Microw. Theory Tech.*, vol. 48, pp. 258–265, Feb. 2000.

[47] R. E. Collin, *Foundations For Microwave Engineering*. New York: McGraw-Hill International Editions, 1966.

[48] R. Mittra and W. W. Lee, *Analytical techniques in the theory of guided waves*. New York: MacMillan, 1971.

[49] R. Sorrentino and T. Itoh, "Transverse resonance analysis of finline discontinuities," *IEEE Trans. Microw. Theory Tech.*, vol. 32, pp. 1633–1638, Dec. 1984.

[50] H. Y. Yee, "Transverse modal analysis of printed circuit transmission lines," *IEEE Trans. Microw. Theory Tech.*, vol. 33, pp. 808–816, Sept. 1985.

[51] R. Vahldieck and J. Bornemann, "A modified mode-matching technique and its application to a class of quasi-planar transmission lines," *IEEE Trans. Microw. Theory Tech.*, vol. 33, pp. 916–926, Oct. 1985.

[52] R. H. MacPhie and K. L. Wu, "A full-wave modal analysis of arbitrarily shaped waveguide discontinuities using the finite plane-wave series expansion," *IEEE Trans. Microw. Theory Tech.*, vol. 47, pp. 232–237, Feb. 1999.

[53] R. H. MacPhie and K. L. Wu, "A full-wave modal analysis of inhomogeneous waveguide discontinuities with both planar and circular cylindrical boundaries," *IEEE Trans. Microw. Theory Tech.*, vol. 49, pp. 1132–1136, June 2001.

[54] M. Leroy, "On the convergence of numerical results in Modal Analysis," *IEEE Trans. Antennas Propagat.*, vol. 31, pp. 655–659, July 1983.

[55] R. Levy, R. V. Snyder, and G. Matthaei, "Design of microwave filters," *IEEE Trans. Microw. Theory Tech.*, vol. 50, pp. 783–793, March 2002.

[56] I. C. Hunter, L. Billonet, B. Jarry, and P. Guillon, "Microwave filters - applications and technology," *IEEE Trans. Microw. Theory Tech.*, vol. 50, pp. 794–805, March 2002.

[57] I. Hunter, *Theory and Design of Microwave Filters*. London: IEE Electromagnetic waves series 4, 2001.

[58] R. R. Mansour, "Filter technologies for wireless base stations," *IEEE microwave magazine*, pp. 68–74, March 2004.

[59] A. Piloto, K. Leahy, B. Flanick, and K. A. Zaki, "Waveguide filters having a layered dielectric structure," Jan. 1995.

[60] J. Gipprich, D. Stevens, M. Hageman, A. Piloto, K. Zaki, and Y. Rong, "Embedded waveguide filters for microwave and wireless applications using cofired ceramic technologies," *Proc. of Int. Symp. on Microelectronics, 1998, San Diego, CA.*, pp. 23–26.

[61] Y. Rong, K. Zaki, M. Hageman, D. Stevens, and J. Gipprich, "Low-temperature cofired ceramic (LTCC) ridge waveguide bandpass chip filters," *IEEE Trans. Microw. Theory Tech.*, vol. 47, pp. 2317–2324, Feb. 1999.

[62] Y. Rong, K. Zaki, J. Gipprich, M. Hageman, and D. Stevens, "Low-temperature cofired ceramic (LTCC) wide-band ridge-waveguide bandpass filters," *IEEE Trans. Microw. Theory Tech.*, vol. 47, pp. 1836–1840, Sept. 1999.

[63] J. Gipprich, L. Dickens, B. Hayes, and F. Sacks, "A compact 8-14 GHz LTCC stripline coupler network for high efficiency power combining with better than 82% combining efficiency," *Proc. 1995 IEEE MTT-S Int. Microwave Symp. Dig.*, pp. 1583–1586.

[64] R. Hayes, J. Gipprich, and M. Hershfeld, "Stripline re-entrant coupler network for cofired multilayer microwave circuits," *Proc. 1996 IEEE MTT-S Int. Microwave Symp. Dig.*, pp. 801–804.

[65] C. Lascaux, F. Rouchaud, V. Madrangeas, M. Aubourg, P. Guillon, B. Theron, and M. Maigna, "Planar Ka-band high temperature superconducting filters for space applications," *Proc. 2001 IEEE MTT-S Int. Microwave Symp. Dig.*, pp. 487–490, June 2001.

[66] M. J. Lancaster, *Passive Microwave Device Applications of High-Temperature Superconductors.* Cambridge, U.K: Cambridge Univ. Press, 1997.

[67] R. Weigel, D. P. Morgan, J. M. Owens, A. Ballato, K. M. Lakin, K. Hashimoto, and C. C. W. Ruppel, "Microwave acoustic materials, devices, and applications," *IEEE Trans. Microw. Theory Tech.*, vol. 50, pp. 738–749, March 2002.

[68] J. D. Larson, R. C. Ruby, P. Bradley, J. Wen, S. Kok, and A. Chien, "Power handling and temperature coefficient studies in FBAR duplexers for 1900 MHz PCS band," *IEEE Ultrason. Symp. Dig.*, pp. 869–874, 2000.

[69] C. T.-C. Nguyen, "Transceiver front-end architectures using high-Q micromechanical resonators," *IEEE Eur. MIDAS MEMS for High-Q Filters Workshop, Surrey, U.K.*, July 2000.

[70] D. Peroulis, S. Pacheco, K. Sarabandi, and L. P. B. Katehi, "Tunable lumped components with applications to reconfigurable MEMS filters," *Proc. 2001 IEEE MTT-S Int. Microwave Symp. Dig., Phoenix, AZ*, pp. 341–344, June 2001.

[71] *Ansoft High Frequency Structure Simulator (HFSS).* Ansoft Corporation.

[72] *SONNET: 3D Planar High-Frequency Electromagnetic Software.* Sonnet Software Inc.

[73] *IE3D: A full-wave, method-of-moments based simulator.* Zeland Software, Inc.

[74] H. Hashemi and A. Hajimiri, "Concurrent multiband low-noise amplifiers-theory, design and applications," *IEEE Trans. Microw. Theory Tech.*, vol. 50, pp. 288–301, Jan. 2002.

[75] E. Lee, P. Hall, P. Gardner, and D. Kitchener, "Multi-band antennas," *Proc. 1999 IEEE Antennas and Propagation Symp. Dig.*, vol. 2, pp. 912–915, June 1999.

[76] S. Holme, "Multiple passband filters for satellite applications," *Proc. 20th AIAA Int. Commun. Satellite Syst. Conf. Exhibit*, pp. 1993–1996, 2002.

[77] H.-M. Lee, C.-R. Chen, C.-C. Tsai, and C.-M. Tsai, "Dual-band coupling and feed structure for microstrip filter design," *Proc. 2004 IEEE MTT-S Int. Microwave Symp. Dig.*, vol. 3, pp. 1971–1974, June 2004.

[78] J.-T. Kuo and H.-S. Cheng, "Design of quasi-elliptic function filters with a dual-passband response," *IEEE Microwave Wireless Compon. Lett.*, vol. 14, pp. 472–474, Oct. 2004.

[79] R. J. Cameron, M. Yu, and Y. Wang, "Direct-coupled microwave filters with single and dual stopbands," *IEEE Trans. Microw. Theory Tech.*, vol. 53, pp. 3288–3297, Nov. 2005.

[80] G. Macchiarella and S. Tamiazzo, "Design techniques for dual-passband filters," *IEEE Trans. Microw. Theory Tech.*, vol. 53, pp. 3265–3271, Nov. 2005.

[81] P. Lenoir, S. Bila, F. Seyfert, D. Baillargeat, and S. Verdeyme, "Synthesis and design of asymmetrical dual-band bandpass filters based on equivalent network simplification," *IEEE Trans. Microw. Theory Tech.*, vol. 54, pp. 3090–3097, July 2006.

[82] J. D. Rhodes, *Theory of electrical filters.* London, New York, Sydney, Toronto: John Wiley & Sons, 1976.

[83] R. J. Cameron, "General coupling matrix synthesis methods for Chebyshev filtering functions," *IEEE Trans. Microw. Theory Tech.*, vol. 47, pp. 433–442, Apr. 1999.

[84] M. E. Valkenberg, *Introduction to modern network synthesis.* New York: John Wiley & Sons, 1960.

[85] R. J. Cameron, "Advanced coupling matrix synthesis techniques for microwave filters," *IEEE Trans. Microw. Theory Tech.*, vol. 51, pp. 1–10, Jan. 2003.

[86] A. E. Atia, A. E. Williams, and R. W. Newcomb, "Narrow-band multiple-coupled cavity synthesis," *IEEE Trans. Circuit Syst.*, vol. CAS-21, pp. 649–655, Sept. 1974.

[87] R. J. Cameron, A. R. Harish, and C. J. Radcliffe, "Synthesis of advanced microwave filters without diagonal cross-couplings," *IEEE Trans. Microw. Theory Tech.*, vol. 50, pp. 2862–2872, Dec. 2002.

[88] R. J. Cameron and J. D. Rhodes, "Asymmetric realizations for dual-mode bandpass filters," *IEEE Trans. Microw. Theory Tech.*, vol. 29, pp. 51–58, Jan. 1981.

[89] G. Macchiarella, "Accurate synthesis of inline prototype filters using cascaded triplet and quadruplet sections," *IEEE Trans. Microw. Theory Tech.*, vol. 50, pp. 1779–1783, July 2002.

[90] W. A. Atia, K. A. Zaki, and A. E. Atia, "Synthesis of general topology multiple coupled resonator filters by optimization," *Proc. 1998 IEEE MTT-S Int. Microwave Symp. Dig.*, vol. 2, pp. 821–824, June 1998.

[91] N. Yildirim, O. A. Sen, Y. Sen, M. Karaaslan, and D. Pelz, "A revision of cascade synthesis theory covering cross-coupled filters," *IEEE Trans. Microw. Theory Tech.*, vol. 50, pp. 1536–1543, June 2002.

[92] S. Tamiazzo and G. Macchiarella, "An analytical technique for the synthesis of cascaded N-tuplets cross-coupled resonators microwave filters using matrix rotations," *IEEE Trans. Microw. Theory Tech.*, vol. 53, pp. 1693–1698, May 2005.

[93] S. Amari and G. Macchiarella, "Synthesis of inline filters with arbitrarily placed attenuation poles by using nonresonating nodes," *IEEE Trans. Microw. Theory Tech.*, vol. 53, pp. 3075–3081, Oct. 2005.

[94] A. E. Atia and A. E. Williams, "Nonminimum-phase optimum-amplitude bandpass waveguide filters," *IEEE Trans. Microw. Theory Tech.*, vol. 22, pp. 425–431, Apr. 1974.

[95] G. Pfitzenmaier, "Synthesis and realization of narrow-band canonical microwave bandpass waveguide filters exhibiting linear phase and tansmission zeros," *IEEE Trans. Microw. Theory Tech.*, vol. 82, pp. 1300–1311, Sept. 1982.

[96] A. I. Grayzel, "A synthesis procedure for transmission line networks," *IRE Transactions on Circuit Theory*, vol. 5, pp. 172–181, Sept. 1958.

[97] R. Levy, "Tables of element values for the distributed low-pass prototype filter," *IEEE Trans. Microw. Theory Tech.*, vol. 13, pp. 514–536, Sept. 1965.

[98] L. Young, "Stepped-impedance transformers and filter prototypes," *IEEE Trans. Microw. Theory Tech.*, vol. 10, pp. 339–359, Sept. 1962.

[99] J. D. Rhodes and R. J., "General extracted pole synthesis technique with applications to low-loss TE011 mode filters," *IEEE Trans. Microw. Theory Tech.*, vol. 28, pp. 1018–1028, Sept. 1980.

[100] J. R. Montejo-Garai and J. M. Rebollar, "Synthesis of N-order filters with N transmission zeros at real frequencies by means of extracted poles," *Electronic Letters*, vol. 39, pp. 182–183, Jan. 2003.

[101] J. D. Rhodes, "A low-pass prototype network for microwave linear phase filters," *IEEE Trans. Microw. Theory Tech.*, vol. 18, pp. 290–301, June 1970.

[102] R. Levy, "Tapered corrugated waveguide low-pass filters," *IEEE Trans. Microw. Theory Tech.*, vol. 21, pp. 526–532, Aug. 1973.

[103] R. Levy, "Inhomogeneous stepped-impedance corrugated waveguide low-pass filters," *Proc. 2005 IEEE MTT-S Int. Microwave Symp. Dig.*, June 2005.

[104] M. Simeoni, S. Cacchione, F. Vanin, J. Molina-Perez, and D. Schmitt, "Automatic dimensional synthesis without optimization for stepped impedance low-pass filters," *Microwave and Optical Technology Letters*, vol. 44, pp. 190–194, Jan. 2005.

[105] R. Levy, "Determination of simple equivalent circuits of interacting discontinuities in waveguides or transmission lines," *IEEE Trans. Microw. Theory Tech.*, vol. 48, pp. 1712–1716, Oct. 2000.

[106] R. Levy, "A generalized design technique for practical distributed reciprocal ladder networks," *IEEE Trans. Microw. Theory Tech.*, vol. 21, pp. 519–526, Aug. 1973.

[107] R. Levy, "Derivation of equivalent circuits of microwave structures using numerical techniques," *IEEE Trans. Microw. Theory Tech.*, vol. 47, pp. 1688–1695, Sept. 1999.

[108] H. Yao, K. Zaki, A. Atia, and R. Hershtig, "Full wave modeling of conducting posts in rectangular waveguides and its applications to slot-coupled combline filters," *IEEE Trans. Microw. Theory Tech.*, vol. 43, pp. 2824–2830, Dec. 1995.

[109] H. Yao and K. Zaki, "Modeling of generalized coaxial probes in rectangular waveguides," *IEEE Trans. Microw. Theory Tech.*, vol. 43, pp. 2805–2811, Dec. 1995.

[110] Y. Rong and K. Zaki, "Full-wave analysis of coupling between cylindrical combline resonators," *IEEE Trans. Microw. Theory Tech.*, vol. 47, pp. 1721–1729, Sept. 1999.

[111] M. E. Sabbagh, H.-T. Hsu, and K. A. Zaki, "Full-wave optimization of stripline tapped-in ridge waveguide bandpass filters," *Proc. 2002 Int. Microwave Symp. Dig.*, pp. 1805–1808, July 2002.

[112] Y. Ramat-Samii and E. Michielssen, *Electromagnetic Optimization by Genetic Algorithms*. John Wiley and Sons, 1999.

[113] R. H. Otten and L. P. V. Ginneken, *The Annealing Algorithm*. Kluwer Academic Publishers, 1989.

[114] W. Press, S. Teukolsky, W. Vetterling, and B. Flannery, *Numerical Recipes in Fortran*. Cambridge University Press, 1992.

[115] J. W. Bandler, R. M. Biernacki, S. H. Chen, P. A. Grobelay, and R. H. Hemmers, "Space mapping technique for electromagnetic optimization," *IEEE Trans. Microw. Theory Tech.*, vol. 42, pp. 2536–2544, Dec. 1994.

[116] J. W. Bandler, R. M. Biernacki, S. H. Chen, and Y. F. Huang, "Design optimization of interdigital filters using aggressive space mapping and decomposition," *IEEE Trans. Microw. Theory Tech.*, vol. 45, pp. 761–769, May 1997.

[117] M. H. Bakr, J. W. Bandler, and N. Georgieva, "An aggressive approach to parameter extraction," *IEEE Trans. Microw. Theory Tech.*, vol. 47, pp. 2428–2439, Dec. 1999.

[118] J. W. Bandler, Q. S. Cheng, S. A. Dakroury, A. S. Mohamed, M. H. Bakr, K. Madsen, and J. Sondergaard, "Space mapping: the state of the art," *IEEE Trans. Microw. Theory Tech.*, vol. 52, pp. 337–361, Jan. 2004.

[119] H.-T. Hsu, Z. Zhang, K. A. Zaki, and A. E. Atia, "Parameter extraction for symmetric coupled-resonator filters," *IEEE Trans. Microw. Theory Tech.*, vol. 50, pp. 2971–2978, Dec. 2002.

[120] G. Pepe, F.-J. Gortz, and H. Chaloupka, "Computer-aided tuning and diagnosis of microwave filters using sequential parameter extraction," *Proc. 2004 IEEE MTT-S Int. Microwave Symp. Dig.*, June 2004.

[121] G. Pepe, F.-J. Gortz, and H. Chaloupka, "Sequential tuning of microwave filters using adaptive models and parameter extraction," *IEEE Trans. Microw. Theory Tech.*, vol. 53, pp. 22–31, Jan. 2005.

[122] M. Kahrizi, S. Safavi-Naeini, and S. K. Chaudhuri, "Computer diagnosis and tuning of microwave filters using model-based parameter estimation and multi-level optimization," *Proc. 2000 IEEE MTT-S Int. Microwave Symp. Dig.*, June 2000.

[123] A. E. Atia and A. E. Williams, "Narrow-bandpass waveguide filters," *IEEE Trans. Microw. Theory Tech.*, vol. 20, pp. 258–265, Apr. 1972.

[124] L. Accatino, G. Bertin, and M. Mongiardo, "Elliptical cavity resonators for dual-mode narrow-band filters," *IEEE Trans. Microw. Theory Tech.*, vol. 45, pp. 2393–2401, Dec. 1997.

[125] C. Wang, H.-W. Yao, K. A. Zaki, and R. R. Mansour, "Mixed modes cylindrical planar dielectric resonator filters with rectangular enclosure," *IEEE Trans. Microw. Theory Tech.*, vol. 43, pp. 2817–2823, Dec. 1995.

[126] H.-W. Yao, C. Wang, and K. A. Zaki, "Quarter wavelength ceramic combline filters," *IEEE Trans. Microw. Theory Tech.*, vol. 44, pp. 2673–2679, Dec. 1996.

[127] J. S. Hong and M. J. Lancaster, *Microstrip filters for RF/Microwave applications*. New York, NY: John Wiley, 2001.

[128] J.-S. Hong and M. J. Lancaster, "Couplings of microstrip square open-loop resonators for cross-coupled planar microwave filters," *IEEE Trans. Microw. Theory Tech.*, vol. 44, pp. 2099–2109, Dec. 1996.

[129] J.-S. Hong and M. J. Lancaster, "Theory and experiment of novel microstrip slow-wave open-loop resonator filters," *IEEE Trans. Microw. Theory Tech.*, vol. 45, pp. 2658–2665, Dec. 1997.

[130] J.-S. Hong and M. J. Lancaster, "Cross-coupled microstrip hairpin-resonator filters," *IEEE Trans. Microw. Theory Tech.*, vol. 46, pp. 118–122, Jan. 1998.

[131] J.-S. Hong, M. J. Lancaster, D. Jedamzik, and R. B. Greed, "On the development of superconducting microstrip filters for mobile communications applications," *IEEE Trans. Microw. Theory Tech.*, vol. 47, pp. 1656–1663, Sept. 1999.

[132] P. Blondy, A. R. Brown, D. Cros, and G. M. Rebeiz, "Low loss micromachined filters for millimeter-wave telecommunication systems," *1998 Proc IEEE MTT-S Int. Microwave Symp. Dig.*, pp. 1181–1184, June 1998.

[133] J.-F. Liang, *CAD of dual mode dielectric-filled and dielectric-loaded miniature waveguide filters and multiplexers and compact dynamic thermo-feedback transistors model*. PhD thesis, University of Maryland, College Park, MD, USA, 1994.

[134] M. A. E. Sabbagh, H.-T. Hsu, K. A. Zaki, P. Pramanick, and T. Dolan, "Full wave optimization of stripline tapped-in ridge waveguide bandpass filters," *Proc. 2002 IEEE MTT-S Int. Microwave Symp. Dig.*, June 2002.

[135] C. Wang and K. A. Zaki, "Modeling of couplings between double-ridge waveguide and dielectric-loaded resonator," *IEEE Trans. Microw. Theory Tech.*, vol. 46, pp. 2404–2411, Dec. 1998.

[136] E. Cristal and S. Frankel, "Hairpin-line and hybrid hairpin-line/half-wave parallel-coupled-line filters," *IEEE Trans. Microw. Theory Tech.*, vol. 20, pp. 719–728, Nov. 1972.

[137] C. Y. Chang, C. C. Chen, and H. J. Huang, "Folded quarter-wave resonator filters with Chebyshev, flat group delay, or quasi-elliptical function response," *Proc. 2002 IEEE MTT-S Int. Microwave Symp. Dig.*, vol. 3, pp. 1609–1612, June 2002.

[138] K. Chang, *Microwave Ring Circuits and Antennas*. New York: John Wiley, 1996.

[139] F. Huang, "Ultra-compact superconducting narrow-band filters using signle- and twin-spiral resonators," *IEEE Trans. Microw. Theory Tech.*, vol. 51, pp. 487–491, Feb. 2003.

[140] L. A. Robinson, "Wideband interdigital filters with capacitively loaded resonators," *Proc. 1965 IEEE G-MTT Symp. Dig.*, vol. 65, pp. 33–38, May 1965.

[141] J. A. Ruiz-Cruz, M. E. Sabbagh, K. A. Zaki, J. M. Rebollar, and Y. Zhang, "Canonical ridge waveguide filters in LTCC or metallic cavities," *IEEE Trans. Microw. Theory Tech.*, vol. 53, pp. 174–182, Jan. 2005.

[142] W. Schwab and W. Menzel, "Compact bandpass filters with improved stopband characteristics using planar multilayer structures," *Proc. 1992 IEEE MTT-S Int. Microwave Symp. Dig.*, pp. 1207–1210, June 1992.

[143] W. Schwab, F. Boegelsack, and W. Menzel, "Multilayer suspended stripline and coplanar line filters," *IEEE Trans. Microw. Theory Tech.*, vol. 42, pp. 1403–1406, July 1994.

[144] O. Fordham, M.-J. Tsai, and N. G. Alexopoulos, "Electromagnetic synthesis of overlap-gap-coupled microstrip filters," *Proc. 1995 IEEE MTT-S Int. Microwave Symp. Dig.*, pp. 1199–1202, June 1995.

[145] C. Cho and K. C. Gupta, "Design methodology for multilayer coupled line filters," *Proc. 1997 IEEE MTT-S Int. Microwave Symp. Dig.*, pp. 785–788, June 1997.

[146] J. A. Curtis and S. J. Fiedzuszko, "Multi-layered planar filters based on aperture coupled, dual mode microstrip or stripline resonators," *Proc. 1992 IEEE MTT-S Int. Microwave Symp. Dig.*, pp. 1203–1206, June 1992.

[147] S. J. Yao, R. R. Bonetti, and A. E. Williams, "Generalized dual-plane multicoupled line filters," *IEEE Trans. Microw. Theory Tech.*, vol. 41, pp. 2182–2189, Dec. 1993.

[148] H.-C. Chang, C.-C. Yeh, W.-C. Ku, and K.-C. Tao, "A multilayer bandpass filters integrated into RF module board," *Proc. 1996 IEEE MTT-S Int. Microwave Symp. Dig.*, pp. 619–622, June 1996.

[149] J.-S. Hong and M. J. Lancaster, "Aperture-coupled microstrip open-loop resonators and their applications to the design of novel microstrip bandpass filters," *IEEE Trans. Microw. Theory Tech.*, vol. 47, pp. 1848–1855, Sept. 1999.

[150] M. Sagawa, K. Takahashi, and M. Makimoto, "Miniaturized hairpin resonator filters and their application to receiver front-end MICs," *IEEE Trans. Microw. Theory Tech.*, vol. 37, pp. 1991–1997, Dec. 1989.

[151] J.-S. Hong and M. J. Lancaster, "Development of new microstrip pseudo-interdigital bandpass filters," *IEEE Microwave Guided Wave Lett.*, vol. 5, pp. 261–263, Aug. 1995.

[152] G. L. Matthaei, N. O. Fenzi, R. Forse, and S. Rohlfing, "Narrow-band hairpin-comb filters for HTS and other applications," *1996 Proc IEEE MTT-S Int. Microwave Symp. Dig.*, pp. 457–460, June 1996.

[153] Y. Rong, K. Zaki, M. Hageman, D. Stevens, and J. Gipprich, "Low-temperature cofired ceramic (LTCC) ridge waveguide multiplexers," *Proc. 2000 Int. Microwave Symp. Dig.*, vol. 2, pp. 1169–1172, June 2000.

[154] T. Shen, *Full-wave modeling and design of waveguide passive components.* PhD thesis, University of Maryland, College Park, MD, USA, 2001.

[155] M. Makimoto and S. Yamashita, "Bandpass filter using parallel-coupled stripline stepped impedance resonators," *IEEE Trans. Microw. Theory Tech.*, vol. 28, pp. 1413–1417, Dec. 1980.

[156] J. T. Kuo and E. Shih, "Microstrip stepped impedance resonator bandpass filter with an extended optimal rejection bandwidth," *IEEE Trans. Microw. Theory Tech.*, vol. 51, pp. 1554–1559, May 2003.

[157] C.-F. Chen, T.-Y. Huang, and R.-B. Wu, "Design of microstrip bandpass filters with multiorder spurious-mode suppresssion," *IEEE Trans. Microw. Theory Tech.*, vol. 53, pp. 3788–3793, Dec. 2005.

[158] H. W. Yao, K. A. Zaki, and A. E. Atia, "Improvement of spurious performance of combline filters," *Proc. 1997 IEEE MTT-S Int. Microwave Symp. Dig.*, vol. 2, pp. 1099–1102, June 1997.

[159] J. F. Liang, X. P. Liang, K. A. Zaki, and A. E. Atia, "Dual-mode dielectric or air-filled rectangular waveguide filters," *IEEE Trans. Microw. Theory Tech.*, vol. 42, pp. 1330–1336, July 1994.

[160] W. Lin, "Microwave filters employing a single cavity excited in more than one mode," *J. Appl. Phys.*, vol. 22, pp. 989–1011, Aug. 1951.

[161] A. E. Williams and A. E. Atia, "Dual-mode canonical waveguide filters," *IEEE Trans. Microw. Theory Tech.*, vol. 25, pp. 1021–1026, Dec. 1977.

[162] A. E. Atia and A. E. Williams, "New types of bandpass filters for satellite transponders," *COMSAT Tech. Rev.*, vol. 1, pp. 21–43, FAll 1971.

[163] W. C. Tang and S. K. Chaudhuri, "A true elliptic function filter using triple mode degenerate cavities," *IEEE Trans. Microw. Theory Tech.*, vol. 32, pp. 1449–1454, Nov. 1984.

[164] R. R. Bonetti and A. E. Williams, "Application of dual TM modes to triple- and quadruple-mode filters," *IEEE Trans. Microw. Theory Tech.*, vol. 35, pp. 1143–1149, Dec. 1987.

[165] S. J. Fiedziusko, "Dual-mode dielectric resonator loaded cavity filters," *IEEE Trans. Microw. Theory Tech.*, vol. 30, pp. 1311–1316, Sept. 1982.

[166] K. A. Zaki, C. Chen, and A. Atia, "Canonical and longitudinal dual mode dielectric resonator filters without iris," *IEEE Trans. Microw. Theory Tech.*, vol. 35, pp. 1130–1135, Dec. 1987.

[167] H.-C. Chang and K. A. Zaki, "Evanescent-mode coupling of dual-mode rectangular waveguide filters," *IEEE Trans. Microw. Theory Tech.*, vol. 39, pp. 1307–1312, Aug. 1991.

[168] X. P. Liang, K. A. Zaki, and A. E. Atia, "Dual mode coupling by square corner cut in resonators and filters," *IEEE Trans. Microw. Theory Tech.*, vol. 40, pp. 2294–2302, Dec. 1992.

[169] J.-F. Liang and K. A. Zaki, "CAD of microwave junction by polynomial curve-fitting," *Proc. 1993 IEEE MTT-S Int. Microwave Symp. Dig.*, pp. 451–454, June 1993.

[170] J.-F. Liang and W. D. Blair, "High-Q TE01 mode DR filters for PCS wireless base stations," *IEEE Trans. Microw. Theory Tech.*, vol. 46, pp. 2493–2500, Dec. 1998.

[171] C. Wang, K. A. Zaki, A. E. Atia, and T. G. Dolan, "Dielectric combline resonators and filters," *IEEE Trans. Microw. Theory Tech.*, vol. 46, pp. 2501–2506, Dec. 1998.

[172] S. J. Fiedziuzko, I. C. Hunter, T. Itoh, Y. Kobayashi, T. Nishikawa, S. N. Stitzer, and K. Wakino, "Dielectric materials, devices and circuits," *IEEE Trans. Microw. Theory Tech.*, vol. 50, pp. 706–720, March 2002.

[173] S.-W. Chen, K. A. Zaki, and R. G. West, "Tunable, temperature-compensated dielectric resonators and filters," *IEEE Trans. Microw. Theory Tech.*, vol. 38, pp. 1046–1052, Aug. 1990.

[174] V. Madrangeas, M. Aubourg, P. Guillon, S. Vigneron, and B. Theron, "Analysis and realization of L-band dielectric resonator microwave filters," *IEEE Trans. Microw. Theory Tech.*, vol. 40, pp. 120–127, Jan. 1992.

[175] J.-F. Liang and K. A. Zaki, "Mixed modes dielectric resonator filters," *IEEE Trans. Microw. Theory Tech.*, vol. 42, pp. 2449–2454, Dec. 1994.

[176] I. C. Hunter, J. D. Rhodes, and V. Dassonville, "Dual-mode filters with conductor-loaded dielectric resonators," *IEEE Trans. Microw. Theory Tech.*, vol. 47, pp. 2304–2311, Dec. 1999.

[177] P. harscher, R. Vahldieek, and S. Amari, "Automated filter tuing using generalized low-pass prototype networks and gradient-based parameter extraction," *IEEE Trans. Microw. Theory Tech.*, vol. 49, pp. 2523–2538, Dec. 2001.

[178] J. Marquardt and G. Muller, "Computer aided tuning of microwave circuits," *Proc. 1977 IEEE MTT-S Int. Microwave Symp. Dig.*, pp. 147–150, June 1977.

[179] P. M. Marshall and P. Tissi, "A new algorithm for the accurate alignment of microwave networks," *IEEE Trans. Microw. Theory Tech.*, vol. 39, pp. 1754–1758, Oct. 1991.

[180] M. H. Chen, "Short-circuit tuning method for singly terminated filters," *IEEE Trans. Microw. Theory Tech.*, vol. 25, pp. 1032–1036, Dec. 1977.

[181] M. Dishal, "Alignment and adjustment of synchronously tuned multiple-resonant-circuit filters," *IEEE Trans. Microw. Theory Tech.*, vol. 39, pp. 1448–1455, Nov. 1951.

[182] J. B. Thomas, "Cross-coupling in coaxial cavity filters-A tutorial overview," *IEEE Trans. Microw. Theory Tech.*, vol. 51, pp. 1368–1376, Apr. 2003.

[183] H.-T. Hsu, H.-W. Yao, K. A. Zaki, and A. E. Atia, "Computer-aided diagnosis and tuning of cascaded coupled resoantors filters," *IEEE Trans. Microw. Theory Tech.*, vol. 50, pp. 1137–1145, Apr. 2002.

[184] J. A. G. Malherbe, *Microwave Transmission Line Filters.* Dedham, MA: Artech House, 1980.

[185] A. I. Grayzel, "A fundamental multiplexer theorem," *Proc. IEEE*, vol. 57, pp. 847–848, May 1969.

[186] J. D. Rhodes and R. Levy, "A generalized multiplexer theory," *IEEE Trans. Microw. Theory Tech.*, vol. 27, pp. 34–40, Feb. 1979.

[187] J. D. Rhodes and S. A. Alseyab, "A design procedure for bandpass channel multiplexers connected at a common junction," *IEEE Trans. Microw. Theory Tech.*, vol. 28, pp. 246–253, March 1980.

[188] J. D. Rhodes and R. Levy, "Design of general manifold multiplexer," *IEEE Trans. Microw. Theory Tech.*, vol. 27, pp. 111–122, Feb. 1979.

[189] A. E. Atia, "Computer-aided-design of waveguide multiplexers," *IEEE Trans. Microw. Theory Tech.*, vol. 22, pp. 332–336, March 1974.

[190] G. Matthaei and E. Cristal, *Theory and design of diplexers and multiplexers in Advances in Microwaves.* New York: Academic Press, 1967.

[191] M. H. Chen et al., "A contiguous band multiplexer," *COMSAT Technical Review*, vol. 6, pp. 285–307, Fall 1976.

[192] R. Levy, "Analytical design of contiguous multiplexers," *Proc. 1999 IEEE MTT-S Int. Microwave Symp. Dig.*, June 1999.

[193] J. Dittloff and F. Arndt, "Rigorous field theory design of millimeter-wave E-plane integrated circuit multiplexers," *IEEE Trans. Microw. Theory Tech.*, vol. 37, pp. 340–350, Feb. 1989.

[194] Y. Rong, H.-W. Yao, K. A. Zaki, and T. G. Dolan, "Millimeter-wave Ka-band H-plane diplexers and multiplexers," *IEEE Trans. Microw. Theory Tech.*, vol. 47, pp. 2325–2330, Dec. 1999.

[195] M. Guglielmi, "Simple CAD procedure for microwave filters and multiplexers," *IEEE Trans. Microw. Theory Tech.*, vol. 42, pp. 1347–1352, July 1994.

[196] A. A. Kirilenko, L. A. Rud, V. I. Tkachenko, and P. Pramanick, "A systematic approach for computer aided design of waveguide E-plane diplexers," *International Journal of RF and Microwave Computer-Aided Engineering*, vol. 9, no. 2, pp. 104–116, 1999.

[197] A. A. Kirilenko, S. L. Senkevich, V. I. Tkachenko, and B. G. Tysik, "Waveguide diplexer and multiplexer design," *IEEE Trans. Microw. Theory Tech.*, vol. 42, pp. 1393–1396, July 1994.

[198] M. Yu, "Design of multiplexer with many channels," *Workshop in IMS 2006, San Francisco, CA*, June 2006.

[199] J. L. Haine and J. D. Rhodes, "Direct design formulas for asymmetric bandpass channel diplexers," *IEEE Trans. Microw. Theory Tech.*, vol. 25, pp. 807–813, Oct. 1977.

[200] R. Levy, "Synthesis of non-contiguous diplexers using broadband matching theory," *Proc. 1991 IEEE MTT-S Int. Microwave Symp. Dig.*, pp. 543–545, June 1991.

[201] G. Macchiarella and S. Tamiazzo, "Synthesis of diplexers based on the evaluation of suitable characteristic polynomials," *Proc. 2005 IEEE MTT-S Int. Microwave Symp. Dig.*, June 2005.

[202] A. Garcfa-Lamperez, M. Salazar-Palma, and T. K. Sarkar, "Analytical synthesis of microwave multiport networks," *Proc. 2004 IEEE MTT-S Int. Microwave Symp. Dig.*, June 2004.

[203] A. Garcia-Lamperez, T. K. Sarkar, and M. Salazar-Palma, "Generation of accurate rational models of lossy systems using the Cauchy method," *IEEE Microwave Wireless Compon. Lett.*, vol. 14, pp. 490–492, Oct. 2004.

[204] H. Yao, X. Liang, K. A. Zaki, and A. Martin, "Wide-band waveguide and ridge waveguide T-junctions for diplexer applications," *IEEE Trans. Microw. Theory Tech.*, vol. 41, pp. 2166–2173, Dec. 1993.

[205] S. B. Cohn, "Properties of ridge waveguide," *Proc. IRE*, vol. 35, pp. 783–788, Aug. 1947.

[206] S. Hopfer, "The design of ridged waveguide," *IRE Trans . Microwave Theory Tech.*, vol. 5, pp. 20–29, Oct. 1955.

[207] A. M. K. Saad, J. D. Miller, A. Mitha, and R. Brown, "Analysis of antipodal ridge waveguide structure and application on extremely wide stopband lowpass filter," *Proc. 1986 IEEE MTT-S Int. Microwave Symp. Dig.*, pp. 361–363.

[208] A. M. K. Saad, "Novel lowpass harmonic filters for satellite application," *Proc. 1984 IEEE MTT-S Int. Microwave Symp. Dig.*, pp. 292–294.

[209] A. M. K. Saad, "Length reduction of evanescent-mode ridge waveguide bandpass filters," *Proc. 2001 IEEE MTT-S Int. Microwave Symp. Dig.*, pp. 1491–1494.

[210] Z. M. Liu, J. A. Ruiz-Cruz, C. Wang, and K. A. Zaki, "An extremely wideband ridge waveguide filter," *Proc. 2004 IEEE MTT-S Int. Microwave Symp. Dig.*, pp. 615–618.

[211] X. P. Liang, K. A. Zaki, and A. E. Atia, "A rigorous three plane mode-matching technique for characterizing waveguide T-junctions, and its application in multiplexer design," *IEEE Trans. Microw. Theory Tech.*, vol. 29, pp. 2138–2147, Dec. 1991.

[212] R. A. Kishek, "Multipactor discharge on metals and dielectrics: Historical review and recent theories," *Physica of Plasmas*, vol. 5, pp. 2120–2126, May 1998.

[213] C. Vicente, M. Mattes, D. Wolk, H. Hartnagel, J. Mosig, and D. Raboso, "Multipactor breakdown prediction in rectangular waveguide based components," *Proc. 2005 IEEE MTT-S Int. Microwave Symp. Dig.*, June 2005.

[214] A. Sivadas, M. Yu, and R. Cameron, "A simplified analysis for high power microwave bandpass filter structures," *Proc. 2000 IEEE MTT-S Int. Microwave Symp. Dig.*, June 2000.

[215] C. Wang and K. A. Zaki, "Analysis of power handling capacity of bandpass filters," *Proc. 2001 IEEE MTT-S Int. Microwave Symp. Dig.*, June 2001.

[216] M. Ludovico, L. Accatino, and M. Mongiardo, "CAD of multipactor-free waveguide components for communication satellites," *Proc. 2002 IEEE MTT-S Int. Microwave Symp. Dig.*, June 2002.

[217] A. Woode and J. Petit, "Diagnostic investigations into multipactor effect, susceptibility zone measurement and parameters affecting a discharge," *ESTEC Working Paper*, no. 1556.

[218] D. Wolk, D. Schmitt, and T. Schlipf, "Novel approach for calculation the multipaction threshold level in multicarrier operation," *Workshop on Multipactor, RF and DC corona and Passive Intermodulation in Space RF Hardware*, Sept. 2000.

[219] S. J. G. Strijk, *Multipactor Calculator*. http://multipactor.esa.int/, Noordwijk, The Netherlands: ESA/ESTEC, 2005.

[220] M. Makimoto and S. Yamashita, *Microwave Resonators and Filters for Wireless Communication*. New York, NY: Springer, 2001.